Scuola Universitaria Superiore IUSS Pavia

INSIGHTS INTO THE SEISMIC RESPONSE OF PILE SUPPORTED WHARVES SUBJECTED TO LIQUEFACTION-INDUCED GROUND DEFORMATIONS: IMPLICATIONS FOR DESIGN.

A Thesis Submitted in Partial Fulfilment of the Requirements
for the Degree of Doctor of Philosophy in

EARTHQUAKE ENGINEERING AND ENGINEERING SEISMOLOGY

Obtained in the framework of the Doctoral Programme in
Understanding and Managing Extremes

by

Ricardo Rodríguez Plata

April, 2024

Scuola Universitaria Superiore IUSS Pavia

INSIGHTS INTO THE SEISMIC RESPONSE OF PILE SUPPORTED WHARVES SUBJECTED TO LIQUEFACTION-INDUCED GROUND DEFORMATIONS: IMPLICATIONS FOR DESIGN

A Thesis Submitted in Partial Fulfilment of the Requirements

for the Degree of Doctor of Philosophy in

EARTHQUAKE ENGINEERING AND

ENGINEERING SEISMOLOGY

Obtained in the framework of the Doctoral Programme in

Understanding and Managing Extremes

by

Ricardo Rodríguez Plata

Supervisors: Prof. Carlo G. Lai, University of Pavia

Prof. Misko Cubrinovski, University of Canterbury

April 2024

ABSTRACT

Current seismic design provisions and guidelines for the seismic design of pile-supported wharves (PSWs) explicitly require considering the combined effect of kinematic and inertial loads. However, there is a lack of consensus regarding the adequate simplified methodologies for assessing and combining inertial and kinematic loads for cases in which the wharf structure is subjected to liquefaction-induced lateral spreading ground deformations. Current seismic design provisions and guidelines are based on the distinction between cases of no-liquefaction and cases of liquefaction. The present study showed that the seismic demands on PSWs can be represented following more general framework, that makes distinction between cyclic and lateral spreading phases (or components) of the response. Meaning that, for a given soil deposit, the relative importance of the cyclic and lateral spreading phases is determined by the earthquake intensity. This was achieved by making extensive use of time-history effective stress dynamic-soil-structure interaction analyses to estimate the seismic response and seismic demands on pile-supported wharves founded on liquefiable ground.

Two case studies were considered, one large diameter PSW located in southern Italy, and one small diameter PSW located in Wellington, New Zealand. The former is found on a heterogenous medium-to-dense sand deposit, while the latter is placed atop of an uncompacted gravelly land reclamation. Numerical simulations were conducted with FLAC. In both cases, advanced soil constitutive models were used to capture the response of the liquefiable ground, namely PM4Sand and SDm (Stress-Density model). These models were successfully calibrated to well-known empirical liquefaction triggering relationships. Likewise, the analyses also considered the non-linear response of the wharf structure by employing a distributed plasticity model. This strategy (1) ensured the rigorous modelling of modes of deformation and interaction between soil and wharf, and (2) maintained consistency with performance-based earthquake engineering assessments.

The large diameter PSW, wharf BAF, was subjected to a more extensive probabilistic seismic demand analysis. In this case, the epistemic uncertainty, represented by using PM4Sand and SDm in parallel, was systematically addressed during the different stages of the study. In essence, for this typology of wharves, inertial demands estimated for the cyclic phase, are well captured by simplified displacement-based methodologies, while kinematic loads were well correlated to 1D ground response estimates. Kinematic loads for the lateral spreading were insensitive to the inertial loads and proved more difficult to be predicted by 1D site response parameters. Lateral spreading displacements were highly dependent on

(1) the post-liquefaction strain rate reproduced by the constitutive models, (2) ground motion characteristics.

In terms of optimal intensity measures, the seismic demand analysis reveals that the modified acceleration spectrum intensity, MASI, is the most suitable candidate for an optimal intensity measure as in resulted in large correlation with all the response parameters considered, while ranking high in proficiency.

ACKNOWLEDGEMENTS

This document is the result and final expression, not of my effort or dedication, but of the support and inspiration I received from the people of all the communities I had the honor to be part of during these years. This manuscript is for them, for my family, my tenacious mother Martha, and sister Sara, my inspiring father Jairo, my supportive uncles Juan and Néstor, and for my little nephew Ismael. To Paula, my lifelong friend, for her staunch support. And to my cherished Hilal, who accompanied me during the steepest tracks of this journey.

I thank my supervisors Prof. Carlo Lai and Prof. Misko Cubrinovski for their continuous support and superb guidance. I am equally honoured and grateful for having the chance of working aside – literally desk apart from – great researchers, in Christchurch Ribu Dhakal, and in Pavia Ali Özcebe and Guido Andreotti. Few other people on this earth have endured FLAC as the four of us had. To my mates and friends in Pavia, Bryan, Berny, Deniz and Du, who added a valuable personal dimension to my PhD experience. Last but not least, I would have not dare to embark on this enterprise if it were not by the inspiration and mentorship I received during my bachelor in Colombia, by the team made of Ing. Hector Garcia Manchola, Ing. William Valencia Mina and Dr. Luis Eduardo Peña.

From the Colombian Andes,
through the Canterbury Plains,
to the Po Plain,
¡Gracias totales!

TABLE OF CONTENTS

LIST OF FIGURES

LIST OF TABLES

1. INTRODUCTION

1.1 MOTIVATION OF THE STUDY

Wharves, and berthing structures in general, are fundamental components of seaports. Past seismic events have caused significant losses and have hindered the operational capacity of seaports. Liquefaction and lateral spreading ground failures have ranked first in terms of damaged caused to waterfront structures and land reclamations. In most caused the severity of the damage impair the normal functioning of the ports, which in turn reduced the resilient capacity of the affected community due to the lack of timely humanitarian aid and inefficient post-emergency recovery operations. Notable examples include the failure of the Takahama Wharf at the port of the city of Kobe due to the widespread liquefaction triggered by the Mw 6.9 Great Hanshin earthquake of 1995 (PIANC, 2001); the collapse of the main wharf at the port of Port-au-Prince, Haiti, caused by the Mw 7.0 event of 2010 (Green et al., 2011); the severe damaged Thorndon Wharf at the port of Wellington in New Zealand after the Mw 7.8 Kaikōura earthquake of 2016 (Cubrinovski et al., 2017)

Therefore, recognizing the importance of berthing structures, special attention has been devoted to revising and updating the seismic design guidelines and procedures for berthing structures over the past two decades. After the pioneering work of the International Navigation Association (PIANC) in 2001 (PIANC, 2001) several other standards have been established, such as the ASCE 61-14 standard for the seismic design of piers and wharves (ASCE, 2014); the Japanese technical standards for port and harbour facilities (OCDI, 2020), the Port of Long Beach wharf design criteria (POLB, 2012), the Port of Los Angeles code for seismic design, upgrade and repair for container wharves (POLA, 2010). All these standards have made headway for the adoption of performance-based design philosophies, particularly for pile-supported wharves. Therefore, the recommended or required design criteria directly address the operationality of these structures after earthquake events, as well as their repairability.

For sites that are likely to exhibit liquefaction-induced lateral spreading, current seismic design provisions and guidelines explicitly require considering the combined effect of kinematic and inertial demands on pile-supported wharves. However, there is a lack of consensus regarding (1) procedures for the adequate assessment of kinematic and inertial demands on the piles, and (2) for the simultaneous application of these loads during simplified analysis procedures. Moreover, in such cases, seismic design, and consequence analysis for pile-supported wharves, as well as for soil-structure systems in general, would require the execution of complex numerical analyses capable of producing reliable estimates

of design and performance quantities. Increasing the uncertainty, and the conservativeness of the estimates produced by simplified approaches.

1.2 RESEARCH OBJECTIVES

This study aims at progressing the current level of knowledge about the assessment and combination of kinematic and inertial loads on pile-supported-wharves founded on liquefiable ground by means of time-history, non-linear, 2D, plain strain, effective-stress, dynamic-soil-structure interaction analyses (DSSI), hereby referred as to effective stress DSSI analyses, of two case studies. The deep waters dock at the Port of Gioia Tauro in Italy (wharf BAF), and the Thorndon Container Wharf (TCW) at the Port of Wellington, New Zealand. The former is a large diameter pile-supported wharf founded on a naturally deposited heterogeneous sandy and gravelly soils. It constitutes the main case study for this thesis, while the study of the TCW is presented as a validation case of the numerical methodology.

The main objectives of this study are, first, to underscore the key features, of the seismic response and performance of wharf BAF, as well as their evolution with earthquake intensity, by means of effective stress DSSI analyses. This objective has two dimensions, one addresses the response of the liquefiable deposit, and the other the kinematic and inertial demands estimated on the piles.

Second, to underscore the effect of epistemic uncertainty on the estimated system response by employing two different constitutive models for the liquefiable materials, namely, PM4Sand (v3.1) developed by Boulanger and Ziotopoulou (2017), and SDm (v1.1) developed by Cubrinovski and Ishihara (1998a, 1998a).

Third, to test the current assumptions and recommendations about the procedures for the assessment of kinematic and inertial loads on pile-supported-wharves, as well as indicating potential modifications. This is achieved by considering the event-to-event variability of the ground motion through a multiple stripe analysis, using a suite of 35 records for 5 different hazard levels (Bradley et al., 2010; Mackie and Stojadinović, 2005; Vamvatsikos and Fragiadakis, 2009). Note that the third objective is transversal with the second, as it also considers the systematic comparison between the results produced by PM4Sand and SDm.

Furthermore, this thesis preliminarily addresses two additional issues and establishes the groundwork for future studies. Firstly, it tackles the selection of optimal intensity measures for the seismic demand modelling (within the performance-based earthquake engineering framework proposed by Cornell et al., 2002) of large-diameter pile-supported wharves which are typologically similar to wharf BAF. This objective is pursued through the utilization of the multiple stripe analysis outlined in the third research objective. Secondly, it involves identifying relevant model parameters through a global, variance-based, yet

straightforward sensitivity analysis, pertinent to the probabilistic treatment of the response of wharf BAF.

1.3 ORGANIZATION OF THE THESIS

This thesis is subdivided into 7 chapters including the introduction and conclusion. The 5 chapters represented the core of the manuscript are described as follows:

- **Chapter 2. Background.** This chapter addresses introduces the reader to the fundamental aspects of the two primary subjects of the thesis: the seismic response and seismic design of marginal pile-supported wharves, and the constitutive modelling of liquefiable soils. introduces the constitutive models used in the study, PM4Sand and SDm, highlighting key differences and similarities.
- **Chapter 3. Seismic response of the Thorndon Container Wharf at Centre Port, Wellington, New Zealand.** Given that this thesis revolves around the insights gained from effective stress DSSI analyses, Chapter 3 serves as a validation case for of the numerical methodology. It presents the overall framework of the numerical modelling strategy, and interpretation of results, which are compared against measurements of lateral spreading displacements and surface recordings made at the Port of Wellington after the Kaikōura earthquake of 2016.
- **Chapter 4. Effective stress seismic response of large diameter pile-supported wharves founded on liquefiable ground, case study of the port of Gioia Tauro, Southern Italy.** The deepwater dock BAF of the port of Gioia Tauro is supported by four rows of reinforced concrete piles, 1.5m in diameter each. This chapter examines the seismic response of wharf BAF effective stress DSSI analyses. A hazard-compatible ground motion record is used as input excitation, scaled with to three different PGA levels. Epistemic uncertainty in numerical modelling of the soil behaviour is addressed using two different advanced constitutive models tailored for soil-liquefaction, namely PM4Sand and SDm. Attention is given to performance of the trailing row of piles by examining the critical loading cycles causing peak inertial and kinematic seismic demands. The analysis also underscores the evolution of damage and lateral spreading ground distress with ground motion.
- **Chapter 5. Seismic demand analysis of large diameter pile supported wharves, case study of the port of Gioia Tauro, Southern Italy.** Following the characterization of the system response made in the previous chapter, this chapter addresses the seismic performance of wharf BAF by the means of a multiple stripe analysis, which considers the interevent variability of ground motion for different hazard levels. Seismic demands are characterized following a probabilistic framework. Current assumptions and methodologies for the assessment of inertial and kinematic demands are tested against the results of the numerical simulations. Moreover, this chapter also addresses the issue of the identification of optimal intensity measure for future studies. A total of 15 intensity measures are ranked

according to the efficiency and proficiency criteria defined by Cornell et al. (2002) and Mackie and Stojadinović (2005)

- **Chapter 6. Treatment of model uncertainties for 2D effective stress analyses: local vs global sensitivity studies.** Finally, this chapter lays the framework for the handling of model uncertainty regarding the input parameters used for the effective stress DSSI analysis by means of simple, yet insightful, global sensitivity study proposed by Saltelli (2008)

2. BACKGROUND

2.1 INTRODUCTION

Berthing structures are key components of seaport infrastructure, given that they provide a stable surface for the mooring and cargo handling operations of container vessels. They are usually classified as open or closed depending on whether they allow seawater to flow below platform level (see Figure 2.1). Marginal wharves are long grade-level platforms build parallel to the shoreline. Piers, in other hand, are platforms extended into the navigable body of water, built on or over the grade. The deck (or platform) can be made of wood or reinforced concrete depending on the wharf functionality, and it usually supported on several rows of piles made of wood, concrete, or steel.

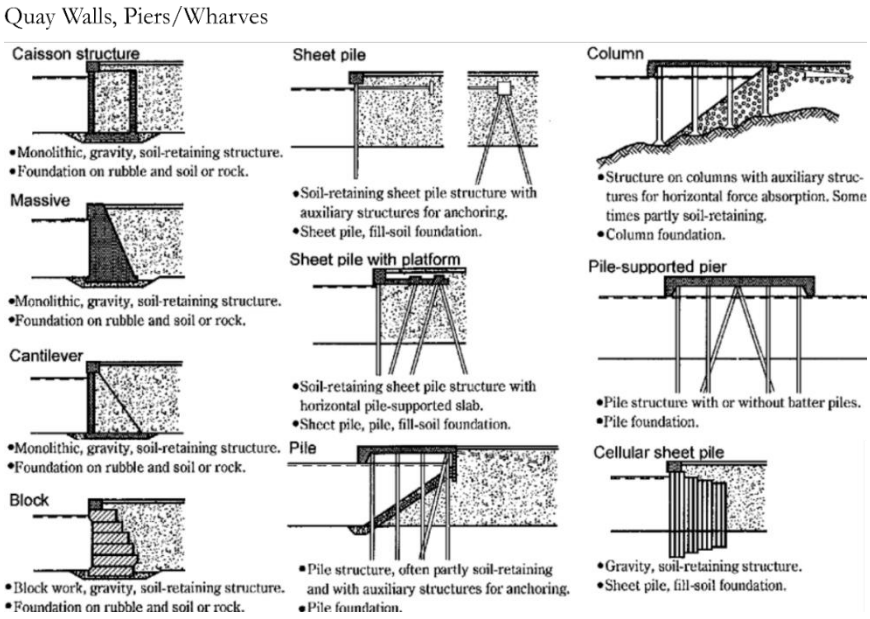

Figure 2.1. Schematics of different typologies of berthing structures. Adapted from PIANC (2001).

The sustained growth in global trade over the last three decades has propelled the expansion of container ports worldwide. In most of the cases port authorities have commissioned expansion works to host additional berthing structures that are usually built on reclaimed land, or along excavated or dredged canals. Sengupta and Lazarus (2023) performed a remote sensing analysis to estimate the growth of land reclamations, between 1990 and 2020, of container ports for 65 of the world's top 100 container seaports by traded volume. The map of Figure 2.2 shows the location of these ports with circles representing the reclaimed land between 1990 and 2020. Fifty-eight ports saw their seaward area expanded by at least two folds, 39 of those quadrupled it. When contrasting Figure

2.2 against the global earthquake hazard map, of Figure 2.3, developed by the GEM foundation (Johnson et al., 2023), it is evident that a great proportion of the seaport expansion took place in areas of high seismic hazard in the Indo-Pacific, the Mediterranean basin and in the Middle East.

Man-made fills and natural soil over which seaports are built have been particularly susceptible to severe liquefaction-induced ground deformations. Non-surprisingly, lateral spreading has been a major cause of earthquake-induced damage to wharves, piers, and other types of waterfront structures. Salient examples are: the failure of the Takahama Wharf at the port of the city of Kobe due to the widespread liquefaction triggered by the Mw 6.9 Great Hanshin earthquake of 1995 (PIANC, 2001); the collapse of the main wharf at the port of Port-au-Prince, Haiti, caused by the Mw 7.0 event of 2010 (Green et al., 2011); the severe damaged Thorndon Wharf at the port of Wellington in New Zealand after the Mw 7.8 Kaikōura earthquake of 2016 (Cubrinovski et al., 2017); among others.

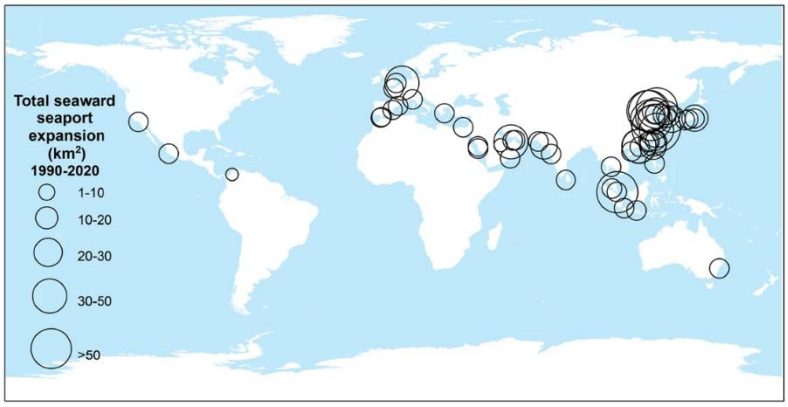

Figure 2.2. World map showing the geographic distribution of 65 of the world's top 100 examples. port by traded volume, circle size indicates the relative magnitude of the seaward land reclamation between 1990 and 2020. Adapted from Sengupta and Lazarus (2023).

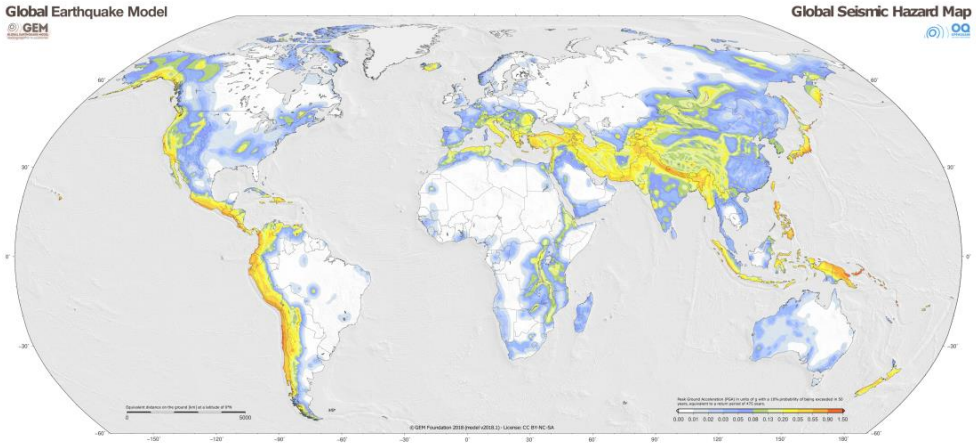

Figure 2.3. GEM Foundation's Global earthquake hazard map (Johnson et al., 2023).

Seismic design codes and guidelines for seaport infrastructure mandate the consideration of liquefaction-induced deformations and dynamic soil-structure-interaction (DSSI) effects. DSSI involves two interrelated load-transfer mechanisms. During intense shaking, the superstructure's response imposes loads on the soil through the foundation, resulting in inertial interaction effects. Conversely, kinematic interaction effects take place in the near field (i.e. near or at the foundation), where the presence the foundation alters the ground response, while also being loading by the surrounding soil.

In liquefiable ground conditions, kinematic effects manifest as excessive ground movement affecting the foundation. For flexible structures like pile-supported wharves, such conditions lead to significant strains in both the subsoil and wharf. Capturing compatible modes of deformation between piles and soil is thus crucial for assessing kinematic and inertial demands, and overall seismic performance of the wharf. For such scenarios, advanced numerical simulations, as discussed in this monograph, are among the few tools adequate to analyze and provide reliable estimates, provided that the modelling assumptions and methodologies are systematically validated.

The first half of this chapter provides a review on the current knowledge about the seismic performance and seismic design guidelines for pile-supported wharves. It will focus on: (1) notable case histories of earthquake-induced failures of wharves and piers, and (2) seismic design aspects for pile-supported wharves. The latter includes the review of building code provisions, design guidelines, and insights from centrifuge tests and numerical simulations.

The final section of the chapter delves into key concepts concerning liquefaction-induced lateral spreading and constitutive modelling of coarse-grained liquefiable soils. These concepts serve as the cornerstone for advanced dynamic effective-stress numerical

simulations, which are essential for accurately predicting the behaviour of pile-supported wharves under seismic loading conditions.

2.2 SEISMIC RESPONSE AND PERFORMANCE-BASED DESIGN OF PILE-SUPPORTED WHARVES.

2.2.1 Seismic performance of pile-supported wharves during past earthquakes

Seismic events have caused significant damage and losses on berthing and approach structures, including piers, wharves, and jetties, due to a combination of complex dynamic-soil-structure interaction (DSSI) and/or by earthquake-induced ground failures. Earthquake-induced soil liquefaction and lateral spreading have certainly bean among the major causes of earthquake-induced damage to seaport and waterfront infrastructure. Considering this, the present section summarizes the key insights gained from case histories of earthquake-induced failures and damage to pile-supported approach and berthing structures. Case histories are presented in chronological order.

The Mw 6.3 Great Hashin earthquake of 1995 produced extensive liquefaction to land reclamations in the Kobe-Osaka Bay in Japan. The excessive ground deformation and strong ground shaking caused severe damage and near collapses of several berthing structures. Figure 2.4 shows a schematic of the reinforced-concrete, pile-supported Takahama Wharf, at the Kobe Port. The wharf displaced seawards for about 1.6m due to the liquefaction of an alluvial sand formation at the base of the dike. Damage concentrated at the in-ground sections of the piles and at the pile-deck connections (PIANC, 2001). Large strains concentrated inside the deep alluvial sand layer, producing double plastic hinges in the piles that compromised the functionality of the wharf.

The Mw 6.9 Loma Prieta earthquake of October 1989 caused extensive damage in the San Fracisco Bay area. Soil liquefaction caused moderate to severe damage at the Marina District north of the city; at Treasure Island; and along the East San Francisco Bay shore, where the port of the city Oakland is located. At the port, hydraulically placed and end-dumped fills liquefied causing lateral spreading, sand boils, and other ground distress that damaged the port facilities (Kayen et al., 1998). Lateral spreading was most severe at the Marine Container Terminal, where large cracks and fissures occurred on the pavement cover with vertical offsets of measuring 0.3 m. Most of the wharves at the time were supported on vertical reinforced concrete piles with the exception of the two trailing rows of the 7th Street Terminal Wharf, which were battered to provide additional shear resistance (Seed et al., 1991). Figure 2.5 depicts the cross section of the wharf prior to the earthquake (Figure 2.5a) along with a photograph showing a damaged connection between a group of battered piles and the deck of the wharf (Figure 2.5b). The pile-caps of these piles suffered massive damage. Seed et al. (1991) concluded that failure at the battered-piles-deck connections resulted from excessive concentration of shear stresses due to the large lateral stiffness contrast between the battered piles and the compliant surrounding soil that underwent liquefaction. As a result, the battered piles were replaced with vertical piles.

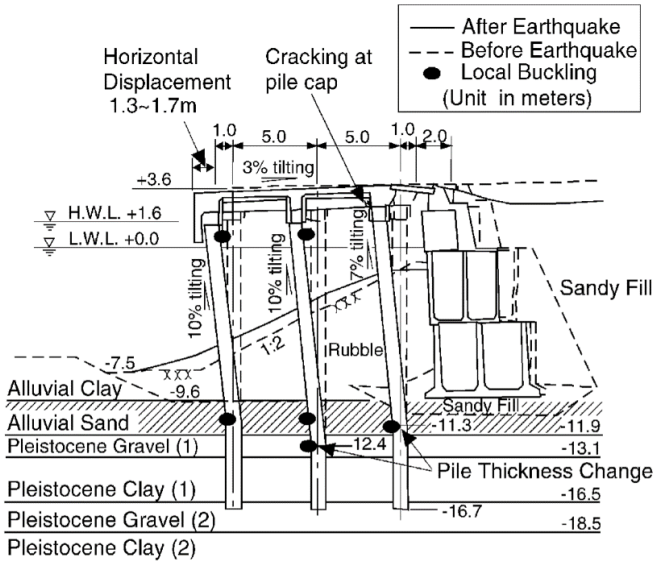

Figure 2.4. Schematic representation of the damage caused by the Great Hashin earthquake, of 1995, to a section of the Takahama Wharf, Kobe Port, Japan. Taken from (PIANC, 2001)

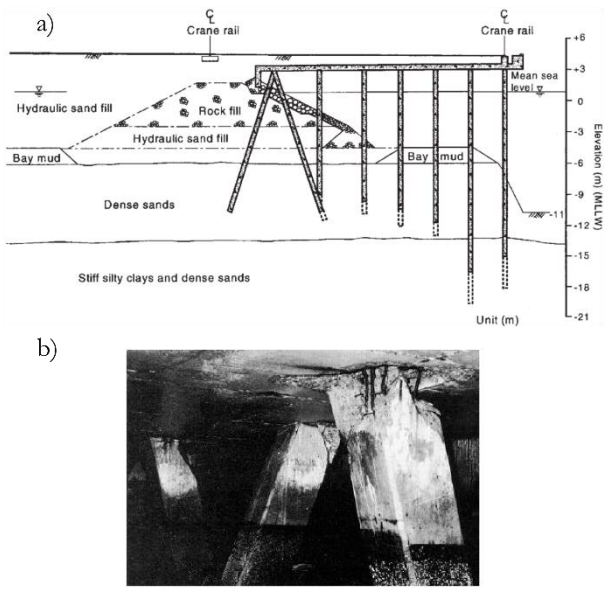

Figure 2.5. Schematic cross section of the 7th Street Terminal Wharf located at the port of Oakland (a) displaying relevant soil units and the original layout of the rows of piles supporting the wharf before the Mw 6.9 Loma Prieta earthquake of October 1989, as reported by Seed et al. (1991). Photo of a severely damaged battered pile-deck connection, taken from Razavi et al. (2007)

The Mw 9.1 Sumatra earthquake of December 25, 2004, caused extensive damage to pile-supported harbour structures in the Adaman Islands in India. The isles were approximately 1000 km North-West from the epicentre. The earthquake resulted in severe damage and rendered non-operational at least 10 approach structures including wharves, piers, and jetties. The most common type of damage observed was shear failure of trailing piles, which are characterized by a relatively shorter unsupported length and larger ground embedment. As consequence, the connections between the deck and trailing piles experienced the highest shear demands. Figure 2.6 exemplifies this type of failure documented by Mondal and Rai (2008).

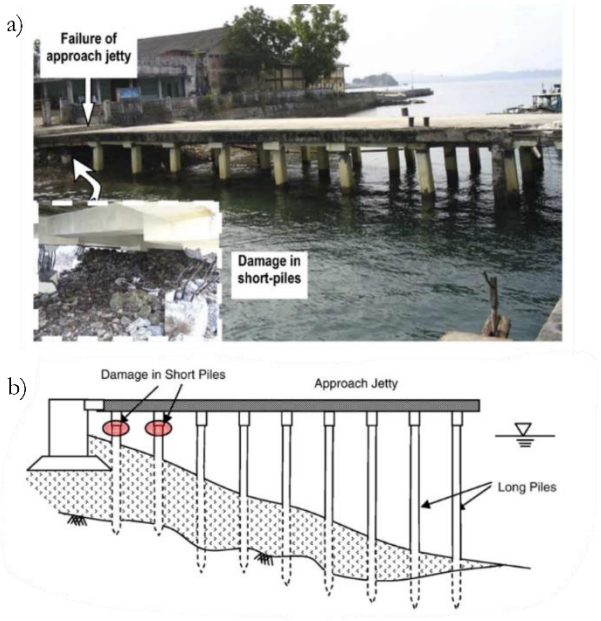

Figure 2.6 Damage to the trailing piles of a approach jetty at Mayabandar harbour in Middle Andaman Islands, as reported by Mondal and Rai (2008)

The Mw 7.0 2010 Haiti earthquake left the Part-au-Prince (PaP) seaport mostly inoperative due to widespread liquefaction-induced damage and lateral spreading. The site-to-source distance for the port was 20 to 25 Km. The state of the port after the event was such that emergency aid and post-recovery efforts took weeks to arrive. Before the earthquake, the North Wharf was the main berth of the port. It collapsed due to the lateral spreading of the relatively clean (FC<5%) calcareous hydraulic fill that was placed during the late 1970's (Green et al., 2011). The berth was a marginal wharf, supported on 0.45x0.45m precast, prestressed concrete piles spaced at 6.7m. Green et al. (2011) reported cumulative crack width measurements of the order of 2.6m in a zone extending 30 to 50m inland from the wharf. Figure 2.7a shows a photograph of the North Wharf taken immediately after the mainshock, while Figure 2.7b shows a photograph of the adjacent container yard, equally damaged by the lateral spreading ground. Extensive cracking and sand ejecta are also evident in the background of Figure 2.7a. The North Wharf was left almost submerged. The same authors performed simplified liquefaction and lateral spreading assessments following the methods proposed by Youd (2002), Rauch and Martin (2000), Zhang et al. (2004) and Idriss and Boulanger (2008). Despite of underestimating the field measurements, the simplified analyses estimates were large enough (around 1.7m) to highlight the need for liquefaction mitigation measures and retrofit of the wharf.

Figure 2.7. Lateral spreading damage to the North Wharf of the Port-au-Prince seaport after 2010 Haiti earthquake. Taken from Green et al. (2011).

On the 27 of February of 2010, along the coast of Chile, a 560 km long section of the Pacific Plate slipped beneath the South American Plate triggering a M_w 8.8 seismic event. The massive earthquake caused severe damage to the harbour and seaport infrastructure of the Bio-Bio region in central Chile, roughly 95 km from the epicentre. The map in Figure 2.8 shows the location of the damaged facilities (Brunet et al., 2012); 10 pile-supported piers, two quay walls, one pile-supported wharf and one jetty. Soil-liquefaction was triggered at all these sites with only two exceptions (see Table 2.1), becoming one of the major sources of damage. Eight of the 11 pile-supported structures experienced severe damage or failure at their pile deck connections. This was partly due to liquefaction-induced lateral spreading, and tpartly due to excessive shear stress concentration at the pile-deck level (Brunet et al., 2012; Ledezma and Tiznado, 2017).

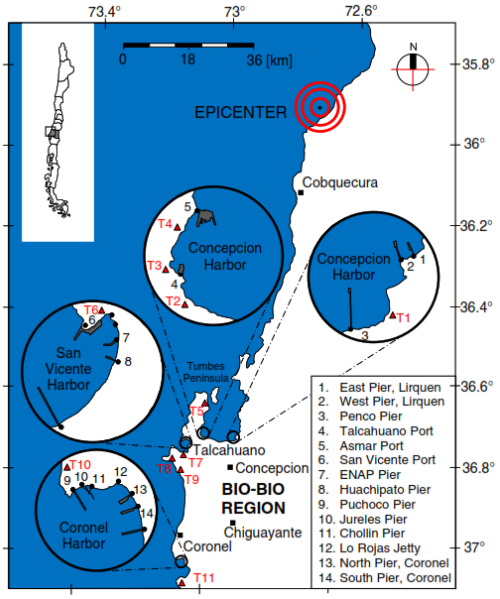

Figure 2.8. Map of the harbour and seaport infrastructure damaged by the M_w 8.8 2010 Maule earthquake. Taken from Brunet et al. (2012).

Brunet et al. (2012) documented the damage distribution along the North Pier at the main port in the city of Coronel, Figure 2.9 summarizes the key findings. The pier is a 500m long berthing structure used for the loading and unloading operations of bulk cargo. Damage caused by the earthquake concentrated at the approach zone (i.e., near the shoreline) and at the berthing zone. As in the case of the Adaman Islands, short piles in the approach zone were among the most damaged elements, out of 139 vertical piles, 6 failed at this section of the pier. In fact, Figure 2.9a shows the distribution of the vertical piles, as evident, the concentration of shear stiffness in the approach section is not only due to the shorter length of the piles but also due to the larger number of piles built in this zone. Due to the length of the pier, the eccentric distribution of lateral stiffness favours large concentrations of shear force at the deck when loaded laterally, but also in case of torsional vibration. Ground displacements were non-uniform along the length of the pier, the approach zone was affected by lateral spreading movements (see Figure 2.9d), while the remaining portion of the pier experienced ground deformations akin to free-field conditions (Brunet et al., 2012). This situation, together with the larger lateral stiffness of the batter piles located towards the berthing end (not shown in Figure 2.9), caused shear failures on 27% of the 169 battered piles supporting the pier.

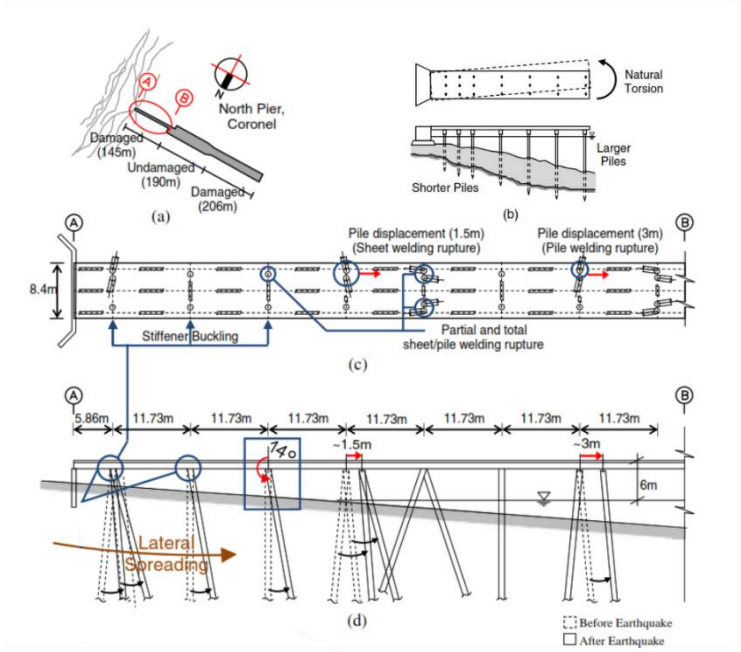

Figure 2.9. Distribution of the earthquake-induced damage of the approach end of the North Pier in the city of Coronel, Chile, after the M_w 8.8 Maule earthquake of 2010 in. Adapted from (Brunet et al., 2012). General plan view of the pier (a). Schematic of the short pile effect and natural torsion (b). Pan view of the approach zone (c). Cross section of the approach zone (d)

Table 2.1 Damage to harbour and seaport structures along the Bio-Bio coast caused by the M_w 8.8 2010 Maule earthquake (Chile). Adapted from Brunet et al. (2012).

Structure ID	Structure type	Liquefaction	Lateral Spreading	Damaged batter pile-deck connection	Other structural damage
1	PSP	X	-	X	X
2	PSP	-	-	-	X
3	PSP	X	-	X	X
4	Quay wall	X	-	-	X
5	Quay wall	-	-	-	X
6	PSW	X	X	-	X
7	PSP	X	-	X	X
8	PSP	X	X	X	X
9	PSP	X	X	-	X
10	PSP	X	X	-	X
11	PSP	X	X	-	-
12	Jetty	X	X	X	X
13	PSP	X	X	X	-
14	PSP	X	X	-	-

*PSP: Pile-supported-pier

*PSW: Pile-supported wharf

2.2.2 Characteristics of lateral spreading ground deformations

The Mw 6.3 Great Hashin earthquake of 1995 caused extensive liquefaction-induced damage in the Port Island district of the city of Kobe, a man-made reclaimed island. Caisson quay walls moved as much as 3 to 4m into the sea. By measuring crack-opening widths, Ishihara et al. (1997) determined that the liquefaction-induced lateral ground movement and settlements were most severe within the first 30 m measured from the waterfront, yet ground distortion was evident up to 150 m inland. From this and other observations from the lateral spreading failures caused by the Kobe earthquake, Ishihara et al. (1997) stated that the affected area behind the waterfront could be subdivided into two zones of non-uniform and uniform spreading (see Figure 2.10). The largest ground movements, along both vertical and horizontal directions, concentrate inside the non-uniform spreading zone, in which notable cracks and vertical offsets occur. Ground displacements diminishes as one moves further inland until no crack or fissures are visible. Reaching the uniform spreading zone, the ground would still exhibit a lateral residual displacement, and liquefaction-induced damage would be mainly due to settlements or loss of bearing capacity.

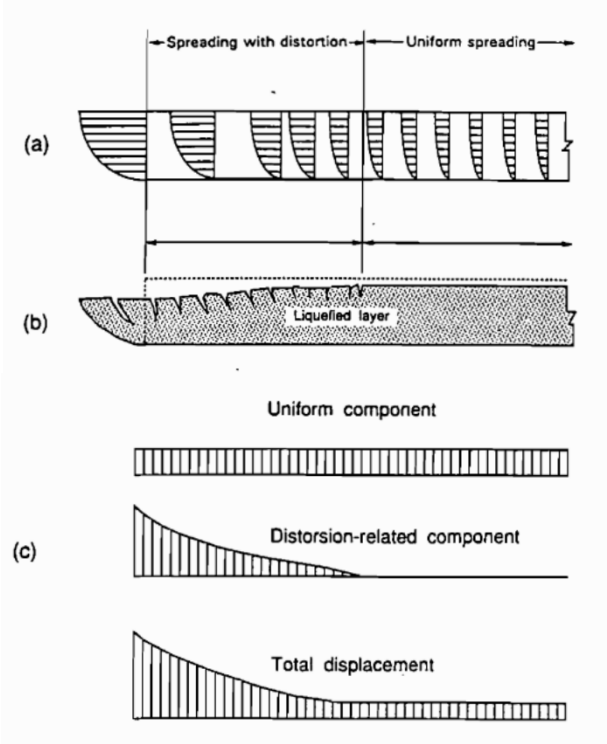

Figure 2.10. Schematics of the different components of liquefaction-induced lateral spreading displacements as interpreted from the field measurements done after the Mw 6.3 Great Hashin earthquake of 1995 by Ishihara et al. (1997).

2.2.3 Seismic design of pile-supported wharves

Beginning with the pioneering work of the International Navigation Association (PIANC) in 2001 (PIANC, 2001), the past two decades have seen significant progress in the development of seismic codes and standards for the performance-based seismic design of piers and wharves. Prominent examples include the latest ASCE 61-14 Standard for the Seismic Design of Piers and Wharves (ASCE, 2014); the Japanese Technical Standards for Port and Harbour Facilities (OCDI, 2020), the Port of Long Beach Wharf Design Criteria (POLB, 2012), the Port of Los Angeles Code For Seismic Design, Upgrade And Repair for Container Wharves (POLA, 2010), among others.

Consistent with modern building code provisions, PIANC (2001) and ASCE (2014) introduced a taxonomy of performance grades, or design classes, for port components, that are to be assigned to by stakeholders. According to these standards, for each seismic hazard level the wharf design should comply with safety, serviceability, and repairability requirements of the corresponding grade or class. Performance criteria represent allowable limits expressed in terms of damage states. Table 2.2 shows an excerpt of the minimum

seismic hazard and performance requirements for the design classification defined by the ASCE 61-14 (ASCE, 2014). Seismic hazard for the Operating Level and Contingency Level earthquakes are defined in terms of probabilities of exceedance in a 50-year period. Actions for the Design Level Earthquake take their definition from ASCE 07-05.

Table 2.3 contains similar information from PIANC's guidelines, it considers two different hazard levels, referred as to L1 and L2, each attached to a ground motion probability of exceedance over the lifespan of the structure of 50% and 10% respectively. Lifespan and performance grade are predefined by the stakeholder. POLA and POLB established a slightly different scheme, whereby the seismic hazard and performance requirements are unified into a single classification, they specify nearly identical performance requirements. In contrast, while providing a more in-detail definition of damage states, PIANC (2001) adopts two hazard levels, limited to those equivalents to OLE and CLE of ASCE (2014).

ASCE 61-14, POLA and POLB adopted nearly identical taxonomies of performance levels (i.e., damage states). Table 2.4 contains a summary of the maximum material strains prescribed by these guidelines for each performance level, for reinforced concrete piles supporting piers or wharves. Damage criteria defined by PIANC (2001) are also defined in terms of system performance parameters, such as residual displacements, and peak stresses (i.e., seismic demands) on the reinforce concrete elements, see Table 2.1Table 2.5. Table 2.6 relates to the reinforced concrete strain limits. The ultimate concrete compressive referenced by (PIANC, 2001) is based on the model proposed by Priestley et al. (1992) and expressed in Equation (2-1).

$$\varepsilon_{cu} = 0.004 + \frac{1.4\rho_s f_{yh}\varepsilon_{sm}}{f'_{cc}} \leq 0.005 \tag{2-1}$$

Where, ρ_s and f_{yh} are the effective volume ratio and yield stress of the confining steel; ε_{sm} is the strain at peak strength of the reinforcement steel; f'_{cc} the confined strength of concrete, approximated as 1.5f'c; being f'_c the compressional resistance of concrete at 28 days.

Table 2.2 ASCE 61-14 Minimum Seismic hazard and performance requirements (ASCE, 2014).

	Design classification	Operating level earthquake (OLE)	Contingency level earthquake (CLE)	Desing Earthquake (DE)
Ground motion probability of exceedance	High	50% in 50 yr (T_R = 72 yr)	10% in 50 yr (T_R = 475 yr)	Desing earthquake as per ASCE 07-05: effects correspond to 2/3 of those of the maximum considered earthquake (MCE*)
	Moderate	N/A	20% in 50 yr (T_R = 224 yr)	
	Low	N/A	N/A	
Performance level	High	Minimal Damage	Controlled and repairable damage	Life safety protection
	Moderate	N/A	Controlled and repairable damage	
	Low	N/A	N/A	

*MCE: Maximum considered earthquake, 2% probability of exceedance in 50 years (T_R=2475 yr)

Table 2.3. PIANC design guidelines minimum seismic hazard and performance requirements (PIANC, 2001).

		Ground motion Level 1	Ground Motion Level 2
Ground motion probability of exceedance		50% in the lifespan of the structure	10% in the lifespan of the structure
Performance level	Grade S	Serviceable	Serviceable
	Grade A	Serviceable	Repairable
	Grade B	Serviceable	Near Collapse
	Grade C	Repairable	Collapse

All the guidelines recommend, or require, the wharf design to comply with a weak-pile strong-deck philosophy, whereby the deck is the capacity protected member. Pile damage is expected to occur at the cap level upon strong shaking while the integrity of the deck is maintained. Damage to the in-ground sections of the piles should be avoided when possible; in-depth repair and retrofit works can render the structural restoration of the piles

unfeasible, more restrictive ductility limits are thus required. Likewise, seismic design guidelines and recommendations are increasingly favouring displacement-based design over force-based design methodologies. For instance, ASCE (2014) permits force-based design for low design classifications, when the expected demand is low, or when members are design to remain elastic. POLB and POLA recommendations for seismic demands are entirely displacement-based.

Batter piles were routinely included in wharf design to provide additional lateral strength against operational loads. However, during strong ground shaking, the rigid deck-batter piles connection is more susceptible to damage due to high stress concentrations, as it was evidenced during. Instead, to accommodate high kinematic demands (i.e., ground movement), the current design philosophy favours the use of vertical piles only, granted with sufficient bending capacity and stiffness. Batter piles are still allowed only if the deck is protected by a tension fuse or other isolation device.

Table 2.4 Material strain limits for reinforced concrete piles prescribed by ASCE 61-14, POLA and POLB standards for the seismic design of piers and wharves.

	Pile-deck hinge		In-ground hinge	
Performance level	Concrete	Reinforcing steel	Concrete	Reinforcing Steel
Minimal damage	$\varepsilon_c \leq 0.005$	$\varepsilon_s \leq 0.015$	$\varepsilon_c \leq 0.005$ Deep in-ground z >10 D_p : $\varepsilon_c \leq 0.008$	ASCE: $\varepsilon_s \leq 0.015$ POLA and POLB: No limit
Controllable and reparable damage	$\varepsilon_c \leq 0.005 + 1.1\rho_s \leq 0.025$	$\varepsilon_s \leq 0.6\varepsilon_{smd} + \leq 0.06$	$\varepsilon_c \leq 0.005 + 1.1\rho_s \leq 0.008$ Deep in-ground z >10D_p: $\varepsilon_c \leq 0.012$	ASCE: $\varepsilon_s \leq 0.6\varepsilon_{smd} + \leq 0.06$ POLA and POLB: No limit
Life safety protection	No Limit	$\varepsilon_s \leq 0.8\varepsilon_{smd} + \leq 0.08$	ASCE and POLB: $\varepsilon_c \leq 0.005 + 1.1\rho_s \leq 0.012$ POLA: $\varepsilon_c \leq 0.005 + 1.1\rho_s \leq 0.025$ Deep in Ground: No limit	ASCE: $\varepsilon_s \leq 0.8\varepsilon_{smd} + \leq 0.08$ POLA and POLB: No limit

Table 2.5. Damage criteria for pile-supported wharves proposed by PIANC (2001).

Limit state	Differential settlement between deck and land	Residual tilting towards the sea	Peak Pile response
Degree I: Serviceable	Les than 0.1 ~ 0.3m	Les than 2 ~ 3°	Essentially elastic with minor or no residual deformation
Degree II: Repairable	N/A	N/A	Limited inelastic ductile response. Structure is repairable
Degree III: Near Collapse	N/A	N/A	Ductile response near collapse. Double plastic hinges may occur at one or limited number of piles.
Degree IV: Collapse	N/A	N/A	Beyond Degree III

Table 2.6 Material strain limits for reinforced concrete pile-supported wharves prescribed by PIANC (2001).

Ground motion level	Pile-deck hinge		In-ground hinge	
	Concrete	Reinforcing steel	Concrete	Reinforcing steel
L1	$\varepsilon_c \leq 0.004$	$\varepsilon_s \leq 0.01$	$\varepsilon_c \leq 0.004$	$\varepsilon_s \leq 0.01$
L2	$\varepsilon_c \leq$ Eq (2-1) ≤ 0.025	$\varepsilon_s \leq 0.05$	$\varepsilon_c \leq$ Eq (2-1) ≤ 0.008	$\varepsilon_s \leq 0.01$

Procedures for the evaluation of seismic demand and capacity for the pile foundations, recommended by POLA, POLB and ASCE 61-14, are mainly based on BNWF (Beam on Non-linear Winkler Foundation) methods. The guidelines state that, seismic design analysis should follow a preliminary design phase of dimensioning for static and serviceability loads. Kinematic loads due to ground deformations must be considered under special circumstances depending on the subsoil conditions and pile performance. Lateral ground deformations can be estimated by means of Newmark-type analyses granted that the deformations are acceptable for the system performance. The requirements for the analysis methodology are more stringent when larger ground displacements are expected (PIANC, 2001). For instance, when limit equilibrium methods result in unacceptable ground displacements, an order of complexity is added to the analysis to account for pile-pinning effects following iterative procedures like those describe by Armstrong et al. (2014), Ashford et al. (2011), and Boulanger and Tokimatsu (2005). When ground deformations impose double-curvature strains on the piles a more detailed soil-dynamic-structure - interaction analysis is required. This is the case, for instance, when large strains concentrate within thin layers due to soil liquefaction or due to the formation of a sliding plane. When the pseudo-static factor of safety of the submerge slope is below 1.1, ASCE 61-14 requires

the assessment of kinematic loads in the form of Free-Field displacements (i.e. in the absence of the foundation superstructure).

Inertial loads tend to control the seismic demand on the upper-most sections of the piles, whereas ground deformations impose larger loads to the deep in-ground sections. While there is a consensus about the nature these loading cases, the simultaneous application of inertial and kinetic loads for pile design is still a point of debate. Inertial loads tend to peak during the initial (cyclic) phase of shaking, while lateral spreading deformations developed from the onset of liquefaction (or sliding) and attain their maximum at the end of shaking.

Based on the results of centrifuge tests (Brandenberg et al., 2005), and finite element simulations, Boulanger et al. (2007) proposed a series of modification factors for the inertial demand of pile foundations for bridges founded on liquefiable ground. Their methodology is applicable for BNWF methods, whereby the lateral displacement profile is applied at the fixed end of the non-linear springs, and a fraction of the inertial load is applied at the pile cap, or superstructure (depending on the end fixities of the foundation). The authors recognize that kinematic and inertial loading cases might not have overlapped influence, yet the actual condition is difficult to predict. In such a case is preferrable to combine kinematic and inertial a load as a more conservative and reliable approach. Equation (2-2) represents the inertial demand modified to account for the effects of liquefaction and lateral spreading. $\Delta_{I,liq}$ is the relative displacement that characterizes the displacement demand of the bridge pier column ; C_{liq} is the ratio of maximum displacement demand with liquefaction to that without liquefaction; and C_{cc} is the fraction of the maximum displacement demand that occurs at the critical loiding cycle (i.e., the instant at which maximum pile shear forces and bending moments occur).Table 2.7 shows an excerpt of the values recommended by Ashford et al. (2011) and Boulanger et al. (2007).

$$\Delta_{I,liq} = C_{cc} C_{liq} \Delta_{I,non\ liq} \quad (2\text{-}2)$$

Table 2.7. Inertial demand coefficients recommended by Ashford et al. (2011) and Boulanger et al. (2007) for BNWF analysis of pile foundations of motorway bridges.

Design spectra for non-liquefied condition. $Sa_{T=1s}/Sa_{T=0s}$	Pile Cap		Superstructure	
1.7-2.4	1.4	0.85	0.75	0.65
0.5-1.6	0.75	0.85	0.55	0.65
≤0.4	0.35	0.85	0.45	0.65

In-lieu with the above findings Caltrans (2012) recommended to combine 100% of the kinematic load with 50% of the inertial load for the design of pile-foundations for bridges, following an non-linear static analysis similar to that employed by Boulanger et al. (2007).

Likewise, the Marine Oil Terminal Engineering and Maintenance Standards (MOTEMS) of California (California State Lands Commission, 2010) prescribes a factor of 0.25 to be applied to the inertial load when simplified analysis procedures are employed. ASCE 61-14 and POLA requires the simultaneous application of kinematic and inertial loads without providing details about combination factors. The two guidelines do allow however, for the separation of both effects on a project-specific basis. In contrast, POLB explicitly requires the consideration of both loading cases for the design of wharves. It permits the separation of both kinematic and inertial loads granted that the wharf typology is that of a marginal-pile-supported wharf.

More recently, Souri et al. (2022a, 2022b) analysed the results of a series of centrifuge tests involving five distinct models of pile-supported wharves. These models were designed to be representative of the wharf typologies found in the western United States. Small diameter (60 cm approximately) reinforced prestressed concrete pile-supported wharves founded on reclaimed land. The piles were modelled using aluminium pipes with yield capacity larger than that expected for the prototype structure, effectively behaving as elastic members. Four of the models consisted of wharves founded on either single-lift or multi-lift rock dikes, while a sliver dike was used for only one model. The authors quantified the relative contribution of kinematic and inertial demands during the critical cycles, defined as the instants of maximum bending moments recorded at the cap and inground cross sections of the piles. On average, the acceleration at the deck reached 84% and 52% of its maximum for the pile cap and in-ground sections at their respective critical cycles. Ground displacements were 67% and 93% of their peak value for the pile-deck and in-ground sections of the piles. Further numerical simulations confirmed the low correlation between deck inertia and bending moments at the inground for cases where widespread liquefaction occurred. Conversely, higher correlation was observed in cases with no liquefaction. Thus confirming the notion that the combination and interaction between kinematic and inertial loads is governed by the mode of ground deformation caused by the earthquake shaking. Shafieezadeh et al. (2012) reached the same conclusion based on the results of finite-element simulations performed on a pile-supported wharf of a similar typology.

2.3 ADVANCED SOIL CONSTITUTIVE MODELS FOR EFFECTIVE STRESS DYNAMIC ANALYSES

Assessing the seismic performance of geotechnical systems affected by soil liquefaction inevitably requires the consideration of the non-linear response of the liquefiable ground. Simplified approaches that focus on force-based safety margins, such as limit equilibrium methods or empirical relationships, often lack the ability to provide quantitative measures of the system response suitable for consequence analysis. This limitation becomes more critical when the characteristics of the given problem deviate from well-documented idealized cases.

With the surge in computing power witnessed over the past three decades, non-linear time-history numerical analyses of soil systems have become increasingly feasible. However, their reliability hinges over the successful integration of complex aspects such as: site-characterization and documentation; selection and calibration of constitutive models; and the management of technical aspects inherent of dynamic boundary-value-problems (e.g., handling of numerical instabilities, definition of boundary conditions, numerical damping, etc).

The present study extensively utilizes these numerical analyses to assess the seismic response of pile-supported wharves on liquefiable soil. Discussion on the treatment of various technical and modelling aspects will continue throughout this monograph. This section will specifically address the second issue, 'selection and calibration of constitutive models for coarse-grained soils,' highlighting the main similarities and differences between two state-compatible models available for the numerical platform FLAC (v8.1) (Itasca Consulting Group, Inc, 2019), namely PM4Sand (v3.1) (Boulanger and Ziotopoulou, 2017) and SDm.(v1.1) (Cubrinovski and Ishihara, 1998a, 1998a). The remainder of the section will introduce the fundamental rationale behind each model, establishing a logical link between model behaviour and the calibration procedures outlined in subsequent chapters of the thesis.

The two models are based on principles of continuum mechanics and are formulated in plane-strain conditions without Lode-angle dependency. Although the plane strain assumption might seem restrictive, it provides a desired degree of simplicity that eases their implementation and improves computational speed. The models make use of the following definitions, tensorial quantities are shown in bold letters, while all stresses are assumed to be effective if not stated otherwise:

- Stress tensor:

$$\boldsymbol{\sigma} = \begin{bmatrix} \sigma_{xx} & \sigma_{xy} \\ \sigma_{xy} & \sigma_{yy} \end{bmatrix} \tag{2-3}$$

- Strain tensor:

$$\boldsymbol{\varepsilon} = \begin{bmatrix} \varepsilon_{xx} & \gamma_{xy} \\ \gamma_{xy} & \varepsilon_{yy} \end{bmatrix} \tag{2-4}$$

- Mean stress:

$$p = \frac{(\sigma_{xx} + \sigma_{yy})}{2} \tag{2-5}$$

- Deviatoric stress (for triaxial conditions and simple-shear conditions) :

$$q = \sigma_1 - \sigma_3$$

$$q = \sqrt{\left(\frac{\sigma_{yy} - \sigma_{xx}}{2}\right)^2 + \tau_{xy}^2} \tag{2-6}$$

- Deviatoric stress tensor:

$$\mathbf{s} = \boldsymbol{\sigma} - p\mathbf{I} \tag{2-7}$$

Where **I** is the identity matrix.

- Deviatoric stress ratio:

$$\mathbf{r} = \frac{\mathbf{s}}{p} \tag{2-8}$$

- Volumetric strain:

$$\varepsilon_v = \varepsilon_{xx} + \varepsilon_{yy} \tag{2-9}$$

- Deviatoric strain:

$$\mathbf{e} = \boldsymbol{\varepsilon} - \frac{\varepsilon_v}{3}\mathbf{I} \tag{2-10}$$

The models follow incremental formulation and share basic features borrowed from classical plasticity theory, such as the additivity of plastic and shear increments, consistency of the yield domain, among others. Stress increments are then defined as:

$$\delta\boldsymbol{\varepsilon} = \delta\boldsymbol{\varepsilon}^{\mathbf{e}} + \delta\boldsymbol{\varepsilon}^{\mathbf{p}}$$

$$\delta\boldsymbol{\varepsilon}^{\mathbf{e}} = \delta\mathbf{e}^{\mathbf{e}} + \frac{1}{3}\delta\varepsilon_{vol}^{\mathbf{e}}\mathbf{I}$$

While the elastic components of the strain tensor are defined as follows:

$$\delta\mathbf{e}^{\mathbf{e}} = \frac{\delta\mathbf{s}}{2G} \qquad \delta\varepsilon_{vol}^{\mathbf{e}} = \frac{\delta p}{K}$$

$$\delta \boldsymbol{s} = \boldsymbol{2G}(\delta \boldsymbol{e} - \delta \boldsymbol{e^p}) \qquad \delta p = K\left(\delta \varepsilon_{vol} - \delta \varepsilon_{vol}^{p}\right)$$

It is worth noting that, the implementation of SDm into FLAC is an ongoing collaboration between workers at the University of Canterbury, University of Pavia and IUSS Pavia. An enhanced version 2.0 of the model is still under development, results obtained with v1.1 are considered preliminary.

The presentation that follows aims at describing the general case for monotonic response, to explain the main characteristics and definitions used by of the models. Additional, albeit brief comments are given about how both models handle cyclic loading paths.

2.3.1 The plasticity model for sands, PM4Sand

PM4Sand is a critical-state-compatible bounding surface plasticity model proposed by Boulanger and Ziotopoulou (2013). It is based upon the foundation work of Dafalias and Manzari (2004).The bounding surface formulation governs the evolution of plastic modulus and dilation based on the current state of soil relative to the critical state. The critical state line is defined in the relative density (D_R) – mean effective pressure (p) space ,as proposed by Bolton (1986) and expressed by Eq(2-11), where p_A is the atmospheric pressure and Q and R model parameters.

$$D_{R,cs} = \frac{R}{Q - \ln\left(100\frac{p}{p_A}\right)} \tag{2-11}$$

The state variable used by PM4Sand is the so-called *relative state index* (ξ_R) defined in Eq(2-12).

$$\xi_R = D_{R,cs} - D_R \tag{2-12}$$

The ensuing discussion presents the fundamentals of the mathematical framework of the model by following a systematic comparison between the triaxial formulation, defined in terms of deviatoric and volumetric components alone, and the multiaxial formulation that uses the entirety of the in-plane stress and strain components. Details of the model formulation can be found in manual of PM4Sand v3.1 (Boulanger and Ziotopoulou, 2017). Figure 2.11 shows the schematic representation of the bounding surface, dilatancy surface, critical state line and elastic domain in the q-p space for the triaxial formulation, and in the deviatoric space for the multiaxial formulation. In the q-p plane, the bounding and dilatancy surfaces are represented by the red and blue dashed lines with their slopes defined in terms of the stress ratios M_b and M_d. The slope of the critical state line is denoted as M_{cs}.

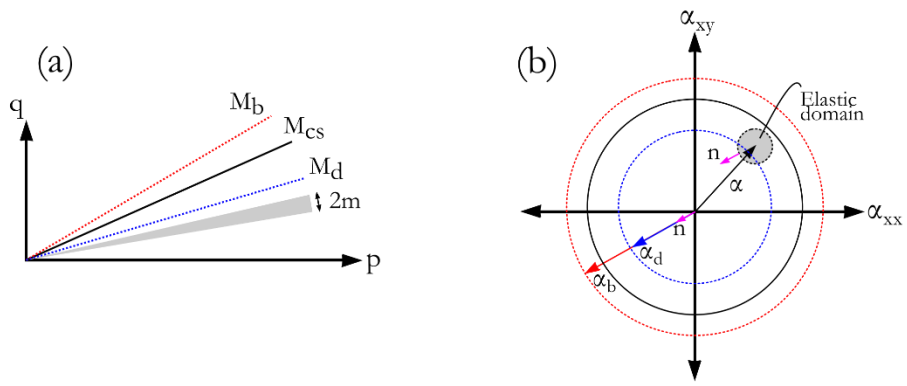

Figure 2.11. Schematics of the bounding surface, dilatancy surface, critical state line and elastic domain employ by PM4Sand in the triaxial space (a) a in the deviatoric space (b) for the multiaxial formulation of the model.

The evolution of bounding and dilatancy surfaces is controlled by the relative state parameter (ξ_R) relating them to the critical state according to:

$$M_b = M_{cs} \exp(-n_b \xi_R) \tag{2-13}$$

$$M_d = M_{cs} \exp(n_d \xi_R) \tag{2-14}$$

As evident, the state of the soil, whether denser or looser than critical, determines the initial position of the bounding and dilatancy surfaces. As loading progresses, and the current state approaches the critical state line in the p-q space, the plastic modulus decreases and the bounding surface M_b collapses into the critical state ratio M_{cs}. Dilatancy operates in a similar manner. The location of the dilatancy surface is initialize according to the initial state, for loose soils it will be closer to the critical state line while for denser soils it will be more distant. For instance, upon loading the soil will response with a contractive tendency until it reaches the dilatancy surface, effectively acting as a state-based phase transformation line.

The elastic domain is cantered at the back-stress ratio α, its size, measured as its diameter in the deviatoric plane, has a fixed value of *m*. The yield surface in the triaxial and deviatoric plane is defined according to:

$$f = |\eta - \alpha| - m = 0$$
$$f = \sqrt{(\mathbf{s} - p\boldsymbol{\alpha}) : (\mathbf{s} - p\boldsymbol{\alpha})} - \frac{p}{\sqrt{2}} m = 0 \tag{2-15}$$

Where η is the current stress ratio for the triaxial formulation.

For the triaxial formulation (Dafalias and Manzari, 2004), the kinematic hardening (i.e., the evolution of the back-stress ratio α) is formulated after enforcing the consistency condition on the yield domain:

$$df = \frac{\partial f}{\partial \eta} d\eta + \frac{\partial f}{\partial \alpha} d\alpha = 0$$

$$df = d\eta - d\alpha = 0$$

$$df = d\eta - \frac{\partial \alpha}{\partial \varepsilon_q^q} d\varepsilon_q^p = 0$$

$$d\alpha = H_p d\varepsilon_q^p$$

$$H_p = h(M_b - \eta) \tag{2-16}$$

Where h is a positive function dependent on the state variables. The plastic (hardening) modulus H_p is thus defined proportional to the difference between the current back-stress ratio and the bounding surface ratio M_b. For the multiaxial case, it is convenient to define $M_b - \eta$ in terms of back stress ratios (given that m is fixed), $(M_b - \eta) = (\alpha_b - \alpha)$, being α the current back stress ratio and α_b the back stress ratio at the image point on the bounding surface:

$$d\boldsymbol{\alpha} = d|\boldsymbol{\varepsilon}^p| \frac{2}{3} h\,(\boldsymbol{\alpha}_b - \boldsymbol{\alpha}) = \langle \lambda \rangle \frac{2}{3} h\,(\boldsymbol{\alpha}_b - \boldsymbol{\alpha})$$

In this case, the plastic module is termed as K_p:

$$K_p = p \frac{2}{3} h\,(\boldsymbol{\alpha}_b - \boldsymbol{\alpha}) : \mathbf{n} \tag{2-17}$$

Plastic strains are defined using the conventional theory of plasticity as the product of the plastic multiplier (within MacCauley brackets) and the gradient of the plastic potential with respect to the current stress state, conveniently termed as **R**:

$$\delta \boldsymbol{\varepsilon}^{\mathbf{p}} = \langle \lambda \rangle \frac{\partial g}{\partial \boldsymbol{\sigma}} = \langle \lambda \rangle \mathbf{R} \tag{2-18}$$

The deviatoric component of the flow rule (**R**) is associative while the volumetric component depends on the dilatancy relationship D:

$$\delta \mathbf{e}^{\mathbf{p}} = \langle \lambda \rangle \mathbf{R}' = \mathbf{n}$$

$$\mathbf{R}' = \mathbf{n} = \mathrm{d}f/\mathrm{d}\boldsymbol{\sigma} \tag{2-19}$$

$$\delta \varepsilon_v^p = \langle \lambda \rangle D = |\delta \mathbf{e}^p| D$$

The small strain shear modulus is dependent on the confining pressure and on the stress history. Yu and Richart (1984) showed that the small strain G is reduced when the maximum stress ratio is overcome by the current stress ratio. This latter feature is accounted by the factor C_{SR}.

$$G = G_o p_a \left(\frac{p}{p_a}\right)^{\frac{1}{2}} C_{SR}$$

$$C_{SR} = 1 - C_{SR,o} \left(\frac{M}{M_b}\right)^{m_{SR}} \tag{2-20}$$

The calibration examples presented by Boulanger & Ziotopoulou (2017) where performed with $C_{SR,o}$.=0.5 and m_{SR}=4, which leads to a 60% reduction of the small strain modulus when the stress ratio is on the bounding surface. Moreover, Eq(2-21) is modified to include fabric effects that lead to further degradation of G as plastic deviatoric strains accumulate. At this stage it is worth recalling that the present discussion aims at presenting the fundamental functioning of the model without the inclusion of the so-called fabric effects, which imply modifications to Eq. (2-20).

Equivalent to the definition used for kinematic hardening, the dilatancy relationship is defined with respect to the dilation surface M_d and the corresponding back-stress ratio $\boldsymbol{\alpha}_d$.

$$D = A_{do} \ (\boldsymbol{\alpha}_d - \boldsymbol{\alpha}) : \mathbf{n} \tag{2-21}$$

Note that, at this stage, Eq(2-21) is valid for dilative response only. The rate of dilation is controlled by the scalar term A_{do}. It follows different expressions for contraction and dilation cases, which are enforced depending on the dot product $(\boldsymbol{\alpha}_d - \boldsymbol{\alpha}) : \mathbf{n}$, positive for contraction and negative for dilation.

Assuming small strain increments, the angle of dilation ψ could be retrieved as:

$$\tan(\psi) = \frac{\delta\varepsilon_{vol}^{p}}{|\delta\gamma^{p}|} = \frac{\delta\varepsilon_{vol}^{p}}{\sqrt{2}|\delta\mathbf{e}^{p}|} = \frac{D}{\sqrt{2}} = A_{do}\,(\boldsymbol{\alpha}_{d} - \boldsymbol{\alpha})\colon \mathbf{n} \approx \psi$$

Consequently, an estimate of A_{do} can be derived by utilizing the simplified dilatancy definition proposed by Bolton (1986) (Eq(2-23)) . Further derivations consider the bounding surface for the definition as representative of peak states, leading to the expression of Eq(2-23)., details can be found in Boulanger and Ziotopoulou (2017).

$$\phi_{pk} - \phi_{cs} = 0.8\,\psi_{\text{peak state}} \tag{2-22}$$

$$A_{do} = \frac{\sqrt{2}}{0.8}\,\frac{\arcsin\left(\frac{M_b}{2}\right) - \arcsin\left(\frac{M_{cs}}{2}\right)}{(M_d - M_b)} \tag{2-23}$$

For contraction, the model follows a more complex definition of D, expressed by Eq(2-24). Dilation is set to be proportional to the square of the term within square brackets, expressed with respect to the apparent initial back-stress ratio of the current cycle α_{in}^{app}. The term to the right ensures a smooth transition towards zero as the α approaches α_d. Fabric affects are accounted for by the scalar C_{in}, allowing the model to generate excess pore-water pressures early during unloading cycles.

$$D = A_{dc}\left[(\boldsymbol{\alpha} - \boldsymbol{\alpha}_{in}^{app})\colon \mathbf{n} + C_{in}\right]^{2}\frac{(\boldsymbol{\alpha}_{d} - \boldsymbol{\alpha})\colon \mathbf{n}}{(\boldsymbol{\alpha}_{d} - \boldsymbol{\alpha})\colon \mathbf{n} + C_{D}} \tag{2-24}$$

As in the case of dilation, the contraction rate is controlled by the parameter $A_{dc,}$ which is in turn to A_{do} through the parameter $h_{p.}$

$$A_{dc} = \frac{A_{do}}{hp}$$

$$hp = \begin{cases} hp_{o}\exp(-0.7 + 7.0(0.5 - \xi_{R})^{2}) & \text{for } \xi_{R} \le 0.5 \\ hp_{o}\exp(-0.7) & \text{for} > 0.5 \end{cases} \tag{2-25}$$

High values of the contraction rate parameter h_{po} will lead to a slower progression of plastic volumetric contraction, thus increasing the soil resistance during cyclic loading. The model limits the value of D in contraction with a lower bound to prevent excessively large contraction rates.

2.3.1.1 *Fabric effects.*

Dafalias & Manzari (2004) concluded that the pore pressure built up given by an expression similar to Eq(2-24) is not sufficient to capture the desired soil response under cyclic loading. The butterfly-like shape of the stress path caused by a progressive reduction of the mean stress was absent, instead, the soil response stabilized before reaching low p values. The model needed to be modified to allow for a further progression of pore pressure built up following a dilative phase, to that a fabric-dilatancy variable (or tensor) was introduced.

From previous micromechanical studies, it was evidenced that soil fabric (i.e. particle-contact orientation) adapts during a dilative response under monotonic loading such that it is biased to allow larger volumetric strains after reversal. As loading in the reversed sense progresses, fabric rearrange and adapts to the current loading direction, leading to a contractive bias upon reversal. Thus, fabric rearrangement is in theory, responsible for the net contractive behaviours during cyclic loading. The preliminary model developed by Dafalias & Manzari (2004) modelled this fabric-related effects by introducing the fabric-dilatancy variable z, and the fabric-dilatancy tensor $\boldsymbol{z}$ for the triaxial and multiaxial formulations of the model respectively.

In PM4SAND v3.1, the formulation for the fabric-dilatancy tensor increment $\delta\boldsymbol{z}$ was revised (Eq(2-26)), it has been made dependent on the evolution of plastic deviatoric strains rather than volumetric; and the rate at which $\boldsymbol{z}$ builds up is now restricted by an additional term depending on the accumulated fabric-dilatancy variable z_{cum}.

$$\delta\mathbf{z} = -C_z \frac{\langle -\delta\varepsilon_v^p \rangle}{D} (\mathbf{n} z_{max} + \mathbf{z}) \frac{1}{1 + \langle \frac{z_{cum}}{2 z_{max}} - 1 \rangle} \tag{2-26}$$

$$\delta z_{cum} = |\delta\mathbf{z}|$$

In addition to z_{cum}, the variable z_{peak} tracks the maximum value of the norm of $\mathbf{z}$.

$$z_{peak} = \max\left(\sqrt{\frac{\mathbf{z}:\mathbf{z}}{2}}, z_{peak} \right)$$

During a contractive phase, the dilatancy parameter D is enhanced by a modified factor A_{dc}

$$D = A_{dc}\left[(\boldsymbol{\alpha} - \boldsymbol{\alpha}_{in}^{app}) : \mathbf{n} + C_{in} \right]^2 \frac{(\boldsymbol{\alpha}_d - \boldsymbol{\alpha}) : \mathbf{n}}{(\boldsymbol{\alpha}_d - \boldsymbol{\alpha}) : \mathbf{n} + C_D} C_{p,min}$$

$$A_{dc} = \frac{A_{do}}{hp\, C_{dz}} (1 + \langle \mathbf{z}: \mathbf{n} \rangle)$$

The term C_{dz} in the denominator of the expression for Adc serves to increase the rate of contraction as z_{peak} nears z_{max} or after a large amount of cumulative fabric formation/destruction has taken place.

For dilation, the model uses an additional dilation surface, referred as a rotated dilatancy surface.

$$M_d^{rot} = \frac{M_d}{C_{rot}}$$

$C_{rot} > 1$ when fabric is unfavorable (toward contraction) $\boldsymbol{n}: \boldsymbol{z} < 0$, and when there is no load reversal. Meaning that it allows for early dilation during irregular loading cycles, yet at a reduced evolution rate D. Moreover, the expression for parameter A_d controlling the dilatancy D is also significantly modified by the inclusion of several fabric-dependent terms, which are not covered in the present document for the sake of brevity.

Further fabric-based modifications were also included to the plastic modulus. For favourable fabric ($\boldsymbol{n}: \boldsymbol{z} > 0$) during contraction, the plastic modulus is reduced at large shear strains. Moreover, being the soil strongly sheared in one direction, upon unloading and reloading the plastic modulus becomes initially stiffer, because of the sustain sheared, if such sustained shear is reasonably higher than the cyclic shear loading.

Fabric effects also impact the elastic stiffness to "*account for the progressive destruction, with increasing plastic shear strains, of any minor cementation bonds or other ageing- or strain history-related phenomena that produced an increase in small-strain shear modulus*".

$$G = G_o p_A \left(\frac{p}{p_A}\right)^{\frac{1}{2}} C_{SR} \left(\frac{1 + \frac{z_{cum}}{z_{max}}}{1 + \frac{z_{cum}}{z_{max}} C_{GD}}\right)$$

Where, C_{gd} is the factor controlling fabric-induced degradation.

2.3.2 Stress-Density model, SDm

The Stress-Density model (SDm) is an elastic-plastic model proposed by Cubrinovski and Ishihara, (1998a, 1998b). The model is motivated on previous works about the monotonic undrained behaviour of sandy soils (Alarcon-Guzman and Leonards, 1988; Ishihara, 1993; Kabilamany and Ishihara, 1990; Verdugo and Ishihara, 1996). The studies presented by Alarcon-Guzman and Leonards (1988) and Ishihara (1993) aimed at characterizing the soil

state at which a strain-softening response occurred under monotonic and cyclic undrained tests performed on sandy soils. The authors indicated that the undrained monotonic response of coarse-grained soils is dictated by: (1) the relative state of the soil with respect to the critical state line in the e-p plane, and (2) the tendency of the soil to exhibit temporary volumetric collapse (i.e., sudden particle rearrangement). The latter state is characterized by a loss in resistance followed by dilation-induced steady recovery of shear strength towards the steady-state, in what can be seen as a phase transformation. This state of minimum resistance, prior to the attainment of the steady-state, is referred to as the quasi-steady-state (QSS).

The plots of Ishihara (1993), depicted in Figure 2.12, demonstrate the QSS exhibited by Touyura sand samples with D_R=18%, sheared under undrained triaxial conditions at two different consolidation stresses. Points P and Q denote the instants of strain-softening that occurred after the samples showed a contractive response. Once the QSS was attained, the stress paths curved back towards the steady state, following a dilative response. In Figure 2.12c the quasi-steady state delineates the points belonging to the QSS. Figure 2.13 presents the various lines in the e-p space more succinctly. IDL refers to the initial demarcation line, which separates the initial states of the samples that exhibited strain-softening during undrained shear (above) from those that did not (below). The bottom and upper lines labelled as ICL correspond to the isotropic compression lines for the densest and loosest states respectively.

To characterize the sand behaviour in reference to the QSS, Ishihara (1993) introduced the state index I_s, expressed in Eq(2-27).

$$I_s = \frac{e_U - e}{e_U - e_Q} \tag{2-27}$$

Where e_U is the void ration on the upper reference (UR) line at the consolidation stress p (see Figure 2.14), e_Q is the void ratio on the QSS line for the same stress level, and e is the initial void ratio of the soil-

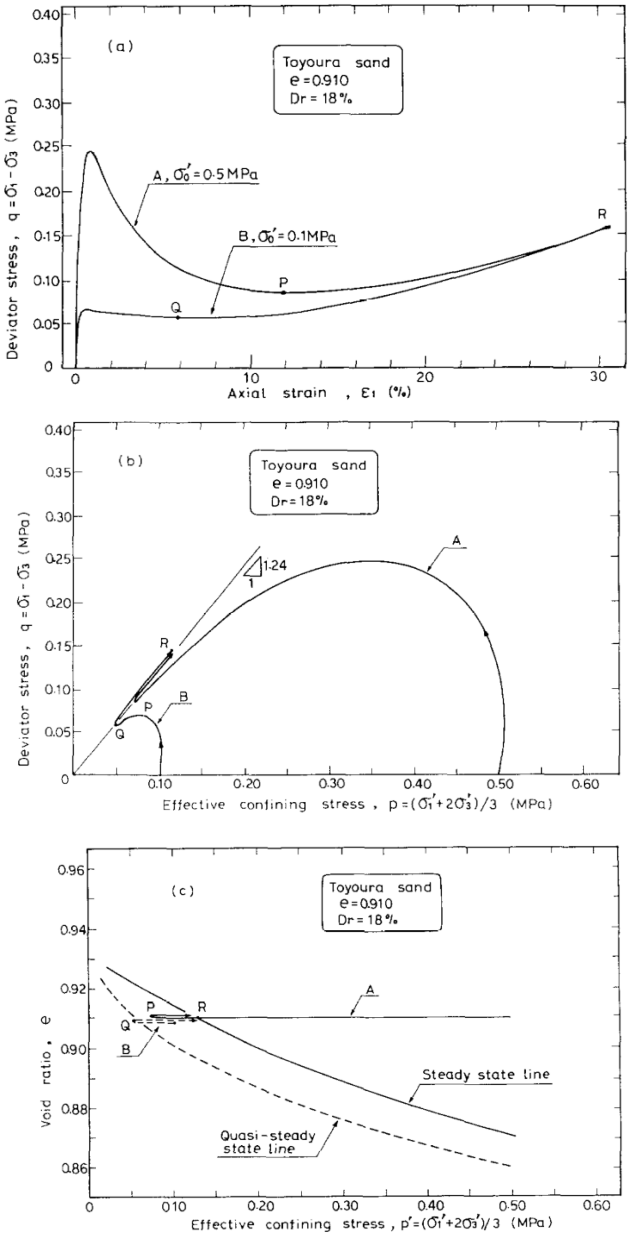

Figure 2.12. Illustration of the quasi-steady state (QSS) observed in the results of two triaxial tests performed on reconstituted Toyoura sand samples with D_R = 18%: (a) stress-strain response, (b) effective stress paths, (c) state diagram in the e-p space. Taken from Ishihara (1993)

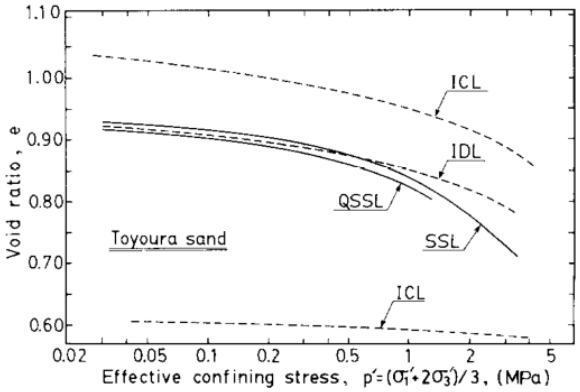

Figure 2.13. Characteristics lines of the undrained response of Toyoura sand in the e-q space. Taken from Ishihara, (1993).

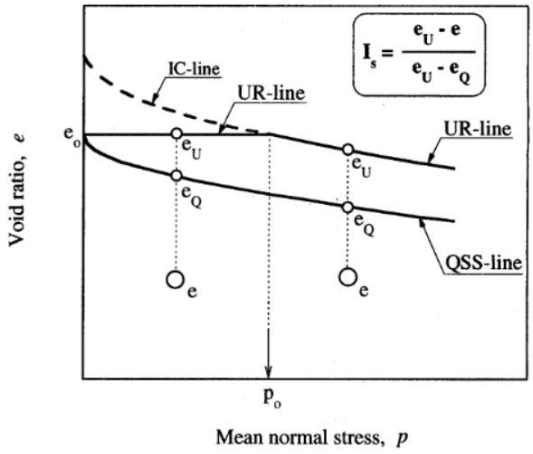

Figure 2.14. Definition of the state index, I_s ,adopted by Cubrinovski and Ishihara (1998a).

From an extensive laboratory testing on Toyoura Sand samples, Cubrinovski and Ishihara (1998a, 1998b) stablished that the soil's strain-stress behaviour can be directly linked to I_s. Figure 2.15 shows an example of the undrained response, in terms of deviatoric stress ratio vs plastic shear strain, of three dry-pluviated Toyoura sand samples prepared at different densities.

Based on the laboratory data, the authors proposed a modified hyperbolic relation for the stress ratio η as function of the plastic deviatoric shear strain defined in Eq(2-30). The shear modulus G_N and maximum shear stress ratio η_{max} are linear function of Is, defined according to the initial mean effective pressure of the soil (Cubrinovski and Ishihara,

1998a). This implies a direct link of the soil undrained resistance and stiffness degradation characteristics to its initial state characterized by I_s.

$$\frac{q}{p} = \eta = \frac{G_N \varepsilon_q^p \eta_{max}}{\eta_{max} + G_N \varepsilon_q^p}$$
$$G_N = f(I_s, ..)$$
$$\eta_{max} = f(I_s, ..) \quad (2\text{-}28)$$

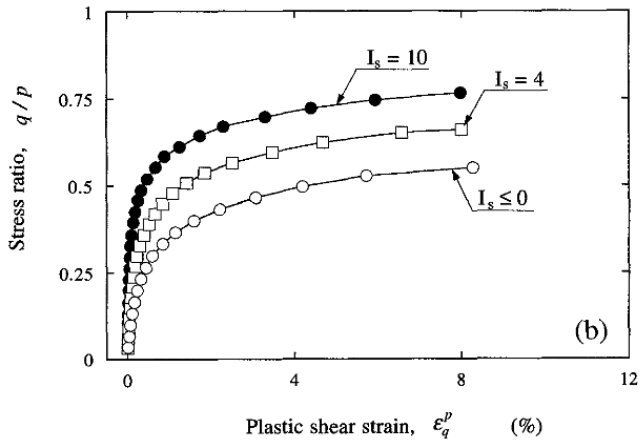

Figure 2.15. Measured stress-strain response of three samples dry-pluviated Toyoura sand from undrained torsional shear tests, as reported by Cubrinovski and Ishihara (1998a).

Unlike classical elastic-plastic constitute models, SDm considers a vanishing elastic domain. Instead of a yield surface encompassing an elastic range, SDm assumes that the current stress state lays on a loading surface denoted as *l*. In the deviatoric stress plane (see Figure 2.16), this loading surface appears as a circle with radius η defined by Eq(2-29). The deviatoric plane shown in Figure 2.16 follows a slightly different convention to that of Figure 2.11. It plots the components, X and Y (see Eq(2-30)), of the deviatoric stress

amplitude in SS conditions (Eq(2-6)). The dotted black circle represents the failure surface *f* with radius η_{max}.

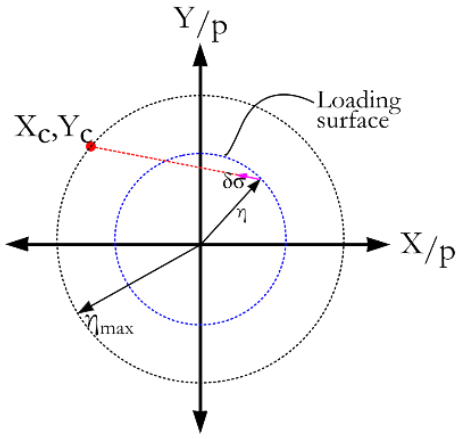

Figure 2.16. Schematic representation of the deviatoric stress plane (X-Y defined by see Eq(2-30)) showing the different surfaces employed by SDm.

$$l = q - \eta p = 0 \tag{2-29}$$

$$X = \frac{1}{2}(\sigma_{yy} - \sigma_{xx}) \qquad Y = \tau_{xy} \tag{2-30}$$

The plastic modulus H_p is retrieved after enforcing the consistency condition on the loading surface, such that:

$$\delta l = \frac{\partial l}{\partial \boldsymbol{\sigma}} \delta \boldsymbol{\sigma} + \frac{\partial l}{\partial \eta} \frac{\partial \eta}{\partial \varepsilon_q^p} \delta \varepsilon_q^p = 0$$

$$\frac{\partial l}{\partial \boldsymbol{\sigma}} \delta \boldsymbol{\sigma} - H_p \, \varepsilon_q^p = 0$$

$$H_p = -\frac{\partial l}{\partial \eta} \frac{\partial \eta}{\partial \varepsilon_q^p} \tag{2-31}$$

The flow rule, defined in Eq(2-32), considers the plastic potential with respect to the failure surface *f*, by taking its gradient at the conjugate point (Xc,Yc). The conjugate stress point lays at the intersection between the extended stress increment vector ($\delta\boldsymbol{\sigma}$) and the failure surface (see Figure 2.16). In Eq(2-31), **I** is the identity matrix and D is the dilatancy relationship.

$$\delta\boldsymbol{\varepsilon}^{\mathbf{p}} = \langle\lambda\rangle \frac{\partial g}{\partial \boldsymbol{\sigma}} = \langle\lambda\rangle \left.\frac{\partial f}{\partial \boldsymbol{\sigma}}\right|_{Xc,Yc} [\mathbf{I} + D] \tag{2-32}$$

Decomposing the flow rule into its deviatoric (X,Y) and volumetric components yields:

$$\delta\varepsilon^{p}_{yy} - \delta\varepsilon^{p}_{xx} = \langle\lambda\rangle \left.\frac{\partial f}{\partial X}\right|_{Xc,Yc}$$

$$\delta\gamma^{p}_{xy} = \langle\lambda\rangle \left.\frac{\partial f}{\partial Y}\right|_{Xc,Yc}$$

$$\delta\varepsilon^{p}_{vol} = \langle\lambda\rangle \left.\frac{\partial f}{\partial Y}\right|_{Xc,Yc} D$$

The dilatancy relationship (D) is defined according to the formulation of Kabilamany and Ishihara (1990). the authors analysed the results of a series of triaxial tests conducted on Fuji River sand. They observed that the variation of the normalized plastic work Ω^{p}_{w} , defined in Eq(2-33), exhibited a distinctive relationship with respect to the cumulative deviatoric plastic shear strain, characterized by the slope μ exemplified by the data . After extending their analysis to the behaviour of other reference sands, they postulated that the parameter μ is almost unique "irrespective of relative density, over consolidation ratio and inherent anisotropy of the sand sample". Consequently, they proposed the dilatancy relation of Eq(2-34).

$$\frac{\delta\Omega^{p}_{w}}{p} = \delta\varepsilon^{p}_{vol} + \eta\delta\varepsilon^{p}_{q} \approx \mu\delta\varepsilon^{p}_{q} \tag{2-33}$$

$$D = \frac{\delta\varepsilon^{p}_{vol}}{\delta\varepsilon^{p}_{q}} = \mu - \eta c \tag{2-34}$$

Cubrinovski and Ishihara, (1998a, 1998b) adopted the nonlinear definition for the dilatancy parameter μ expressed in Eq(2-35). Therefore, the primary parameters governing the dilatancy relationship, and consequently the rate of pore pressure built up, are the initial slope μ_o and the critical state ratio M_{cs}. Note that these parameters that are independent of

the initial state of the soil. Nevertheless, the effects of the initial state are integrated through the cumulative plastic shear strain ε^{q}_{p}, as its evolution is controlled by the hyperbolic relation of Eq(2-28).

$$\mu = \mu_o + \frac{2}{\pi}(M_{cs} - \mu_o)\arctan\left(\frac{\varepsilon_q^p}{S_c}\right) \tag{2-35}$$

The elastic response is determined according to the definition of the shear modulus of Eq(2-36). Where *A* and *n* are non-dimensional material parameters.

$$G = Ap_A\frac{(2.17 - e)^2}{1 + e}\left(\frac{p}{p_A}\right)^n \tag{2-36}$$

Finally, Table 2.8 presents a summary of the comparison of the main features of the two models.

Table 2.8. Summary of the different features of PM4Sand and SDm.

Model Feature	PM4SAND (Boulanger and Ziotopoulou, 2017)	SDm (Cubrinovski and Ishihara, 1998a, 1998b)
Yield (elastic) domain	Yield domain cantered at the back stress ratio	No yield domain
Sate variable	Initial states are defined according to the state parameter ψ (Been and Jefferies, 1995) with respect to the critical state line	Initial states are determined by the state index Is (Ishihara et al., 1997) with respect to the QSS-line
Plastic modulus	Plastic modulus determined by the distance between the current state (represented by the back stress ratio) and the bounding surface. $K_p = f(\eta_b - \eta_\alpha, \dots.)$ $K_p = 0\ for\ \eta = \eta_\alpha$	Plastic modulus determined by the relative size of the current stress ratio with respect to the maximum stress ratio. $K_p = f\left(1 - \frac{\eta}{\eta_{max}}, \dots.\right)$ $K_p = 0\ for\ \eta = \eta_{max}$

Evolution of plastic modulus	Bounding surface collapses towards the critical state line according to the state parameter. It increases in size for looser than critical initial states while shrinking for denser than critical states. Bounding surface is based on the evolution of the state parameter ψ (Been and Jefferies, 1995) Critical state line based on the model proposed by Schofield and Wroth (1968), using the values proposed by (Bolton, 1986).	η evolves with respect to the plastic shear strain according to a hyperbolic relationship until reaching η_{max}. η_{max} is defined according to the initial value of the state index. So far, the model does not consider the evolution of the state index. $\eta_{max} - I_s$ relationships were defined from laboratory testing on Touyura Sand (Ishihara et al., 1997).
Dilatancy relationship	Contractive and dilative response take place according to the distance between the current state (represented by the back stress ratio) and the dilatancy surface. $$\frac{\delta\varepsilon_{vol}^{p}}{\delta\varepsilon_{q}^{p}} = f(\eta_d - \eta_\alpha, \dots.)$$ Contractive and dilative responses are modelled separate. Contraction $(\eta_d - \eta_\alpha > 0)$: n $$\frac{\delta\varepsilon_{vol}^{p}}{\delta\varepsilon_{q}^{p}} \propto \frac{A_{do}}{hp}(\eta_d - \eta_\alpha)$$ Dilation $(\eta_d - \eta_\alpha < 0)$: $$\frac{\delta\varepsilon_{vol}^{p}}{\delta\varepsilon_{q}^{p}} \propto A_{do}(\eta_d - \eta_\alpha) \approx 0.8\psi$$ Values calibrated such that it satisft relation for the peak states as presented by Bolton (1986) $$\phi_{pk} - \phi_{cs} = 0.8\,\psi_{at\ the\ peak\ state}$$	It is based on the energy-based formulation of Kabilamany and Ishihara (1990): $$\frac{\delta\varepsilon_{vol}^{p}}{\delta\varepsilon_{q}^{p}} = \mu - \eta c$$ Were μ evolves with cumulative plastic shear strain from an initial value μ_0 until reaching M_{cr}. For loose soil: $\mu_{(\varepsilon_q^p)}$ is general greater and grows faster than $\eta_{(I_s,\varepsilon_q^p)}$ Dense sand: $\eta_{(I_s,\varepsilon_q^p)}$ grows faster than $\mu_{(\varepsilon_q^p)}$. Phase transformation occurs when $\mu_{(\varepsilon_q^p)} = \eta_{(I_s,\varepsilon_q^p)}c$

	Dilatancy surface collapses toward the critical state as ψ evolves. For looser than critical initial states, dilatancy surface is within the bounding surface, for denser states it is outside.	
Small strain shear modulus	Dependent on the mean effective pressure and distance to the bounding surface. $$G = G_o p_A \left(\frac{p}{p_A}\right)^{\frac{1}{2}} C_{SR}$$ $$C_{SR} = 1 - C_{SR,o}\left(\frac{M}{M_b}\right)^{m_{SR}}$$ Additional terms were added to reproduce further stiffness degradation due to fabric effects.	Pressure dependent definition. $$G = A p_A \frac{(2.17 - e)^2}{1 + e}\left(\frac{p}{p_A}\right)^n$$
Fabric effects	Fabric tensor evolves with cumulative plastic shear strain, used to: • Degrade the plastic modulus at large strains during fabric-favourable loading, while stiffening after unload. • Reduce the small strain shear modulus as plastic strains accumulate. Allow for further contraction during cyclic loading and reducing the volumetric dilation after several cycles of fabric creation-destruction.	Not considered.

3. SEISMIC RESPONSE OF THE THORNDON CONTAINER WHARF AT CENTRE PORT, WELLINGTON, NEW ZEALAND.

3.1 INTRODUCTION

On the morning of November the 13th of 2016 a powerful Mw 7.8 earthquake struck the South Island of New Zealand with the epicentre near the town of Kaikōura. In the North Island, almost 70 km source-to-site distance, the port of the city of Wellington (CentrePort Limited, herein called CentrePort) suffered extensive damage due to widespread liquefication of the uncompacted reclaimed land. Lateral spreading and differential settlements damaged critical components of the port. At the Thorndon Container Terminal (TCT, see Figure 3.1), cumulative crack-width measurements indicated that the ground moved around 0.8 m to 1.0 m towards the sea (Cubrinovski et al., 2017). Visual inspections revealed that several of the concrete piles supporting the deck of the Thorndon Container Wharf (TCW) were sheared at their cap. The Gantry cranes mounted on the wharf derailed and tilted around 1° to 2.5° towards the sea.

Damage caused by the 2016 Kaikōura earthquake rendered the TCW non-operational for at least 10 months, while securing and interim infrastructure solutions were in place for another 5 years (Juno et al., 2021). Damage and disruptions caused by this event were certainly major, however it was not first time the port was affected by liquefaction-induced ground movements. During the 2013 Cook Strait and Lake Grassmere earthquakes (both Mw 6.6) the reclaimed land at the port exhibited limited manifestation of liquefaction on isolated areas (Dhakal et al., 2020). However, liquefaction-induced lateral spreading and settlements, caused by the Cook Strait event, led to the partial collapse of the roadway that runs parallel to the southern end of the Thorndon Reclamation.

Taking advantage of measurements of ground deformation and strong motion records from these three events, this study aims to underscore the applicability and limitations of advanced 2D plane strain, effective stress, dynamic-soil-structure-interaction (DSSI) analyses for the estimation of liquefaction-induced lateral spreading ground movements at TCW. The numerical simulations are performed with the commercial software FLAC version 8.1 (Itasca Consulting Group, Inc, 2019). The analyses consider the non-linear response of both the soil deposit beneath the TCW and its superstructure. The soil deposit is comprised by uncompacted gravelly reclamations overlaying marine sediments interbedded with alluvium materials. TCW is small diameter pile-supported wharf, with pile diameter (D_p) of 0.6m. Its non-linear response is captured by means of a distributed plasticity model implemented in FLAC by Andreotti and Lai (2017a,b). For the land reclamation, the analyses employ the critical state compatible bounding surface plasticity model PM4Sand version 3.2 (Boulanger and Ziotopoulou, 2013, 2022), and PM4Silt (Boulanger and Ziotopoulou, 2019) and (total stress) UBCHyst for the other soil units.

3.2 BACKGROUND AND OBSERVATIONS

Land reclamation works at CentrePort took place during different periods since the late 1800s, the areas of the different construction stages are outlined by different shades in Figure 3.1. Most of the reclamation works were made by end-dumping gravelly soils borrowed from nearby quarries. Hydraulic fills were also placed around the northern section of the buried seawall (shown in cyan). The Thorndon reclamation (green shading in Figure 3.1) was built between the mid 1960's and mid 1970's. Note that Figure 3.1 shows an approximation of the boundaries between the different types of fills, the precise bounds were difficult to establish from the available historical and technical data (Cubrinovski et al., 2017). The Thorndon reclamation is mainly comprised by an uncompacted gravelly fill 7 to 22 m thick, overlaid by a roller-compacted layer above GWT levels, which was estimated to be between 2 to 3 meters from the ground surface.

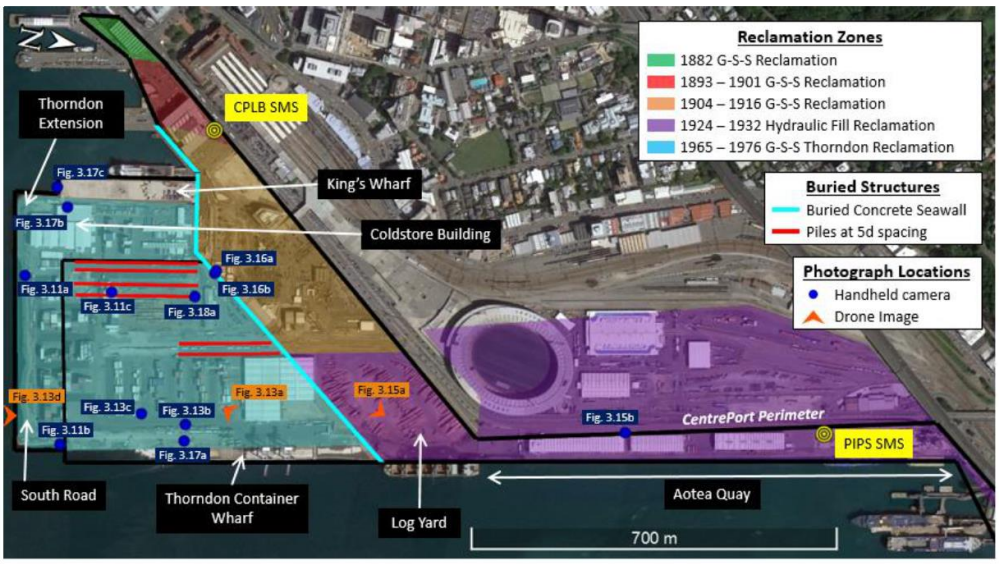

Figure 3.1. Plan view of the port of Wellington (CentrePort) showing the land reclamation areas (in different shades), key buried structures and strong motion stations (SMS, yellow markers). Taken from Dhakal et al. (2020).

Damaged caused by the 2013 lake Grassmere and Cook Strait earthquakes was either negligible or minor, with the notable exception of the partial collapse of Thorndon reclamation during the later event along the South Road (see Figure 3.2a). Additional damage due to the liquefaction of the Thorndon reclamation took place in the form of differential settlements of 50 to 90 mm, bulging of pavement, subsidence around buried pipes and sand ejecta. Large cracks also occurred within the land between King's Wharf and TCW. After the 2013 sequence, rehabilitation works mainly concerned the

conformation a gentler slope at the southern end of the Thorndon reclamation, there is however no record about ground improvement works made on the reclamation itself.

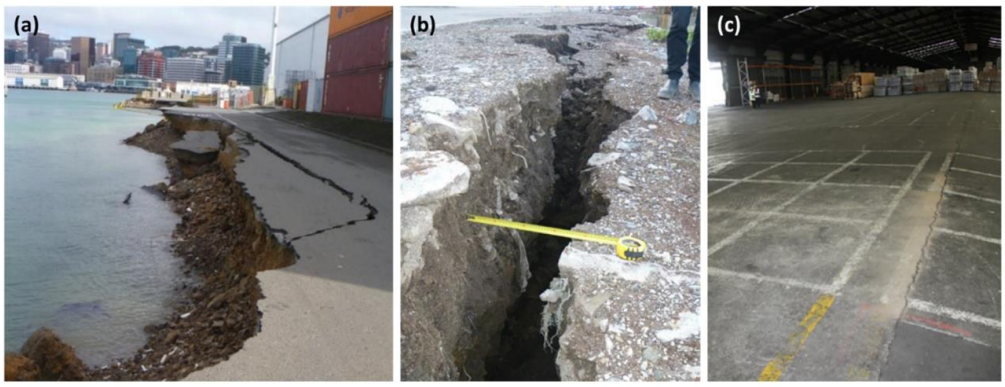

Figure 3.2. Photographs of liquefaction-induced damage at CentrePort after the 2013 Mw 6.6 Cook Strain earthquake as reported by Tonkin & Taylor Ltd (2013) and Dhakal et al. (2020): (a) partial collapse of South Road, (b) cracks at the Thorndon Reclamation Extension, and (c) localized sand ejecta trace and cracking of pavement inside Shed 37.

The Kaikōura event caused widespread liquefaction of the end-dumped fills and hydraulic fills alike. Large volumes of ejected soils were found on the pavement surface. Horizontal and vertical ground movements were notorious in the form of fissures, cracks, and offsets between buildings and the surrounding soil (Cubrinovski et al., 2017). Grain size distributions of samples obtained from the ejected materials matched those of the different fills. Gravelly ejecta found on the Thorndon reclamation were 150-200 mm thick, the largest volumes of ejected material observed throughout the port. Indeed, the Thorndon reclamation was the most affected section of the port, it also experienced the largest vertical offsets, reaching about 600 mm at TCW, as it can be appreciated from the photographs displayed in Figure 3.3. Ground movement towards the sea measured approximately 1 m, with cracking and other forms of ground distress propagating for at least 180 m inland. However, as noted by Cubrinovski et al. (2017), those estimates were based on surface observations of asphalt cover movement, and thus, would not necessarily coincide with the movement of the underlying soil.

Across the region of the city of Wellington, a danse array of strong motion stations (SMS) recorded the ground motion produced by the 2013 and 2016 events. The most proximate to TCW are stations CPLB and TFSS, located 200 m and 500 m from Thorndon Reclamation respectively. The former is found on end-dumped gravelly fills and the latter sits on top of marine deposits found along the original shoreline. Furthermore, station POTS, 1 km away in NW direction, is found on rock site and therefore considered as the reference station. Figure 3.4 shows the acceleration time histories and acceleration response spectra (with 5% of critical damping) for the ground motion recorded at the three stations

along the North-South direction. With respect to POTS, spectral ordinates at CPLB and TFSS were notoriously amplified between 1 and 1.5 seconds. This was due to a combination of complex 2D site effects and local ground response. The later stations are located on top the western margins of the Thorndon basin. Bradley et al. (2018) examined the ground motion amplification characteristics across the lower Wellington region. Based on the recorded data and on ambient noise horizontal-to-vertical (H/S) spectral ratios they concluded that the long period amplification that took place during the Kaikōura earthquake was caused by basin-induced surface waves that emanated from the edges of the Thorndon and Te Aro basins.

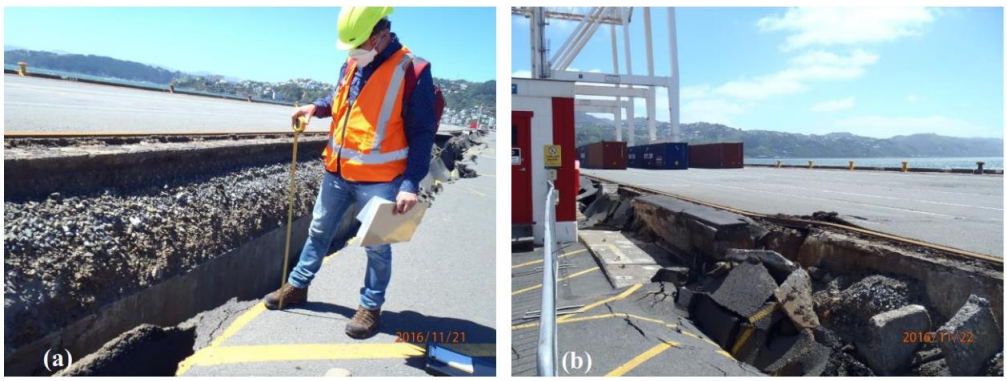

Figure 3.3. Liquefaction-induced damage to the Thorndon Container Wharf after the Mw 7.8 Kaikōura earthquake (Cubrinovski et al., 2017).

3.3 SITE CHARACTERIZATION

In the two years following the 2016 Kaikōura earthquake, several subsoil exploration campaigns at Centre Port resulted in a comprehensive dataset of field measurements. A total of 116 Cone Penetration Tests (CPTs) were executed using 10 cm² and 15 cm² A. P. van den Ber I-cones: 75 were pushed into the Thorndon gravelly reclamation, 24 in the hydraulic fills, and 17 in older gravel-sand-silt reclamation (Cubrinovski et al, 2018). Dhakal et al. (2020) utilized the CPT data, along with additional shear wave measurements, to develop the cross sections of the TCT displayed in Figure 3.5. These sections illustrate the simplified disposition of soil units found in the Thorndon reclamation zone, together with the representative CPT profiles. Note that the vertical scale is exaggerated by a factor of 10. The cross sections are representative of two transects 280 m apart approximately, being that of Figure 3.5a located at southern end of the Thorndon reclamation. Ground water table level (GWT) is situated at a depth of approximately 3 m depth, coinciding with the top of the uncompacted fills. Tidal oscillations are likely to be within the range of ± 1 m.

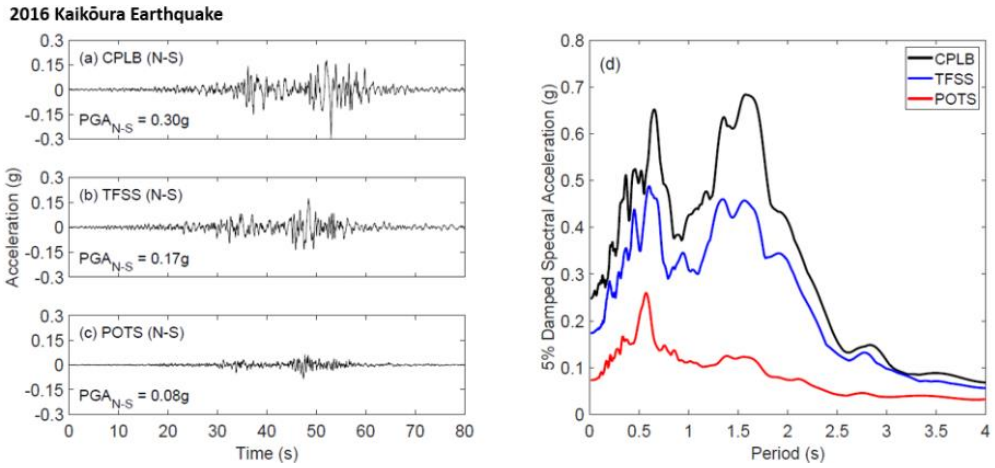

Figure 3.4. Acceleration time histories and 5% acceleration response spectra of the ground motion recorded at station CPLB (reclaimed soil), TFSS (native deposit) and POTS (rock-stiff soil site) during the 2016 Kaikōura earthquake. Taken from Dhakal (2022).

The Thorndon reclamation fill predominantly consists of gravel-sand-silt mixtures, with values of q_c and I_c ranging between 6.5 to 8.0 MPa, and 2.1 to 2.2, respectively (25th and 75th percentiles). For a gravelly soil, the latter values of I_c imply that the soil behaviour is controlled by the finer silty-sand matrix (Dhakal et al., 2020). CPT traces, and evidence of sandy ejecta found along the eastern margin of the reclamation, indicate the presence of a loose-to-medium dense sandy fill at depths of 7 to 20 m, with characteristics ranges (i.e. 25th and 75th percentiles) of q_c of 13.3 – 16.8 MPa and I_c between 1.5 and 1.7. The reclamation rests on top a 1-4 m thick layer of Holocene marine sediments comprised of sands, clays, and silty clays with an important presence of shell fragments. Beneath the marine sediments lays the 90-135 m thick Wellington alluvion formation, characterized by interlayered gravels and stiff silts. The respective q_c and I_c 25th and 75th percentiles for the marine sediments are: 1.2 – 2.7 MPa and 2.8 – 3.1. For the Wellington alluvion gravels: q_c = 21.5 – 26.8 MPa and I_c = 1.74 – 1.9; and for the alluvion silts: q_c = 4.6 – 6.3 MPa and I_c = 2.5 – 2.74.

Although the CPT measurements may include the effect of the 2013 and 2016 earthquakes, during the 2013 events soil liquefaction was limited. Moreover, blow counts from Standard Penetration Tests (SPTs) taken before the 2016 event, albeit nonstandard, were consistent with the post-event CPT data. Thus, while the CPT data may have been slightly affected by the earthquakes, it is considered to be sufficiently reliable (Bray et al., 2019; Dhakal et al., 2020).

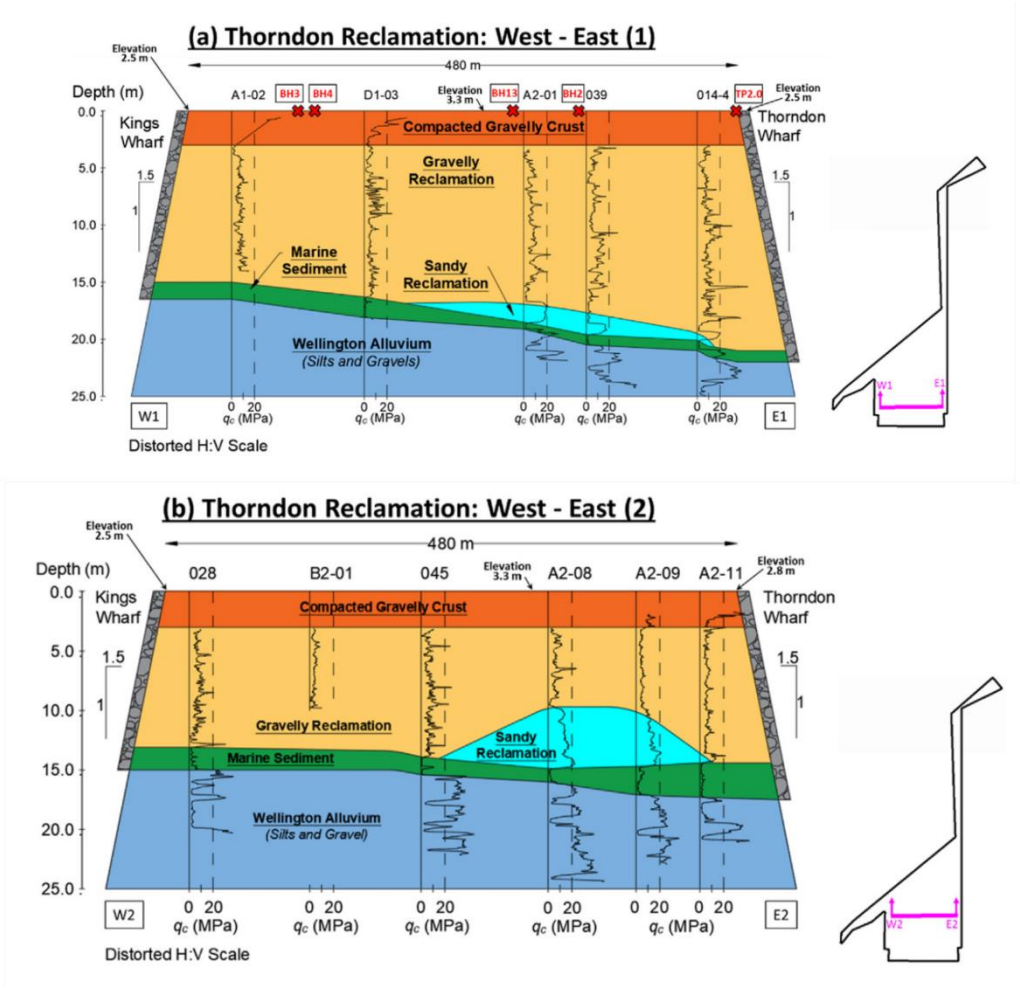

Figure 3.5. Cross sections of the Thorndon outlining the representative soil unites with traces of cone tip resistance (q_c). Vertical scale is exaggerated by a factor of 10. Taken from Dhakal et al. (2020).

3.4 NUMERICAL MODELLING

The seismic response of TCW was assessed through 2D, time history, non-linear, effective-stress, soil-structure-interaction analyses conducted with the explicit finite difference software FLAC v8.1 (Itasca Consulting Group, Inc, 2019). These types of analyses will be hereby referred as to effective stress dynamic-soil-structure interaction (DSSI) analyses. FLAC utilizes a two-phase-soil formulation to solve the governing equations of balance of momentum and balance of mass for saturated soils. Kinematic and inertial effects were examined through the analysis of two types of numerical models: one consisting in the 2D soil-slope model without the wharf, referred as to Free-Field (FF) model, and the Soil-

Structure (SS) model incorporating the TCW structure. The comparison of results from these models offers insights into dynamic-soil-structure-interaction features and their effect on the response of the system, at the global and local levels.

Figure 3.6 shows the schematic of the SS model, which is 42 m tall and 204 m wide. It is representative of cross section West-East (1) of Figure 3.6a. It is comprised by roughly more than 7500 1x1 m finite difference zones (i.e., elements). The base of the model consists of 2-m thick elastic elements attached to a viscous boundary, which is idealized as a series of dashpots placed along the normal and transverse directions. Free-field boundary conditions were enforced at the lateral boundaries following the formulation of Lysmer and Kuhlemeyer (1969), which employs 1D soil columns modelled in-parallel to the main grid (not shown in Figure 3.6). The lateral boundary is placed 130 m from the waterfront, which prevents any unrealistic interaction between the area of interest and the free-field boundary.

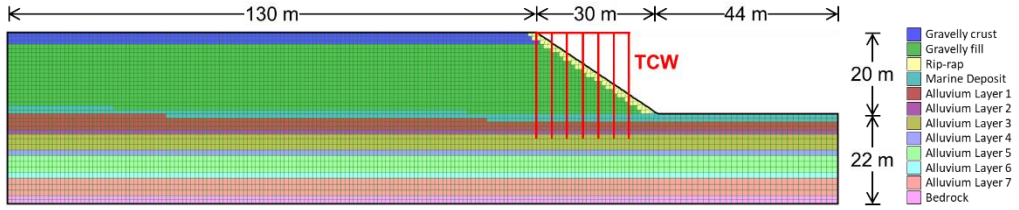

Figure 3.6 Schematic of the SS numerical model of the Thorndon Container Wharf (TCW) of CentrePort (Dhakal, 2023).

Geostatic stresses were determined for a water table depth of 2.7 m and for anisotropic initial conditions. During shaking, the groundwater flow feature of FLAC was activated, effectively simulating drained conditions.

The wharf was modelled using FLAC's beam and pile elements for the deck and piles, respectively. The approximately 23-m long deck is made of 18 elements, with nodes at each of the seven pile-deck connections. The 26-m deep piles were modelled using 25 elements, with nodes placed at 1 m intervals. The nodes were attached to the soil grid, except in cases wherewith the exception of the nodes located within the rip-rap, gravelly crust layer, or and above the slope submerged in the sea (Dhakal, 2023). The trailing pile is fully embedded in the soil, with its nodes attached to main grid from approximately 3 m depth, whereas the lead pile is embedded below approximately 15.5 m depth and attached to the soil grid from 17 m depth. Plastic zones were placed along the length of each pile to enforce the nonlinear constitutive model of Andreotti and Lai (2017a; 2017b). This model is capable of simulating the cyclic degradation of the pile structural properties. It follows a distributed plasticity formulation and is therefore suitable for dynamic soil-structure interaction problems. The parameters of the model were calibrated to reproduce appropriate moment-curvature

relationships characteristics of the pre-stressed reinforced concrete piles, including degradation of stiffness due to cracking, cyclic loading, and after the onset of yielding.

3.4.1 Input motions

The numerical simulations used input motions obtained from the deconvolution of the time histories recorded at the station VUWS. The station is on top of a shallow land reclamation, it is located at approximately 200 meters from the southeastern boundary of the port, also within the Thorndon basin. Dhakal et al. (2022) concluded that conducting ground response analyses using motions deconvolved at VUWS, compared with the other nearby stations atop of the land reclamation, produces the best estimates of surface motion. Records at this station are less affected by non-linear soil response as the seismic bedrock is, in relative terms, shallow at 85 meters depth.

To examine the evolution of the system response with increasing intensity of the input excitation, this study considered three different input intensities. The input motions were generated by scaling and deconvolving the records from the Kaikoura and Lake Grasmere events, so that they match outcropping motion peak acceleration (Ag) of 0.1g, 0.2g and 0.3g. The Lake Grassmere record was used to generate the input for the lowest intensity, while the Kaikoura event was used for Ag=0.2g and Ag=0.3g. For each intensity, the input motion was applied as a traction at the base of the model via viscous dashpots. Figure 3.7 shows the acceleration time histories and (5%-damped) acceleration response spectra of the outcropping motions.

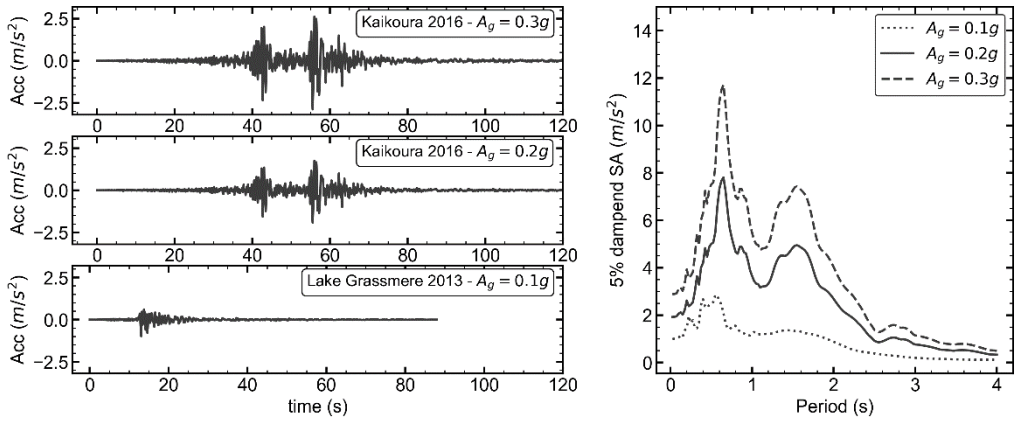

Figure 3.7. Input (outcropping) motion applied at the base of the FF and SS numerical models deconvolved from the record of station VUWS. Left acceleration time history for Ag values of 0.1g, 0.2g and 0.3g. The plot on the right panel shows the respective 5% - damped acceleration response spectra.

Note that, station CPLB, which is within the reclamation, registered PGAs of 0.13g and 0.25g for the 2013 and 2016 events respectively. Therefore, the results of these analyses are a basis for comparison with measurements of ground displacements.

3.4.2 Soil modelling

This study modelled the gravelly fills using PM4Sand (Boulanger and Ziotopoulou, 2022); a critical state compatible, bounding surface plasticity model that simulates the contractive–dilative response of soils under drained and undrained monotonic and irregular cyclic loading conditions. Model parameters are calibrated through a series of element-test, cyclic simple shear simulations to simulate target liquefaction resistance curves (LRCs). LRC represents the combination of the Cyclic Stress Ratio (CSR) and number of uniform cycles (N_{cyc}) required to cause liquefaction, or 5% double-amplitude strain, for a range of densities and vertical effective stresses.

In the absence of laboratory data regarding the cyclic resistance of the gravelly fills, this study opted for implementing a robust CPT-based calibration procedure. It consists in generating target LRCs from well-accepted empirical relationships commonly used within the framework of liquefaction susceptibility assessments (i.e., Boulanger and Idriss, 2014). The reference LRC for the fills corresponds to a normalized clean-sand-equivalent tip resistance (q_{c1Ncs}) of 85. This value is the best-estimate obtained for the gravelly fill based on the CPT-based characterization of the site. Figure 3.8 shows reference and simulated LRCs together with the verification of the effects of effective vertical stress, and sustain static shear stress, taking as reference the relations proposed by Boulanger and Idriss (2014) and Idriss and Boulanger (2008).

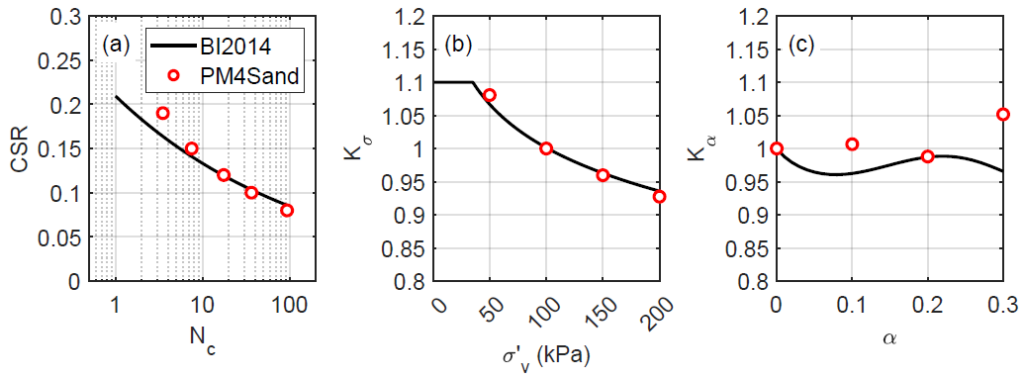

Figure 3.8. PM4Sand calibration and verification of the LRCs, Kσ, and Kα effects for qc1Ncs value of 85, representative of the gravelly reclamation at TCT. As reported by Dhakal (2023).

The datapoints in Figure 3.8 were generated from simple shear, single element simulations using PM4Sand by setting the primary model parameters D_R, Go, and h_{po} to 48%, 606, and

0.53, respectively. The secondary parameter C_ε was also set to 5.5 (i.e., different from its default value) to obtain a post-liquefaction rate of strain increase consistent with the laboratory observations reported by Tasiopoulou et al. (2020) (Dhakal, 2023).

The marine sediments were modelled using PM4Silt (Boulanger and Ziotopoulou, 2023), which is based on the PM4Sand bounding surface plasticity framework, with modifications that account for the monotonic and cyclic undrained strength, and energy dissipation characteristics of clays and plastic silts (as opposed to those for purely non-plastic silts or sands). The naturally deposited alluvial layers were modelled using UBCHYST5d which is an adaptation of the Mohr-Coulomb model developed for non-liquefiable soils. Further modelling details for the marine sediments and the alluvion are presented in a separate publication by Dhakal (2023).

3.4.3 Structural modelling

The nonlinear behaviour of the piles was modelled with the distributed plasticity model formulated by Andreotti and Lai (2017a, 2017b). The model effectively reproduces key aspects of the dynamic behaviour of reinforced concrete sections, namely, inelastic behaviour after yielding and cyclic degradation of stiffness, rendering it compatible with PBEE principles. Input parameters are reported in Table 3.1, they represent the nominal reinforced concrete properties of the piles supporting TCW. The bending capacity of the piles was inferred from the available, albeit limited information about the distribution and characteristics of the reinforcement steel. The top panel (a) of Figure 3.9 shows the adopted moment – axial load (M-N) interaction diagram. Bottom panel (b) shows the moment-curvature response reproduced by the model after monotonic and cyclic simulations performed on a 6.5 m tall cantilever column. The column was laterally loaded under displacement-controlled conditions, without axial loading. The bottom elements were assigned with the non-linear model while the remainder of the column was assumed elastic. Details about the sensitivity of the response to the length of the bottom elements are presented in Appendix A.1.

The yield bending moment (M_y) and yield curvature (χ_y), for the case of null axial load, are 0.47 MN and 2.7 rad/Km respectively. After failure is detected, the model assigns a flexural post-failure strength of about 20 to 50% of the nominal capacity depending on the type failure (i.e., ductile or brittle) (Andreotti and Lai, 2017a, 2017b). However, besides adding one more source of uncertainty, this feature poses critical limitations in terms of computational time as the simulation time-step reduces dramatically. Therefore, this the post-failure feature was not activated during the 2D analysis of the wharf BAF.

Table 3.1 Nominal material properties for the reinforced concrete used to model the piles of TCW with the distributed plasticity model of Andreotti and Lai (2017a, b).

Concrete compressive strength, f'_c	50 MPa
Concrete tensile strength, f_{tc}	3.0 MPa
Yield strength of longitudinal reinforcement, $f_{y,l}$	300 MPa
Yield strength of transverse reinforcement, $f_{y,s}$	300 MPa
Concrete Young's modulus, E_c	35.4 GPa
Steel Young's modulus, E_s	200 GPa

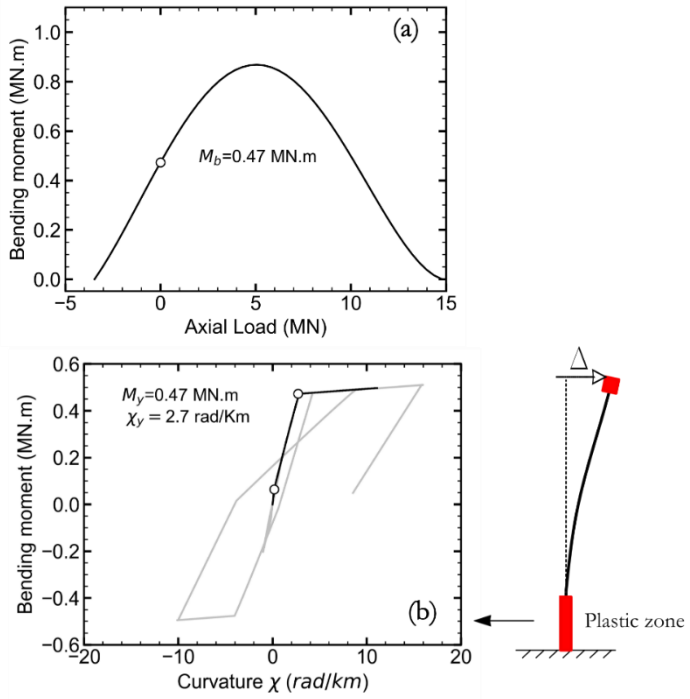

Figure 3.9. Nominal bending moment and axial load interaction diagram (a) for the piles of TCW. Response of a 6.5m cantilever column (b) modelled using the distributed plasticity model of Andreotti and Lai (2017a, b). The plastic zone was modelled with two beam elements 0.75 m long with the properties defined in Figure 4.20Figure 4.6 and Table 4.4.

3.5 SYSTEM RESPONSE

The following discussion delves into the outcomes of the numerical simulations executed with the FF and SS models of TCW for two input motion intensities (Ag), 0.2g and 0.3g. For Ag=0.1g the gravelly reclamation didn't liquefy, maximum strains were below 1%, thus results from this analysis are excluded from the present discussion. Reference to the highest and the lowest input intensities will refer to Ag = 0.3g and 0.2g, respectively.

The evolution of the FF response is illustrated by the contour maps shown in Figure 3.10,Figure 3.11 and Figure 3.12, for final horizontal displacement, maximum shear strain (γ_{max}), and maximum excess-pore-water-pressure ratio ($r_{u,max}$) respectively. Displacements were computed relative to the base of the model.

Results show that the FF simulations predicted two distinct modes of deformation, namely, lateral spreading and toe failure. For the lower input intensity, the slope crest experienced a lateral movement of 1.0m towards the sea, accompanied by a 0.27m slump. For the higher intensity input, the crest moved 2.4m laterally and 0.36m downwards. At the toe, ground shaking induced the formation of a 70m-long shear plane, resulting in a lateral movement of 1.27m and a 0.18m heave. Large shear strains concentrated at the end of the slip plane, reaching values as high as 50% for Ag=0.3g and 35% for Ag=0.2g (see Figure 3.10).

As the input intensity increased, larger lateral ground movement developed due the excessive liquefaction-induced deformations that took place within the gravelly fill behind the slope, (see Figure 3.11 between 440m and 490m in the horizontal axis). For Ag=0.2g, shear strains in this area reached 12%, escalating to 40% for the Ag=0.3. It is noteworthy that for these analyses, the large deformation feature of FLAC was activated. This implies that the deformed shape of the model favoured the generation of sustain shear stresses along the band of elements that were more strained.

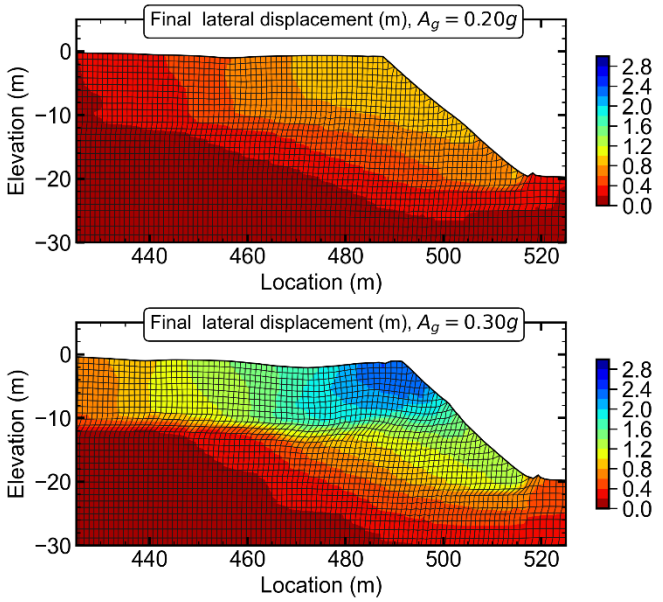

Figure 3.10. Contours of final lateral displacements (after 120s) obtained from the FF-model simulations with input Ag of 0.2 (top) and 0.3g (bottom). Mesh is shown distorted with magnification factor of 3.0.

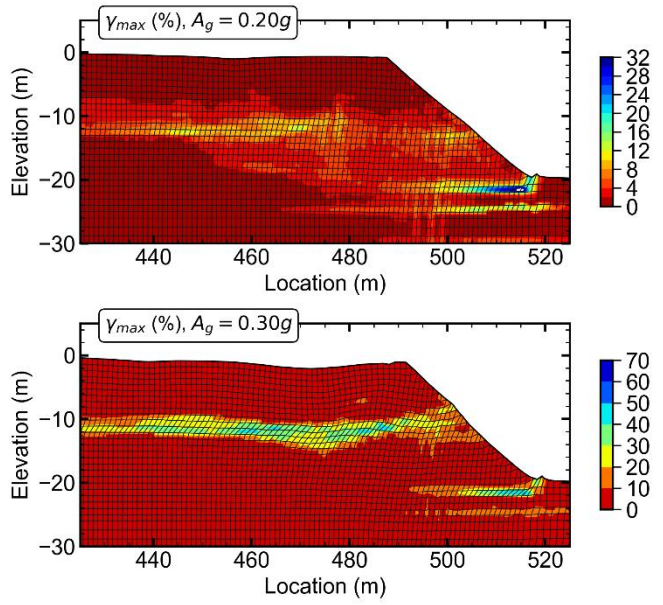

Figure 3.11. Contours of maximum shear strains obtained from the FF-model simulations with input Ag of 0.2 (top) and 0.3g (bottom). Mesh is shown distorted with magnification factor of 3.0.

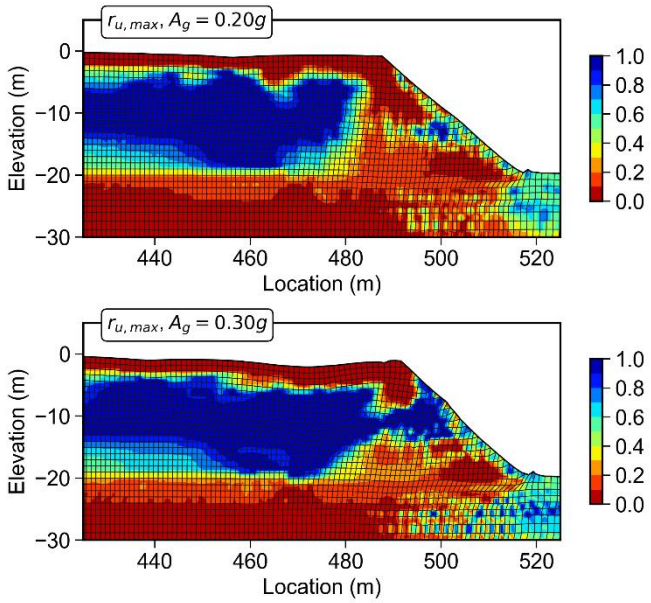

Figure 3.12. Contours of maximum EPWPR, $r_{u,max}$, obtained from the FF-model simulations with input Ag of 0.2 (top) and 0.3g (bottom). Mesh is shown distorted with magnification factor of 3.0.

Despite triggering liquefaction in the gravelly fill, the lower intensity input did not cause significant pore-pressure build-up inside the slope, creating a wedge of non-liquefied elements behind the scarp (see Figure 3.12).Several mechanisms contribute to this behaviour, such as the effects of static shear stresses within the slope, and lateral extension of the elements at the base of the slope. This uneven distribution of excess pore water pressures and maximum shear strains along the horizontal direction are presented in a more compact form in Figure 3.13. Figure 3.13a shows the maximum shear strains recorded inside the gravelly reclamation (RC) and marine sediments (MS) below each vertical. Figure 3.13b shows the variation of the cumulative thickness of liquefied (CTL) soils (i.e., $r_{u,max}$>0.98 and γ_{max}>3%) along the horizontal direction. The latter plot captures the non-liquefied wedge between 475 and 425m, that coincides with the location of the sliding plane at the toe, as per the distribution of γ_{max} inside MS. CTL exhibits additional variations. Behind the slope, where the lateral spreading strains concentrate, a 10m-by-10m area of the gravelly fills liquefied, creating a bell like shape of the CTL distribution cantered at approximately 460m. It is followed by the non-liquefied wedge and preceded by a zone of limited liquefaction where CTL is as low as 4m. Point A and Point B are located on the valleys around the largest CTL at 460m, they coincide with the locations at which the lateral spreading strains were the highest. All in all, it can be stated that the lateral spreading strains took place along a 40 m to 60 m wide section behind the slope at x=435m.

Figure 3.14 shows the results for Ag=0.3g in the same fashion as Figure 3.13. It can be noted that lateral spreading strains besides reaching significantly larger values, were also concentrated over a wider area. Nonetheless the distribution of CTL and γ_{max} are remarkably like those computed for the lower input intensity. Likewise, the highest strains levels were attained behind the slope in the zones before and after the thickest zone of liquefaction.

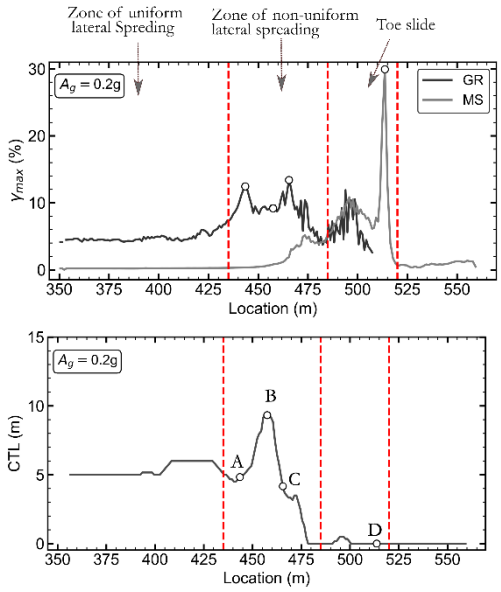

Figure 3.13. Distribution of maximum shear strain and cumulative thickness of liquefiable soils along the verticals of the FF model for Ag=0.2g.

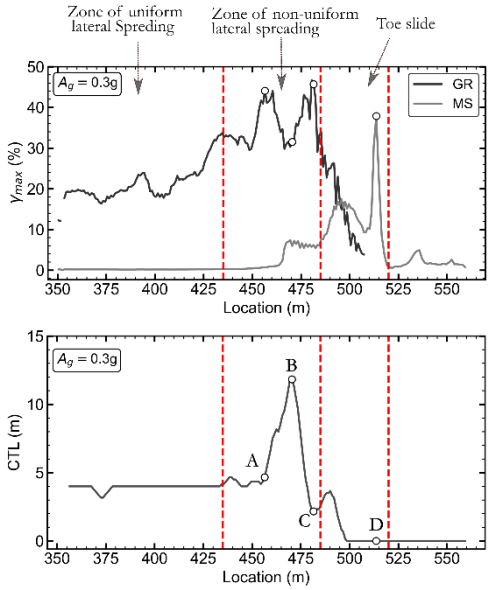

Figure 3.14. Distribution of maximum shear strain and cumulative thickness of liquefiable soils along the verticals of the FF model for Ag=0.3g.

For the Soil-Structure (SS) analyses, Figure 3.15, Figure 3.16 and Figure 3.17 show the results in terms of contours of final horizontal displacements, maximum shear strain and maximum excess-pore-water-pressure. In general terms, the inclusion of the TCW structure resulted in seemingly opposing effects on the system response. While it restrained ground movement at the toe, it led to an increase in the lateral spreading deformations behind the slope.

The piles restrained the ground movement at the base of the base of the slope, yet they did not reduce the magnitude of the lateral spreading displacement, instead it increased slightly. As in the FF case, lateral spreading displacements were mainly caused by the post-liquefaction shear strain accumulation within the area behind the wharf. With the notable difference that the inclusion of the wharf led to larger strains and an extension of the lateral spreading displacements 20m further inland.

Large strains that developed behind the wharf were concentrated at the centre of the gravelly reclamation, around x=480 m. At the base of the layer excess pore water pressure was limited in elements near the wharf. This less contractive response at the base of the gravelly fill increased demands on elements at the middle of the layer. Moreover, the wharf facilitated liquefaction within the slope, particularly within the non-liquefied wedge. This behaviour may be associated with a "more rigid base" effect due to reduced movement at the toe.

The larger estimates of ground displacements obtained from the SS analyses could be an effect of the modelling methodology, for two potential reasons. First, being the wharf attached to the main grid, its inertial movement could have aggravated the ground movement. Second, the lateral free-field boundaries loose efficiency for low frequency motion, thus they are incapable of providing full restraint against lateral spreading. The latter condition can be tested by comparing the performance of the current models against other methodologies, such as the use of reflected models.

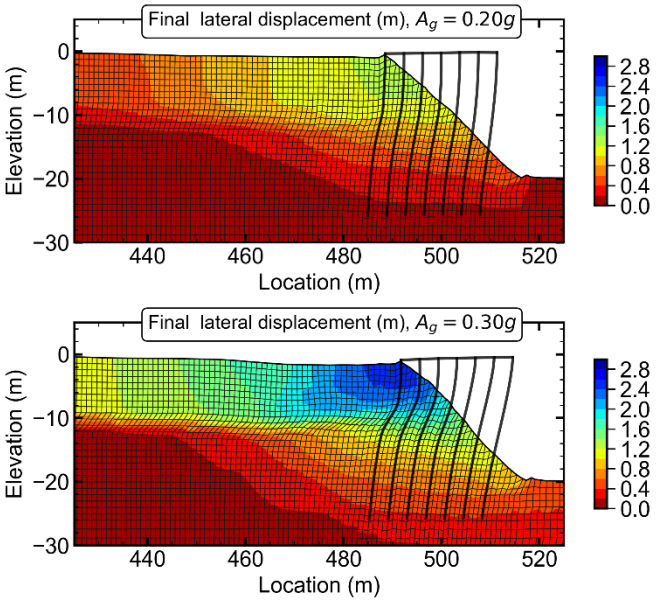

Figure 3.15. Contours of final lateral displacements (after 120s) obtained from the SS-model simulations with input Ag of 0.2 (top) and 0.3g (bottom). Mesh is shown distorted with magnification factor of 3.0.

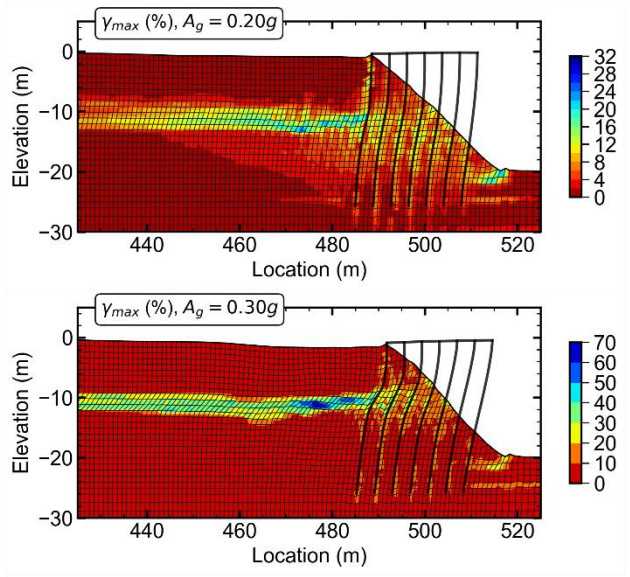

Figure 3.16. Contours of maximum shear strains obtained from the SS-model simulations with input Ag of 0.2 (top) and 0.3g (bottom). Mesh is shown distorted with magnification factor of 3.0.

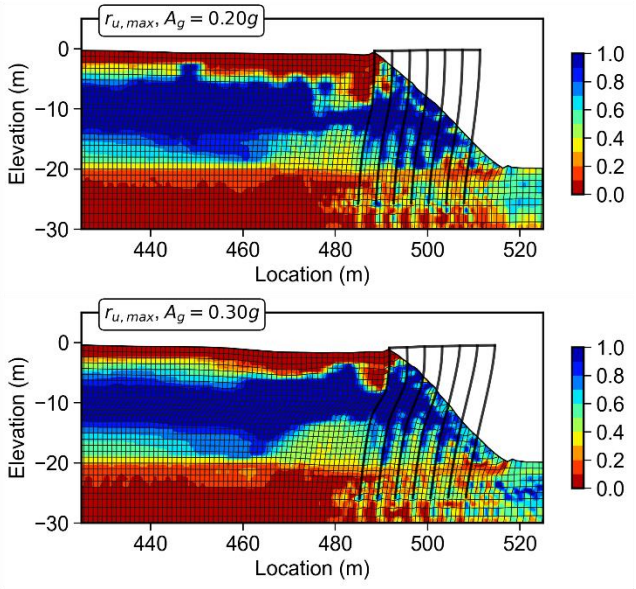

Figure 3.17. Contours of maximum EPWPR, $r_{u,max}$, obtained from the SS-model simulations with input Ag of 0.2 (top) and 0.3g (bottom). Mesh is shown distorted with magnification factor of 3.0.

3.6 COMPARISON WITH FIELD MEASUREMENTS

After examining the ground deformations produced by the the Mw 6.9 Great Hashin earthquake of 1995, Ishihara et al. (1997) concluded that the areas affected by lateral spreading could be subdivided into zones of non-uniform and uniform spreading. The largest ground movements, along both vertical and horizontal directions, concentrate inside the non-uniform spreading zone, in which notable cracks and vertical offsets occur. Ground displacements diminishes as one moves further inland until no crack or fissures are visible. Reaching the uniform spreading zone, the ground would still exhibit a lateral residual displacement, and liquefaction-induced damage would be mainly due to settlements or loss of bearing capacity.

Figure 3.18 illustrates the distribution of residual horizontal displacements estimated from the FF analysis of TCW for an input intensity of 0.3g. Displacements are computed with respect to the base of the mode, and residual surface displacements are denoted with the greek character Δ. Results from the 2D effective stress analysis are consistent with the lateral spreading pattern described by Ishihara et al. (1997). In terms of ground displacement, three response parameters are worth examining, namely the uniform spreading displacement (Δ_U), the residual displacement of the slope crest (Δ_{Crest}), and the relative lateral displacement of the crest ($\Delta_{Lateral}$). This latter matric corresponds to difference between the former two, it is a direct measurement for the non-uniform (i.e., distortion related) component of the liquefaction-induced lateral spreading ground movement.

In interpreting the results, the distinction between the different components of lateral spreading has the additional benefit of isolating the effects of the free-field lateral boundary on Δ_U. Likewise field measurements for this quantity are also affected by the choice of the reference point (Cubrinovski et al., 2017; Ishihara et al., 1997). Figure 3.19 compares the estimates of Δ_{Crest} , $\Delta_{Lateral}$ against the field measurements reported by (Cubrinovski et al., 2017). Results for Ag=0.2g are in reasonable agreement with the field measurements, they represent equally acceptable conservative estimate considering that: (1) surface PGA for the Kaikoura event ranged between 0.22g and 0.25g, (2) the type of analysis poorly predicts offset, or cracks, between the wharf and the surrounding ground, which would increase the values of Δ_{Crest}. Note that for Ag=0.3g the magnitude of the lateral ground deformations nearly doubled those of Ag=0.2g.

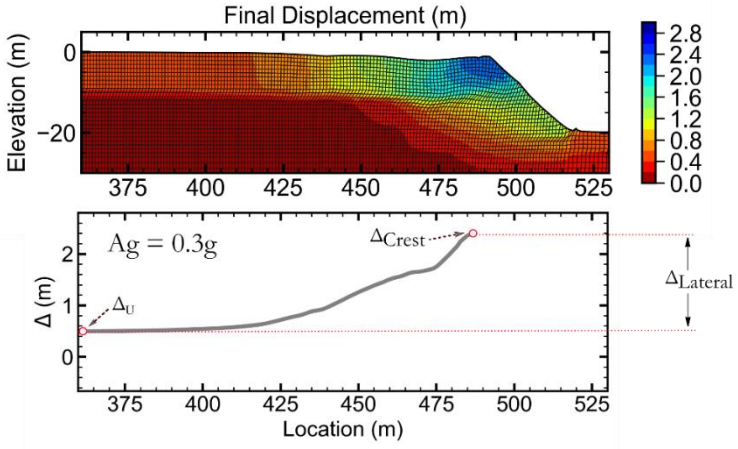

Figure 3.18. Top, contours of residual horizontal displacement computed with respect to the base of the FF model from the simulation that considered Ag=0.3g. Bottom, schematic representation of residual lateral displacements (Δ) estimated from the FF analysis with Ag=0.3g.

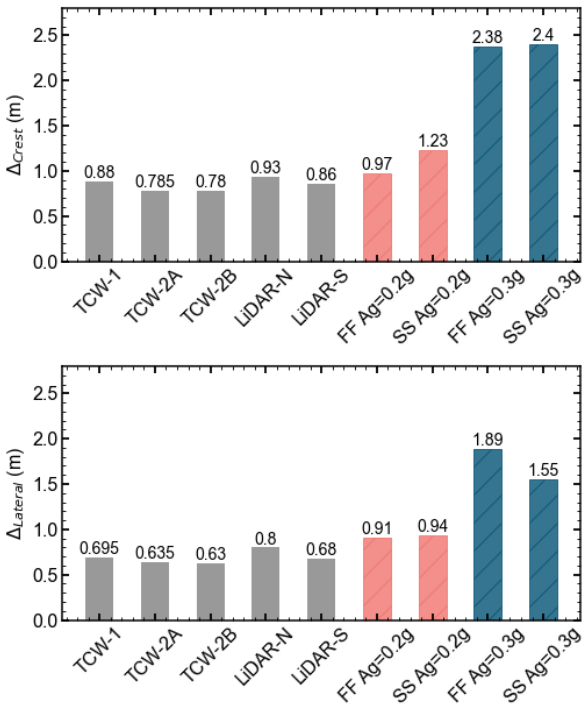

Figure 3.19. Comparison between measurements of ground displacements and results from the 2D effective DSSI analyses. TCW-1, TCW-2A, TCW-2B represent cumulative crack width measurements along three transects reported by Cubrinovski et al. (2017). Likewise, LiDAR measurements reported by the same study are referred to as LiDAR-N and LiDAR-S.

Lastly, Figure 3.20 and Figure 3.21 compare the distribution of the ground distortion behind the wharf with the cumulative crack measurements for residual horizontal and relative lateral displacements, respectively. Note that the field measurements reported in the bottom panels of both figures are presented without the offset between the wharf and the immediately adjacent ground. The distribution of residual displacements estimated form the SS analysis with Ag=0.2g, bear close agreement with the field measurements. Both measurements and numerical simulations indicate that the ratio between Δ_U and Δ_{Crest} is about 0.2. Likewise, from the bottom panel of Figure 3.21 one could infer that the non-uniform component of lateral spreading extended 60m to 80m inland from the wharf.

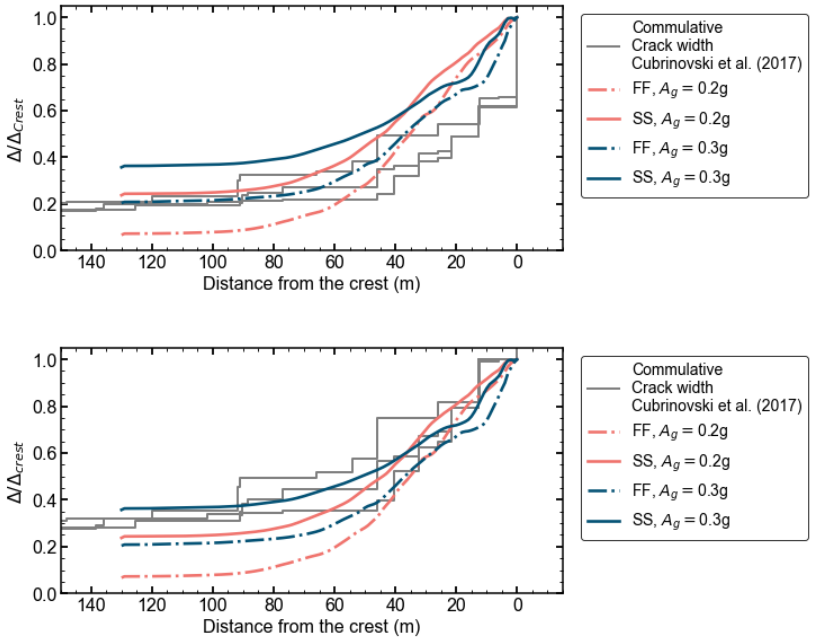

Figure 3.20. Comparison between field measurements and results from 2D effective stress DSSI analyses for the distribution of normalized residual horizontal displacements along the surface. Displacements are normalized with respect to the displacement of the slope crest. In the bottom panel. the offset between the wharf and the backland is subtracted from the field measurements

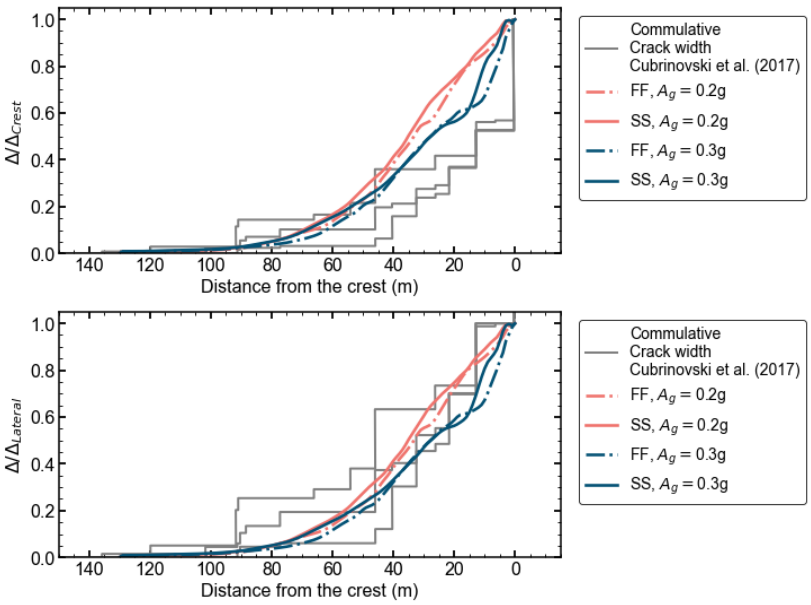

Figure 3.21. Comparison between field measurements and results from 2D effective stress DSSI analyses for the distribution of normalized lateral displacements. Displacements are normalized with respect to the displacement of the slope crest. In the bottom panel. the offset between the wharf and the backland is subtracted from the field measurements.

3.7 SUMMARY AND DISCUSSION

This chapter has presented the methodology and results from effective stress DSSI analyses performed on the TCW of Wellington Centre Port. The simulations addressed the free-field and soil-structure responses obtained by using three ground motions records for input Ag of 0.1g, 0.2g and 0.3g. The 2013 Lake Grassmere record was used to generate the input for the lowest intensity, while the 2016 Kaikoura event was used the latter two. For Ag=0.1g liquefaction of gravelly fills did not occurred, which is in accordance with the observations of the 2013 event. In contrast, simulations with Ag=0.2g and Ag=0.3g resulted in severe liquefaction and large lateral spreading displacements. The estimated residual horizontal displacements at the crest of the slope (i.e., behind the deck) were around 1.2 and 2.4 m for Ag=0.2g and Ag=0.3, respectively.

Lateral ground displacements were primarily caused by the large strains that occurred with the gravelly fill, in the area immediately behind the wharf, reaching maxima of 12% and 40% for the highest ground motion intensities. Non-uniform lateral spreading was caused by an uneven distribution of liquefaction behind the slope. Maximum shear strains concentrated along the verticals with shorter CTL. By and large, the lateral spreading strains took place along a 40 m to 60 m wide section.

The effect of the wharf structure on these estimates was limited. The distribution of the lateral spreading distortion was similar for FF and SS analyses. The wharf mainly restrained the movement at the base of the slope.

Results for Ag=0.2g were in reasonable agreement with the field measurements made after the 2016 Kaikoura earthquake. They can be regarded acceptable conservative estimates considering that: (1) surface PGA for the Kaikoura event ranged between 0.22g and 0.25g, (2) the type of analysis poorly predicts offset, or cracks, between the wharf and the surrounding ground, which would increase the estimated values of Δ_{Crest}. Note that for Ag=0.3g the magnitude of the lateral ground deformations nearly doubled those of Ag=0.2g. Both measurements and numerical simulations indicated that the ratio between uniform component of lateral spreading, Δ_U and Δ_{Crest} was about 0.2.

4.SEISMIC PERFORMANCE OF LARGE DIAMETER PILE SUPPORTED WHARVES, CASE STUDY: PORT OF GIOIA TAURO. PART A: CHARACTERISTIC SEISMIC RESPONSE

4.1 INTRODUCTION

Wharves, along with berthing structures in general, are fundamental components of seaports. Past seismic events have caused significant losses and have hindered the operational capacity of seaports. Damage to these key infrastructures reduced the resilient capacity of the affected community as these facilities are critical for the regional economy, businesses and post-emergency recovery operations. Notable examples include the failure of the Takahama Wharf at the port of the city of Kobe due to the widespread liquefaction triggered by the Mw 6.9 Great Hanshin earthquake of 1995 (PIANC, 2001); the collapse of the main wharf at the port of Port-au-Prince, Haiti, caused by the Mw 7.0 event of 2010 (Green et al., 2011); the severe damaged Thorndon Wharf at the port of Wellington in New Zealand after the Mw 7.8 Kaikōura earthquake of 2016 (Cubrinovski et al., 2017); among others.

Therefore, recognizing their importance, special attention has been devoted to revising and updating the seismic design guidelines and procedures for berthing structures over the past two decades. There has been a growing emphasis on performance-based design philosophies. This is evident in recent standards such as the latest ASCE 61-14 standard for the seismic design of piers and wharves (ASCE, 2014); the Japanese technical standards for port and harbour facilities (OCDI, 2020), the Port of Long Beach wharf design criteria (POLB, 2012), the Port of Los Angeles code for seismic design, upgrade and repair for container wharves (POLA, 2010)

Assessing the seismic performance of geotechnical systems affected by soil liquefaction inevitably is a complex task that requires the careful consideration of the non-linear response of the liquefiable ground. This study addresses the seismic response of the deepwater wharf of the port of Gioia Tauro, in Southern Italy by means of non-linear, large-strain, soil-structure-interaction time history analyses. The structure is a large diameter pile-supported-wharf founded on an heterogenous coarse-grained deposit. While small diameter piles are widely used in the U.S. and Japan to support wharves ($D_p < 0.7 \div 0.8$m), in the mediterranean basin the use of larger piles is more common (Ntritsos, 2015). Thus, the study aims to contribute to the understanding of the critical modes of deformation and loading conditions relevant for the seismic design of large diameter pile-supported wharves.

The numerical analyses are conducted using the commercial software FLAC (v8.1) FLAC (v8.1) (Itasca Consulting Group, Inc, 2019). FLAC is an explicit finite difference code designed for solving geotechnical engineering problems, specifically tailored for the coupled solution of momentum and mass balance equations for two-phase porous media.

To address crucial aspects of model uncertainty and potential limitations in analysing the response of liquefiable soils, the study considers the use of two advanced constitutive models: PM4Sand (v3.1) developed by Boulanger and Ziotopoulou (2017), and SDm (v1.1) developed by Cubrinovski and Ishihara (1998a, 1998a). Soil-structure interaction effects are investigated by analysing the response of two numerical models of wharf BAF: a Free-Field model (without the wharf) and a Soil-Structure model. The evolution of the ground and wharf responses is examined by scaling the input ground motion to three different intensity levels, which are compatible with characteristic levels of the hazard at the site.

Finally, this chapter addresses the seismic response of the wharf BAF by: (1) studying the evolution of plastic hinge activation with ground motion intensity, (2) examining the inertial and kinematic seismic demands on the trailing pile, (3) systematically comparing the results from the simulations that used PM4Sand and SDm to model the response of the liquefiable soils.

4.2 PORT OF GIOIA TAURO: BACKGROUND

The Port of Gioa Tauro is a major transhipment terminal located along the Tyrrhenian cost of the of Reggio Calabria region in southern Italy. The port was initially planned as a component of a large industrial hub that would house a siderurgical complex and a power generation plant. Construction works begun in the earlies 70s, however, by the late 80s the steel industry was facing a severe economic crisis that rendered the port inoperative. The port facilities were gradually repurposed to serve as a container transport terminal to take advantage of its favourable geographical location in the Mediterranean basin. During the mid-90s, the activity of the port experienced its fastest growth, as a result, the Italian state granted it with the status of "international economic relevance". Nowadays it serves as a key transhipment facility along the Suez-Gibraltar maritime route (Famà et al., 2014). Between the years 2000 and 2015 the port mobilized around 3 million TEU per year (Twenty Foot Equivalent Units) placing it among the top 5 transhipment hubs in the Mediterranean basin (Grifoll et al., 2018).

The port consists of an artificial channel, 220 m wide and 3.8 km long, that extends north-south parallel to the Tyrrhenian cost of the Regio Calabria region (see Figure 4.1). The port entrance is located at the southern end of the channel, connected to the sea by a turning basin of 750 m of diameter. Most of the berthing operations take place along the eastern bank of the channel, which accommodates three sets of berthing structures, they are highlighted by different shades in Figure 4.1.

Docks ABC and D are quay walls built during the early construction stages of the port. They were constructed by driving reinforced concrete sheet piles into the ground prior to the excavation of the main channel. The sheet piles were anchored by means of prestressed concrete rods to a set of battered piles spaced every 3m. Dock BAF, which is the acronym in Italian for "Banchina Alti Fondali" (deep water dock), is a large-diameter pile-supported

wharf built in 2005. The wharf was built on top of the dredged slope; additional details about the ground improvement carried out at the site (if any) are however not available. Being the only terminal located on deep waters, Dock BAF allows for the berthing and mooring operations of large draft Postpanamax vessels, and thus crucial for the transhipment operations of the port.

The cross section of wharf BAF is shown in Figure 4.2, its main components and characteristics are described as follows. The deck is supported by four rows of reinforced concrete piles, 1.5 m in diameter. The leading pile reaches a depth of 40 m from the sea level, while the tips of the trailing and central piles reach depths of 25 m and 30 m respectively. The reinforced concrete deck is 2.4 m tall and it is composed of 15 segments, each 28.8 m in length. The four rows of piles supporting the deck are spaced at 6 m (4D). Tiebacks were also installed to provide additional support to the wharf. However, detailed information about the tiebacks is not available. As illustrated in Figure 1, the slope of the submerged embankment is protected by a 2.6 m thick riprap layer.

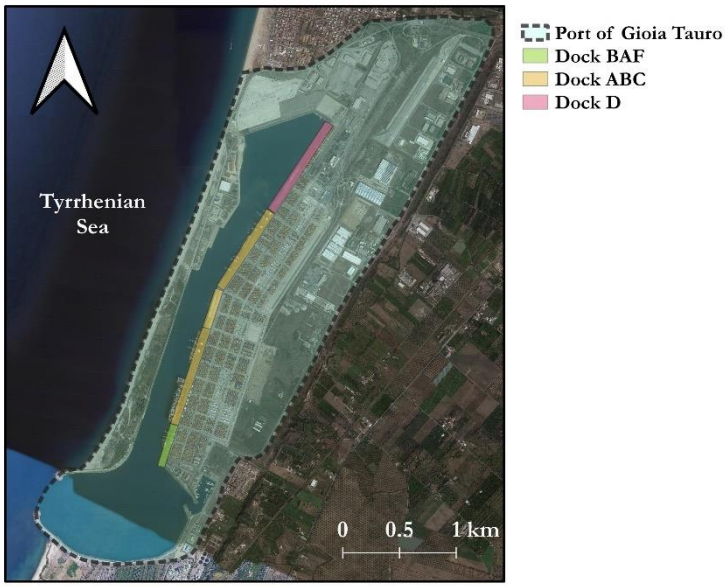

Figure 4.1. Satellite view of the port of Gioia Tauro.

Due to its location in an earthquake-prone area, the port authorities and academic community have engaged in various initiatives and projects related to seismic risk assessment for the port facilities. For example, Facciorusso & Vannucchi (2003) conducted a liquefaction susceptibility study. The authors utilized data from 115 Cone Penetration Tests (CPT) and 121 Standard Penetration Test (SPT), with the majority conducted in the container yard adjacent to the docks, and fewer near the waterfront structures. The study

employed a deterministic estimation of the liquefaction potential index, P_L (Iwasaki et al., 1984) for a return period of 475 years, which was considered consistent with events with expected magnitude of 7.3. A kriging technique was then utilized to generate a liquefaction hazard map for the area. The majority of the area was classified with low liquefaction risk, with P_L values smaller than 5%. However, the area surrounding dock BAF exhibited P_L values above 15%, the authors to designated it as an area of high liquefaction hazard.

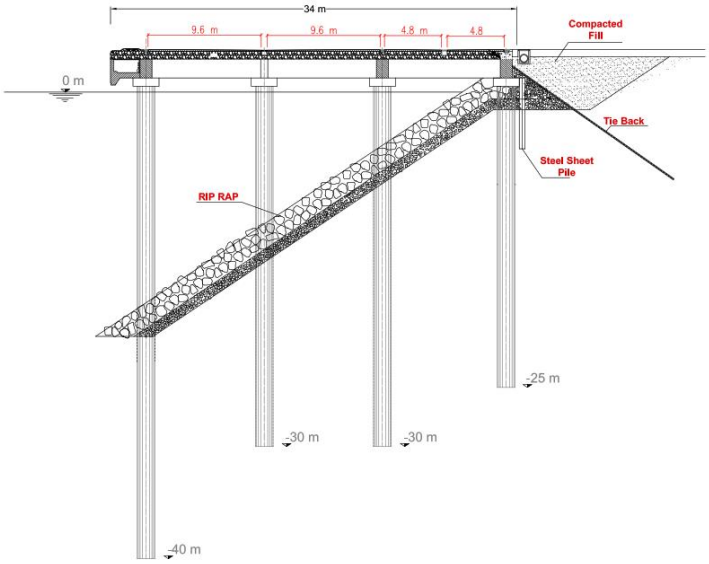

Figure 4.2. Cross section of the wharf BAF of the port of Gioia Tauro.

A decade later, Bozzoni et al. (2014) performed a seismic fragility analysis of some waterfront structures of the port. The analysis specifically accounted for site-specific seismic amplification effects and liquefaction susceptibility. After integrating the filed data gathered from geophysical surveys, boreholes, and previous scientific publications, the authors defined two representative geotechnical models. One model was developed for the southern portion of the port and another for the northern portion.

The study of Bozzoni et al. (2014) was divided into two main tasks, the first dealt with the assessment of seismic site effects and liquefaction susceptibility; and the second with the fragility analysis of two berths. Ground response was estimated by means of stochastic, frequency-domain equivalent-linear 1D ground response analyses. For each soil layer, its thickness, shear wave velocity and unit weight were treated as normally distributed random variables. The interevent variability was accounted for by using a suite of 7 hazard consistent ground motion records as base excitations. For the southern section of the port,

the values of peak ground acceleration at the surface obtained by Bozzoni et al. (2014) are reported on Table 4.1.

In terms of liquefaction susceptibility and ground response, Bozzoni et al. (2014) generated a map in terms of lateral displacement index (LDI) for the port area. The values of maximum shear strains were computed using the method of Zhang et al., (2005); while the safety factors were estimated following the proposal of Cetin et al. (2009). For a return period of 950 years, LDI reached values below 10 cm for most of the port area, which is in agreement with findings of Facciorusso and Vannucchi (2003), indicating a relatively low liquefaction hazard at the port. Nonetheless, the BAF site was one of the exceptions, LDI was estimated to be between 19 and 24 cm.

Table 4.1.Values of peak ground acceleration obtained by Bozzoni et al. (2014) for the southern section of the port of Gioia Tauro,

Return period (years)	PGA at the surface (g)		
	μ	μ-σ	μ+σ
100	0.186	0.156	0.217
475	0.299	0.239	0.359
950	0.365	0.271	0.459

4.3 GEOTECHNICAL SITE CHARACTERIZATION

The port of Gioia is placed on top of a Quaternary sedimentary deposit, primarily consisting of heterogeneous coarse-grained materials, which extend to depths of 55 to 80 meters (Famà et al., 2014). Beneath these granular deposits lies a thick layer of compacted clay and silty clay which extends to approximately 600m below the ground surface. The mean shear wave velocity of this lower layer was measured to be around 800 m/s, which was interpreted as the seismic bedrock of the site.

The relevant geotechnical information of the site was obtained from past technical reports and research projects that dealt with the assessment of the liquefaction hazard and seismic risk for the port (Bozzoni et al., 2014; Conca et al., 2020; Facciorusso and Vannucchi, 2003; Famà et al., 2014). These studies used field-data from Standard Penetration Tests (SPT), Cone Penetration Tests (CPT), and Flat Dilatometer Test (DMT), as well as from geophysical measurements of compressional and shear wave velocity, and laboratory testing of disturbed samples. However, data collection was unevenly distributed across the port area. Figure 4.3 shows a plan view of the locations of the CPT and SPT tests carried out at the southernmost portion of the port. Some CPT tests reported by Facciorusso and Vannucchi (2003) lacked measurements for of sleeve friction (f_s), denoted by the orange markers with thick blue-coloured borderline. It is also worth mentioning that most of the

CPT and DMT tests reported by Bozzoni et al. (2014), and Facciorusso and Vannucchi (2003) , were conducted in the northern and central parts of the port, respectively.

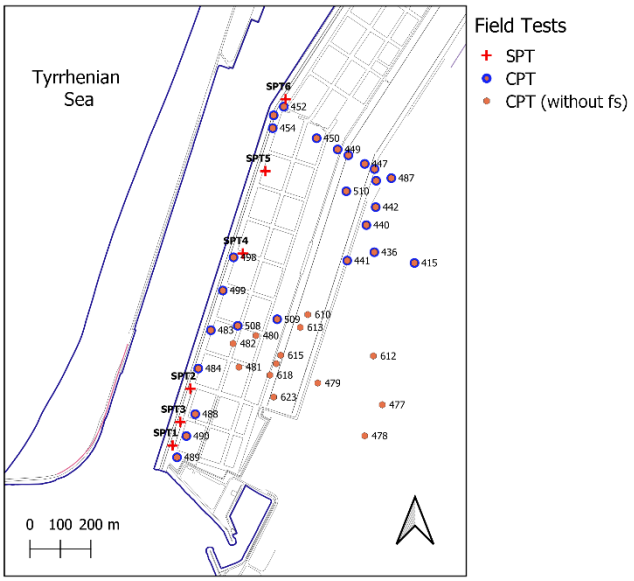

Figure 4.3. Locations of site investigations performed at the southernmost portion of the port of Gioia Tauro.

The SPT boring logs indicate that the upper 5 to 10 meters are comprised of heterogenous deposit of coarse sands, with an important fraction of gravels. At greater depths, the sand fraction becomes finer, with an increasing proportion of silt. Between 18 and 20 meters, some logs reported lenses of gravels, mainly composed by pebbles with diameters between 0.5 and 10 cm. Below 30m, the soil deposit mainly consists of coarse sands and gravels with a small fraction of silt. Overall, the studies cited above consistently showed that the granular materials in the superficial layers correspond to medium to dense coarse gravelly sands, with relative densities (D_R) raging between 50% and 70% across the entire area of the port.

4.3.1 Characteristic CPT profiles

At the site of wharf BAF, a total of six field tests were executed during the geotechnical site investigations that took place prior to the construction of the wharf in 2005. These investigations involved the execution of three SPTs and three CPTs, with their locations shown in Figure 4.3 and denoted as SPT1, SPT2, SPT3, CPT488, CPT490, and CPT489. The test locations were spaced approximately 100 meters apart along the North-South direction. The SPTs were carried out either near or on the crest of the submerged slope, while the CPTs were conducted 10 to 30 meters inland.

Figure 4.4 shows the profiles of CPTs 489, 490 and 488, plotted in terms of normalized clean-sand equivalent tip resistance (q_{c1Ncs}) and soil behaviour type index (I_c) (Boulanger and Idriss, 2016; Robertson and Cabal, K. L., 2015). Reference lines are included for q_{c1Ncs} values of 110, 135, and 155, corresponding to cyclic resistance ratios (CRRs) of 0.15, 0.21, and 0.35, respectively. I_c values indicate that the composition of the upper 12 meters of the deposit varies from clean sands ($1.31<I_c \leq 2.05$) to dense sands and gravelly sands ($I_c \leq 1.31$). Tip resistance exhibits significant variability within the first 5 meters, ranging from $q_{c1Ncs} = 70$ to $q_{c1Ncs} = 300$. Below 5m, and down to a depth of 12m, the soil deposit is consistently denser, with values of q_{c1Ncs} exceeding 200. At such depths I_c points at the presence of a coarser soil. SPT logs also reported the presence of coarse sands with sporadic presence of pebbles. At greater depths, between 12 and 20m, the soil has lower penetration resistance with values of q_{c1Ncs} ranging from 100 to 200.

Conversely, data from CPT489 indicates the presence of considerably looser ($q_{c1Ncs} <70$) sandy silt ($2.05<I_c \leq 2.6$). Three equally soft sites were identified, namely, CPT 484, 509 and 510. The presence of these soft sites, particularly those close to the waterfront, can be attributed to the construction process of the port. The conformation of the slope could have necessitated the placement of fill material. This latter hypothesis is supported by the fact that the soil composition – as per the I_c values – of CPT488 and CPT484 differs from what is interpreted as the native soil. It is important to note that these field investigations took place prior to the construction of the wharf.

When compared to the entire CPT dataset of the port, the data from CPT490 and CPT488 exhibit trends consistent with most of the CPT profiles computed for the southern portion of the port .The plots shown in Figure 4.5 summarize the *q1ncs* and *Ic* data of the CPTs performed in the southernmost section of the port (i.e., the area coloured by the light shade of blue in the map of Figure 4.6).Considering the large extension of this area, the CPT profiles suggest that the native deposit is fairly uniform.

Comparing Figure 4.5 with Figure 4.6, it can be inferred that CPT488 and CPT490 are representative of the first 20 m of the native deposit at the southern section of the port, which is interpreted to be comprised by three distinct layers of coarse-grained materials with boundaries located at 5 and 12 meters approximately. The middle layer considerably denser and can be regarded as non-liquefiable, whereas the upper and bottom layers are looser and may trigger liquefaction under high seismic demands.

The map of Figure 4.6 shows a subdivision of the site of the port into different units that share similar q_{c1ncs} and I_c distributions, all of them exhibiting the three-layered disposition. Figure 4.7 to Figure 4.5 show the detailed CPT data for each unit. Exceptionally softer sites, namely, CPT 509, 510, 489 and 484, were excluded from the zones shown in Figure 4.6. The zoning was mainly based on the q_{c1ncs} values computed for the bottom medium dense layer (between 12 and 20m depth). This layer is softer towards Dock BAF while stiffer towards Dock B in the south-north direction. The zones coloured with yellow and

light orange are near and further inland of Dock B. In these areas, the mean values of q_{c1ncs} of the deepest layer were found to be mostly above 200 (as reported on Figure 4.7 and Figure 4.8). As shown in Figure 4.6, near the waterfront and further inland of Dock BAF (blue-coloured zone), the values of q_{c1ncs} were, on average, between 135 and 200. Finally, at the waterfront of Dock A (light-cyan zone), the tip resistance of the bottom layer spans over a wider range above 135 (see Figure 4.9).

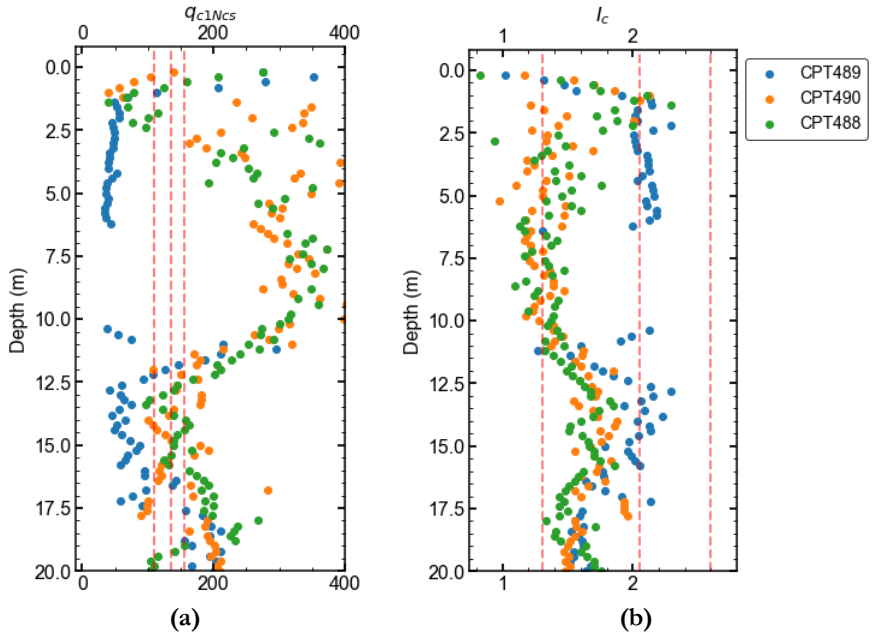

Figure 4.4. CPT profiles near the site of BAF wharf; (a) normalized clean-sand equivalent tip resistance (q_{c1Ncs}) and (b) soil behaviour type index (I_c).

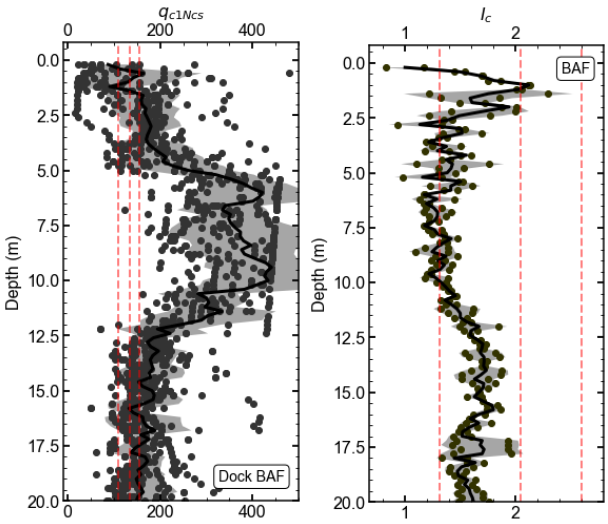

Figure 4.5. CPT profiles (q_{c1Ncs}, I_c) for the waterfront zone of Dock BAF and inland area behind Dock A. Dashed reference lines at q_{c1ncs} equal to 110,135, 155; and at I_c equal to 1.31, 2.05 ad 2.6

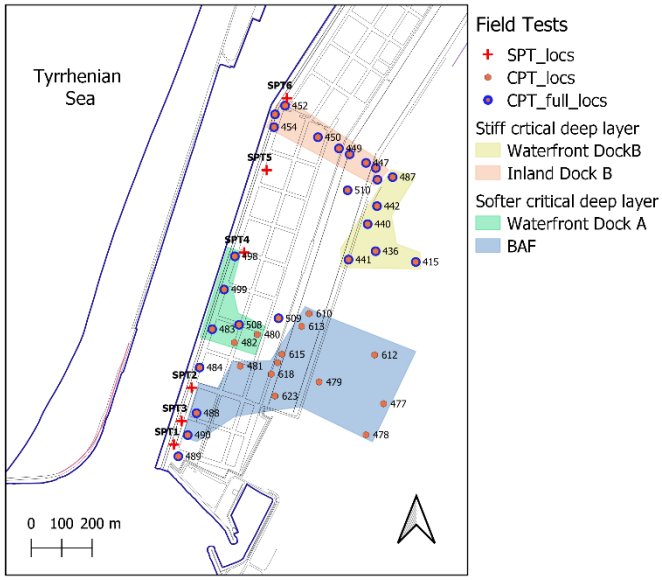

Figure 4.6. CPT-based characterization into distinct subsoil zones for the southern portion of the port of Gioia Tauro

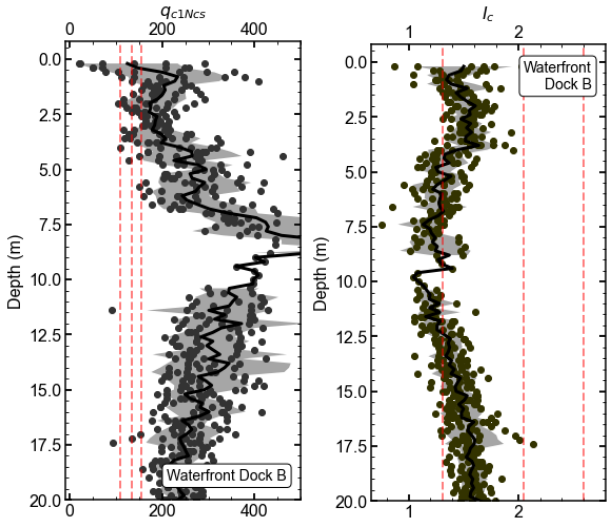

Figure 4.7. CPT profiles (q_{c1Ncs}, I_c) for the waterfront area of Dock B. Dashed reference lines at q_{c1ncs} equal to 110,135, 155; and at I_c equal to 1.31, 2.05 ad 2.6

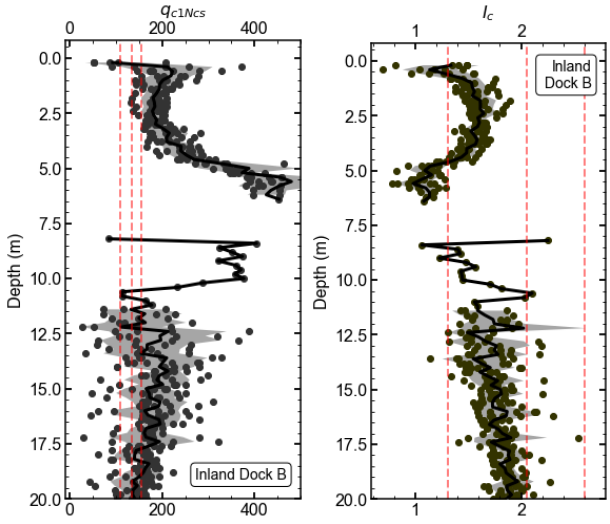

Figure 4.8. CPT profiles (q_{c1Ncs}, I_c) for the inland area behind Dock B. Dashed reference lines at q_{c1ncs} equal to 110,135, 155; and at I_c equal to 1.31, 2.05 ad 2.6

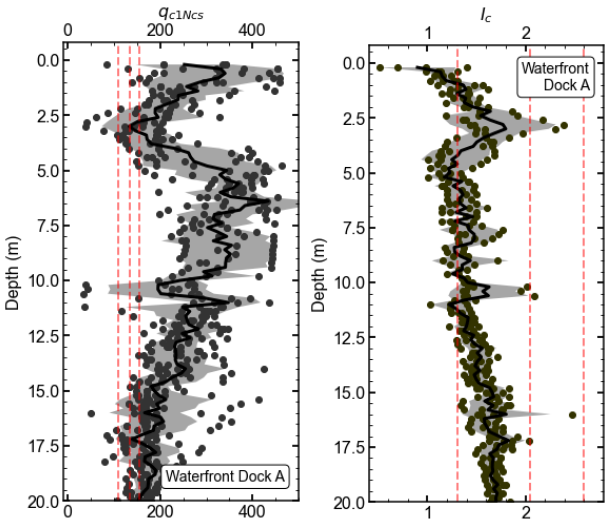

Figure 4.9. CPT profiles (q_{c1Ncs}, I_c) for the waterfront area of Dock A. Dashed reference lines at q_{c1ncs} equal to 110,135, 155; and at I_c equal to 1.31, 2.05 ad 2.6.

4.3.2 Simplified profiles for nonlinear dynamic analysis.

Simplified, uniform-properties, soil profiles were determined based on the CPT characterization for the uppermost 20 m and based on SPT and Vs measurements for greater depths. Figure 4.10 depicts the idealized profiles, illustrating soil stratigraphy and soil resistance properties.

The CPT characterization revealed that the uppermost 20 m of site of the port are comprised by a heterogeneous coarse-grained natural deposit. However, at least four CPTs reported the presence of considerably looser and finer materials, probably placed during the construction of the port. For this reason, Figure 4.10b shows an idealized profile thought as representative of the sites with man-placed fills. The thickness of the fill layer was assumed to be equal to the depth between the sea-level and mudline.

The idealized layered distribution for the native deposit (Figure 4.10) was determined on the basis of the q_{c1Ncs} and I_c distributions shown in Figure 4.4 and Figure 4.5. For each layer the characteristic tip resistance was established as a conservative estimate of the mean q_{c1Ncs} distribution for the southern section of the port, represented by the thick black line in Figure 4.5. For the coarse sand layer at 20 m depth, values for the normalized SPT blow count, $(N1)_{60}$, were determined following the same reasoning.

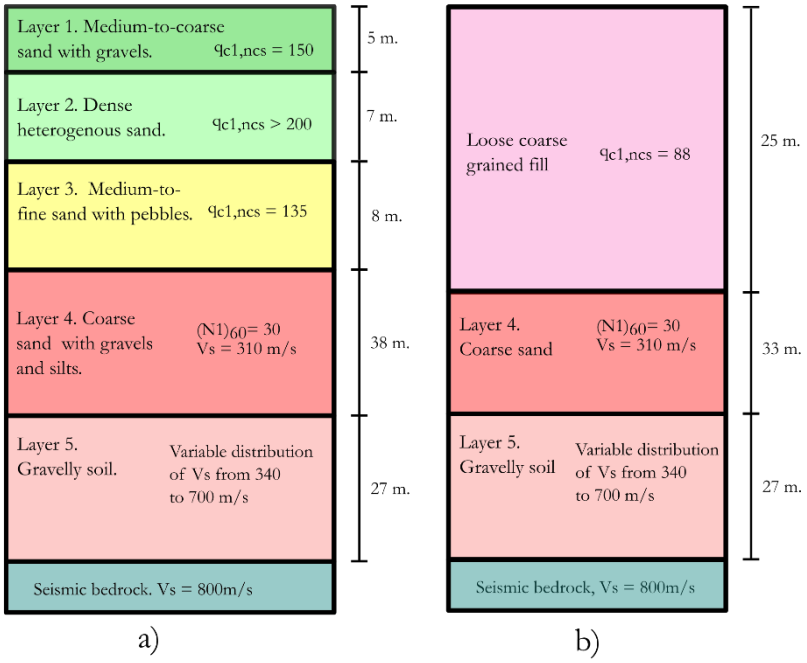

Figure 4.10. Characteristic simplified soil profiles of the southern portion of port of Gioia Tauro, native soil deposit (a) and soft fill deposit (b)

4.4 NUMERICAL MODELLING METHODOLOGY

The analysis of complex Dynamic-soil-structure interaction (DSSI) problems requires the adequate representation of the interplay between the soil behaviour and the foundation response. The choice of complex analysis methodologies over simplified approaches depends on whether large displacements or strains are expected to occur for either the soil or in the pile foundation.

For stiff ground conditions, simplified methods treating soil and superstructure responses separately may provide reasonable estimates. However, as the likelihood for developing higher strains increases, the analysis methodology should focus on reproducing compatible modes of deformation between the soil and foundation. One option is to employ one-way interaction analyses, like methods based on the Beam on Non-linear Winkler Foundation (BNWF) theory, which considers free-field ground response as input for the analysis of the pile foundation. However, these methods are unsuitable for cases in which the soil behaviour is expected to be highly non-linear and influenced by the superstructure response.

The consideration of large strains and compatible modes of deformation is crucial for accurately assessing the seismic response of Wharf BAF, a flexible structure founded on liquefiable ground. Consequently, the numerical analyses presented in this section incorporate both the superstructure and the ground within the same numerical model. It is noteworthy that this analytical approach inherently aligns with the principles of performance-based earthquake engineering assessments.

Non-linear, large-strain, time history analyses were carried out with FLAC 2D, an explicit finite difference commercial code developed by Itasca Consulting Group Inc. (2019). FLAC is specifically tailored to address coupled hydro-mechanical problems in geotechnical engineering. Special attention was giving to two different aspects of the problem. Firstly, addressing the epistemic uncertainty regarding the dynamic response of liquefiable soils involved conducting analyses with two different constitutive models: PM4Sand (Boulanger and Ziotopoulou, 2013, 2017) and SDm (Cubrinovski and Ishihara, 1998a,b). Secondly, kinematic and inertial effects were examined by studying the response of two different types of numerical models. Free-field models, representing the submerged slope without the wharf, referred to as FF models. Models considering the wharf with its full weight, labelled as SS models.

Figure 4.11 shows the schematic of the finite difference model of wharf BAF. It is representative of the cross section shown in Figure 4.2. The grid is comprised of 6250 zones, it is capable of accurately propagating frequencies up to 12 Hz. The widths of the upper most elements are, on average, about 1.5 m while the average height is approximately 1.2m. The entire model is 250 m wide, and 85 m tall. The piles comprising the wharf were modelled using the distributed plasticity model formulated by Andreotti and Lai (2017a,b). The model is tailored for DSSI problems to simulate the cyclic degradation of structural elements.

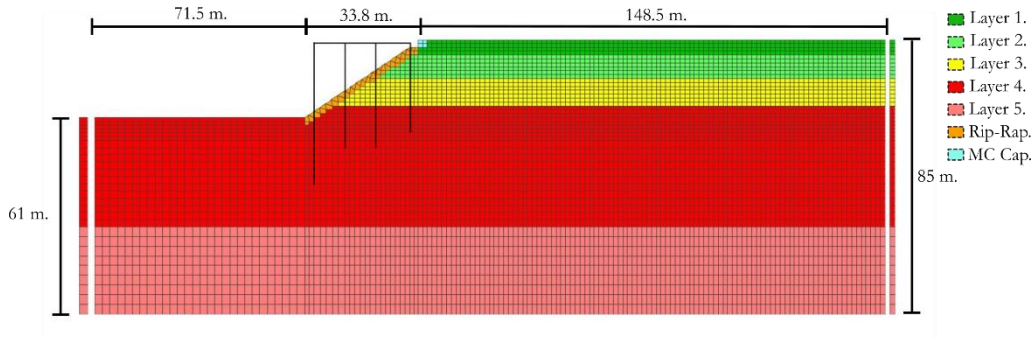

Figure 4.11. Schematic of the finite difference model of the BAF wharf implemented in Flac 2D.

The soil layers (i.e., material units) comprising the model depicted in Figure 4.11 have uniform properties. Based on the geotechnical site characterization (Section 4.3), Table 4.2 summarizes the characteristic values adopted for soil properties, along with other modelling

considerations. The values for the hydraulic conductivity were estimated based on the $_{Ic}$ distributions shown in Figure 4.5 and Figure 4.6, by means of the correlation proposed by Robertson and Cabal (2015).

Table 4.2. Soil characteristics and constitutive models used for the baseline FF and SS models of wharf BAF.

Layer	Description	q_{c1Ncs}	$N_{1,60}$	K_{hyd} (m/s)	γ_{sat} (kN/m^3)	Constitutive Model	V_s (m/s)
1	Medium to coarse sand with gravel and traces of silt	150	-	$2.50x10^{-5}$	19.33	PM4Sand or SDm	As interpreted by the constitutive model
2	Heterogeneous dense sand	>200	-	$1.00x10^{-3}$	19.03	PM4Sand or SDm	
3	Medium to fine sand with pebbles	135	-	$6.85x10^{-5}$	19.03	PM4Sand or SDm	
4	Dense coarse sand with gravels and silt	-	30	$5.28x10^{-5}$	20.5	Mohr-Coulomb with Hysteretic damping	350
5	Gravelly soil	-	45	$2.5x10^{-4}$	20.5	Elastic with Rayleigh damping	according to Bozzoni et al. (2014)
6	Rip rap	-	45	$2.50x10^{-4}$	21.48	Mohr coulomb with Rayleigh damping	400

The anchored sheet pile wall was not included in the model. The additional lateral restraint it provides could produce a reduction of the lateral displacements and, consequently. the kinematic demand on the piles. Conversely, a stiffer system does not necessarily guarantee smaller inertial demands on the piles. Certainly, considering the tie-back would add an additional layer of complexity to the problem. Nevertheless, the aim of the present study is to underscore the seismic demand on the wharf given the much general but still complex scenario posed by (1) the inertial demands transferred by the deck, (2) the driving static shear stress – due to sloping ground conditions – and (4) the nonlinear response of the liquefiable soils. The inclusion of the anchored wall would overshadow the effects of the previously mentioned conditions.

4.4.1 Modelling of liquefiable soils

As mentioned above, two separate set of analyses were performed by using PM4Sand and SDm for the liquefiable layers constituting the first 20 m of the native soil deposit. Both are advanced constitutive models tailored to reproduce key aspects of the dynamic behaviour of liquefiable soils for a wide range of densities and ground motion intensities. The models are based on the conventional theory of plasticity, and their theoretical framework is comprised by similar key modules: critical state line, elastic stress-strain relationship, plastic (hardening) modulus, flow-rule (based on loading or bounding surfaces), and dilatancy relationships. PM4Sand further incorporates fabric effects through a fabric tensor that is included within the definition of the dilatancy relationship and used for plastic and elastic moduli.

Model parameters were selected according to the CPT-based calibration procedure employed by Ntritsos and Cubrinovski (2020). The procedure considers the determination of model liquefaction resistance curves (LRCs), from single-element undrained simple-shear simulations. The LRCs define the evolution of the cyclic resistance ratio (CRR) with the number of equivalent unfirm shear stress cycles (N_{cyc}) needed to cause 5% double amplitude shear strain under dynamic-simple-shear (DSS) conditions (Ishihara, 1993). The rationale behind this approach is that the computed LRCs approximate well-accepted CPT-based empirical relationships. The empirical LRCs were computed from the liquefaction triggering relationship of Boulanger and Idriss (2014), following the procedure described by Ntritsos and Cubrinovski (2020):

1. For reference conditions, that is, earthquake magnitude M = 7.5 and vertical effective stress σ'_{vo} = 1 atm, CRR is estimated from the CPT empirical relationship defined by Boulanger and Idriss (2014).

$$CRR_{M=7.5,\,\sigma'_{vo}=1} = \exp\left(\frac{q_{c1ncs}}{113} + \left(\frac{q_{c1ncs}}{1000}\right)^2 - \left(\frac{q_{c1ncs}}{140}\right)^3 + \left(\frac{q_{c1ncs}}{137}\right)^4 - 2.8\right) \quad (4\text{-}1)$$

2. The relationship between CRR and N_{cyc} is approximated by the power law of Equation (4-2).

$$CRR_{Ncyc,\,\sigma'_{vo}=1} = CRR_{M=7.5,\,\sigma'_{vo}=1}\left(\frac{N_{M=7.5}}{N_{cyc}}\right)^b \quad (4\text{-}2)$$

3. As shown by Idriss and Boulanger (2008), the CRR-N_{cyc} relationships determined from laboratory data are consistent with the correlation between M and N_{cyc}. Thus, the Magnitude Scaling Factor (MSF) can be computed from Equation (4-3).

$$MSF = \left(\frac{N_{M=7.5}}{N_{cyc}}\right)^{b} \quad (4\text{-}3)$$

Where, $N_{M=7.5}$ is the number of equivalent uniform shear stress cycles for an earthquake magnitude of 7.5, which is estimated through Equation (4-4).

$$N_{M=7.5} = N_{min}(MSF_{max})^{\frac{1}{b}} \quad (4\text{-}4)$$

$$N_{min} = \frac{3}{4}\left(\frac{1}{0.65}\right)^{\frac{1}{b}}$$

MSF_{max} is computed from the empirical q_{1ncs} relationship of Equation (4-5) formulated by Boulanger and Idriss (2014) .

$$MSF_{max} = 1.09 + \left(\frac{q_{c1Ncs}}{180}\right)^{3} \leq 3 \quad (4\text{-}5)$$

PM4Sand employs a total of 19 input variables, divided into 3 primary and 16 secondary parameters. The primary parameters consist of: apparent relative density ($Dr_{PM4Sand}$), needed to determine the soil initial state; the (small strain) shear modulus coefficient (Go), related to shear modulus G; and the contraction rate parameter (h_{po}), which gives the user control over the rate of excess pore-water-pressure buildup and by extension over the cyclic resistance. In the absence of sufficient laboratory data, Boulanger and Ziotopoulou (2017) recommend to calibrate only the primary parameters while assigning default values to the secondary ones.

SDm makes use of 5 sets of parameters, Cubrinovski and Ishihara (1998b, 1998b) presented the original version of model calibrated to reproduce the behaviour reported by a comprehensive set of laboratory data of Touyura sand specimens. For the general use of SDm, the user should calibrate (1) the equivalent Toyoura sand void ratio ($e_{Toyoura}$), that represents the initial soil state, (2) three elastic constants (A, υ, n), (3) four parameters for the dilatancy relationship (M, μ, μ_{cyc} and Sc), (4) seven parameters for the hyperbolic stress-strain relationship and (5) the constants needed to define the critical state line (or quai steady state line). For the last three sets of parameters can be assigned to with the default values given by Cubrinovski and Ishihara (1998b, 1998b) or by Ntritsos and Cubrinovski (2020).

The simulated LRCs were constructed by performing several single-element DSS tests in FLAC2D with both models. Figure 4.12 shows the comparison between the empirical and simulated LRCs. The calibrated models reproduce the cyclic resistance for a range of values of q_{c1ncs} values between 100 and 150, accuracy diminishes for lower q_{c1ncs} values.

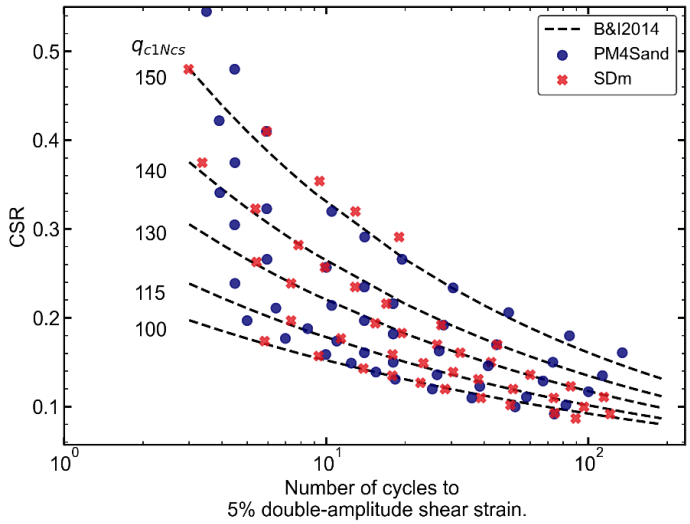

Figure 4.12. Comparison between empirical and modelled LRCs obtained from DSS simulations with PM4Sand and SDm.

Equation (4-6) and (4-7) define the calibration for the apparent relative density and the contraction rate parameter h_{po} of PM4Sand. The secondary parameter h_o was assigned with a value of 0.6. It controls the ratio between plastic and elastic moduli, and thus it influences the shear modulus reduction characteristics reproduced by the model. Its calibration is embedded within the trial-and-error process previously described.

$$Dr_{PM4Sand} = \left(\frac{q_{c1ncs}}{142.85}\right)^2 - \frac{q_{c1ncs}}{156.5} + 0.62 \tag{4-6}$$

$$hp_o = 0.15(Dr_{PM4Sand})^{-1.25} \tag{4-7}$$

For SDm, Equation (4-8) relates q_{c1ncs} and $e_{Toyoura}$. The remaining model parameters reported in Table 4.3. Note that with the model parameters of Table 4.3, for qc1ncs greater than 140 Equation (4-8) yields quite low values for eToyoura. In this case, SDm reproduces the response of very dense soil, limiting the development of shear strains at large number of cycles. For such densities, and under DSS conditions, high excess porewater pressure buildup is prevented due to the highly dilative response of the soil. This is why Figure 4.12 does not reports the cyclic resistance for more than 20 uniform loading cycles when for qc1ncs = 150. For equally high qc1ncs, and under the same loading conditions, PM4Sand (v3.0) reproduces a different response as the fabric-related effects considered by the model allow for more pronounce development of plastic shear strains.

Table 4.3

$$e_{Toyoura} = \left(\frac{q_{c1ncs}}{384.477}\right)^2 - \frac{q_{c1ncs}}{259.61} + 1.105 \quad (4\text{-}8)$$

Note that with the model parameters of Table 4.3, for q_{c1ncs} greater than 140 Equation (4-8) yields quite low values for $e_{Toyoura}$. In this case, SDm reproduces the response of very dense soil, limiting the development of shear strains at large number of cycles. For such densities, and under DSS conditions, high excess porewater pressure buildup is prevented due to the highly dilative response of the soil. This is why Figure 4.12 does not reports the cyclic resistance for more than 20 uniform loading cycles when for q_{c1ncs} = 150. For equally high q_{c1ncs}, and under the same loading conditions, PM4Sand (v3.0) reproduces a different response as the fabric-related effects considered by the model allow for more pronounce development of plastic shear strains.

Table 4.3 SDm calibration parameters for values of $e_{Toyoura}$ computed with Eq(4-8)-.

Elastic parameters			Hyperbolic stress-strain relationship	
Shear constant A	260		Peak stress ratio coefficients a_1, b_1	0.592, 0.021
Poisson's ratio υ	0.25		Max. shear strain modulus coefficients a_2, b_2	291, 55
Exponent n	0.8		Min. shear strain modulus coefficients a_3, b_3	98, 14
			Degradation constant f	4
Reference lines			Dilatancy parameters	
Minimum confinement, $p_{min,}$ kPa	3.0		Dilatancy coefficient for small strains, μ	0.22
UR-line (Void ratios and mean effective stress in kPa) (p_U, e_U)	(≤ 400, 0.895)			
QSS-line (Void ratios and mean effective stress in kPa) (p_Q, e_Q)	(10, 0.874)		Dilatancy coefficient for cyclic loading, μ_{cyc}	-0.004
	(30, 0.873)			
	(50, 0.872)			
	(100, 0.871)		Critical strain ratio, M	0.62
	(200, 0.868)			
	(400, 0.860)			

Further verifications were made to examine the model response for a more general initial stress conditions, in relation to effective confinement and sustain shear stress. These effects are customarily represented by the correction factors K_σ and K_α respectively, as expressed

by Equation (4-9). The term α refers to the ratio between the initial shear stress τ and the initial vertical effective stress σ'$_v$.

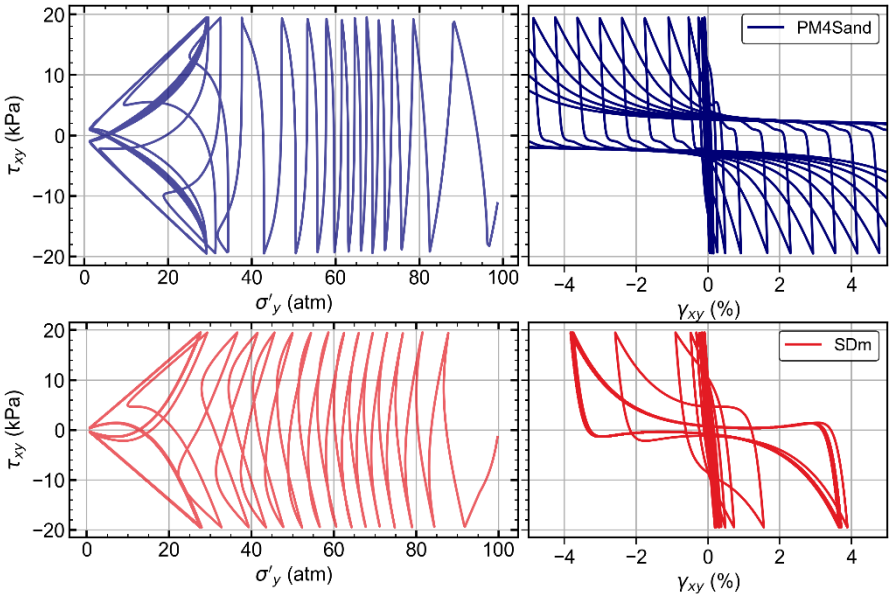

Figure 4.13. Stress path and stress-strain response of a single element DSS test performed in FLAC2D for q_{c1ncs}=135 and target CSR=0.205.

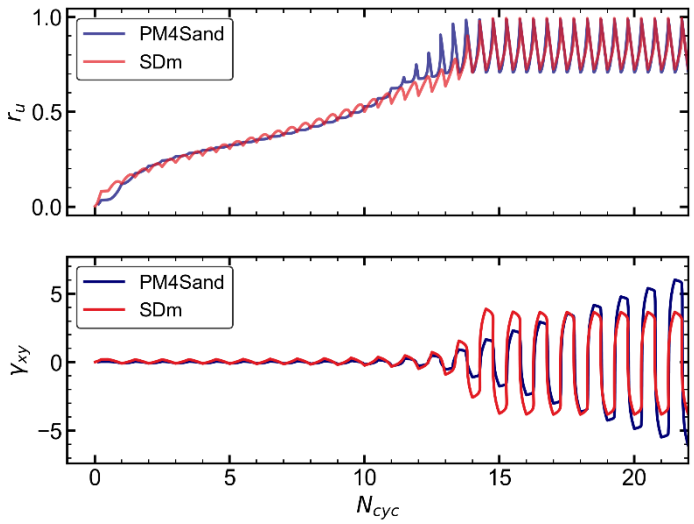

Figure 4.14. Evolution of excess porewater pressure ratio (r_u) and shear strain (γ_{xy}) for a single element test performed in FLAC2D under DSS conditions with target q_{c1ncs}=135 and CSR=0.205.

$$\mathrm{CRR}_{\sigma,\alpha} = \mathrm{CRR}_{\sigma=1,\alpha=0}\,\mathrm{K}_{\sigma}\mathrm{K}_{\alpha}$$

$$\mathrm{K}_{\sigma} = \frac{\mathrm{CRR}_{\sigma}}{\mathrm{CRR}_{\sigma=1\ \mathrm{atm}}} \qquad (4\text{-}9)$$

$$\mathrm{K}_{\alpha} = \frac{\mathrm{CRR}_{\alpha}}{\mathrm{CRR}_{\alpha=0}}$$

Figure 4.15 shows the results of DSS simulations performed with the models, compared against the K_σ relationship defined by Boulanger and Idriss (2014). At low confinement, σ'_v<0.5 atm, the simulated responses overestimate the cyclic resistance provided by the empirical relationships. While for higher initial vertical stresses the simulated and empirical cyclic resistances are in good agreement.

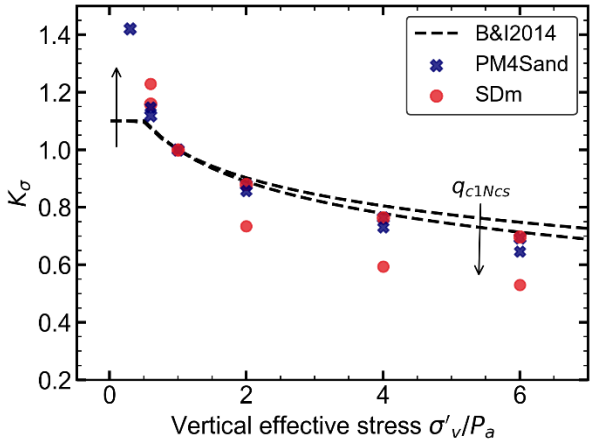

Figure 4.15. Comparison between the simulated K_σ relationship for PM4Sand and SDm against the empirical formulae defined by Boulanger and Idriss (2014) .

As in the case of K_σ, Figure 4.16 compares the simulated K_α against the relationship of Idriss and Boulanger (2008). With increasing τ_{st}, PM4Sand response is not dilative enough to produce large cyclic resistances as implied by the empirical relation.

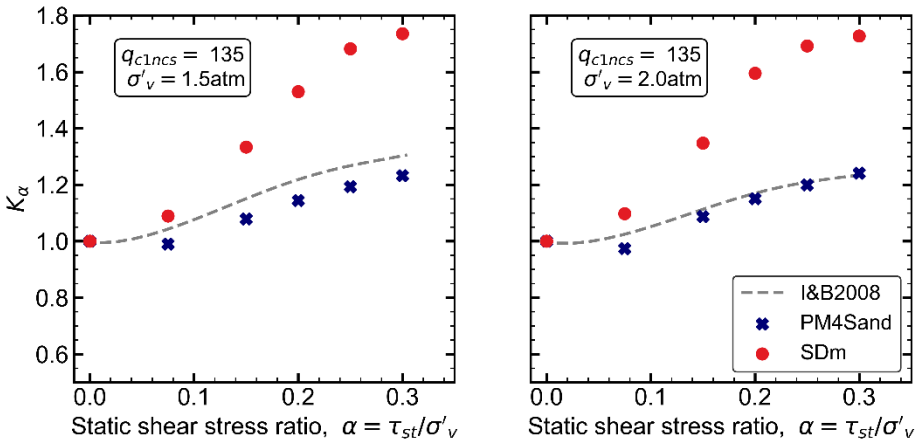

Figure 4.16. Comparison for K_α between the simulated DSS response with PM4Sand and the empirical relationship defined by Idriss and Boulanger (2008).

4.4.2 Modelling of non-liquefiable soils

The baseline, finite difference numerical model displayed in Figure 4.11, contains the upper 85 meters of the native soil. PM4Sand and SDm are used to model the first 20 m of liquefiable coarse-grained materials, the underlaying coarse-sand layer (see of Figure 4.10) is model with an elastic-perfectly-plastic Mohr-Coulomb (M-C) model with hysteretic damping as reported by Table 4.2. The model response was calibrated and verified for the

target modulus degradation, backbone and damping ratio curves derived from the relationships proposed Zhang et al. (2005). Deeper and stiffer layers (e.g., the rip rap) were also model with a M-C model coupled with Rayleigh damping.

Due to its high (normalized) tip resistance (q_{c1ncs}>200), the dense heterogeneous sand found between 5- to 12-meters depth is expected to act as non-liquefiable layer, developing negligible to limited excess pore-water-pressures depending on the seismic demand. It is therefore needed to verify the modulus degradation characteristics reproduced by PM4Sand and SDm for this layer. To that end, the relationships defined by Zhang et al. (2005) for non-plastic quaternary coarse-grained materials were used as reference.

Figure 4.17 shows the comparison between the simulated and reference modulus degradation and damping ratio curves for a confining pressure of 1 atm, corresponding to a depth of about 8 meters. The simulated curves were computed from the results of single-element drained cyclic direct-simple-shear tests. The modulus degradation curve computed with PM4Sand appears to be in closer agreement with the reference curve, while that computed with SDm seems to be overestimating the shear modulus degradation. However, despite its high resistance, the dense sand layer is also expected to undergo moderate to large deformations, in which case, capturing the target shear strength becomes of primary importance (Yee et al., 2013). Figure 4.18 shows the backbone curves derived form the cyclic simple-shear simulations compared against the Zhang et al. (2005) relationship using a shear wave velocity of 287 m/s ($G_{max} \approx 133$MPa). The parameters of the reference curve were adjusted according to the recommendations of Yee et al. (2013), so that it asymptotically approaches the soil resistance after $\gamma_{cyc} \geq 0.5$, while preserving its original small strain features. As observed, results from PM4Sand and SDm are in good agreement with the reference backbone curve, yet PM4Sand yields a larger, still acceptable, strength at $\gamma = 3\%$.

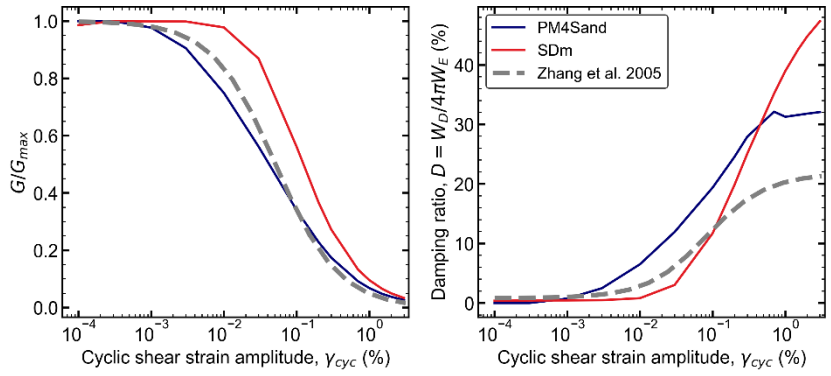

Figure 4.17. Simulated and empirical shear modulus reduction and damping ratio curves for the dense sand layer found between 5 to 12 m depth. The curves were derived for a confining pressure of 1 atm.

Similarly, the single-element response of the coarse-sand layer was calibrated for the target strength-adjusted curves of Zhang et al. (2005). This layer was assigned to with a M-C model. Modulus degradation and damping ratio characteristics were introduced via the build in "*sigmoidal model 3*" of FLAC, which effectively models the shear stress-strain behaviour according to a hyperbolic model. For each element of the layer, the hysteretic model parameters were calibrated to intersect the (1D) free-field M-C resistance at γ = 0.5%. Figure 4.19 exemplifies the rationale behind the modelling approach, used to preserve most of the small strain characteristics of the hysteretic model, while reproducing the adequate shear strength of the non-liquefiable layer.

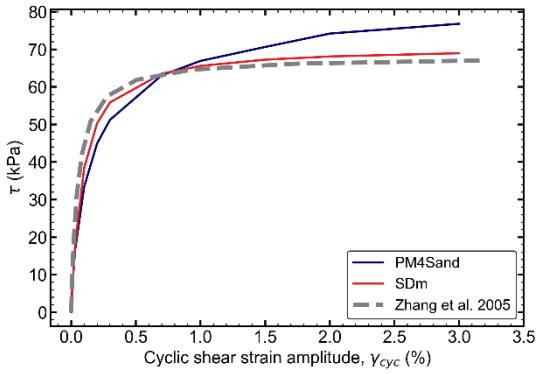

Figure 4.18. Comparison between the simulated and refenced backbone curves computed from the modulus degradation curves shown in Figure 4.17.

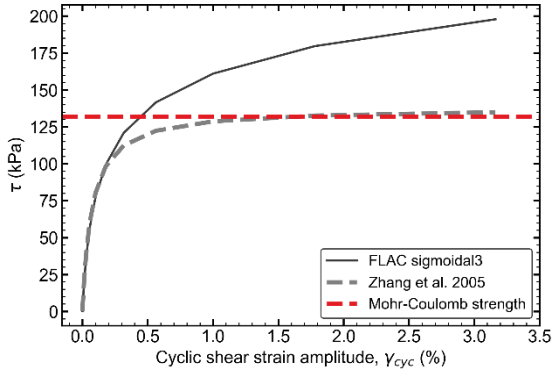

Figure 4.19. Schematic representation of the calibration of the backbone curves for the dense sand layer found below 20 m depth. The plotted curves were estimated for a confining pressure of 2.1 atm.

4.4.3 Structural modelling.

The nonlinear behaviour of the piles was modelled with the distributed plasticity model formulated by Andreotti and Lai (2017a, 2017b). This model was developed to overcome the usual limitation of geotechnical engineering software in simulating the non-linear response of structural elements. Despite its relatively simplicity, the model effectively reproduces key aspects of the dynamic behaviour of reinforced concrete sections, namely, inelastic behaviour after yielding and cyclic degradation of stiffness, rendering it compatible with PBEE principles.

The input parameters for the distributed plasticity model for the piles supporting wharf BAF are reported in Table 4.4, they correspond to nominal reinforced concrete properties. The left panel of Figure 4.20 shows the respective moment – axial load (M-N) interaction diagram, while the right panel schematically illustrates the representative cross section of the piles. Figure 4.21 reports the typical moment-curvature response reproduced by the model after monotonic and cyclic simulations performed on a cantilever column 6.5 m tall. The column was laterally loaded under displacement-controlled conditions, without axial loading. The elements at the base were assigned with the non-linear model while the remainder of the column was assumed elastic.

The moment-curvature plot shown in Figure 4.21 clearly exemplifies how the model captures key features such as: degradation of flexural stiffness after concrete cracking, during unloading and reloading cycles; isotropic hardening following yielding; and post failure behaviour. The yield moment (M_y) and yield curvature (χ_y), for the case of zero axial load, are 4.4 MN and 2.86 rad/Km respectively.

After failure is detected, the model assigns a flexural post-failure strength of about 20 to 50% of the nominal capacity depending on the type failure (i.e., ductile or brittle) (Andreotti and Lai, 2017a, 2017b). However, besides adding one more source of uncertainty, this feature poses critical limitations in terms of computational time as the simulation time-step reduces dramatically, further details can be found in appendix A.1. Therefore, this the post-failure feature was not activated during the 2D analysis of the wharf BAF.

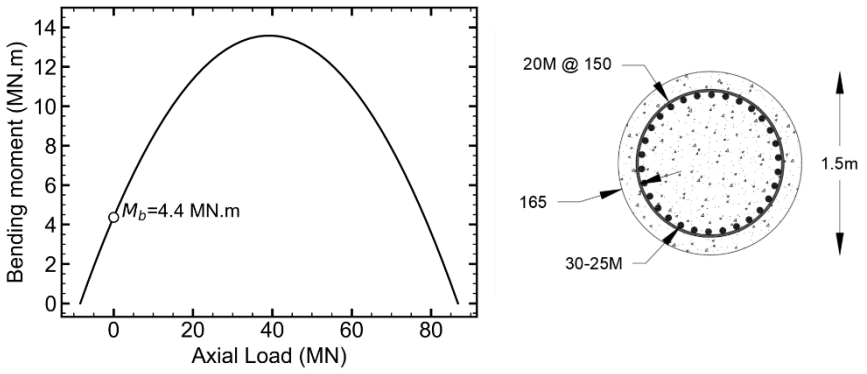

Figure 4.20. Left, nominal bending moment and axial load interaction diagram for the piles of wharf BAF. Right, schematic of the target cross section for the reinforced concrete piles.

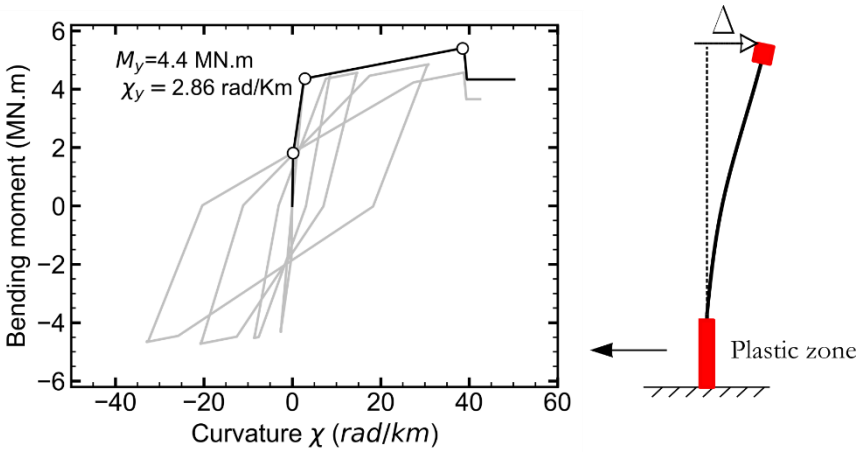

Figure 4.21. Response of a 6.5m cantilever column modelled using the distributed plasticity model of Andreotti and Lai (2017a, b). The plastic zone was modelled with two beam elements 0.75 m long with the properties defined in Figure 4.20Figure 4.6 and Table 4.4.

Table 4.4. Nominal material properties for the reinforced concrete piles of wharf BAF used by the distributed plasticity model of Andreotti and Lai (2017a, b).

Concrete compressive strength, f'_c	45 MPa
Concrete tensile strength, f_{tc}	3.1 MPa
Yield strength of longitudinal reinforcement, $f_{y,l}$	414 MPa
Yield strength of transverse reinforcement, $f_{y,s}$	429 MPa
Concrete Young's modulus, E_c	33.5 GPa
Steel Young's modulus, E_s	200 GPa

4.4.4 Input ground motions.

The numerical analyses in this study aim to reproduce critical scenarios that yield conservative estimates while still representative of the seismic hazard and seismo-tectonic setting of the area. The analyses will provide a robust baseline for the assessment of soil-liquefaction, lateral spreading and DSSI effects on wharf BAF. To that end, a hazard-consistent accelerogram, recorded on stiff ground conditions, was applied, after deconvolution, to the base of models FF and SS. The outcrop ground motion was linearly scaled to three different PGA levels compatible with the median values for return periods (T_R) of 201, 475 and 975 years, as defined by the Seismic Hazard Map of Italy (Stucchi et al., 2011). Table 4.5 presents data from the seismic disaggregation of the seismic hazard at the port of Gioia Tauro in terms of median peak ground acceleration for reference conditions Ag (i.e., outcropping rock site with flat surface), mean magnitude and mean source-to-site distance (Barani et al., 2009).

For the hazard levels reported in Table 4.5, the seismic hazard in the Gioia Tauro region is controlled by shallow crustal earthquakes with magnitudes ranging from 4.5 and 7.5, and source-to-site distances below 30 Km, indicated the prevalence of near-source events.

Table 4.5. Data from the disaggregation of the seismic hazard at the site of the port of Gioia Tauro, as reported by Barani et al. (2009)

TR	Median peak ground acceleration Ag (g)	Mean magnitude $\bar{M}$	Mean source to site distance $\bar{R}$ (km)
975	0.353	6.15	7.15
475	0.261	5.97	8.41
201	0.178	5.77	10.6

The ground motion, selected as input for the analyses, was recorded at station MZ50 during the Mw 6.6 mainshock of the Central Italy sequence on October the 10th 2016. Figure 4.22 displays the recorded acceleration time history. Station MZ50 is located on stiff ground conditions, classified as site Class B according to Eurocode 8. The distance between the station and the epicentre was 27.8 km approximately. The unscaled record has a PGA of 2.55 m/s² (0.26g), matching the Ag value for a return period of 475 years in Table 4.5. The record was scaled to PGA values of 1.7 m/s² and 3.5 m/s², corresponding to the values of Ag for T_R=201 and 975 respectively. Figure 4.23 shows the respective acceleration response spectra (with 5% of critical damping), compared against the uniform hazard spectra (UHSs) considered by the Seismic Hazard Map of Italy (Stucchi et al., 2011). The UHSs correspond to reference site conditions (i.e., outcropping rock, and flat surface conditions). Figure 4.23 also includes the UHS for T_R=2475. Comparatively, the inputs exhibit stronger spectral ordinates in the intermediate to long period range compared to the hazard data. Nonetheless, it is noteworthy that exceeding the UHS spectral ordinates is a known characteristic in near-source conditions due to the nature of probabilistic seismic hazard assessment (Iervolino et al., 2017).

It is worth recalling that the finite difference models represent an idealization of the subsoil stratigraphy found on top the seismic bedrock. Therefore, the input motions represent outcropping-rock motions applied at the base of the model as horizontal tractions via well-known viscous boundaries.

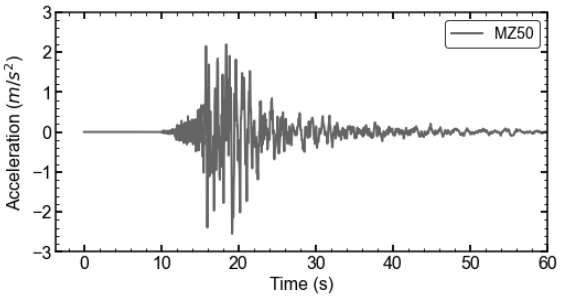

Figure 4.22. EW component of the Oct-10-2016 M6.6 Central Italy mainshock recorded at station MZ50.

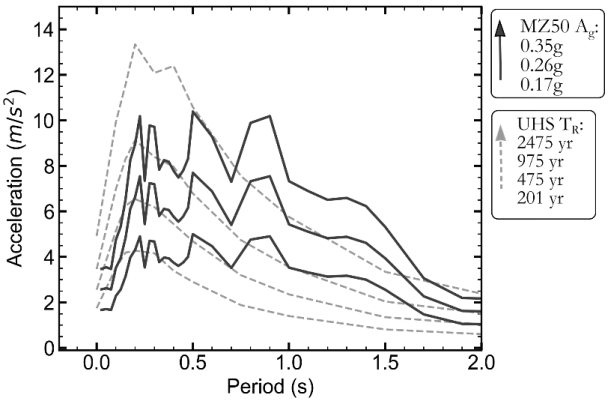

Figure 4.23. Comparison in terms of 5% acceleration response spectra between the input ground motion (EW component of the Oct-10-2016 M6.6 Central Italy mainshock recorded at station MZ50), scaled for PGAs of 1.8, 2.6 and 3.5 m/s², and the uniform hazard spectra for TR=475,975 and 2475 yr.

4.5 1D GROUND RESPONSE

The seismic response of the native soil deposit (depicted in Figure 4.10a) was examined through a series of 1D effective stress analyses using the numerical modelling framework outline the previous sections. These analyses aim to (1) characterize the evolution of cyclic shear strains and ground deformations with ground motion intensity and (2) identify hydraulic and dynamic interactions among the different layers (i.e., system effects). It is important to note that cyclic shear strains are those that develop solely due to the horizontal earthquake excitation, excluding higher-order effects such as those produced by sustained (static) shear stresses, pore-pressure diffusion, non-planar incident waves, etc. These analyses serve as a baseline for systematic interpretation of the subsequent 2D analyses. Likewise, and additional key objective is to identify the key differences and similarities between PM4Sand and SDm.

For each input intensity level (A_g=0.17g, 0.26g and 0.35g), Figure 4.24 to Figure 4.26 show profiles of maximum shear strain (γ_{max}), excess pore water pressure (EPWP), and lateral displacement index (LDI) computed as the integral of γ_{max} down to a depth of 30m, expressed by Eq(4-10). This latter parameter relates to the most severe phases of the response that occur at different time instants, it serves as a conservative metric for surface manifestation of liquefaction, not to be confused with an estimation of lateral ground displacements.

$$\mathrm{LDI_{ESA}} = \int_0^{30} \gamma_{\mathrm{xy,1D}} \mathrm{dy} \tag{4-10}$$

Two aspects controlling the surface manifestation are worth examining, one relates to the peak values of γ_{max}, and the other to the thickness of the layer that underwent large strains (i.e., γ_{max} >2%). For the former, differences are noticeable between the results produced by PM4Sand and SDM. They reflect the trend observed in the element test simulations performed during the calibration phase (see Figure 4.13). Maximum shear strains reproduced by PM4Sand progressively increased with input intensity from 2% to 6%. SDm produced larger shear strains for the lowest intensity, around 4.5%, equivalent to the response obtained between 12 and 15 cycles in the case of element test simulations of Figure 4.13. However, the rate of evolution of γ_{max} produced by SDm was lower than that of PM4Sand, for the highest intensity, both models reproduced similar peak values of γ_{max}.

The profiles of EPWP pertain to two instants of time: one after 50 seconds of shaking (shown in dashed lines), and the other between 1 and 2 seconds after liquefaction triggering (shown in solid lines). At the latter instant, the models predicted similar distributions for EPWP, while reproducing different dissipation patterns at 50 seconds. In the case of SDm, seepage effects seem to be limited to the upper medium sand layer, which developed γ_{max} up to 2% due upward water flow. This feature was note noted in the analyses that used PM4Sand.

Regarding the thickness of liquefied soils, large strains produced by SDm consistently spread along a thicker zone. This zone enlarged with input intensity until int covered the entirety of the medium sand layer. PM4Sand led to less a severe response, although the thickness of the liquefied soil also enlarged with input intensity. This difference could stem from various factors or a combination of thereof. These include the fact that the models reproduce different modulus reduction and dilation characteristics that determine the seismic energy being transferred into the liquefiable layer. Additionally, they follow different implementation schemes within FLAC.

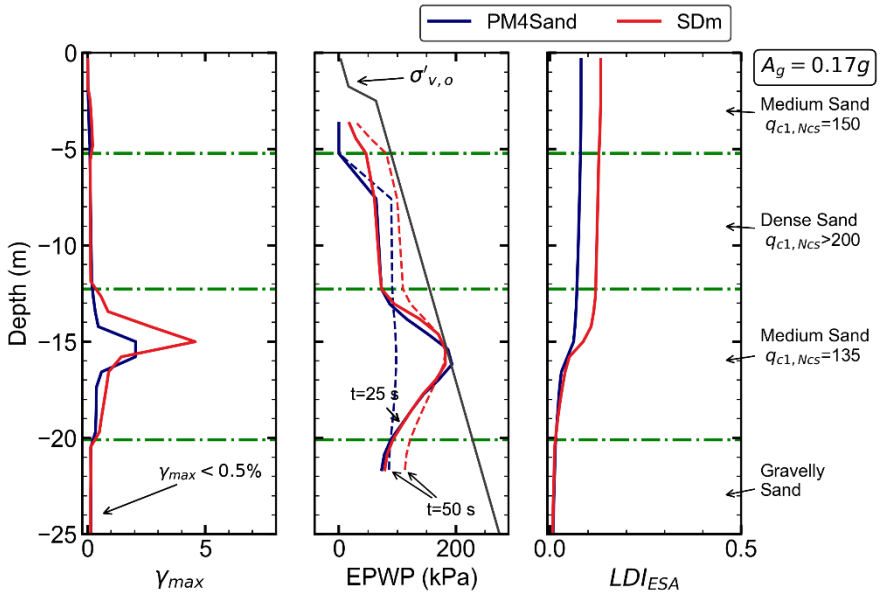

Figure 4.24. Results of 1D effective-stress analysis of the native deposit performed with PM4Sand and SDm with input Ag of 0.17g.

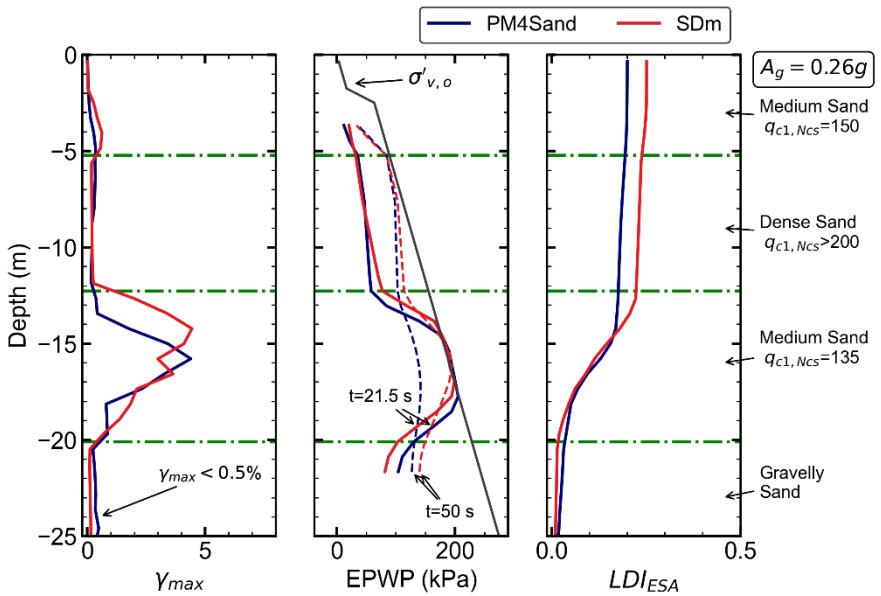

Figure 4.25. Results of 1D effective-stress analysis of the native deposit performed with PM4Sand and SDm with input Ag of 0.26g.

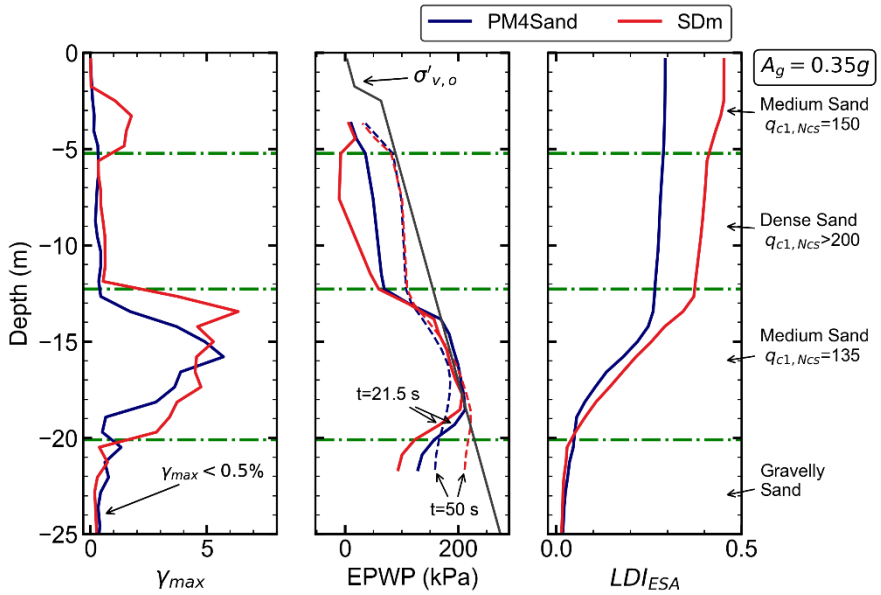

Figure 4.26. Results of 1D effective-stress analysis of the native deposit performed with PM4Sand and SDm with input Ag of 0.35g.

4.6 2D SYSTEM RESPONSE: FREE-FIELD ANALYSES

This section presents the results from the 2D analyses conducted with the FF and SS models, for input motion intensities (A_g) of 0.17g, 0.26g and 0.36g. For each model and intensity level, two numerical simulations were conducted, changing the constitutive model assigned to soil elements of the upper 20 m of the deposit between PM4Sand and SDm. Thus, a total of 12 analyses were carried out: three input intensities × two finite difference models × two constitutive models for the upper 20 m. The ensuing discussion will address the evolution of the seismic response of the 2D models, focussing on the discrepancies and similarities observed between PM4Sand and SDm. Recall that both models have been calibrated to the same target liquefaction resistance for q_{c1Ncs} = 135.

For the free-field ground (FF) models, Figure 4.27 displays contours of final horizontal displacements after 55 seconds of shaking for the simulations that utilized PM4Sand and SDm. The displacements are computed relative to the base of the models. The patterns illustrate the evolution of two modes of earthquake-induced ground deformation: toe failure and lateral spreading.

As expected, the simulations with PM4Sand and SDm revealed that both the magnitude and spatial extent of the lateral spreading displacements increased with the input intensity. However, PM4Sand resulted in significantly larger residual displacements. For the highest

earthquake intensity, the crest of the slope displaced 0.87 m seawards and ground encroachment (i.e., displacements larger than 0.3 m) propagated 100 m away from the crest. In contrast, with SDm, the crest moved laterally 0.61 m and ground encroachment extended 60 m inland.

To further illustrate the extension and evolution of the free filed ground deformation, Figure 4.28 shows contour of maximum shear strain ($\gamma_{xy,max}$), while Figure 4.29 outlines the different zones that liquefied during the analyses. Elements coloured in yellow indicate liquefaction, defined as $\gamma_{xy,max} > 3\%$ and $r_{u,max} > 0.95$. Elements in blue and cyan denote areas with significant EPWPs ($0.75 \leq r_{u,max} \leq 0.95$) due to water pressure diffusion, with limited shear strains for the former ($\gamma_{xy,max} \leq 2\%$) while slightly larger for the latter ($\gamma_{xy,max} > 2\%$). Differences between the two constitutive models are apparent; however, both predicted the triggering of liquefaction (i.e., $\gamma_{xy,max} > 3\%$) within the medium sand layer (between elevations of 73 and 65 meters), as well as the progression the liquefiable zone towards the face of the slope with stronger ground shaking. PM4Sand showed larger shear strains accumulated inside and behind the slope, while the thickness of the liquefiable zone slightly increased. In contrast, SDm predicted smaller shear strains, but the thickness liquefiable zone grew considerably more than with PM4Sand.

Toe failure was characterized by the generation of large strains within the non-liquefiable dense sand, hereafter referred to as base layer. This base layer was modelled with Mohr-Coulomb in conjunction with FLAC's built-in hysteretic damping model. Therefore, it is unable to reproduce any degree of coupling between volumetric and shear responses. However, shear strain concentrations within the base layer diverge between PM4Sand and SDm analyses. This was partly ought to the hydromechanical nature of the analyses. Pore pressure changes propagated outside the liquefiable soil into its neighbouring layers. For soil exhibiting a contractive tendency, the base elements would experience an excess pore water pressure increase, not as dramatic, but still large enough to alter the soils response. FLAC inherently considers shear strength in effective stress, and therefore total stress modelling of the base layer could not be done unless a fixed value of shear resistance were to be assume.

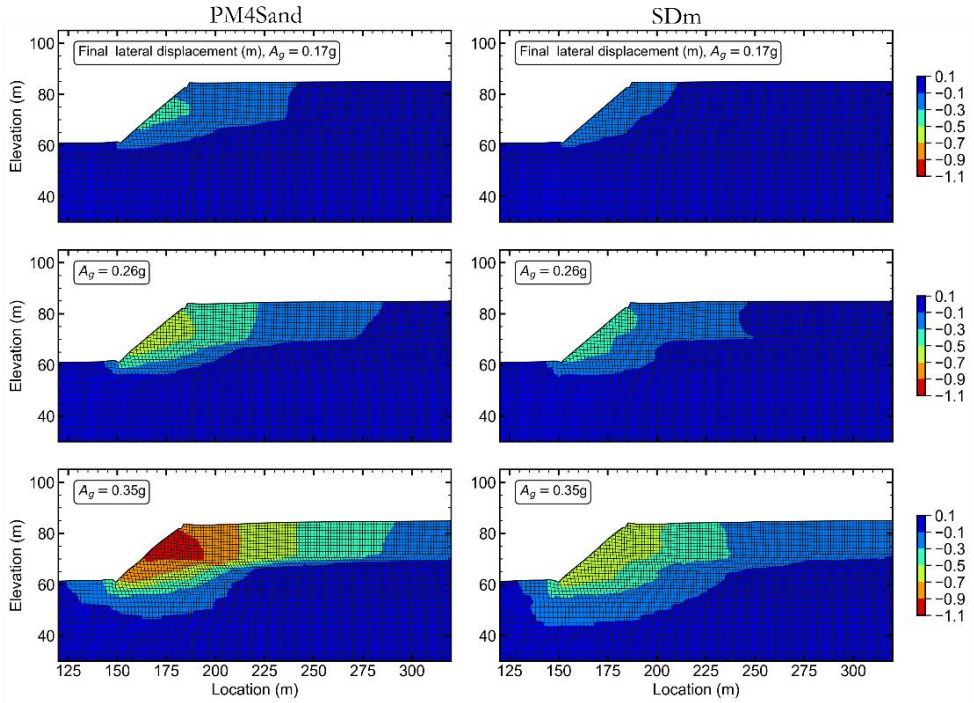

Figure 4.27. Results in terms of contours of lateral displacements after 55 seconds for the FF model. Deformed Mesh is shown with an exaggeration factor of 5. Panels on the left show results for the analyses that used PM4Sand for the first 20m, while those on the right are for SDm.

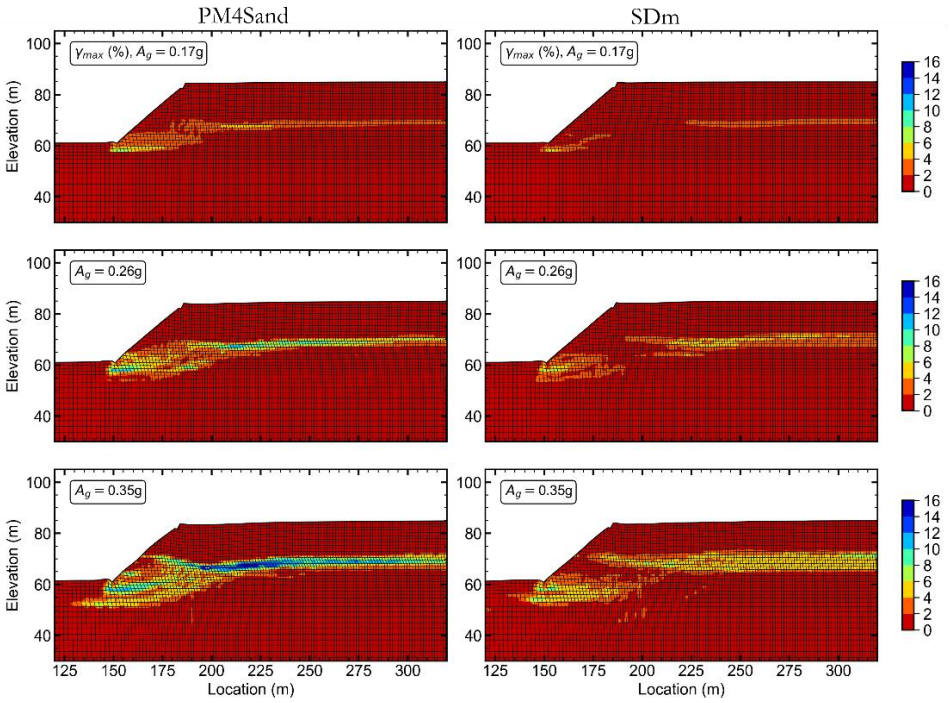

Figure 4.28. Contours of maximum shear strains obtained after 55 seconds of shaking for the FF analyses. Deformed Mesh is shown with an exaggeration factor of 5. Panels on the left show results for the analyses that used PM4Sand for the first 20m, while those on the right are for SDm.

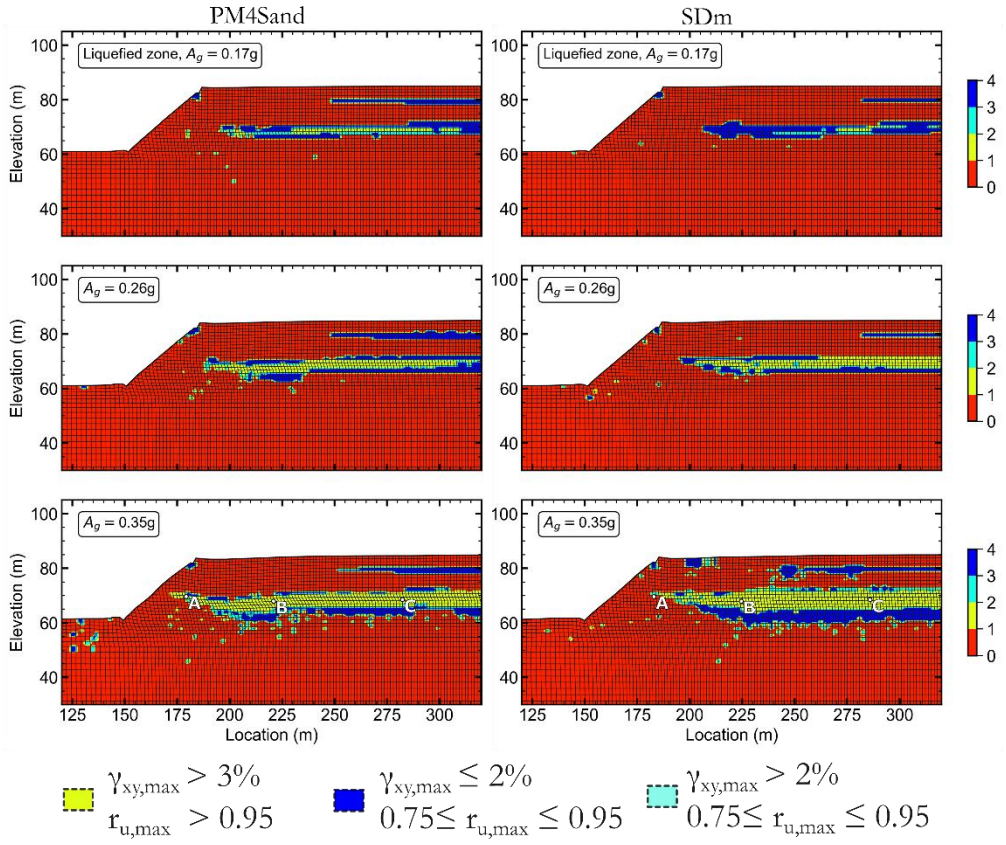

Figure 4.29. Zones of soil liquefaction predicted by the 2D effective stress analyses with PM4Sand (left contours) and SDm (right contours). Deformed Mesh is shown with an exaggeration factor of 5.

To underscore the soil features of the soil behaviour responsible for the lateral spreading deformations, the discussion will focus on examining the response recorded at points A to D depicted in Figure 4.29, for the analysis carried out with A_g of 0.35g only. Point D is within the 1D free-field column at the same elevation (depth) of point C. It is worth starting by stressing the different loading conditions expected at each location. Firstly, sustained static shear stresses increase as one moves from point C to point A. In this case, for q_{c1ncs}=135, K_α effects would limit the excess-pore-water-pressure buildup. Secondly, inside the slope (below Point A), large strains occurred within the base layer, causing the slope to move at its toe. This compliant behaviour is opposite to the stiffer response of the base layer far away from the waterfront, which translates into different loads being transferred to the liquefiable soil.

For the case of PM4Sand, Figure 4.30 shows the stress-strain response and stress paths recorded at each point. Soil liquefaction triggered at all four locations, with the response at point C, which is 120 m away from the waterfront, similar to that of the 1D soil column of point D. It is important to note that within the 1D free-field column, soil experiences cyclic shearing solely due to seismic excitation. Additional shearing caused seepage effects (i.e., loss of strength due to water pressure diffusion) was negligible in the present case. Inside the main grid, as opposed to the 1D column, the lateral variation of the effective confinement, and complex load-transfer among the different soil layers, produced a sufficiently large lateral disturbance that exceeded the soil resistance during and after liquefaction was triggered. For instance, at point B post-liquefaction shear strains were the largest, reaching 18%. Point A exhibited a less contractive behaviour, due to K_α effects, yet it exhibited large post-liquefaction shear strains, reaching a maximum of 7%.

Indeed, the post-liquefaction development of shear strains is perhaps the most notable characteristic of the response reproduced by PM4Sand. This aspect, coupled with the Lagrangian formulation of FLAC resulted in second-order deformations. A clear example of this condition was the soil response recorded point B, where the deformation of the liquefiable layer was significant enough to induce the sliding of the overlaying dense sand, which effectively behaved as a non-liquefiable crust. As it slid, it imposed an additional sustained shear load on the liquefiable layer, causing further strains. Conversely, inside the slope, larger strains were limited, on one hand due to K_α effects, and on the other, due to a more complaint base layer.

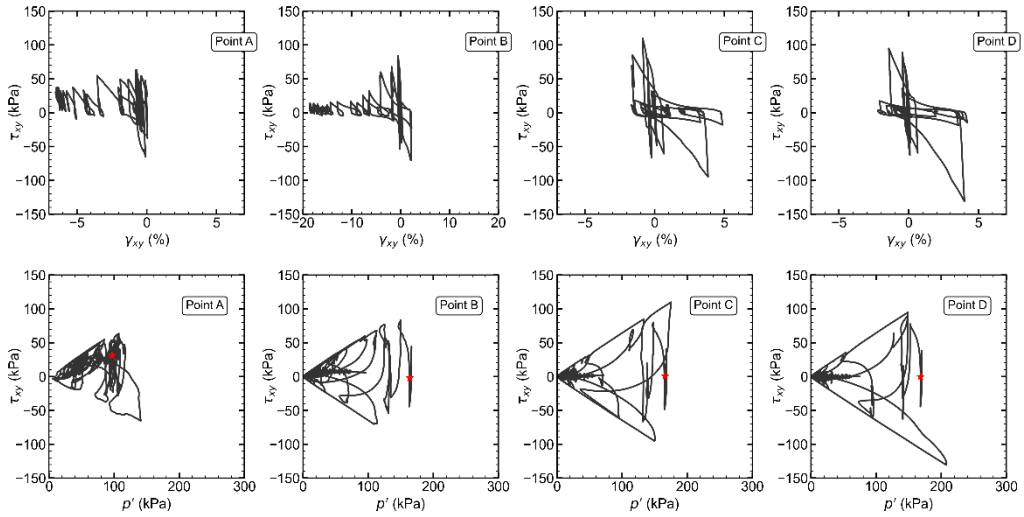

Figure 4.30. Results of PM4Sand analysis with Ag=0.35g in terms of stress-strain diagrams and stress paths recorded at points A to D inside the liquefiable layer. Point D, not shown in Figure 4.29, is inside the right-side 1D column, at the same elevation of Point C. For the stress paths, the red star indicates the initial stress state.

Regarding SDm, Figure 4.31 shows the stress-strain diagrams and stress paths as Figure 4.30 does for PM4Sand. For Point A, inside the slope, the predicted response was more dilative in relation to K_α effects, with shear strains reaching maximum values of around 5%, slightly smaller than those predicted by PM4Sand. Cyclic strains at points C and D were within the same order of magnitude for both models. However, significant differences were seen at Point B, within the lateral spreading ground, where SDm resulted in significantly smaller strains. Note that, despite predicting smaller strains SDm created a relatively larger thickness of the liquefiable soils. Around point B the soil column that liquefied grew from 3.65 m to 8.40 m for the two highest input intensities, whereas for PM4Sand it did from 3.6 m to 6 m.

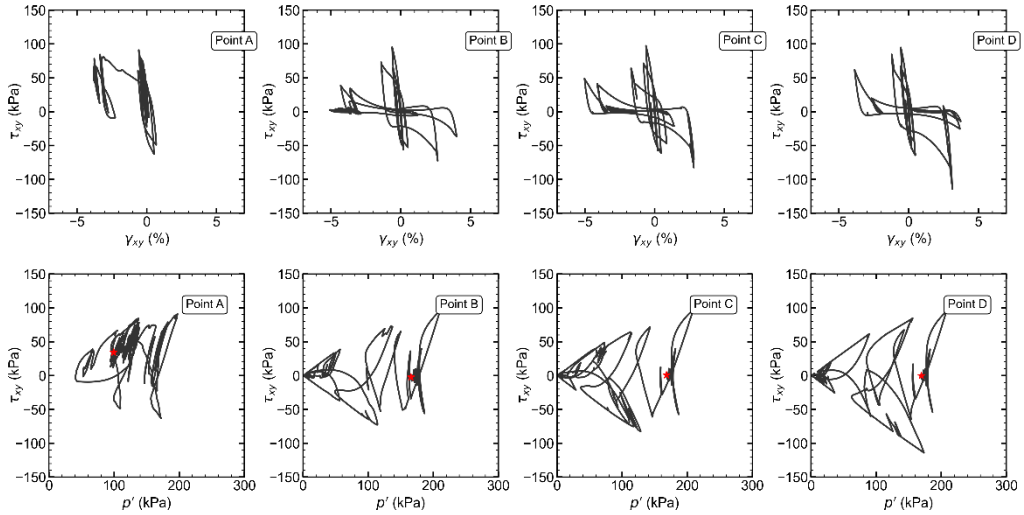

Figure 4.31. Results of SDm analysis with Ag=0.35g in terms of stress-strain diagrams and stress paths recorded at points A to D inside the liquefiable layer. Point D, not shown in Figure 4.29, is inside the right-side 1D column, at the same elevation of Point C.

To further underscore the different soil responses produced by PM4Sand and SDm, Figure 4.32 compares time histories of γ_{xy} and r_u recorded at points B and D. For the latter, the two models predicted similar traces of cyclic shear strains. The onset of liquefaction occurred at 19 and 21 seconds for PM4Sand and SDm respectively. In fact, shear strains at point B were remarkably similar for the first 22 seconds of shaking. Afterwards, PM4Sand produced a pronounce evolution of post-liquefaction shear strain that reached a residual value of 18%, whereas SDm predicted shear strains of the same order of magnitude as the (1D) cyclic strains. These differences manifested in the overall system response, with the residual displacement at the crest (Δ_{crest}), predicted by PM4Sand being approximately 0.8 m, compared to 0.55 m for SDm. Notably, during the first 21 seconds, both models produced similar horizontal displacements at the crest, as observed in the plots of Figure

4.33. The predicted crest displacements began to deviate 1 or 2 seconds after liquefaction triggering, consistent with the recorded shear strains.

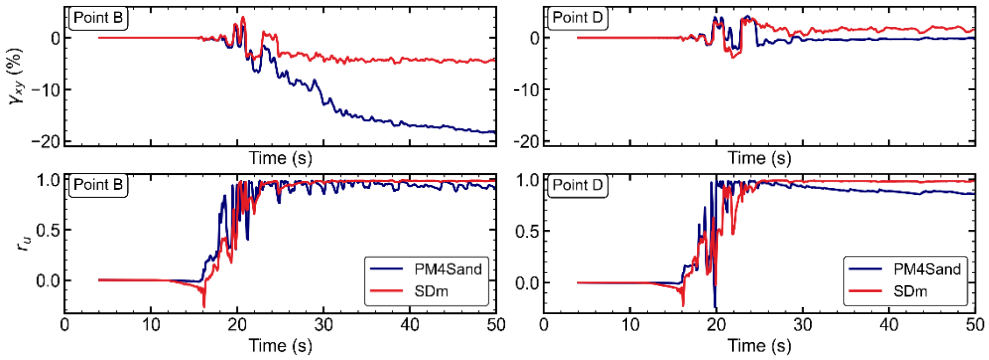

Figure 4.32. Time histories of shear strain and excess pore pressure ratio recorded at points B (behind the slope) and D (1D-column) during the FF simulations for Ag=0.35g.

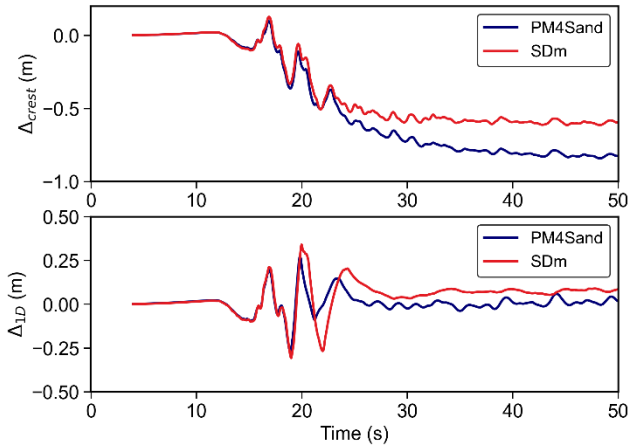

Figure 4.33. Time histories of horizontal displacement at the crest (Δ_{crest}) of the slope and at the 1D column Δ_{1D}, recorded during the FF simulations.

4.7 2D SYSTEM RESPONSE: SOIL-STRUCTURE ANALYSES

Similar to the preceding section, this section presents a systematic comparison of the outcomes generated by the simulations that employed PM4Sand and SDm for the liquefiable soils within the upper 20 meters of the native soil deposit. Figure 4.27 and Figure 4.28 display contours for final lateral displacement and $\gamma_{xy,max}$ respectively. A preliminary comparison between these set of results with those shown in Figure 4.27 and Figure 4.28 reveals that the large-diameter pile-supported wharf fully restrained the sliding at the toe and significantly reduced the lateral spreading movement.

Despite of the restraining action provided by the wharf; lateral spreading ground deformations exhibited several of the key features studied in the preceding section when using both PM4Sand and Sdm. The inclusion of the wharf led to a reduction in the accumulated post-liquefaction shear strains produced by PM4Sand. Similar to the FF case, large shear strains concentrated behind the slope (wharf). For the largest input intensity, residual shear strains reached 12 %, down from nearly 20% for the FF model. For Ag equal to 0.35g, ground encroachment extended 60 meters inland from the crest of the slope, representing a reduction of 40 meters compared to the FF model. Interestingly, for the Ag equal to 0.26g, both FF and SS analysis with PM4Sand reported lateral displacements larger than 0.3m up to a distance of 40 m to 50 m from the crest.

In the case of SDm, the wharf structure reduced the lateral displacements, measured at the crest of the slope, from nearly 0.38 m (for FF analysis) to 0.14 m for Ag=0.26g. Likewise, for Ag=0.35g, the crest displaced 0.27 m with the wharf, compared to 0.53 m for the FF case. Residual lateral displacements larger than 0.3 m, at the surface, were obtained within the first 30 m measured horizontally from the crest of the slope, half of the distance obtained from the FF case. Shear strains were also reduced within the slope and in the zone behind the wharf. The thickness of the liquefiable zone was seemingly unaffected by the presence of the wharf for both input intensities.

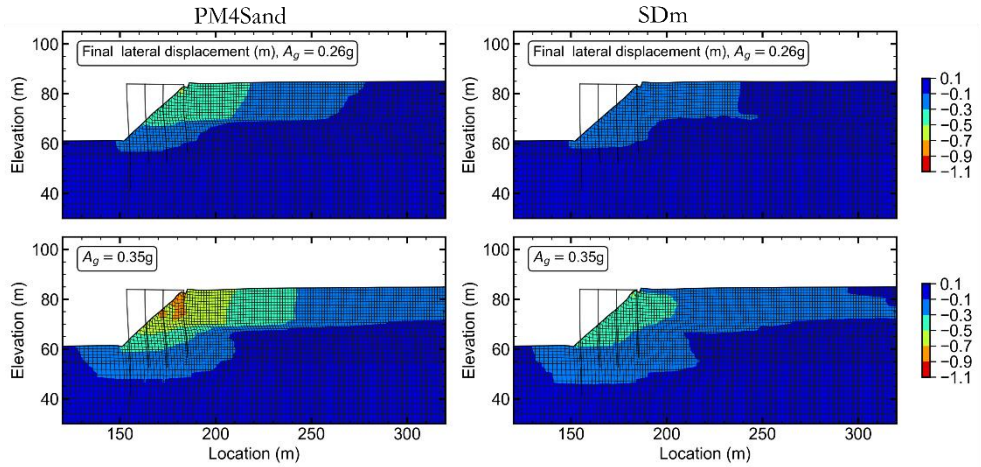

Figure 4.34. Results in terms of contours of lateral displacements after 55 seconds for the SS model. Deformed Mesh is shown with an exaggeration factor of 5. Panels on the left show results for the analyses that used PM4Sand for the first 20m, while those on the right are for SDm.

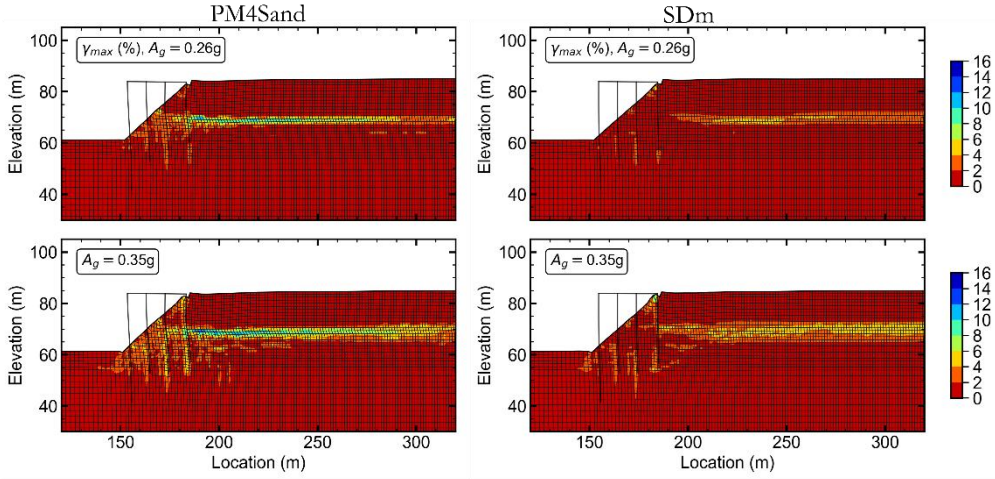

Figure 4.35. Contours of maximum shear strains obtained after 55 seconds of shaking for the SS analyses. Deformed Mesh is shown with an exaggeration factor of 5. Panels on the left show results for the analyses that used PM4Sand for the first 20m, while those on the right are for SDm.

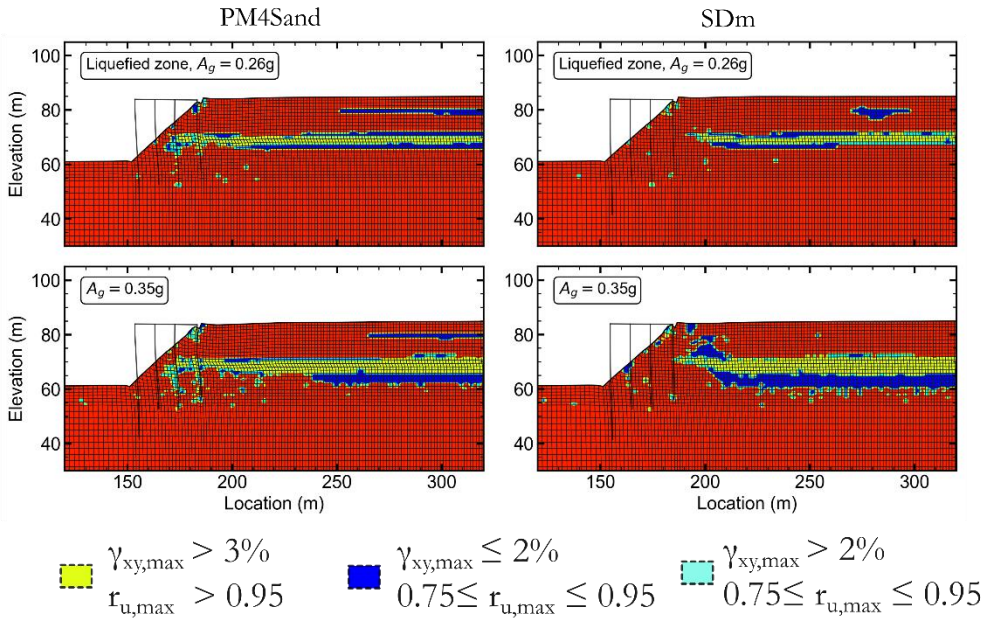

Figure 4.36. Zones of soil liquefaction predicted by the 2D effective stress analyses with PM4Sand (left contours) and SDm (right contours). Deformed Mesh is shown with an exaggeration factor of 5.

Figure 4.37 shows the evolution of the FF and SS residual displacements measured at the crest and at the toe of the slope against the input intensity. Left and right panels display results for the FF and SS analyses respectively. The reduction in ground response caused by the presence of the wharf is summarized in Figure 4.38. It shows the relationship between SS and FF estimates for the displacement at the crest and at the toe.

The comparison between the bottom panels of Figure 4.37 with the right panel of Figure 4.38, reveals that the wharf restrained the ground movement at the toe to almost equally for PM4Sand and SDm, in spite of the differences reported by the FF analyses, likely caused by different EPWPs distribution in the zones neighboring the liquefiable layer.

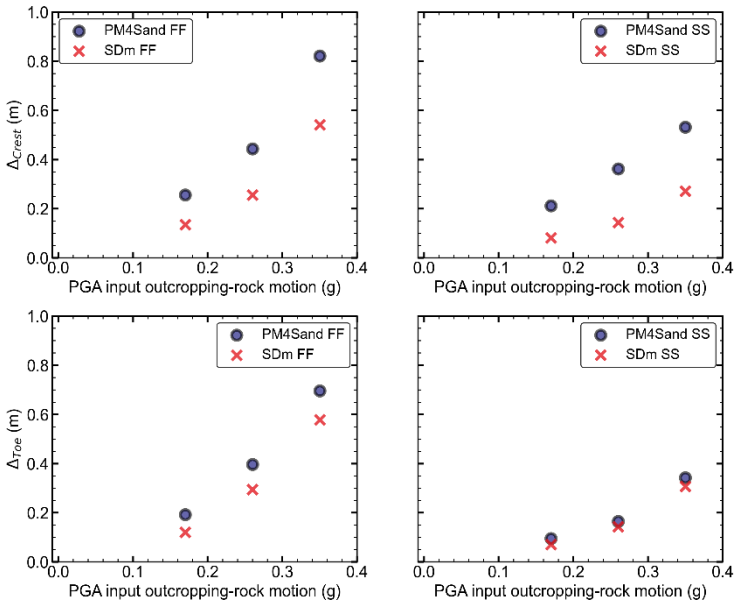

Figure 4.37. Scatters of residual horizontal displacements estimated at the crest and toe of the slope with the FF and SS analysis for Ag=0.17g, 0.26g and 0.35g.

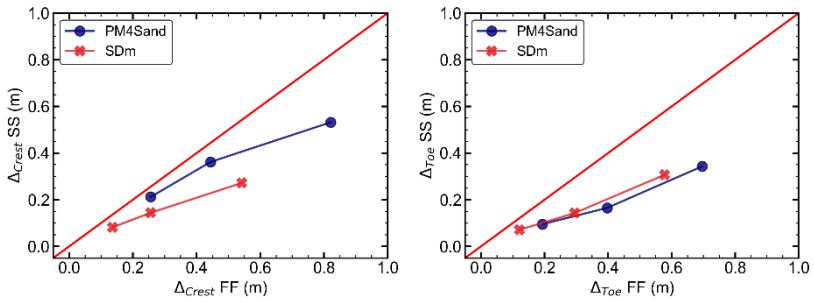

Figure 4.38. Comparison between SS and FF estimates of residual horizontal displacements at the crest (right) and at the toe (left) of the slope.

4.8 WHARF PERFORMANCE

The SS analyses employed the distributed plasticity model of Andreotti and Lai (2017a, 2017b) to model the response of the four rows of piles. The model allowed for the natural development and enlargement of plastic zones within the piles. Consequently, the ground deformations discussed in the preceding section were accompanied by varying degrees of non-linearity of the wharf's response.

Figure 4.39 provides a schematic representation of the deformed shape of the wharf (exaggerated by a factor of 3) after the analyses carried out with Ag = 0.35g. The blue and red markers indicate the sections of the pile that reached their yield capacity at least once, signifying the formation of plastic hinges. Figure 4.39 also includes results for the simulations with Ag=0.26g, as the blue markers represent cross sections that underwent inelastic deformation, not only for Ag=0.35g, but also for Ag=0.26g.

The left panel of Figure 4.39, illustrating results from simulations that used PM4Sand for the liquefiable soils, strongly suggests that the damage pattern meets the criteria for the collapse limit state defined by PIANC (2001) for both input intensities. The ground deformation induced severe damage to the in-ground sections of the two trailing rows of piles closer to the slope. As it will be later shown, double-plastic hinges formed in more than one pile (i.e., double-curvature bending modes) compromised the satisfactory performance of the piles (ASCE, 2014).

The yield capacity of the lead pile was also exceeded. As detailed in previous sections, the lead pile is founded on a non-liquefiable soil (as per the modelling assumptions), and it is mostly responsible for restraining the slope against toe sliding. The kinematic loads imposed by the moving ground at the toe resulted in the development of plastic hinge at an elevation of 55 m approximately. It is not clear however, whether the other plastic hinges along the pile formed due to kinematic or inertial loads alone. Those located on the upper sections of the pile are loaded by the deck due to the inertial movement of the dynamic mass. However, the deck also distributes the loads that the lateral spreading ground exerted on the trailing piles onto all the piles.

As indicated by the position of the red and blue markers in the right panel of Figure 4.39, double curvature bending of the trailing piles also occurred for the analyses that used SDm with Ag = 0.35g. Note that, the embedment depth of the trailing piles is shorter, thus their tips could rotate if the base-soil sufficiently deforms and rotational restrain is limited at the end of the pile. For a more comprehensive evaluation of the pile response, a detailed analysis will be presented later. In contrast to the case of PM4Sand, during the analysis with SDm for Ag = 0.26g, only the sections at the pile-deck level yielded, potentially leaving wharf in a repairable state. More significant pile yielding in the analyses with PM4Sand compared to SDm simply reflect the differences in lateral ground displacements predicted in the two sets of analyses.

Due to its relatively larger lateral stiffness, the trailing pile was the most affected structural element, as it has been case in case-histories of seismic-induced failures of pile-supported wharves. The ensuing discussion will then focus the response of this critical pile. Special attention will be given to the characterization of the seismic demand in terms of forces (e.g., shear force and bending moment), but also in terms of strains (e.g., relative rotations, and curvature) quantities compatible with PBEE procedures.

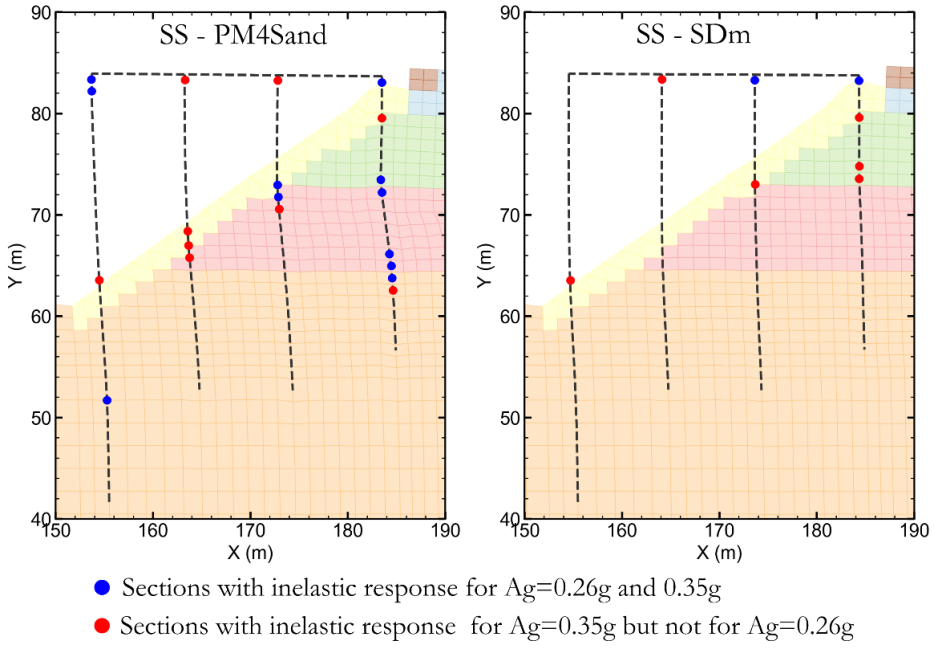

Figure 4.39. Schematic of the deformed shape of wharf BAF after 55 seconds of shaking with Ag=0.35g, for the analysis that used PM4Sand (right) and SDm (left) to model the upper 20 m of the soil deposit. Markers denote the pile sections that underwent inelastic deformations during the analysis using Ag equal to 0.26 and 0.35g.

Recall that in the SS analyses, the mass of the gantry crane was lumped to the deck of the wharf. Consequently, significant inertial loads are expected to be transferred by the deck onto the piles. Figure 4.40 shows plots of (5% critically damped) response spectra computed from the acceleration recorded at the deck. For reference, the response spectra of the outcropping input motions are also shown in the plots. Figure 4.40 indicates that the analyses using PM4Sand and SDm resulted in almost identical response spectra at the deck for all input intensities. The clear exception is the higher spectral ordinates yielded by the analyses with SDm between 0.6s and 1.0 approximately. Moreover, the change in input intensities induced little modification to the spectral ordinates recorded at the deck.

Figure 4.41 verifies the trends observed in the acceleration response spectra of Figure 4.40, it displays time histories of shear force recorded at the node connecting the trailing and the deck, hereafter referred as to node PD. The deck shears estimated by the different simulations are remarkably similar, being those of the SDm analyses slightly stronger after 20s in the case of Ag=0.26g, and after 25s for Ag=0.35g. For all shaking intensities, the shear force exhibits similar maximum amplitudes, oscillating around ±3.8MN.

Moment-curvature diagrams shown in Figure 4.42 were also recorded at the trailing pile-deck connection (node PD in Figure 4.42c). Results for Ag=0.17g are omitted for brevity. Yielding occurred for all the input intensity levels, although for Ag = 0.35g, the hinge at PD underwent a larger number of unloading-reloading cycles leading to a higher curvature demand. Also in this case, SDm and PM4Sand caused similar responses, yet the former led to a slightly stronger demand, in terms of curvature.

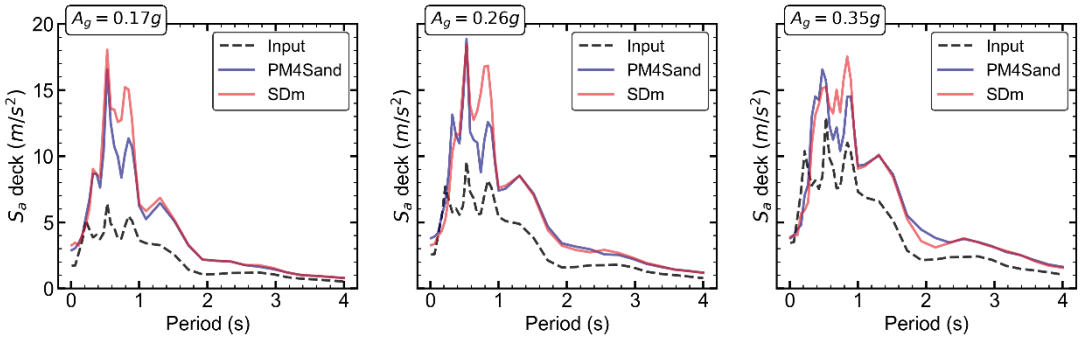

Figure 4.40. Solid lines: response spectra, with 5% of critical damping, of the acceleration time histories recorded at the deck of wharf BAF after the simulations with Ag=0.17g, 0.26g and Ag=0.35g. and with PM4Sand or SDm assigned to the upper 20 m of the native soil. Dashed lines: 5% critically damped response spectra of the input rock-outcropping motion for each simulation.

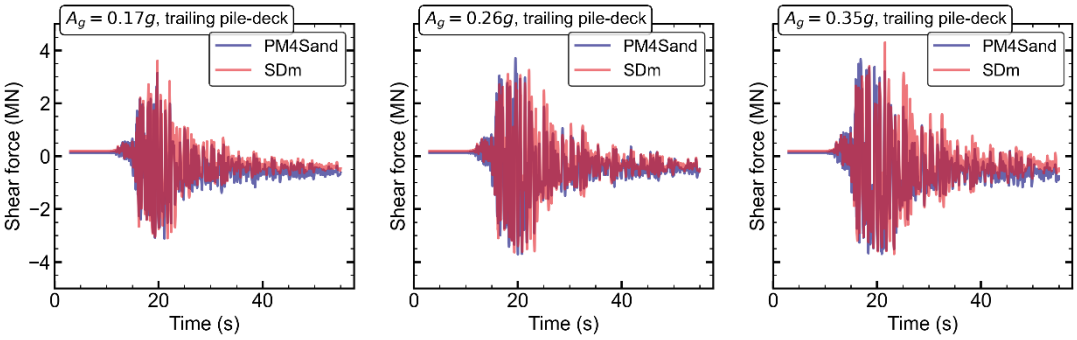

Figure 4.41. Time histories of shear force recorded at the pile-deck connection of the trailing pile of wharf BAF.

Focusing on a different, yet still critical section of the pile, Figure 4.43 shows the moment-curvature (M-χ) diagrams of the hinge that formed inside the dense layer, which overlays the liquefied medium-dense sand. The hinge at this depth is denoted as the in-ground hinge IG (see Figure 4.43c). Note that the curvature, plotted in the horizontal axis, is on a larger scale than that of Figure 4.42. In fact, the IG hinge experienced significantly larger deformations than PD. The M-χ diagrams resemble a case of monotonic loading quite remarkably, as opposed to the cyclic response obtained for PD.

Consistent with the discussion around Figure 4.39, when modelling the liquefiable soils with PM4Sand, larger ground displacements were exerted on the trailing pile. For Ag = 0.26g, pile deformations, measured in terms of curvature, were 4 to 5 times larger than those reported by the analysis that employed SDm. For Ag=0.35g both SDm and PM4Sand cause significant strains on the pile, being the former half of the latter. This is in high contrast with the PD hinge, which was significantly less sensitive to the behaviour of the liquefiable layer.

The rather sharp increase in bending moment reported by the analysis with PM4Sand are caused by an equally large increase of the pile axial load, which in turn increases the capacity of the section, as considered by the model of Andreotti and Lai (2017a, 2017b).

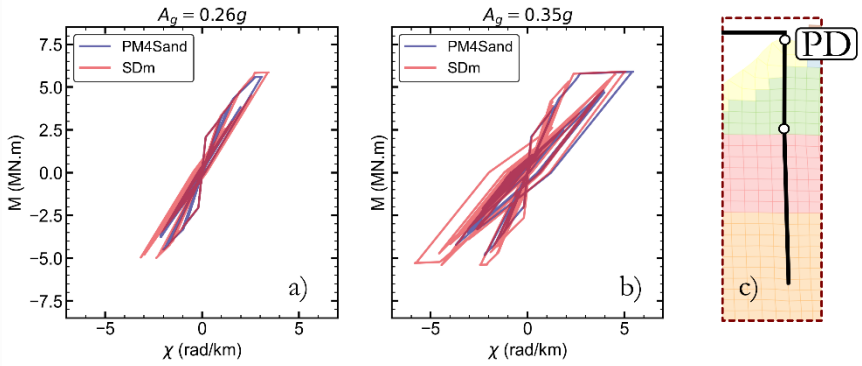

Figure 4.42. Moment-curvature response recorded at the pile-deck connection (PD) of the trailing pile of wharf BAF (c), for inputs Ag of 0.26g (a) and 0.35 (b).

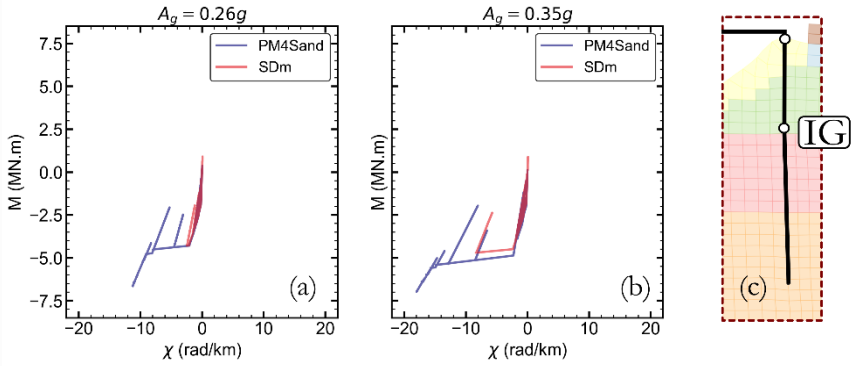

Figure 4.43. Moment-curvature response recorded at an in-ground (IG) section of the trailing pile of wharf BAF (c), for inputs Ag of 0.26g (a) and 0.35 (b).

Summarizing the seismic response of the pile, Figure 4.44 and Figure 4.45 show profiles of SS and FF residual ground displacements, and maximum ductility ratios, i.e., the ratio between the maximum and yield curvatures recorded along the length of the pile. Figure 4.44 shows evidence of kinematic interaction between the pile and the soil. It reveals that the lateral demands on the pile were mainly caused by the deformation of the medium dense sand and the thrust of the overlaying dense sand that acted as a non-liquefied crust that displaced together ith the underlying liquefied soil.

Figure 4.45 adequately captures the distribution of the seismic demand along the length the pile. The largest demands occur are just above the liquefied layer as a result of large laterally spreading ground deformations, reproduced at different degrees by PM4Sand and SDm. Closer to the deck however, the inertial loads transfer by the deck seemed to be unaffected by the response of the liquefied ground, attaining similar values regardless of the magnitude of the lateral spreading ground deformations.

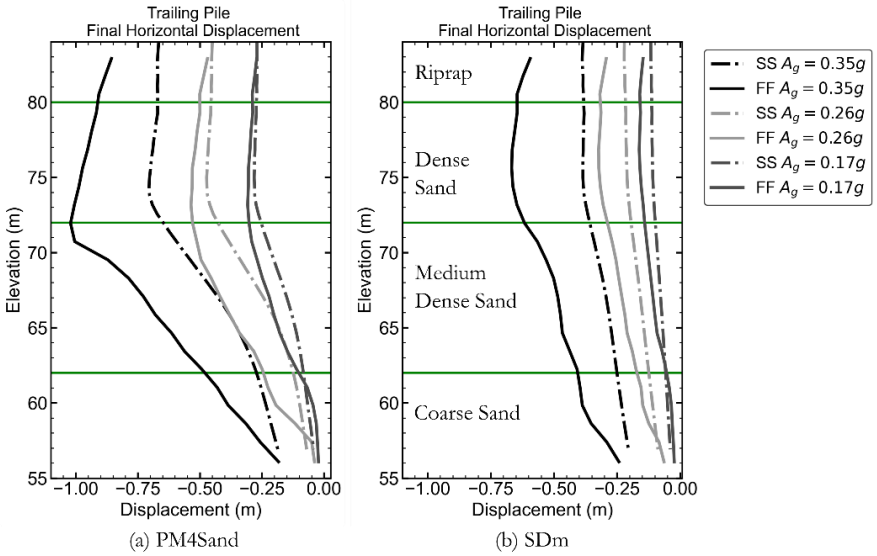

Figure 4.44. Profiles of residual horizontal displacements along the trailing pile of wharf BAF obtained from the simulations that used PM4Sand (a) and SDm (b) to model the upper 20 m of the soil deposit.

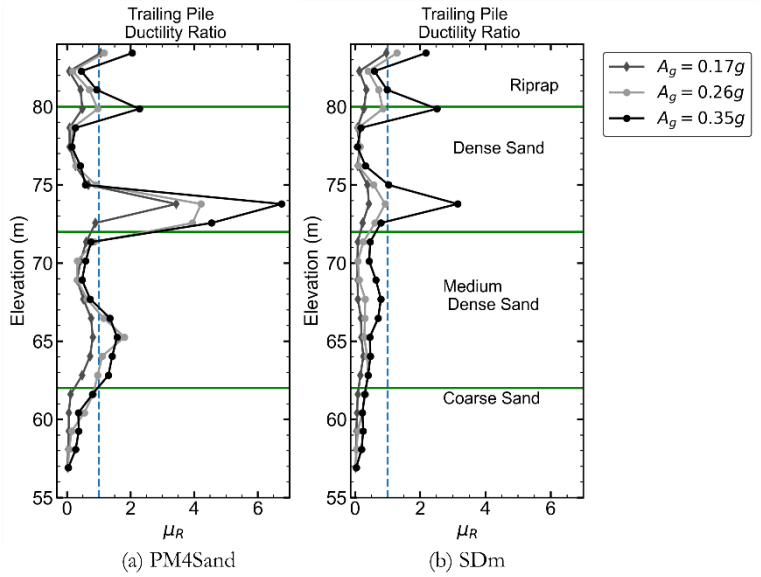

Figure 4.45. Distribution of ductility ratio ($\mu_R = \theta / \theta_y$) estimated for the trailing pile of wharf BAF from the simulations that used PM4Sand (a) and SDm (b) to model the upper 20 m of the soil deposit. Dashed blue line corresponds to $\mu_R = 1.0$.

4.9 SUMMARY AND DISCUSSION

This chapter has presented a systematic examination of the seismic response and seismic demands of a large diameter pile-supported wharf by means of plane strain, time history, effective stress DSSI analyses. The wharf is critical component of the Port of Gioia Tauro, located in Southern Italy, it is founded on a liquefiable natural soil deposit. Aimed at reproducing large deformations, the numerical analyses involved modelling the non-linear response of both the superstructure and the liquefiable ground. Two dimensions of the problem were addressed in parallel. First, the evolution of the system response with ground motion intensity, which was considered by scaling a single hazard-compatible record to three different intensity levels. Second, epistemic uncertainty regarding the behaviour of the liquefiable ground. This latter feature was addressed by testing and comparing the results obtained by using PM4Sand and SDm to model the liquefiable ground.

The free-field system response (i.e., the sloping ground without the inclusion of the wharf) was characterized by two ground deformation mechanisms, toe failure and liquefaction-induced lateral spreading. Residual horizontal displacements for Ag=0.35g were estimated at 0.8 m and 0.5 m by PM4Sand and SDm respectively.

The differences between the ground displacements estimated with PM4Sand and SDm were primarily due to different shear strain rates, and K_α effects reproduced by the models.

As it was demonstrated by element test simulations, PM4Sand produces a constant rate strain rate prior and after liquefaction. Conversely, SDm generates a rapid progression of shear strains prior and during the cycles immediately after liquefaction, which reduces to a constant value, between 4% and 5%, during cyclic mobility.

In terms of K_α effects, cyclic resistances simulated by SDm, under the application of sustained shear stress, were 1.2 to 1.4 higher than those predicted by PM4Sand. Note that, K_α effects are present in both models as the soil behind the scarp of the slope only liquefied once the ground motion intensity became severe. This was also because the base layer underwent large deformations which reduced the seismic demands passed on to the liquefied layer behind the scarp.

The largest contribution to the lateral spreading displacements occurred in the zone next to the non-liquefied wedge of the slope. In this area large post-liquefaction shear strains accumulated. These strains were either caused by the kinetic energy of the non-liquefiable crust crushing the liquefiable layer as the base of the slope moves, or by the larger demand transfer by the relatively stiffer base soil, or a combination of both. Both mechanisms were influenced by the behaviour of the dense soil underlying the liquefiable layer.

The fast progression of post liquefaction shear strains and lower cyclic resistance within the slope explain the larger ground displacements predicted by PM4Sand, Nevertheless, the system response captured by SDm was characterised by a thicker and wider zone of liquefiable soil (i.e., $\gamma_{xy,max} > 3\%$ and $r_{u,max} > 0.95$), as large shear strains produced by PM4Sand ($\gamma_{xy,max} > 10\%$) concentrated over a thin band. It is worth to note that, the soil response of PM4Sand and SDm also differed in terms of modulus degradation characteristics, being the latter stiffer at lower strains.

Both models predicted the triggering of liquefaction around the same instant of time. They reproduced comparable 1D cyclic shear strains, as well as similar crest displacements during and immediately after liquefaction. Afterwards, crest displacement deviated primarily due to differences in terms of post-liquefaction strain rate.

With the inclusion of the wharf, movement at the toe of the slope was fully restrained while the lateral spreading displacements were considerably reduced for both constitutive models. In particular for PM4Sand the residual strains were almost halved. The most demanded pile was the trailing pile, as the input intensity was increased the soil deformation produced excessive kinematic demands on the pile. For the highest input intensity, ground deformations produced by PM4Sand caused a severe double curvature mode of deformation, which is deemed as failure mode by PIANC (2001).

Plastic hinges not only developed along the trailing pile. The lead pile underwent plastic deformations around the base and scarp of the slope because of the toe failure. Moreover, at the pile deck connection plastic deformations also occurred also, which were likely

caused by the lateral loads transferred by the deck from the ground movement acting on the trailing pile. This is also verified when examining the results of SDm, which produced larger accelerations at the deck, yet the pile-deck connection of the lead pile was not as damaged as in the case of PM4Sand.

Time histories of shear force recorded at the trailing pile-deck connections were almost the same for both constitutive models. Slightly larger values were reported by the simulation that used SDm, likely due to the less compliant soil response it produced behind the scarp. Equally interesting, with greater input intensity, deck shear and response spectra ordinate exhibited a marginal increase, as opposed to the ground displacements.

The response at the deck was characterized by several unloading-reloading cycles while the response at the inground sections was resemblant of a monotonic loading case, with peak demands recorded at the end of shaking.

The inertial demand was proven to be highly insensitive to the response of the liquefied soil and directly related to the cyclic phase of the system response, as previously described by Cubrinovski et al. (2009) Tokimatsu and Asaka (1998). Cyclic and lateral spreading phases were clearly differentiated for the two higher input intensities. In these cases, large residual ground displacements occurred when the inertial loads at the pile-deck were almost negligible. In other words, lateral spreading displacements took place after the pile-deck connection of the trailing pile was damaged by the inertial loads transmitted by the deck, denoting the evolutionary nature of the system response.

5.SEISMIC PERFORMANCE OF LARGE DIAMETER PILE SUPPORTED WHARVES, CASE STUDY: PORT OF GIOIA TAURO. PART B: SEISMIC DEMAND ANALYSIS.

5.1 INTRODUCTION.

Seismic design and consequence analysis for pile-supported wharves, as well as for soil-structure systems in general, require the execution of complex numerical analyses capable of producing reliable estimates of design and performance quantities. Most of the current seismic design provisions and guidelines explicitly require considering kinematic and inertial demands. However, there is a lack of consensus regarding (1) procedures for the adequate assessment of kinematic demands on the piles, and (2) the combination of kinematic and inertial loads during simplified analysis procedures.

Design methodologies mostly rely on conventional Beam on Non-linear Winkler Foundation (BNWF) methods, for which the inertial loads are customarily derived from (design) response spectrum procedures. Assessing the kinematic loads for cases of soil liquefaction is a less straight forward process, often involving a progressive application of simplified to complex procedures depending on: subsoil conditions, seismic hazard, and project importance (PIANC, 2001). There is even less agreement about the combination factors for kinematic and inertial loads when using BNWF, or similar, methods. The latest ASCE 61-14 Standard for the Seismic Design of Piers and Wharves (ASCE, 2014), and the Port of Los Angeles Code For Seismic Design, Upgrade And Repair for Container Wharves (POLA, 2010) require the simultaneous application of kinematic and inertial loads without providing details about combination factors. Nonetheless, these guidelines allow to separate both effects on a project-specific basis. In contrast, the Port of Long Beach Wharf Design Criteria (POLB, 2012) the consideration of both loading cases for the design of wharves, although it permits the separation of kinematic and inertial loads, provided the wharf typology is that of a marginal-pile-supported wharf.

For motorway infrastructure, Caltrans (2012) recommended to combine 100% of the kinematic load with 50% of the inertial load in designing pile-foundations for bridges following an non-linear static analysis, similar to that employed by Boulanger et al. (2007). Based on the same study, the Marine Oil Terminal Engineering and Maintenance Standards (MOTEMS) of California (California State Lands Commission, 2010) requires the consideration of 100% of the kinematic load and 25% for the inertial load when simplified analysis procedures are employed.

Aimed at providing a robust rationale for future studies about the calibration of simplified analysis procedures for the seismic design purposes, this chapter entails a probabilistic seismic demand analysis of large-diameter pile-supported wharves. The study focuses on: (1) assessing the relation between kinematic and inertial demands, (2) evaluating the

adequacy of response spectrum methods in estimating inertial loads, (3) underscoring the relevant system response parameters controlling the kinematic demands for the in-ground cross sections of the trailing pile.

The seismic demand analysis is conducted with reference to the case study presented in the previous chapter, which focused on a large-diameter pile-supported-wharf of the port of Gioia Tauro in Southern Italy. The wharf, referred to as Wharf BAF (an acronym in Italian for "Banchina Alti Fondali"), it is the primary component of the deep waters dock at the port. The wharf is founded on a quaternary heterogenous coarse-grained soil deposit, with the upper 20 m are comprised by liquefiable soils of varying degrees of density. The seismic response of the wharf was analysed by means of 2D fully coupled, time history, dynamic-soil-structure interaction (DSSI), effective stress analyses (ESA) performed with FLAC (v8.1) (Itasca Consulting Group, Inc, 2019). Additionally, uncertainty in modelling the liquefiable soils was addressed by employing two different advanced constitutive models: PM4Sand (v3.1) developed by Boulanger and Ziotopoulou (2017), and SDm (v1.1) developed by Cubrinovski and Ishihara (1998a, 1998a).

Estimates of system response parameters are derived from a multiple stripe analysis, consisting in performing effective stress DSSI analyses with a suit of input ground motions for five intensity levels. Each analysis set includes simulations from Free-Field (FF) and Soils-Structure (SS) models. Moreover, consistent with the approach outlined in the previous chapter, the study addresses the epistemic uncertainty in modelling the liquefiable soils by performing separate numerical simulations with PM4Sand and SDm. As a result, a total of 140 simulations were executed: 2 models (FF and SS) × 5 ground motion intensities × 7 (hazard consistent) input motions × 2 constitutive models for the liquefiable layers. It is important to note that the uncertainty associated to model parameters is beyond the scope of the present study.

The first section of this chapter lays down the probabilistic framework utilized for the demand analysis, which is subdivided into two main items: (1) probabilistic seismic response analysis, and (2) identification of efficient and proficient intensity measures. This will be followed by a presentation of the case study and the numerical modelling strategy. Fourth and fifth sections will delve into the results of the probabilistic analysis of the system response, along with the characterization of inertial and kinematic demands on the trailing pile. The last section will conclude with the identification of potentially optimal intensity measures.

5.2 SEISMIC DEMAND ANALYSIS.

The Pacific Engineering Research Centre (PEER) developed a robust performance-based earthquake engineering (PBEE) framework for the seismic performance assessment of structures. The methodology integrates uncertainties related to the earthquake ground motion, system response and associated damage to provide information about the rate of

exceedance of relevant decision variables (DV). The scheme is presented in terms of annual rate of exceedance of decision variable $\lambda_{DV,}$ expressed in Eq(5-1), in which DM, EDP and IM refer to damage measure, engineering demand parameter, and ground motion intensity respectively.

$$\lambda_{DV} = \iiint P[DV|DM]\, dP[DM|EDP]\, dP[EDP|IM] d\lambda_{IM} \quad (5\text{-}1)$$

The PBEE framework "decouples" the performance assessment into three main modules, (1) seismic hazard, and (2) seismic demand and (3) seismic fragility. The seismic demand module directly refers to the seismic response of the structure, or soil-structure system, measured by a scalar or vectorial response parameter, EDP, that can be directly related to a damage measure DM. This document makes a distinction between EDPs and other response parameters (R_p) that are not necessarily used for damage assessment. For a given R_p, the demand model consists in the conditional probability:

$$P[EDP|IM] = P[Rp > r_p|IM] \quad (5\text{-}2)$$

It is widely accepted that, for most engineering applications, the IM-conditioned demand of Eq(5-2) follows a lognormal distribution (e.g., Cornell et al., 2002; Porter et al., 2007), such that:

$$P\left[Rp > r_p\middle|IM\right] = 1 - \Phi\left[\frac{\ln(R_p) - \ln(\widehat{R}_p)}{\beta_{Rp|IM}}\right] \quad (5\text{-}3)$$

In Eq (5-3) $\widehat{R}_p$ is the median, or best estimate, of the model adopted for R_p, and $\beta_{RP|IM}$ is the standard deviation of the model. Under this assumption it follows that the predicted, conditional median of the response parameter can be determined using a one- or two-parameter logarithmic regression model. Such models have been used for common structural engineering applications (Cornell et al., 2002; Mackie and Stojadinović, 2005), as well as for soil structure-systems (e.g., Bradley et al., 2010; Wang et al., 2018), and for waterfront structures(e.g, Na et al., 2009; Shafieezadeh, 2011).

The present study adopted the two-parameter model expressed Eq(5-4), where N is the number of data points (representing the result of a single realization of the system response). $\beta_{RP|IM}$, defined in Eq(5-5) is conveniently assumed independent of IM.

$$\ln(\widehat{R}_p) = \ln(a) + (b)\ln(IM) \quad (5\text{-}4)$$

$$\beta_{Rp|IM} \cong \sqrt{\frac{\sum_i^N \left(\ln\left(\widehat{R}_p\right) - \ln\left(R_{p,i}\right)\right)^2}{N-2}} \tag{5-5}$$

Parameters *a* and *b* are estimated following a conventional least-squares regression, as well as the coefficient of determination (R^2), which is taken as a preliminary estimator of the efficiency of the model, to be discussed in the following sections. The data points were generated via a multiple stripe analysis to account for the ground motion variability over a wide range of hazard levels. Thus, $\beta_{RP|IM}$ essentially contains information about the ground motion uncertainty.

Readily, the framework presented above aims at producing a demand model R_P-IM (EDP-IM) that is latter introduced into a seismic fragility analysis or seismic risk analysis as defined by Eq(5-1). In addition to that, the results of the multiple stripe analysis can be examined following the same regression analysis, to underscore the relationship between the EDPs for the piles and system response parameters that are usually used, or could be potentially used, in design practice. For instance, as demonstrated in previous chapters, for a pile-supported-wharf, inertial loads tend to dominate the seismic demand at the pile-deck level of the trailing piles, whereas the in-ground sections of the piles are mostly affected by ground deformations. The relationship between inertial and kinematic demands could be assessed by examining the regression parameters between the peak relative rotations (or curvatures) at the pile-deck and in-ground plastic hinges.

Let us represent a pair of system response parameters by Rp1 and Rp2, applying the same rationale of Eq(5-4) and Eq(5-5) leads to:

$$\ln\left(\widehat{R}_{p1}\right) = \ln(\dot{a}) + \left(\dot{b}\right)\ln\left(R_{p2}\right) \tag{5-6}$$

$$\beta_{Rp1|Rp2} \cong \sqrt{\frac{\sum_i^N \left(\ln\left(\widehat{R}_{p1}\right) - \ln\left(R_{p1,i}\right)\right)^2}{N-2}} \tag{5-7}$$

In this case, the uncertainty measured by $\beta_{Rp1|Rp2}$ would not only account for the record-to-record variability, it would also reflect the model uncertainty, in the sense that the relationship expressed by Eq(5-6) might not be adequate for the particular pair of response parameters being tested. The following sections of this chapter will delve into these details and other findings arising from the probabilistic analysis of the response of wharf BAF.

As mentioned in the introduction, simplified seismic design procedures for pile foundations are mainly based on sub-structuring or decoupled approaches. These methodologies estimate design quantities by using equally simple definition of seismic demand parameters. For instance, the inertial loads on the pile cap are usually estimated

from (design) response spectrum methods, that may account for site-specific amplification and DSSI effects (e.g., Ashford et al., 2011). For BNWF methods, kinematic loads can be idealized as passive or active pressures, depending on the subsoil conditions. In cases of liquefaction-induced lateral spreading it is often preferred to apply the distribution of free-field ground displacements at the free end of non-linear springs.

5.2.1 Conditions of an optimal IM

In the current form of Eq(5-1), the demand model propagates the variability of the earthquake ground motion into the system response, provided that the selected IM effectively represents the characteristics of the earthquake motion that better explain R_p. In essence, the pair Rp-IM (or EDP-IM) must be optimal. Luco and Cornell (2007) outlined two conditions for an optimal IM. Firstly, recognizing that a single intensity measure is a simplistic representation of the complex time-varying characteristics of the ground motion, it inherently introduces uncertainty into the demand model. Thus, an optimal IM contributes the least to the uncertainty in Rp, a criterion referred to as *efficiency*. Secondly, the *sufficiency* of IM in rendering the demand model independent of other ground motion characteristics, such as magnitude (M) and source-to-site distance (R).

Conditional approaches for selecting ground motion records, as proposed by Baker and Allin Cornell (2006), and Bradley (2012), directly address the issue of sufficiency. The present study does not make use of such methods as it does not aim to produce a damage or fragility model. Instead, it focuses on examining the system response of wharf BAF via a probabilistic framework to inform future decisions about more in-detail assessments.

Additional conditions for an optimal IM can be found in the literature: practicality (Mackie and Stojadinović, 2005), proficiency (Padgett et al., 2008), and hazard computability (Giovenale et al., 2004) are among the most widely used. As it will be discussed in the following sections, the present study delt with the conditions of efficiency, practicality, and proficiency.

The model dispersion measured by $\sigma_{RP|IM}$ also includes the contribution of the model uncertainty, such that the choice of a suboptimal model would overshadow the effects of ground motion variability and model uncertainty. Hence, $\sigma_{RP|IM}$ is a direct measure for efficiency. Nonetheless, the coefficient of determination can be also used to referred to the model efficiency (Wang et al., 2018).The slope *b* of *Eq*(5-4*)* is used a measure of practicality, it represents the dependence of the response parameter R_p on IM. Proficiency is taken as the combined measure of practicality and efficiency, computed as the ratio ξ expressed in Eq(5-8). Lower values of ξ indicate a more proficient IM.

$$\xi = \frac{\beta_{Rp|IM}}{b} \tag{5-8}$$

5.3 CASE STUDY AND NUMERICAL MODELLING

Fully coupled effective stress DSSI analyses were executed with FLAC (v8.1) (Itasca Consulting Group, Inc, 2019), details about the modelling considerations and boundary conditions can be found in Chapter 4. Figure 5.1 shows a schematic representation of the cross section modelled with FLAC, the complete finite difference model is depicted in Figure 4.11. The model is representative of the native soil profile reported in Figure 5.2. The upper 20 meters are comprised by a heterogeneous sedimentary coarse-grained deposit. The soil properties reported in Figure 5.2 correspond to the characteristic values derived from a CPT-based site characterization, and from measurements of SPT blow count and shear wave velocity, for further details about the site characterization refer to Section 4.3.

The grid is comprised by 6250 zones, it is capable of accurately propagating frequencies up to 12 Hz. The widths of the upper most elements are, on average, about 1.5 m while the average height is approximately 1.2m. The entire model is 250 m wide, and 85 m tall. The piles comprising the wharf were modelled using the distributed plasticity model formulated by Andreotti and Lai (2017a,b). The model is tailored for DSSI problems to simulate the cyclic degradation of structural elements, rendering it compatible with performance-based earthquake engineering principles. Additional energy dissipation due to the relative movement between piles and soil was not considered, however, interface elements will be included in future studies.

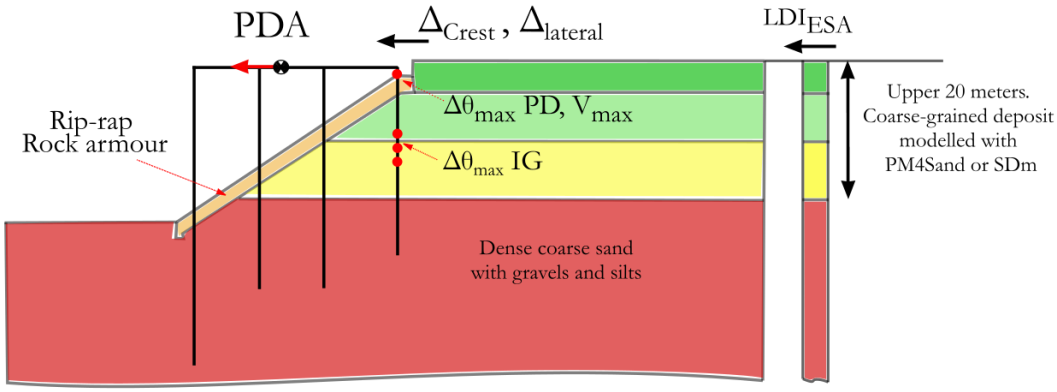

Figure 5.1. Schematic representation of the cross section of Wharf BAF used for the 2D DSSI effective stress analyses performed with FLAC.

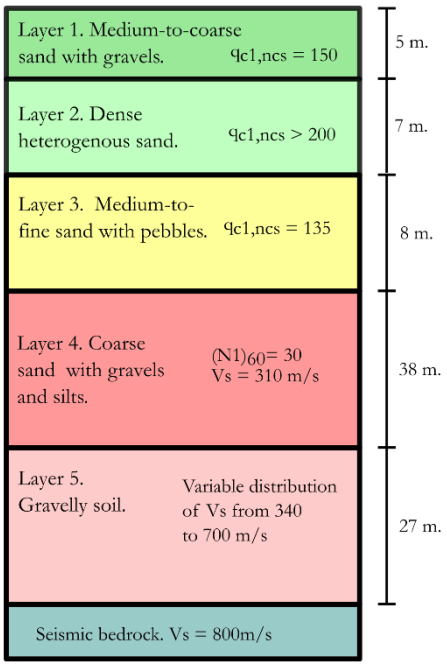

Figure 5.2. Simplified soil profile representative of the native deposit found at the southern portion of the port of Gioia Tauro (Southern Italy).

The nonlinear behaviour of the liquefiable layers was accounted for by means of PM4Sand (Boulanger and Ziotopoulou, 2013, 2017) and SDm (Cubrinovski and Ishihara, 1998a,b). Both are state-based, elastic-plastic constitutive models. PM4Sand follows a bounding-surface-plasticity formulation.

Model parameters for PM4Sand and SDm were selected according to the CPT-based calibration procedure employed by Ntritsos and Cubrinovski (2020). The procedure considers in reproducing the target liquefaction resistance curves (LRCs), from single-element undrained simple-shear simulations. The LRCs define the evolution of the cyclic resistance ratio (CRR) with the number of equivalent unfirm shear stress cycles (N_{cyc}) needed to cause 5% double amplitude shear strain under dynamic-simple-shear (DSS) conditions (Ishihara, 1993). The rationale behind this approach is that the computed LRCs approximate well-accepted CPT-based empirical relationships. The empirical LRCs were computed from the liquefaction triggering relationship of Boulanger and Idriss (2014). Details about the calibration procedure, and selected parameters can be found in Section 4.4.1.

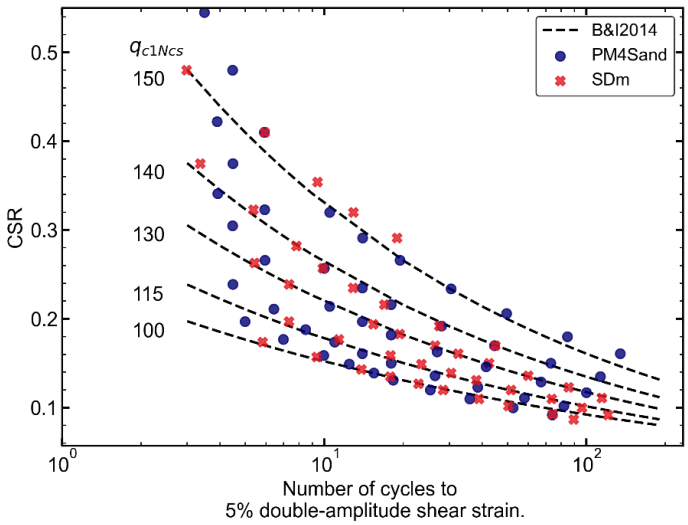

Figure 5.3. CPT-based calibration PM4Sand and SDm for the native soil deposit shown in Figure 5.1.

5.4 MULTIPLE STRIPE ANALYSIS: INPUT GROUND MOTIONS

The numerical analyses of the FF and SS models employed a suite of 35 input motions to capture a wide range of seismic demands and system responses. These input motions consisted of single-component, outcropping-rock accelerograms selected for 5 seismic hazard levels corresponding to return periods (T_R) of 201, 475, 975, 1950 and 2475 years. For each intensity level, seven ground motion records were selected using the Ascona toolbox (Corigliano et al., 2012). Ascona selects spectrum compatible accelerograms, queried from a local database comprised by records retrieved from three different internationally accredited data banks, namely: the PEER-NGA West 2 database (Ancheta et al., 2013, http://peer.berkeley.edu/smcat/) the Engineering Strong Motion database ESM, (Lanzo et al., 2018, https://esm-db.eu/), and the Kyban Kyoshin network (Kik-net) of the National Research Institute for Earth Science and Disaster Resilience of Japan (http://www.k-net.bosai.go.jp/).

Preliminary simulations of the FF and SS models indicated that the fundamental periods for the entire system, and for the wharf structure, ranged from 0.7s to 2.0s, and from 0.35s to 0.55s, respectively. Given that liquefaction-induced lateral spreading is expected to be the primary cause of damage, ground motion records were linearly scaled to match the spectral ordinate of the uniform hazard spectrum (UHS) at 0.7 seconds (S_A(T=0.7s)) for each return period. Adopting values at longer periods produced sets with either an insufficient number of records or large scaling factors. Furthermore, estimates from the probabilistic seismic hazard assessment were not available in terms of intensity measure

other than UHS ordinates. Therefore S_A(T=0.7s) was chosen as a practical comprise between sufficient number of records and limited scaling factor.

The selection of the scaled records was made based on the following criteria:

1. *Compatibility with reference free-field conditions*, indicating that the selected accelerograms were recorded on stiff soil and flat surface conditions. As the seismic bedrock is relatively shallow, 80m deep, the 2D analyses directly reproduce local site effects.
2. *Seismo-compatibility*, which constrained the selection, as much as possible, to events with magnitude and source-to-site distance within the ranges reported by the seismic hazard disaggregation for the site (Barani et al., 2009).
3. *Hazard compatibility* with the uniform hazard spectrum (UHS) produced by Gruppo di Lavoro MPS (2004). This condition implied that the difference between the UHS and the average (5% damped) acceleration response spectrum for the selected set was the minimum among all the possible sets. Compatibility with the UHS was enforced for the range of periods between 0.1 seconds and 1.8 seconds. Sets were not admitted if: the mean S_A was below 85% and above 130% of the UHS, on average, or when the maximum spectrum deviation (Corigliano et al., 2012) exceeded 1.5.

For each return period, Figure 5.4 compares the response spectra of the selected input motions with the UHS. Additional details about the selected set of motions are provided in Table 5.1. As it can be noted, due to data availability, some records were used more than one hazard level.

Table 5.1. Input motions used for the 2D DSSI effective stress analysis.

T_R (yr)	Input motion number	Magnitude of the unscaled record	Source-to-Site distance (km)	Scaling factor	Database	File name
201	1	5.74	12.57	1.87	NGA	RSN146_COYOTELK_G01320.AT2
	2	5.6	36.9	1.44	ESM	IT.SRT..HNE.D.19901213.002426.C.ACC.ASC
	3	5.6	18	0.71	ESM	IT.LRS..HNN.D.19980909.112800.C.ACC.ASC
	4	6.6	31	1	KiKnet	SMNH100010061330.EW2
	5	6.5	57.74	1.93	NGA	RSN8167_SANSIMEO_DCPP247.AT2
	6	6	8.5	0.53	ESM	IT.AMT.00.HGE.D.EMSC-20160824_0000006.ACC.MP.ASC
	7	5.9	10.4	0.96	ESM	IT.CLO.00.HGN.D.EMSC-20161026_0000095.ACC.MP.ASC
475	1	5.6	36.9	2.41	ESM	IT.SRT..HNE.D.19901213.002426.C.ACC.ASC
	2	6.69	38.07	2.02	NGA	RSN1091_NORTHR_VAS000.AT2

T_R (yr)	Input motion number	Magnitude of the unscaled record	Source-to-Site distance (km)	Scaling factor	Database	File name
	3	6.6	31	1.68	KiK-net	SMNH100010061330.EW2
	4	6.6	62	2.37	KiK-net	SAGH050503201053.EW2
	5	6	8.5	0.52	ESM	IT.AMT.00.HGN.D.EMSC-20160824_0000006.ACC.MP.ASC
	6	6.6	11.6	0.51	ESM	IV.T1212..HNE.D.EMSC-20161030_0000029.ACC.MP.ASC
	7	5.9	10.4	1.61	ESM	IT.CLO.00.HGN.D.EMSC-20161026_0000095.ACC.MP.ASC
975	1	6.9	62.9	1.29	ESM	EU.HRZ..HNE.D.19790415.061941.C.ACC.ASC
	2	6.93	103.91	2.89	NGA	RSN789_LOMAP_PTB297.AT2
	3	6.69	38.07	2.98	NGA	RSN1091_NORTHR_VAS000.AT2
	4	5.6	18	1.74	ESM	IT.LRS..HNN.D.19980909.112800.C.ACC.ASC
	5	6.6	31	2.48	KiK-net	SMNH100010061330.EW2
	6	6	8.5	0.76	ESM	IT.AMT.00.HGN.D.EMSC-20160824_0000006.ACC.MP.ASC
	7	6.6	11.6	0.75	ESM	IV.T1212..HNE.D.EMSC-20161030_0000029.ACC.MP.ASC
1950	1	6.9	62.9	1.28	ESM	EU.HRZ..HNN.D.19790415.061941.C.ACC.ASC
	2	6.93	28.64	2.23	NGA	RSN765_LOMAP_G01000.AT2
	3	6.69	38.07	2.51	NGA	RSN1091_NORTHR_VAS090.AT2
	4	7.62	80.53	2.53	NGA	RSN1257_CHICHI_HWA003-N.AT2
	5	6.6	31	3.22	KiK-net	SMNH100010061330.EW2
	6	6	8.5	0.99	ESM	IT.AMT.00.HGN.D.EMSC-20160824_0000006.ACC.MP.ASC
	7	6.6	6.8	0.78	ESM	IT.CLO.00.HGE.D.EMSC-20161030_0000029.ACC.MP.ASC
2475	1	6.9	62.9	1.56	ESM	EU.HRZ..HNN.D.19790415.061941.C.ACC.ASC
	2	6.69	38.07	3.06	NGA	RSN1091_NORTHR_VAS090.AT2
	3	7.62	80.53	3.09	NGA	RSN1257_CHICHI_HWA003-N.AT2
	4	6.6	31	3.93	KiK-net	SMNH100010061330.EW2
	5	6.6	6.8	0.67	ESM	IT.CLO.00.HGN.D.EMSC-20161030_0000029.ACC.MP.ASC
	6	6	8.5	1.2	ESM	IT.AMT.00.HGN.D.EMSC-20160824_0000006.ACC.MP.ASC
	7	5.9	10.4	3.75	ESM	IT.CLO.00.HGN.D.EMSC-20161026_0000095.ACC.MP.ASC

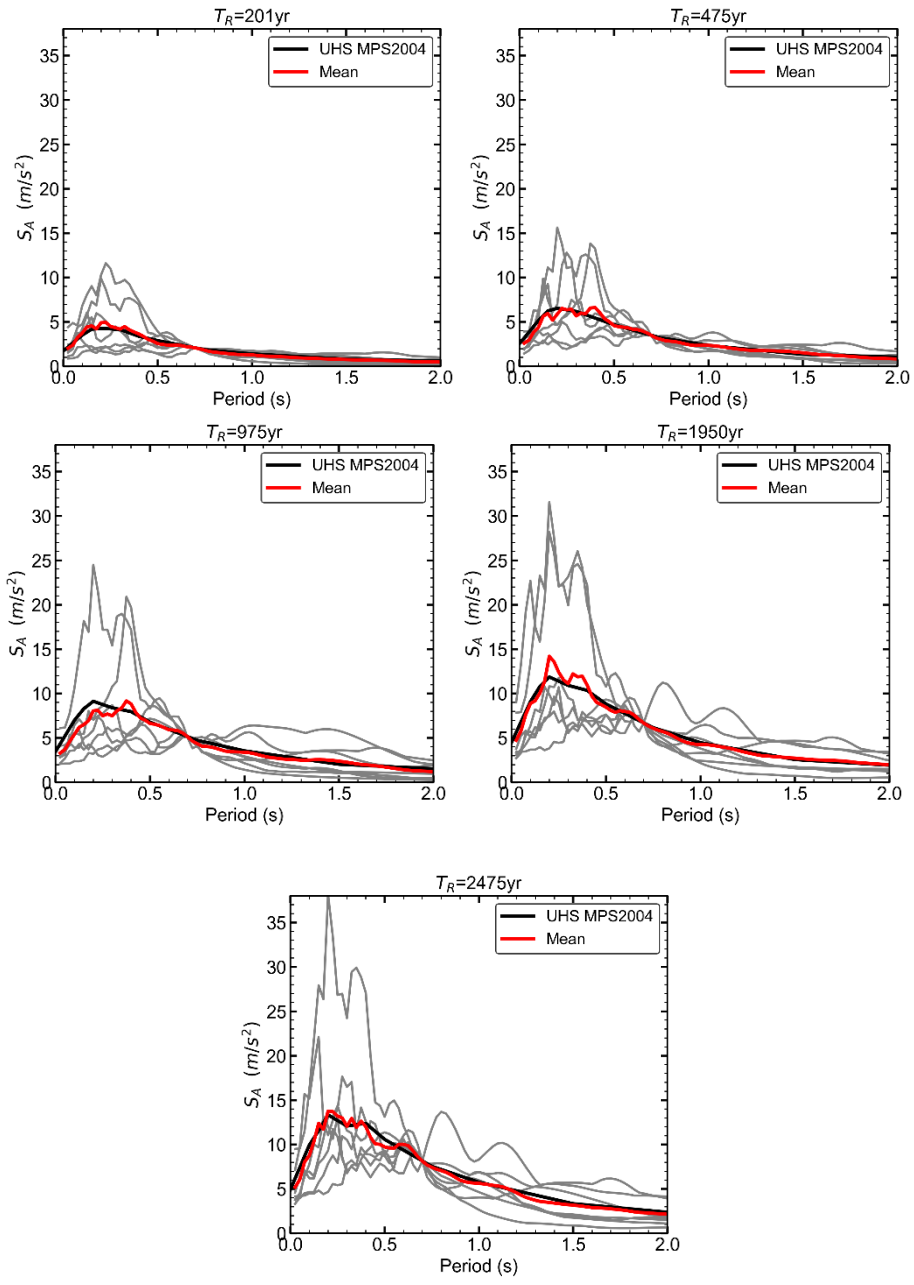

Figure 5.4. Acceleration response spectra (with 5% of critical damping), S_A, of the input motions selected for the 2D DSSI effective stress analyses, for return periods of 201, 475, 975, 1975 and 2475 years. Red line: mean acceleration response spectra of the selected records. Black line: uniform hazard spectra (UHS) produced by Gruppo di Lavoro MPS (2004).

5.5 MULTIPLE STRIPE ANALYSIS: SEISMIC DEMAND AND SYSTEM RESPONSE PARAMETERS

Seismic demands on piles are generally grouped into inertial and kinematic, depending on the source of the external loads (i.e., forces and displacements) exerted on the piles. The first category corresponds to the loads transmitted to the piles by the superstructure, the wharf's deck for the present case, during intense shaking. The second category relates to the forces and displacements that the moving ground imposes onto the piles. The terms inertial and kinematic demands are not interchangeable with inertial and kinematic DSSI effects.

The present analysis aims at assessing the system response parameters (Rp) controlling the seismic demands estimated from a multiple stripe analysis. The schematic of the numerical model shown in Figure 5.1, reports the seismic demand parameters examined in the present study, Table 5.2 gives a summery for their descriptions. Maximum (or peak) relative rotations recorded at the pile-deck (PD) and inground sections (IG) serve as direct measurements of the seismic demands exerted on the trailing pile. Inertial loads transmitted by the deck onto the pile were characterized by means of the maximum shear force (V_{max}) and peak acceleration recorded at the deck level (PDA).

The response of the 2D system is expressed in terms of the residual displacement of the slope crest, measured relative to the base of the model (Δ_{Crest}), and relative to the residual displacement recorded at the lateral boundary of the main grid ($\Delta_{lateral}$), not to be confused with the 1D column. The latter parameter serves as direct measurement of the non-uniform lateral spreading described by Ishihara et al. (1997). The 1D response is assessed by means of the lateral displacement index, LDI_{ESA}, of the upper 20 meters, ESA stands for effective-stress-analysis. It is defined by Eq(5-9) similar to the response parameter D_{max} used by Cubrinovski and Ntritsos (2023).

Table 5.2. System response parameters computed from the 2D DSSI effective stress analyses.

Response Parameter	Symbol
System response parameters	
Residual horizontal displacement of the crest (m)	Δ_{Crest}
Relative residual lateral displacement of the crest, with respect to the residual displacement obtained at the surface of the lateral boundary (m)	$\Delta_{Lateral}$
Lateral displacement index (m) computed from the maximum shear strains computed along the upper 20 meters of the 1D	LDI_{ESA}

column, according to Eq(5-9) . ESA stands for effective-stress-analysis, to distinguish the index from the widely used empirical LDI computed from field test data.	
Wharf response parameters	
Maximum relative rotation (rad). recorded at the plastic zones formed at the in-ground sections (IG) located within the upper 20 m of the soil deposit	$\Delta\theta_{max}$ IG
Maximum relative rotation (rad) recorded at the trailing-pile deck connection (plastic zone) node (PD)	$\Delta\theta_{max}$ PD
Deck shear, maximum shear force obtained at the trailing pile-deck node (PD) (kN)	V_{max}
Peak deck acceleration (m/s^2)	PDA

$$\mathrm{LDI_{ESA}} = \int_0^{20} \gamma_{xy,1D}\,dy \tag{5-9}$$

Before delving into the probabilistic dimension of the estimated seismic demands, it is worth presenting an overview of the results obtained from the multiple analysis. Figure 5.5 shows scatter plots of the results for Δ_{Crest} and $\Delta_{Lateral}$ estimated from the FF and SS analyses. The term SS refers to the Soil-Structure model, hance it makes direct reference to DSSI effective stress analysis. Marker shape denotes the constitutive model used for the upper 20 meters of the native soil deposit, PM4Sand or SDm. Cases that triggered liquefaction of the medium sand are represented by coloured markers, whereas those in black belong to cases of no-liquefaction. Note that the adopted methodology of multiple stripe analysis differs from conventional incremental dynamic analysis (e.g., Mackie and Stojadinović, 2005; Vamvatsikos and Fragiadakis, 2009), in the sense that the set of unscaled ground motions is different for each hazard level, yet some records were used for more than one level. This was done to preserve compatibility between earthquake intensity and the seismological characteristics of each record.

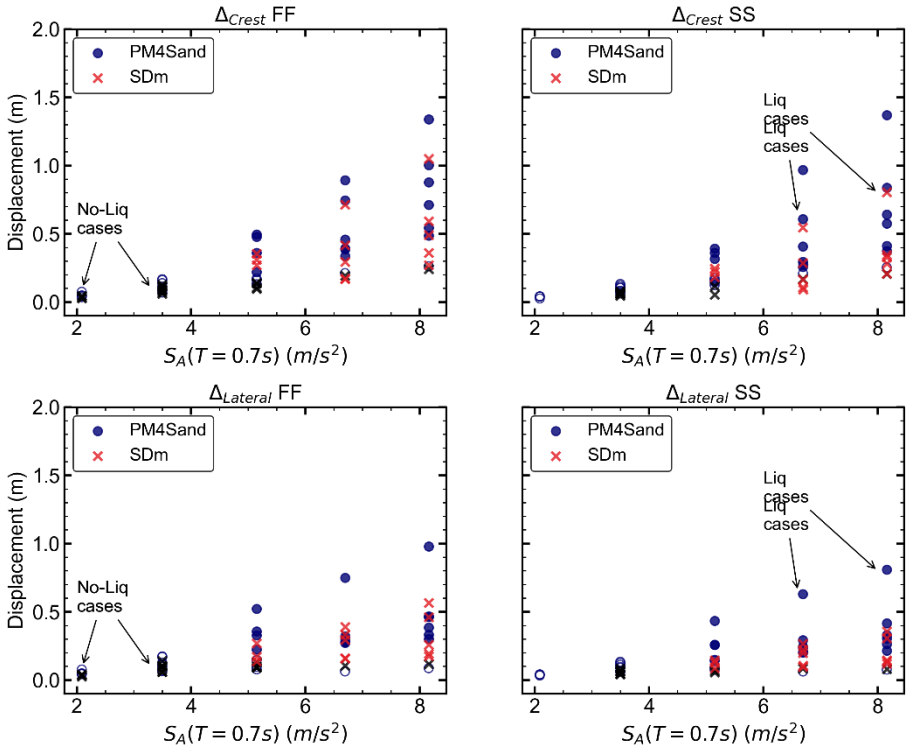

Figure 5.5. Distribution of residual (top) and lateral (bottom) crest displacements obtained from the multiple stripe analysis. Left panels, results from Free-Field (FF) simulations. Right panels, results from Soil-Structure (SS) simulations. Coloured markers represent cases with liquefaction. The strips correspond to seismic hazard levels of 201, 475, 975, 1950 and 2475 years.

Based on the distributions depicted in Figure 5.5, it is evident that the severity of the system response, in relation to the chosen IM, demonstrates a clear upward trend with an acceptable dispersion, even though the IM was selected based solely on engineering judgement. Moreover, results produced by PM4Sand and SDm are apparently within the same order of magnitude. In general, both models indicate that liquefaction within the medium sand was triggered for return periods longer than 475 years. However, SDm predicted the occurrence of liquefaction for two input motions of T_R=475 yr. Interestingly, the dispersion of the distribution of $\Delta_{Lateral}$ is apparently smaller than that of Δ_{Crest} specially when making a distinction between liquefaction and no-liquefaction cases.

Figure 5.6 shows the distributions of maximum relative rotation recorded at the pile-deck (PD) and in-ground (IG) sections of the trailing pile (see Figure 5.1). The dotted grey lines correspond to the cracking ($\Delta\theta_{crack}$), yield ($\Delta\theta_y$), and failure ($\Delta\theta_f$) relative rotations estimated from single element analysis without axial load, with respective values of 0.29x10^{-3} rad,

4.29x10^{-3} rad and 42.0 x10^{-3}rad. The dotted coloured lines map the sample mean for each strip.

The seismic demands at the PD and IG sections exhibit opposing trends. At the in-ground levels, as the input intensity increases for $T_R > 475$ years (S_A(T=0.7s)>4 m/s^2), liquefaction induced ground deformations caused a pronounced increase of the kinematic loads exerted on the trailing pile. Larger post-liquefactions strains produced by PM4Sand led to larger demands. Conversely, at the pile-deck node, the seismic demand exhibited an upward trend for $T_R \leq 975$ (S_A(T=0.7s)>5 m/s^2) years on average, yet it remained almost unchanged for longer return periods. In this case, SDm caused a stiffer ground response which in turn caused a stronger cyclic loading of the pile-deck connection.

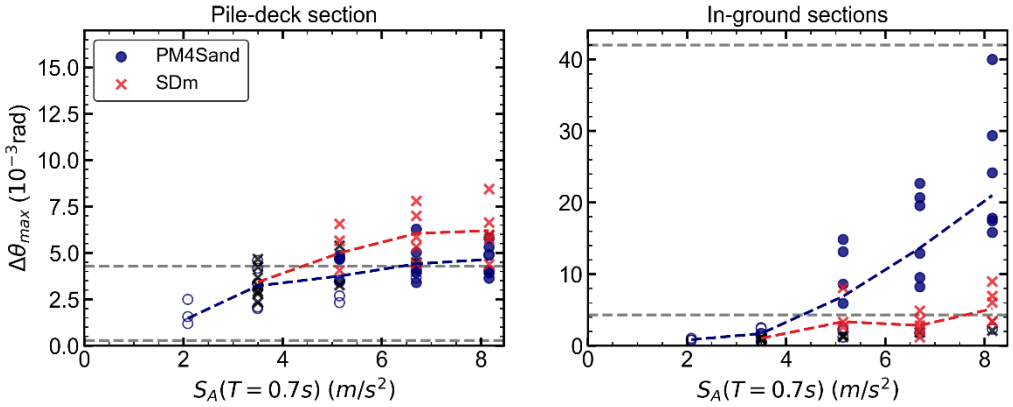

Figure 5.6. Distributions of maximum relative rotations recorded at the pile-deck connection (left) and at the in-ground sections of the trailing pile of wharf BAF during SS simulations. Coloured markers denote cases with liquefaction.

5.5.1 Inertial demand

The inertial demand is characterized by the maximum shear force (V_{max}) and the maximum acceleration recorded at the pile-deck node (i.e., peak deck acceleration, PDA). Figure 5.7 illustrates scatter plots between the maximum relative rotations at the pile-deck and in-ground hinges, against the inertial load parameters. Figure 5.7 reports the outcomes of the regression analyses next to each plot, they are presented according to the framework laid down in Section 5.2.

Results for node PD reveal a high correlation between the seismic demands and the inertial movement of the deck. This is however unspringing, instead what is worth to highlight is the non-linear relation between $\Delta\theta_{max}$ PD and V_{max}. When compared against the shear force – displacement characteristics of the wharf (i.e., push over curve), shown in Figure 5.8, it becomes evident that the capacity of the connection is controlling the response at this

section, as the trend of $\Delta\theta_{max}$-V_{max} and $\Delta\theta_{max}$-PDA curve upwards, beyond the point of yielding, in agreement with the shear capacity.

The correspondence between the inertial loads and $\Delta\theta_{max}$ PD appeared to be insensitive to the constitutive model used for the upper 20 meters of the native soil deposit. The estimated trends for PM4Sand and SDm are almost coincident, characterized by nearly identical logarithmic slopes (*b*). Consequently, this section will not make further distinction between the results obtained when using PM4Sand and SDm when examining the demands at the pile-deck level. Moreover, this study will hereby regard seismic demands at the deck level as inertial demands.

Opposite to the case of the pile-deck section, high demands for the in-ground sections, as measured by $\Delta\theta_{max}$ IG, are unrelated to the inertial response of the deck. This trend was observed for PM4Sand and SDm cases alike, albeit with nuances as PM4Sand resulted in significantly larger demands, which are discussed in the next section.

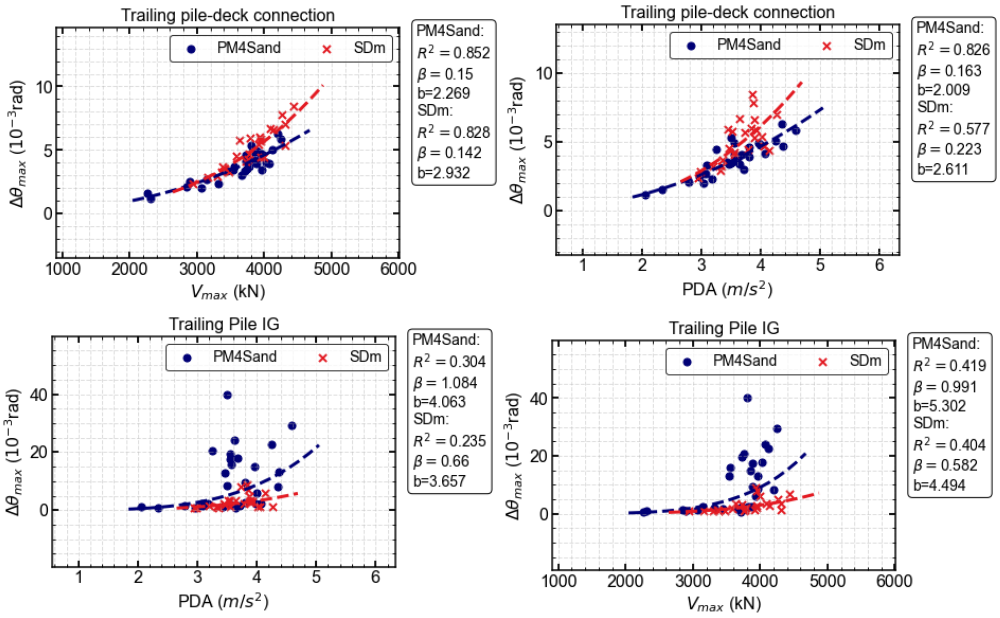

Figure 5.7. Regression analysis for maximum relative rotation at the PD (top) and IG (bottom) sections of the trailing pile, against peak deck acceleration (left) and maximum pile-deck shear force (right).

5.5.1.1 *Force-based vs displacement-based estimates of inertial demands.*

Current seismic design guidelines recommend displacement-based design methodologies over force-based methods. POLA (2012) and POLB (2013) prohibit the use of force-based

methods to favour the ductile design of the pile-deck connection. In contrast, the ASCE 12-14 code allows force-based design under project-specific conditions, although it also emphasizes that such methodology tends to produce uneconomical designs.

For comparison purposes, estimates of the design deck shear (V_D) were obtained by following the procedures outlined in ASCE 12-14 with important modifications. For the force-based estimates, the deck shear was computed according to Eq(5-10). On the right side, the first term corresponds to the (5% damped) acceleration spectrum evaluated at the fundamental period of the wharf, the second term corresponds to the dynamic mass. Both terms were estimated from the results of the SS simulations. Likewise, the fundamental period of the wharf T_{wharf} was estimated to be around 0.45s, and the respective dynamic mass of 1050 ton. The last term corresponds to the ratio between the importance factor I=1.25 and the force reduction factor R=2.

$$V_{D,force-based} = S_{A,1D}(T = T_{wharf})\, M_{Dynamic} \left(\frac{I}{R}\right) \tag{5-10}$$

The displacement-based estimate of V_D was obtained by following the substitute structure method recommended by the ASCE 12-14 standard, according to Eq(5-11). Similar to the case of the force-based estimate, the design displacement in Eq(5-11) was estimated using the displacement response spectrum evaluated at T_{wharf} and following the recommended iterative procedure to find the effective damping ratio ξ_{effe}. V_D was then back-calculated from the push-over curve reported in Figure 5.8.

$$V_{D,displacement-based} = V_{pushover}\,(\delta = \delta_D)$$
$$\delta_D = S_{D,1D}(T = T_{wharf}, \xi = \xi_{effe}) \tag{5-11}$$

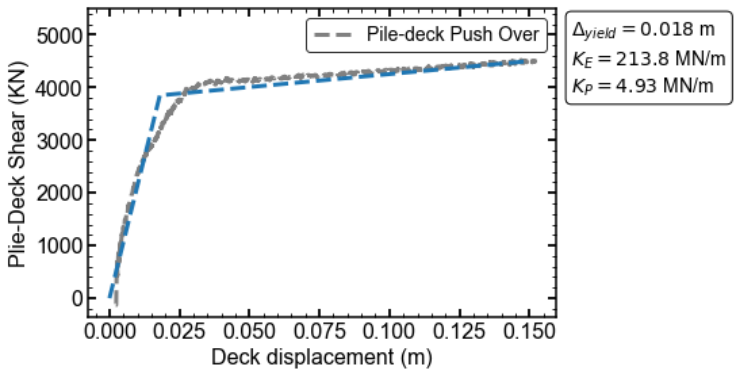

Figure 5.8. Shear force-displacement characteristics of wharf BAF at the deck level (pushover curve) estimated with FLAC using the constitutive relationship proposed by Andreotti and Lai (2017a, 2017b).

Figure 5.9 compares the force- and displacement-based estimates of the shear force with V_{max}. Results show that the former estimates are the most conservative, potentially over conservative, as they are 1.5 to 2.5 greater than V_{max}, note that the importance factor I was set to 1.25. Conversely, the displacement-based estimates were comparable to Vmax, although in some cases the methodology underestimated the DSSI-ESA results. This was likely because nominal and not effective reinforced concrete properties were used to derive the pushover curve.

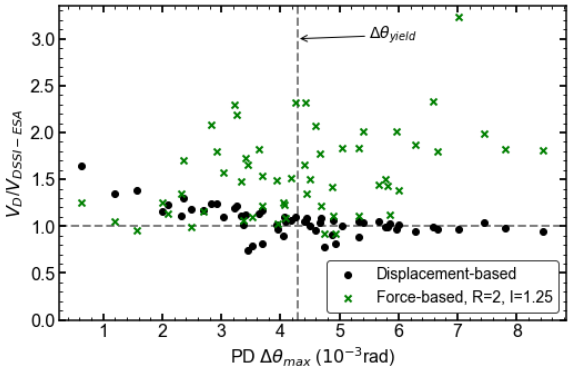

Figure 5.9. Comparison between the estimated design shear (V_D) and the maximum shear force at the PD node recorded during the DSSI effective stress analyses.

5.5.2 Kinematic demand

Before continuing the discussion about the probabilistic response of wharf BAF, it is worth recalling some insights gained from the incremental, effective stress, DSSI analyses of Chapter 4. They indicated that the soil responses reproduced by PM4Sand and SDm were

markedly different. Two distinct features of the constitutive models were identified as responsible for the discrepancies seen in the 2D system response. First, post liquefaction strains produced by PM4Sand were 2 to 3 times greater than those predicted by SDm. Although, it is worth noting that despite this difference, simulations that used SDm saw a faster and larger expansion of the area that liquefied. Second, K_{alpha} effects. SDm generated cyclic resistances, under sustained (static) shear stress, 1.4 larger than those of PM4Sand, which caused a stiffer ground response of the medium sand layer within the slope. This resulted in an equally stronger motion at the deck and smaller lateral ground displacements. However, for the highest input intensity, ground shaking was sufficiently strong to overcome the cyclic resistance inside the slope, leading to a lateral spreading mode of deformation that PM4Sand predicted for a lower level of shaking.

All the above resulted in larger estimates of seismic demands at the in-ground sections of the trailing pile (i.e., around the interface between liquefiable and non-liquefiable soils) when using PM4Sand, whereas the demands obtained at the pile-deck level were comparable between the two models, albeit SDm produced slightly larger estimates. The results of the multiple stripe analysis aim to add robustness to these observations.

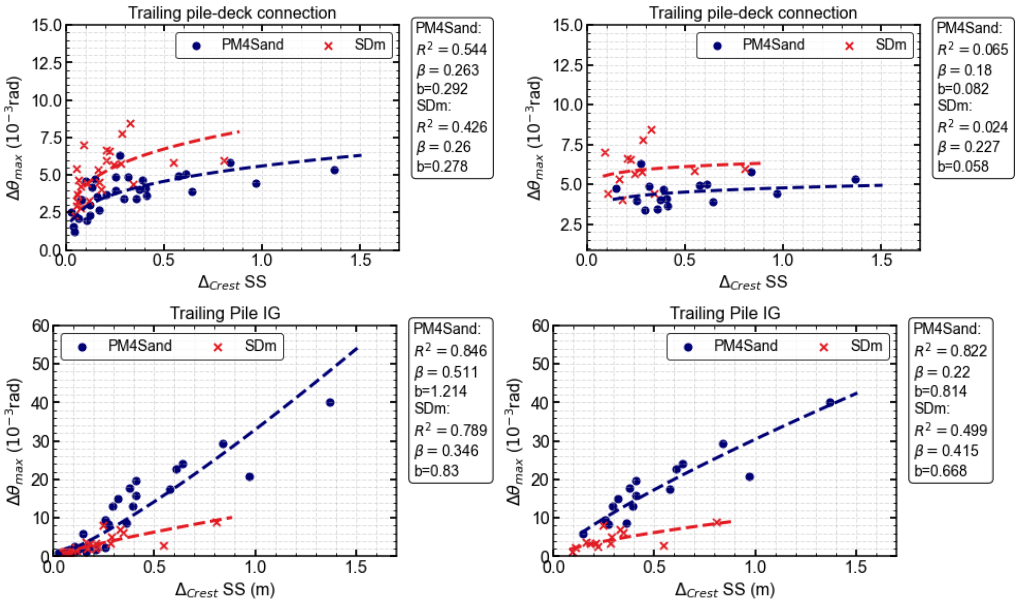

Figure 5.10 shows scatter plots between $\Delta\theta_{max}$ recorded at PD and IG nodes against estimates of Δ_{crest} obtained from the SS simulations. The panels to the right show results only for those cases in which liquefaction triggered inside the medium sand. Those on the left show the complete set of results.

The regression analysis between ground displacements and seismic demand of the pile-deck section ($\Delta\theta_{max}$ PD) indicates that kinematic DSSI effects played a non-negligible role. Once liquefaction triggered in the medium sand and post-liquefaction strains develop in the case of PM4Sand, the response at the pile-deck level became insensitive to the magnitude of the lateral ground deformation. Moreover, considering that the yield curvature is approximately $\Delta\theta_y = 4.29x10^{-3}$ rad, the correspondence between $\Delta\theta_{max}$ PD and Δ_{Crest} is only apparent for cases in which liquefaction did not trigger and the pile-deck connection remained elastic. This last observation is only valid for PM4Sand, as the stiffer response reproduced by SDm led to a larger correlation between the Δθmax PD and $\Delta_{Crest,,}$ yet as in the case of PM4Sand, the relationship tends to a flat slope for larger displacements. This is because with stronger earthquake excitation the cyclic component of ground deformation reduces relative to the lateral spreading component, hence lateral spreading deformations become less influential on the response at the deck.

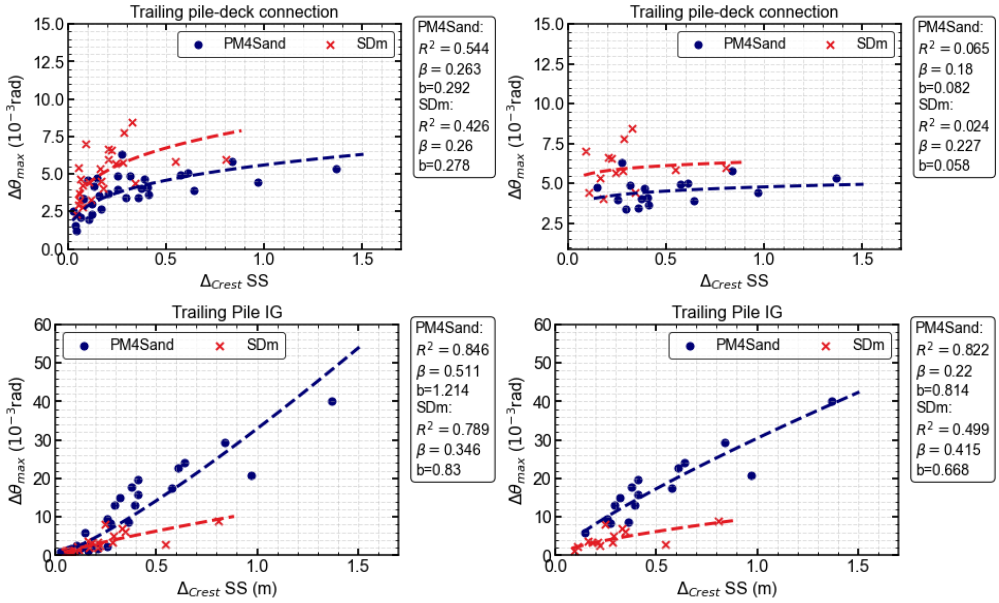

Figure 5.10. Regression analysis for maximum relative rotation at the PD (top) and IG (bottom) sections of the trailing pile, against the horizontal residual displacement of the crest obtained from SS simulations. Figures to the right show results only for the simulations that triggered liquefaction of the medium sand.

All the above is in-line with the well-accepted assumptions (Cubrinovski et al., 2009; Tokimatsu and Asaka, 1998) that at the critical loading cycle for the pile-deck section: (1) the inertial demand is the highest, (2) it is in-phase with cyclic ground deformations, and (3) it is unrelated to lateral spreading deformations.

Bearing the above considerations and after examining the demands at the IG sections (bottom panels of Figure 5.10), one could state that the demarcation between cyclic and lateral spreading displacements occurred at approximately $\Delta_{Crest\ SS}$= 0.25 m. Below this level, IG sections remained mostly elastic while PM4Sand and SDm yielded comparable estimates, although SDm indicates that liquefaction triggered for some in these cases. For larger displacements PM4Sand predicts a steeper evolution of pile curvature than SDm, still both models indicate equally high levels of correlations between the peak response at the in-ground sections and the residual displacement of the crest.

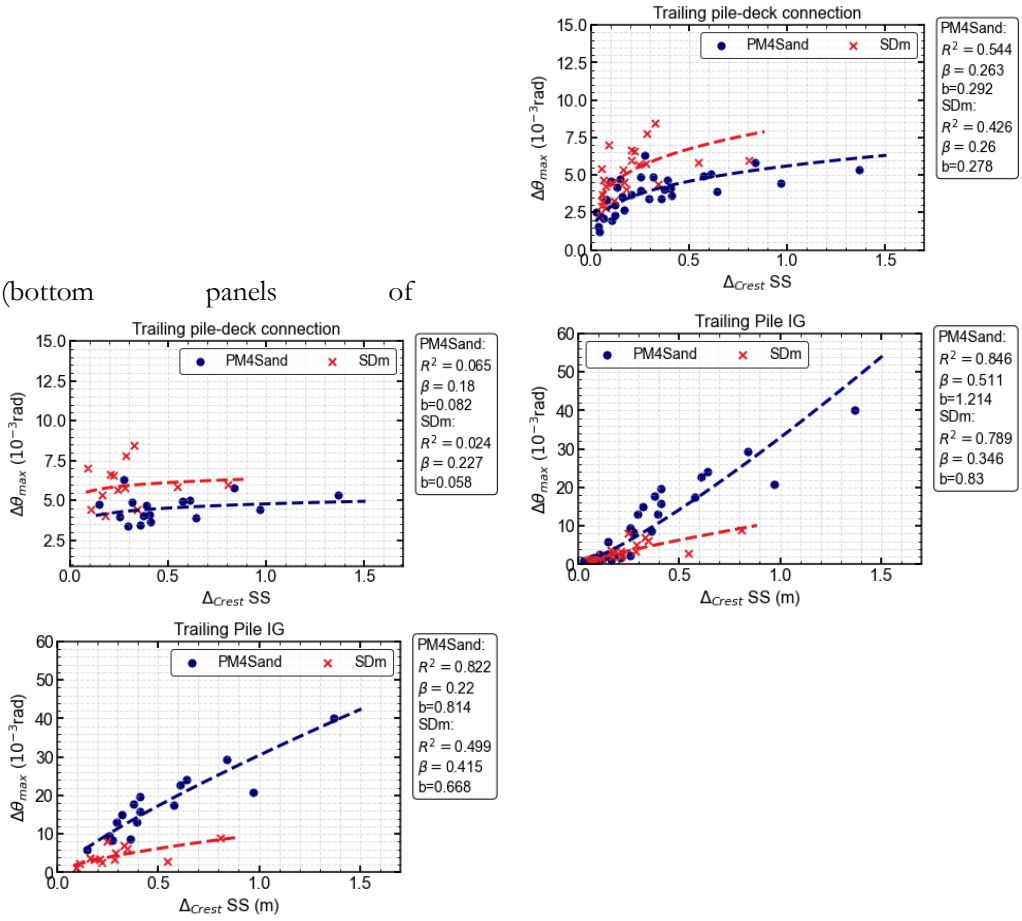

5.5.2.1 *Uniform and non-uniform lateral spreading displacements.*

As mentioned in previous chapters of this thesis, and elsewhere (Ishihara et al., 1997), liquefaction-induced lateral spreading displacements can be decomposed into their uniform and non-uniform components. The latter refers to the ground distortion that increases in

magnitude and severity as one moves closer to the waterfront. The former relates to the residual lateral displacements that takes place far inland from the wharf. Consequently, the response parameter $\Delta_{Lateral}$ is a measure of the non-uniform lateral spreading ground distortion reproduced by the numerical simulations near the wharf.

To underscore the sensitivity of the estimated demands of the trailing pile with respect to the total and non-uniform lateral spreading displacements, Figure 5.11 shows scatter plots between $\Delta\theta_{max}$ recorded at PD and IG nodes against Δ_{crest} (left panels) and $\Delta_{Lateral}$ (right panels) obtained from the SS simulations. Note that Figure 5.11 includes the data from the simulations that reported liquefaction of the medium sand only. The seismic demands at PD exhibited equivalent trends with Δ_{crest} and $\Delta_{Lateral}$. In contrast, the cases for the IG nodes show that Δ_{crest} is a better predictor of $\Delta\theta_{max}$ than $\Delta_{Lateral}$. However, these results are partial, as the uniform component of lateral spreading (i.e., the residual displacement computed far away of the wharf, within the 2D finite difference model) is likely to be more affected by the lateral boundary.

For severe cases of liquefaction-induced lateral spreading, the efficiency of the lateral boundary, modelled according to Lysmer and Kuhlemeyer (1969), diminishes. The extend of the effect of the lateral boundary on the accuracy of the displacements computed at the crest remains uncertain Therefore, in the absence of observational data from real events, it is necessary to verify the robustness of the modelling strategy by comparing the results against those obtained using a so-called *reflected model*. Instead of modelling the lateral boundary as a compliant system through a viscous dashpot, the reflected model consists in a larger model comprised by the main finite difference grid extended for an additional 100 m and mirrored in the opposite direction. More details about the modelling considerations and results obtained with the reflected model can be found in Appendix A.2.

Figure 5.12 depicts the comparison between the lateral displacement distributions obtained with the SS and SS-reflected models for the input motions No 4,5, and 6 for T_R=2475 yr (see Table 5.1). The results were obtained by modelling the liquefiable layers with PM4Sand. At the crest, the comparison between the SS and SS-reflected simulations indicate that the effect of the lateral boundary is limited.

There is no agreement among the SS and SS-reflected results about the uniform component of lateral spreading, which is likely to be affected differently by the two models. The lateral boundaries of the former would not provide sufficient restraint for large displacements, while in the latter, the ground closer to the midpoint of the model could be pulled in the opposite direction by the reflected half.

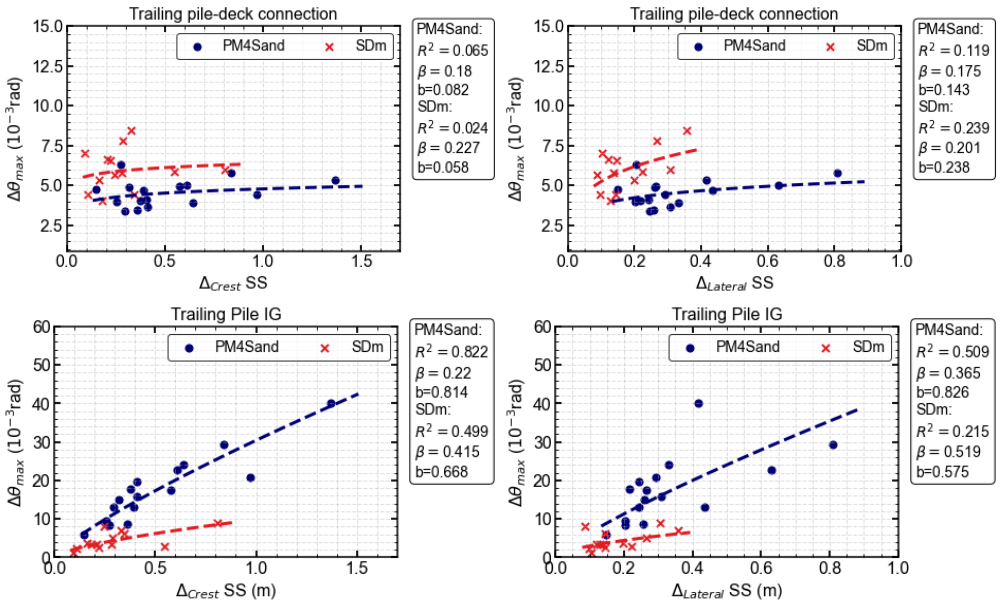

Figure 5.11. Regression analysis for maximum relative rotation at the PD (top) and IG (bottom) sections of the trailing pile, against the residual and lateral displacement of the crest obtained from SS simulations. Results correspond to the simulations that triggered liquefaction of the medium sand.

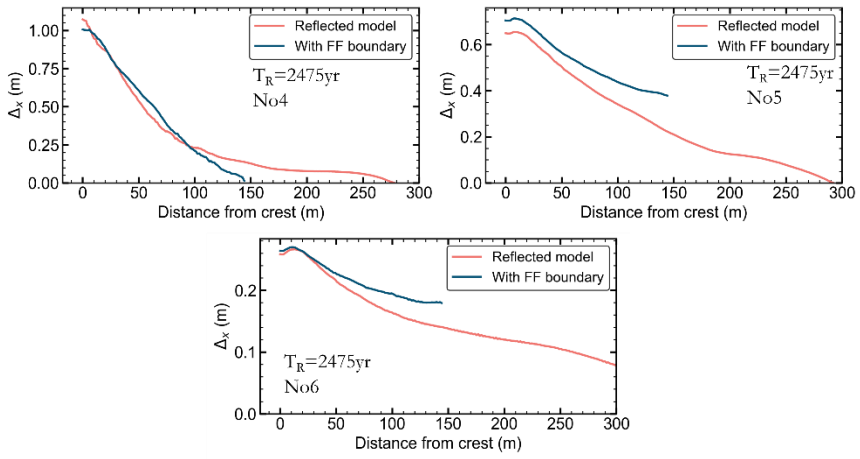

Figure 5.12. Comparison between the results obtained using the SS model with free-field lateral boundary and SS reflected models with PM4Sand, for the input motions number 4, 5 and 6 of T_R=2475yr.

5.5.2.2 *Seismic demands vs cyclic ground deformations.*

One fundamental assumption is that maximum seismic demands at the pile cap level (i.e., node PD) occur during the cyclic phase of motion (i.e., before the development of liquefaction induced-lateral spreading displacements). During this phase, the peak inertial loads transmitted by the deck are accompanied by cyclic ground deformations (Tokimatsu et al., 2005).

For design methodologies using equivalent static procedures, Bowen and Cubrinovski (2008) and Tokimatsu and Asaka (1998) suggested the application of (1D) free-field ground displacements along the pile length, while assigning an equivalent lateral force at the pile cap to represent the inertial demand. Ground displacements are computed as the integral of the estimated maximum cyclic shear strains with depth, equivalent to the parameter LDI_{ESA}. Such approach aims at estimating peak seismic demands during the cyclic phase of shaking. For the lateral spreading phase, authors recommend the application of lateral spreading ground displacements along the pile length, without considering the inertial force. Thus, the rationale driving this procedure makes distinction between two seismic designs, one for the cyclic, and one for the lateral spreading phase.

In contrast, the seismic design guidelines proposed by Ashford et al. (2011) make distinction between cases of no-liquefaction and liquefaction. For the former, simplified analysis should consider inertial forces only, while considering both lateral spreading displacements and inertial loads for the latter. These guidelines recommend modifying the inertial demands according to the ground response.

Without discussing the merits of the methodologies mentioned above, this section aims at testing one assumption they both make. That is, the influence of the ground response on the seismic demands that take place during the cyclic phase of the system response, or, viewed from an equivalent perspective, its effect on the inertial demands.

Previous section showed that the seismic demand at the node PD is controlled by the inertial loading of the deck and that it is insensitive to lateral spreading ground deformations. It is now worth making a similar analysis with respect to the cyclic ground response represented by LDI_{ESA}. To that end, Figure 5.13 illustrates the regression analysis conducted on the pairs $\Delta\theta_{max}$ PD - LDI_{ESA}, and Vmax - LDI_{ESA}.

Results corroborate the assumed relationship between cyclic ground response and peak inertial demands at node PD. First, correlation coefficients between $\Delta\theta_{max}$ and LDI_{ESA} were found between 65% and 75%, with relatively low model dispersion ($\beta \approx 0.2$). Second, PM4Sand and SDm resulted in remarkably similar trends, considering that both models reproduced significantly different system response in terms of lateral spreading displacements.

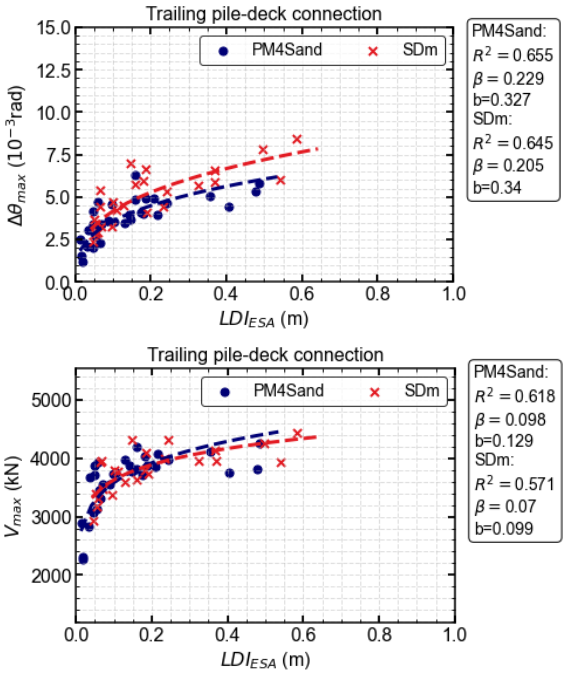

Figure 5.13 Regression analysis between inertial demand and load parameters and LDI_{ESA}.

The second aspect to consider during simplified assessments concerns the estimation of kinematic loads in the form of lateral spreading displacements. In this case, simplified methodologies would also rely on empirical 1D response parameters, in terms of maximum strains (Tokimatsu and Asaka, 1998; Zhang et al., 2004) or other relationships (Youd et al., 2002), to conservatively estimate lateral spreading displacements without resorting to 2D effective stress simulations.

The assumption that 1D ground response could explain or could constitute a basis for estimating lateral spreading displacements is hereby tested by examining the relationship of Δ_{Crest} and $\Delta_{Lateral}$ with LDI_{ESA}. Results are depicted in Figure 5.14. In this case the analysis considers the results from FF simulations to isolate them from the response of the wharf. Cases of no-liquefaction are represented by black markers. As it can be noted, results are significantly scattered, or at least they are not sufficient to establish a clear trend. Differences between PM4Sand and SDm are also evident, as the former predicted Δ_{Crest} - LDI_{ESA} ratios of 2 to 3 folds, whereas for SDm results are distributed between ratios of 1:1 and 2.5:1.

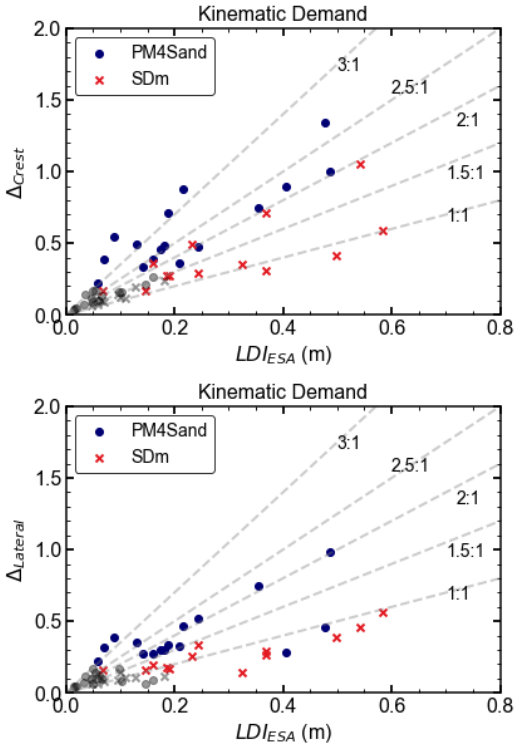

Figure 5.14. Scatter plots between Δ_{Crest} and $\Delta_{Lateral}$ vs LDI_{ESA} computed from the FF simulations.

The scatter in Figure 5.14 is also explained by the characteristics of the input motions, which were interpreted differently by the constitutive models. In this regard, the following effects were noted:

- *Frequency content*. Strong energy carried at low frequencies caused a thicker layer of soils to liquefy, which translated into lager values of LDI_{ESA}. This was more pronounced during the simulations that employed SDm. With PM4Sand the thickness of liquefied soils was shorter, and post-liquefaction strains tend to be accumulated over a narrow band of elements.
- *Number of intense cycles*. Ground motion with many intense cycles after liquefaction produces larger lateral spreading deformations. This was particularly acute in the case of PM4Sand, as the model predicted a relatively mild 1D response, while the 2D response was more severe because large post-liquefaction strains developed due to the energy transferred to the fluidized materials.
- *Toe failure*. The parameter Δ_{Crest} not only accounts for the response of the liquefiable soils, it is also influenced by the behaviour of the base layer. Large deformations

at the base of the slope were caused by ground motion with important high frequency energy, which is not reflected by $LDI_{ESA.}$

Lastly, Figure 5.15 quantitively summarizes the information presented in Figure 5.14, it shows the distribution of the ratio Δ_{Crest} - $LDI_{ESA.}$ If the predictive potential of LDI_{ESA} were to be accepted, a factor of Δ_{Crest} / LDI_{ESA} equal to 3 would represent a conservative estimate. for LDI_{ESA} >0.2m.

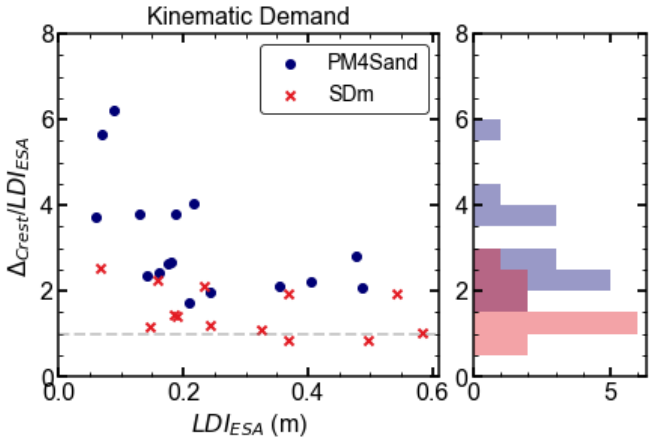

Figure 5.15. Distribution of the cyclic and lateral spreading displacements computed from FF simulations.

5.6 EFFICIENCY AND PROFICIENCY RANKING OF GROUND MOTION INTENSITY MEASURES

Seismic demand modelling, within the PBEE framework, requires the seismic hazard and demand models to be expressed in terms of meaningful IM-Rp pairs. Response parameters should be adequate damage indicators and intensity measures should be equally good predictors of those response parameters. However, ground motion characteristics and ground motion variability have different implications on the system response depending on the type of system under consideration and the type of parameter being described. The present section will address the issue of optimal intensity measures for pile-supported wharves, of the same typology of wharf BAF, by identifying the most efficient and proficient IMs according to the methodology outlined in Section 5.2.

The response parameters under examination are: Δ_{Crest}, $\Delta_{Lateral}$, $LDI_{ESA,}$ θ_{max} IG, and θ_{max} PD. The first three parameters are a direct measure of the wharf response and of the response of liquefiable deposits (as per LDI_{ESA} , Cubrinovski and Ntritsos, 2023).The latter two parameters are commonly used by seismic design guidelines and academic publications

to define damage states for wharf structures (e-g., PIANC, 2001; POLA, 2010; POLB, 2012). A comprehensive list of the tested IMs is reported in Table 5.3.

For the parameters θ_{max} IG, θ_{max} PD,

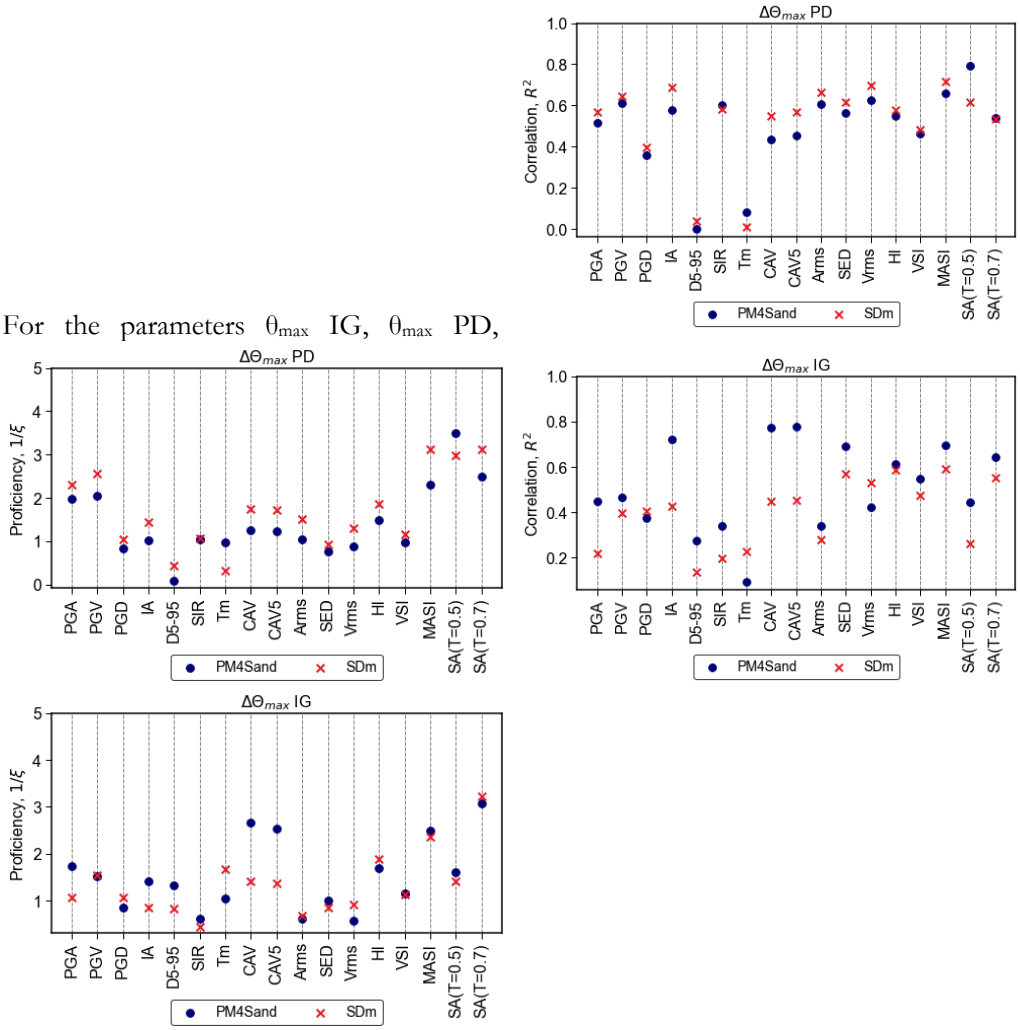

Figure 5.16 shows the performance of these IMs in terms of correlation (R^2) and proficiency, measured by means of the complement of ξ, as defined by Eq(5-8). Likewise,

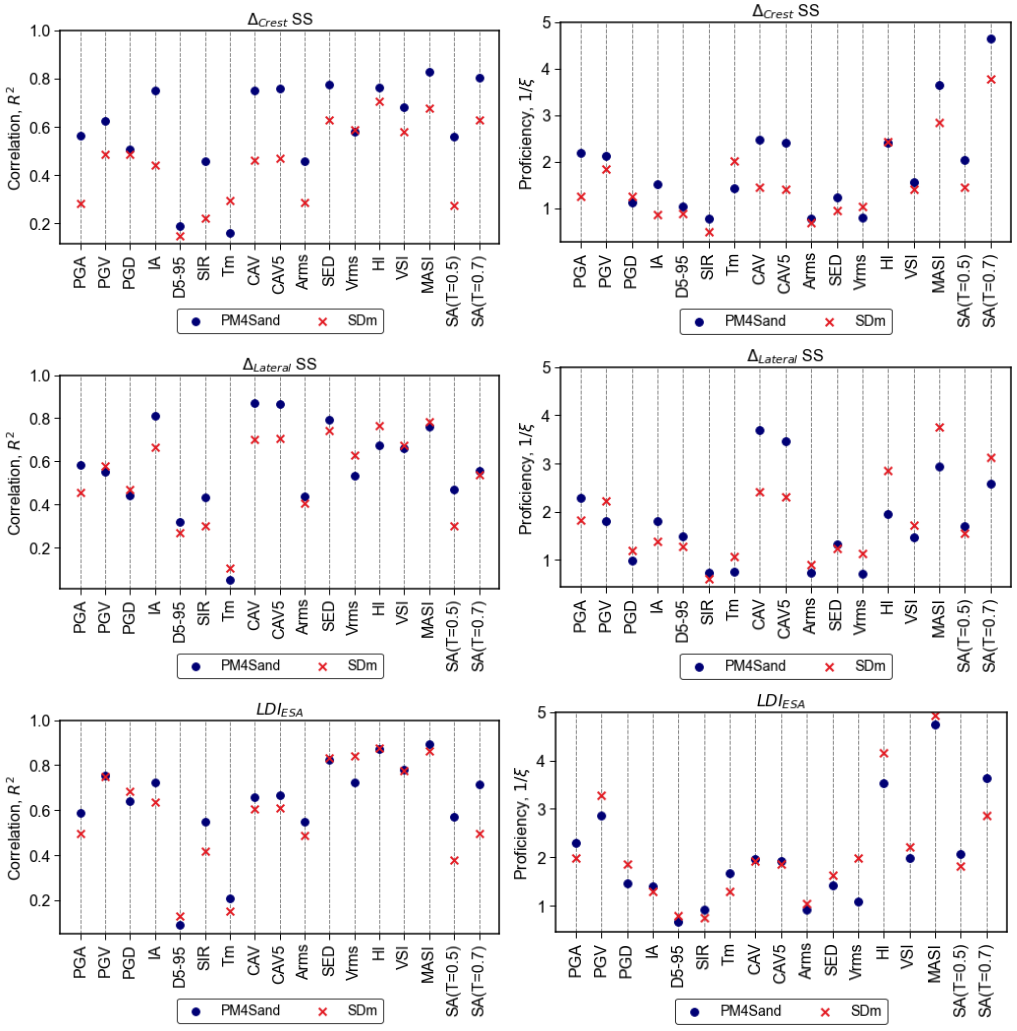

Figure 5.17 shows results for the system response parameters Δ_{Crest}, $\Delta_{Lateral}$, and LDI_{ESA}.

The final ranking of the most efficient and proficient IMs is presented in Table 5.4. As anticipated, different IMs controlled different response parameters, while results from PM4Sand and SDm also highlight different set of optimal IMs. Nonetheless, two IMs consistently ranked among the most efficient for the response parameters and for both constitutive models. These were the specific energy density, SED (Wang et al., 2018), and the modified acceleration spectrum intensity, MASI (Cubrinovski and Ntritsos, 2023). However, the former displayed lower of values of the coefficient *b*, which reduced is practicality and proficiency. Opposite to MASI, which ranked consistently among the four most proficient.

There is one additional key detail worth mentioning, that is the high relative dispersion (i.e., low efficiency) all the IMs exhibited with respect to θ_{max} IG. As an alternative, damage and fragilities models could be defined in terms of Δ_{Crest} or $\Delta_{Lateral}$, which are also directly related to the severity of the lateral spreading displacements on the wharf. Lastly, it is worth noting that the present study is not exhaustive, as the IMs ranked in Table 5.4 still need to be tested for sufficiency and hazard computability.

Table 5.3. Intensity measures tested for efficiency and proficiency.

Intensity Measure	Definition
Peak ground acceleration (m/s²)	$\mathrm{PGA} = \max\lvert a(t)\rvert$ Where $a(t)$ is the acceleration time history
Peak ground velocity (m/s)	$\mathrm{PGV} = \max\lvert v(t)\rvert$ Where $v(t)$ is the velocity time history
Peak ground displacement (m)	$\mathrm{PGD} = \max\lvert d(t)\rvert$ Where $d(t)$ is the displacement time history
Arias Intensity	$\mathrm{Ia} = \frac{\pi}{2g}\int_0^{t_{tot}} a(t)^2 dt$
Significant duration between 5% and 95% of Arias Intensity	$D_{5-95} = t_{5-95} = t_{95\%} - t_{5\%}$
Shake intensity rate between 5% and 95% of Arias Intensity (Ghayoomi and Dashti, 2015)	$\mathrm{SIR} = \frac{Ia_{75\%} - Ia_{5\%}}{t_{5-75}}$
Mean period (Rathje et al., 1998)	$\mathrm{Tm} = \frac{\sum\left(\mathrm{FAS}(f_i)^2 \frac{1}{f_i}\right)}{\sum \mathrm{FAS}(f_i)^2}$

Intensity Measure	Definition
Cumulative absolute velocity	$\mathrm{CAV} = \int_0^{t_{tot}} \lvert a(t) \rvert \mathrm{dt}$
Cumulative absolute velocity beyond 0.05 m/s² (Kramer and Mitchell, 2006)	$\mathrm{CAV_5} = \int_0^{t_{tot}} \langle \chi \rangle \lvert a(t) \rvert \mathrm{dt}$ where $\langle \chi \rangle = \begin{cases} 0 \text{ for } \lvert a(t) \rvert < 0.05 \text{ m/s}^2 \\ 1 \text{ for } \lvert a(t) \rvert \geq 0.05 \text{ m/s}^2 \end{cases}$
Root-mean-square (RMS) of acceleration	$\mathrm{A_{rms}} = \sqrt{\frac{1}{t_{5-95}} \int_{t_{5\%}}^{t_{95\%}} a(t)^2 \mathrm{dt}}$
Specific energy density (Wang et al., 2018)	$\mathrm{SED} = \int_0^{t_{tot}} v(t)^2 \mathrm{dt}$
Root-mean-square (RMS) of velocity	$\mathrm{V_{rms}} = \sqrt{\frac{1}{t_{5-95}} \int_{t_{5\%}}^{t_{95\%}} v(t)^2 \mathrm{dt}}$
Housner intensity	$\mathrm{HI} = \int_{0.1}^{2.5} \mathrm{PSV}(\xi = 0.05, T) \mathrm{dT}$
Velocity spectrum intensity (Cubrinovski and Ntritsos, 2023)	$\mathrm{VSI} = \int_{0.1}^{1.5} S_V(\xi = 0.05, T) \mathrm{dT}$
Modified acceleration spectrum intensity (Cubrinovski and Ntritsos, 2023)	$\mathrm{MASI} = \int_{0.1}^{1.5} S_A(\xi = 0.05, T) \mathrm{dT}$

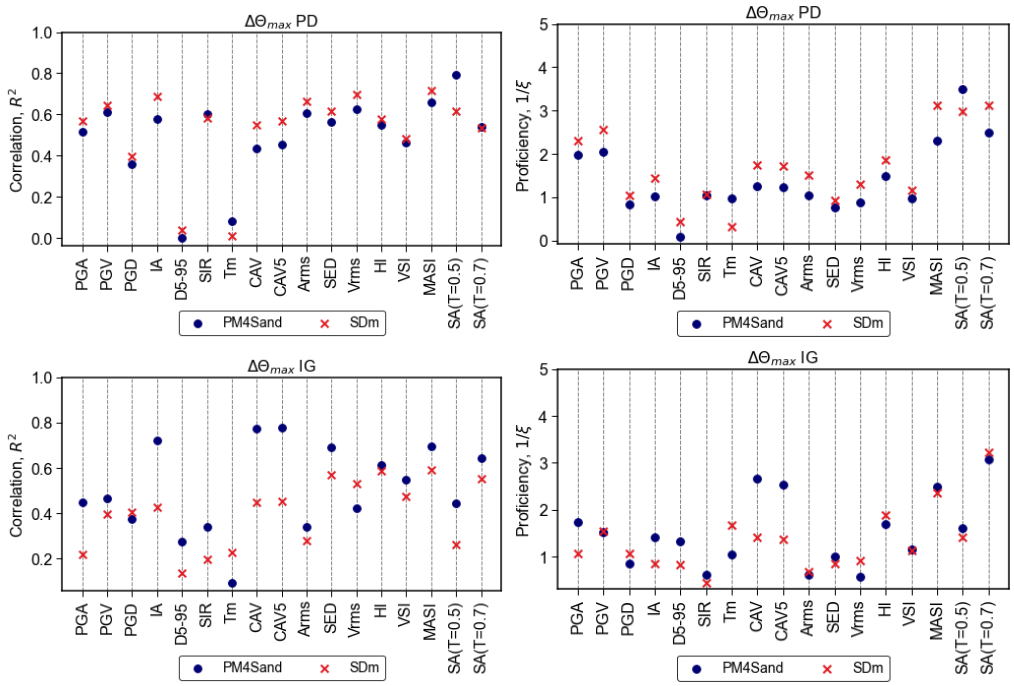

Figure 5.16 Correlation and proficiency of the intensity measures for $\Delta\theta_{max}$ PD and $\Delta\theta_{max}$ IG.

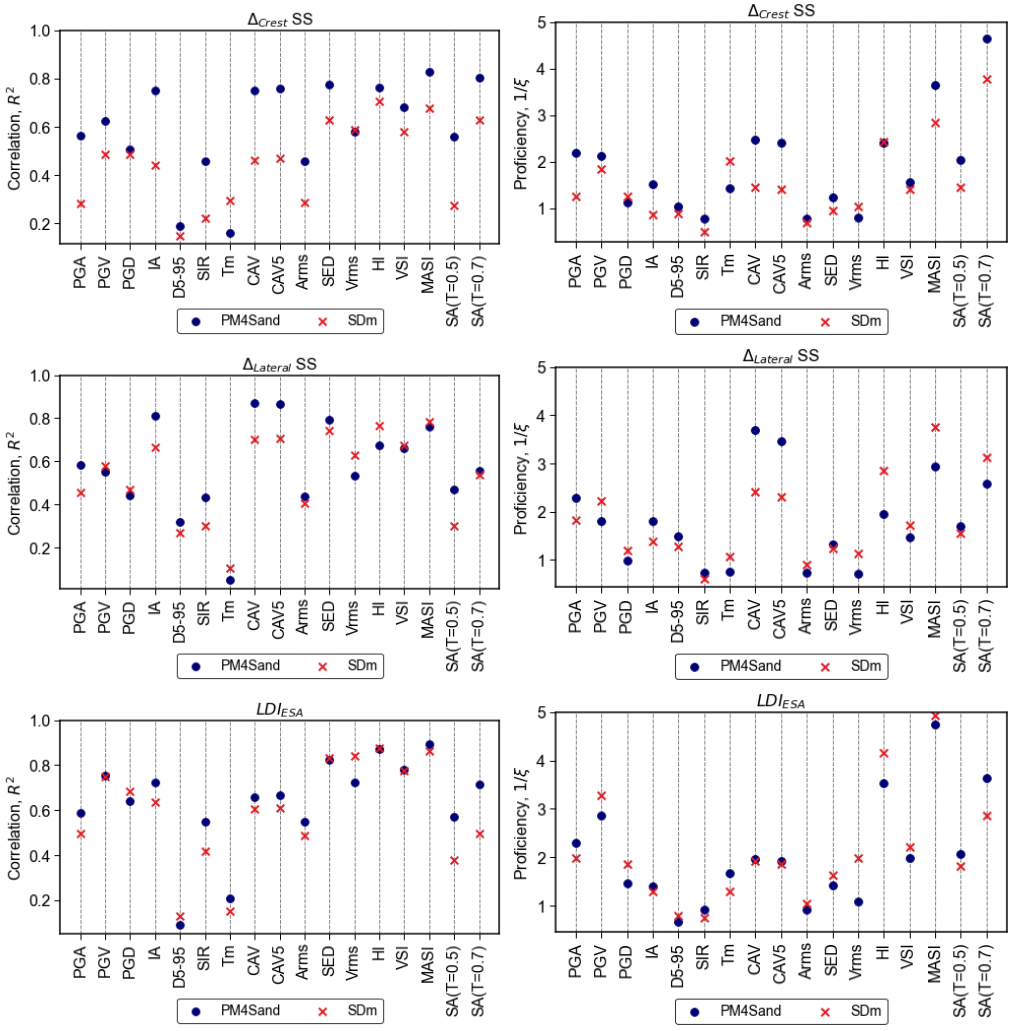

Figure 5.17. Correlation and proficiency of the intensity measures for Δ_{Crest} FF, $\Delta_{Lateral}$ SS, and LDI_{ESA}

Table 5.4. Ranking of efficient intensity measures for the seismic response of wharf BAF.

		PM4SAND				SDm			
Δ_{Crest} SS	IM	MASI	SA(T=0.7s)	SED	HI	HI	MASI	SA(T=0.7s)	SED
	R^2	0.828	0.802	0.775	0.761	0.704	0.678	0.630	0.626
	$\beta_{IM\|Rp}$	0.407	0.437	0.466	0.532	0.439	0.458	0.491	0.493
$\Delta_{Lateral}$ SS	IM	CAV	IA	SED	MASI	MASI	HI	SED	CAV
	R^2	0.868	0.811	0.745	0.725	0.786	0.766	0.741	0.706
	$\beta_{IM\|Rp}$	0.331	0.375	0.437	0.454	0.287	0.300	0.316	0.336
$\Delta\theta_{MAX}$ IG	IM	CAV	IA	MASI	SED	MASI	HI	SED	SA(T=0.7s)
	R^2	0.774	0.722	0.692	0.691	0.592	0.588	0.569	0.553
	$\beta_{IM\|Rp}$	0.617	0.684	0.720	0.722	0.481	0.484	0.492	0.504
$\Delta\theta_{MAX}$ PD	IM	SA(T=To)	MASI	HI	PGV	MASI	Vrms	IA	PGV
	R^2	0.791	0.659	0.626	0.612	0.717	0.696	0.686	0.646
	$\beta_{IM\|Rp}$	0.178	0.227	0.293	0.242	0.0.182	0.189	0.192	0.204
LDI_{ESA}	IM	MASI	HI	SED	VSI	HI	MASI	Vrms	SED
	R^2	0.891	0.873	0.822	0.780	0.874	0.863	0.842	0.830
	$\beta_{IM\|Rp}$	0.227	0.261	0.257	0.285	0.289	0.301	0.324	0.336

[1] Light blue shade indicate that the IM ranked among the top four most proficient.

[2] To is the fundamental, elastic period of the wharf.

5.7 SUMMARY AND DISCUSSION.

This study dealt with the probabilistic seismic response and demand analysis of wharf BAF, of the port of Gioia Tauro. The study consisted in examining the results obtained from a multiple stripe analysis of 2D effective stress DSSI simulations, performed with PMSand and SDm in parallel. The analysis focused on the seismic demands estimated for the trailing pile of the wharf at the pile-deck level section (PD), and at the sections located within the liquefiable deposit, denoted as in-ground sections (IG).

With few exceptions, PM4Sand and SDm indicated that liquefaction occurred within the medium sand for T_R>475 yr. IG sections remained elastic for $T_R \leq 475$ yr. PD sections reached their yield capacity for $475 \leq T_R \leq 975$. For longer return periods, peak inertial

loads remained constant on average. This highlights the effect the wharf capacity on the inertial demands estimated at sections PD. In fact, the comparison of V_{max} with force-based and displacement-based estimates for the peak shar load at the deck, indicated that the former lead to overconservative estimates, 1.5 to 2.5 times larger than the recorded force. However, force-based estimates were reasonable agreement with V_{max} for the cases in which the piles remained elastic (i.e., for low return periods) This in-line with the recommendation given by the design guideless, which discourage the use of force-based methods for the assessment of design inertial loads.

Inertial and kinematic demands were unrelated for $T_R > 475$ yrs, coinciding with the demarcation between cases of liquefaction and no-liquefaction. Seismic demands at the IG nodes were insensitive to the inertial movement of the wharf's deck. Inertial demands, characterized by V_{max} and $\Delta\theta$max PD, were uncorrelated to the lateral spreading displacements generated by the input motions that triggered liquefaction within the medium sand. In this cases, maximum relative rotations recorded at the IG nodes were one order of magnitude greater than those at the pile-deck connection. Thus, seismic demands recorded at node PD were regarded as inertial demands. This is confirmed by the fact that PM4Sand and SDm produced comparable estimates for these demands.

The above observations Indicate that the cyclic response of the system controlled the seismic demands obtained for $T_R \leq 475$ yrs. Seismic design for this condition, in the absence of lateral spreading, could consider the use of force-based method for estimating inertial demands, although displacement base methods would yield more economical designs. Results also indicate that, within the framework of BNWF, kinematic demands could be represented by the distribution of ground displacements obtained from the estimated profile of cyclic strains, as recommended by Cubrinovski et al. (2009) and Tokimatsu and Asaka (1998). Note that cyclic strains are estimated from 1D response analyses.

The situation would be different in cases of lateral spreading, as the design inertial load for the cyclic phase of motion should be obtained from displacement-base methods only. On the other hand, a separate verification should be made considering lateral spreading displacements without any inertial load. In this case, the predictive capability of 1D analyses, as indicated in this study, is more limited. The comparison between LDI_{ESA} and the lateral spreading parameters Δ_{Crest} and $\Delta_{Lateral}$ exhibited a large scatter. PM4Sand and SDm resulted in different trends between the 2D and 1D response parameters, aggravated by the input ground motion variability, which was interpreted differently by the two models. If the predictive potential of LDI_{ESA} were to be accepted, a factor of Δ_{Crest} / LDI_{ESA} equal to 3 would represent a conservative estimate for the lateral spreading displacements, provided that LDI_{ESA} >0.2m.

In comparing the predictive capability of Δ_{Crest} and $\Delta_{Lateral}$ for $\Delta\theta_{max}$, one key limitation of the numerical analyses was identified. Three verification analyses were performed with a

so-called reflected model, it consisted in a larger model comprised by the main finite difference grid extended for an additional 100 m and mirrored in the opposite direction. Results indicated that $\Delta_{Lateral}$ the latter is more affected by free-field boundary effects.

In terms of optimal intensity measures, the efficiency and proficiency ranking reported in Table 5.4 indicated that the modified acceleration spectrum intensity MASI, is the most suitable candidate for an optimal intensity measure as in resulted in large correlation with all the response parameters considered, while ranking high in proficiency.

6. TREATMENT OF MODEL UNCERTAINTIES FOR 2D EFFECTIVE STRESS ANALYSES: LOCAL VS GLOBAL SENSITIVITY STUDIES.

6.1 INTRODUCTION.

Previous chapter demonstrated the influence of ground motion variability on the seismic response of wharf BAF. Epistemic uncertainty was partially addressed by conducting parallel simulations with two different constitutive models for the liquefiable ground. Model uncertainty is usually addressed, within the framework of probabilistic seismic demand analysis, by treating model parameters as random variables. The application of such methodology for the current modelling approach is impractical, given the high computational burden associated to the effective stress DSSI analyses. However, model uncertainty could be accounted for by randomizing a reduced number of key parameters that are known to have the largest influence on the system response. To that end, sensitivity analyses have proven to pride valuable insights.

The most common type of sensitivity studies for simple, and even complex, mathematical, and numerical models consists in one-at-a-time methods (OAT), such as the well-known "Tornado diagrams". These methods are also referred to as local sensitivity analysis (Saltelli, 2008), as they require to test the model response around a single point in the space of input parameters. For instance, in the case of Tornado diagrams, reference is taken with respect to model response obtained by using the mean (or median) values of model inputs. Local variation of the model output is obtained by changing one parameter individually from a its minimum to maximum values. These values are often represented by the 16th and 84th percentiles in case of normally distributed random variables. This approach poses two major limitations. First, it assumes linearity of the model response around the reference point, obtained by using median values in the case of Tornado diagrams. Second, it neglects higher effects that stem from the interaction among different input parameters.

As opposed to local sensitivity methods, global sensitivity analyses aim at identifying key model parameters by testing the response of the model across the entire space of input parameters. The most versatile and effective global sensitivity analyses are based on variance decomposition methods, which provide estimates of the contribution of each input parameter, and combination of parameters, to the output variance. These indexes are commonly referred as first and higher order sensitivity indices or Sobol' indices as per (Sobol', 2001). These type of sensitivity studies are usually byproducts of a probabilistic analysis of model outputs; hence their application is a posteriori. For instance, using the results of Monte Carlo simulations Cremen and Baker (2021) estimated first-order variance-based sensitivity indices for the seismic loss estimation of 7- and 14-story buildings .Similar indices have been recently included within the uncertainty quantification

module of the NHERI Simulation Center (SimCenter) for structural and geotechnical models (Yi et al., 2023).

This chapter presents a brief and simple comparison between local and global sensitivity analyses of the 1D and 2D free-field response of the site of wharf BAF. Readily, 2D seismic effective stress analyses, as presented in previous chapters, limit the applicability of the most robust, a posteriori, types of global sensitivity analyses, like those performed on the results of Monte Carlo simulations. Instead, this study opted for a simpler method to estimate first-order sensitivity indices including those related to the interaction among a pair of parameters. The method is generalized form of the OAT approaches, referred as to in the literature as the Elementary Effects method or Morris method (Saltelli, 2008). The method is a screening technique, as it provides proxy values of the sensitivity indices that used to rank the input parameters of a model according to their potential contribution to the output variance.

6.2 THE ELEMENTARY EFFECTS METHOD

6.2.1 Variance-based sensitivity indices

The importance that a given input parameter X_i has on a numerical model that yields the outcome Y can be deduce by examining the conditional variance of Y on a given value of X_i. The conditional variance of the outcome Y on X_i is denoted as $V_{X_{\sim i}}$, it is calculated as the variance of Y at $X_i = x_i^*$:

$$\mathrm{V}_{\mathrm{X}_{\sim \mathrm{i}}} = \mathrm{V}(\mathrm{Y} \mid \mathrm{X}_{\mathrm{I}} = \mathrm{x}_{\mathrm{i}}^{*}) \tag{6-1}$$

It is therefore reasonable to assume that small values of $V_{X_{\sim i}}$ signal a high relative importance of X_i. However, as it might be evident for the reader, the inherent weakness of this approach is the non-uniqueness of the result due to the choice of x_i^*. This drawback is overcome by applying the expectation operator to $V_{X_{\sim i}}$, such that it is computed over the entire space of X_i.

$$\mathrm{E}\left(\mathrm{V}_{\mathrm{X}_{\sim \mathrm{i}}}\right) = \mathrm{E}\left(\mathrm{V}_{\mathrm{X}_{\sim \mathrm{i}}}(\mathrm{Y} \mid \mathrm{X} = \mathrm{x}_{\mathrm{i}}^{*})\right) \tag{6-2}$$

Figure 6.1b illustrates schematically the concept behind Eq(6-2). Likewise, one could apply the same reasoning for the conditional expectation of $\mathrm{E}_{\mathrm{X}_{\sim \mathrm{I}}}$, as schematized in Figure 6.1a. This reasoning leads to the total variance identiy:

$$\begin{gathered} \mathrm{E}(\mathrm{V}(\mathrm{Y} \mid \mathrm{X}_{\mathrm{I}} = \mathrm{x}_{\mathrm{i}}^{*})) + \mathrm{V}(\mathrm{E}(\mathrm{Y} \mid \mathrm{X}_{\mathrm{I}} = \mathrm{x}_{\mathrm{i}}^{*})) = \mathrm{V}(\mathrm{Y}) \\ \mathrm{E}\left(\mathrm{V}_{\mathrm{X}_{\sim \mathrm{i}}}\right) + \mathrm{V}\left(\mathrm{E}_{\mathrm{X}_{\sim \mathrm{i}}}\right) = \mathrm{V}(\mathrm{Y}) \end{gathered} \tag{6-3}$$

Thus, X_i can be singled out as a relevant input parameter provided that the value of $E(V_{X_{\sim i}})$ is small or $V(E_{X_{\sim i}})$ is large. The latter is referred as the first-order effect of X_i on Y and it is used to compute the (first-order) sensitivity index (or Sobol' index) S_i.

$$S_i = \frac{V(E_{X_{\sim i}})}{V(Y)} \tag{6-4}$$

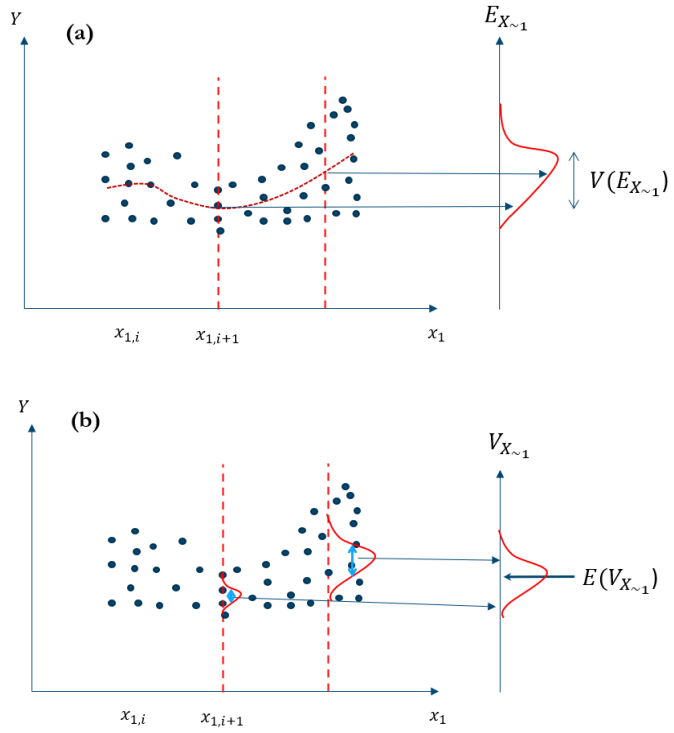

Figure 6.1. Conceptual representation for the variance decomposition of the model output Y expressed by Eq(6-2)(6-3) and Eq(6-3) .

6.2.2 The elementary effects (EE) method

As mentioned in the introduction, the accurate estimation of S_i requires many realizations to capture the actual variance of the model output V(Y), which is impractical for the present application. Alternatively, proxies for $V(E_{X_{\sim i}})$ could be use as semi-quatitative indications of the model sensitivity to the input X_i.

Similar to the OAT methods, one could examine local derivatives distributed across the space of X_i (e.g., Na et al., 2008), as schematized in Figure 6.2. These local derivatives are hereby referred as to elementary effects (EE). Exhaustive derivation and explanation of the

method can be found in Saltelli, (2008) and in Feng et al. (2019). In the latter reference the authors proved the analytical link the outputs of the EE method and the variance-based sensitivity indices S_i

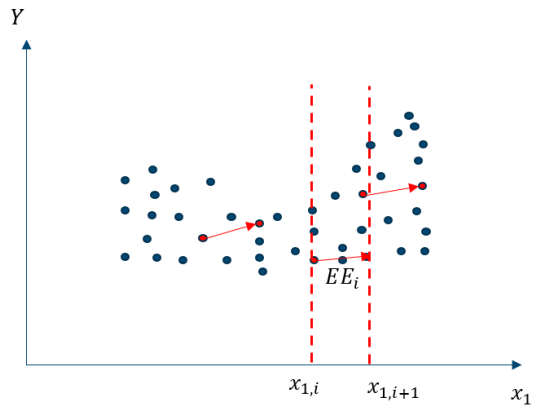

Figure 6.2. Schematic representation of the elementary effects (EE) method.

For a model with independent input parameters X_i for $I = 1, 2, \ldots, k$, a gridded sample space Ω is constructed at p levels for each X_i. For a given value of X_i found in p, the elementary effect on the output Y is defined as:

$$\mathrm{EE_i} = \frac{\mathrm{Y(X_1, X_2, \ldots, X_i + e_i\Delta, \ldots, X_k) - Y(X_1, X_2, \ldots, X_I, \ldots, X_k)}}{\Delta} \tag{6-5}$$

Each level p is related to a given percentile, such that Δ represents the difference in terms of the percentiles corresponding to $X_i + e_i\Delta$ and X_i. The distribution F_i, of the elementary effects EE_i of parameter X_i, can be estimated by randomly sampling the grid space Ω, comprised by p levels of percentiles. The mean and standard deviation of F_i (μ and σ) can therefore be interpreted as sensitivity measures of Xi on Y.

$$\mu_i = \mathrm{E(EE_i)} \cong \frac{1}{r}\sum_{j=1}^{r} \mathrm{EE_i}$$
$$\sigma_i^2 = \mathrm{V(EE_i)} \cong \frac{1}{r-1}\sum_{j=1}^{r} (\mathrm{EE_i} - \mu)^2 \tag{6-6}$$

A large value μ_i indicates that the model output Y is highly sensitive to the input parameter X_i. The variance σ_i^2 contains information about higher order effects, as it signals a large variation among the EE of X_i. In other words, when μ_i and σ_i^2 are high, signifies that, despite Y being sensitive to X_i, other parameters are influencing the model response.

Finally Saltelli (2008) proposed a modification to the method, by considering the distribution of the absolute values of EE, and proposed the sensitivity index μ_i^*, expressed in Eq(6-7). This modification allows the calculation of elementary effects produced by changing more than one parameter at a time, thus serving as a higher order sensitivity measure.

$$M_i^* = E(|EE_i|) = \frac{1}{r}\sum_{j=1}^{r}|EE_i| \qquad (6\text{-}7)$$

6.2.2.1 *Sampling strategy.*

The objective of the sampling strategy is to randomly generate a given number r trajectories of elementary effects over the input space Ω, spread as much as possible from each other. As illustrated by the schematic of Figure 6.3. A single trajectory of k parameters is comprised by k+1 vectors of inputs. The first vector x^* is generated by producing a random realization of each input parameter, among the number levels p considered. The subsequent vector x_1 is generated from x^* by changing one randomly selected parameter by a positive or negative value of Δ, which is also determined randomly. Vector x_2 is generated in the same fashion from x_1 as schematically illustrated in Figure 6.3.

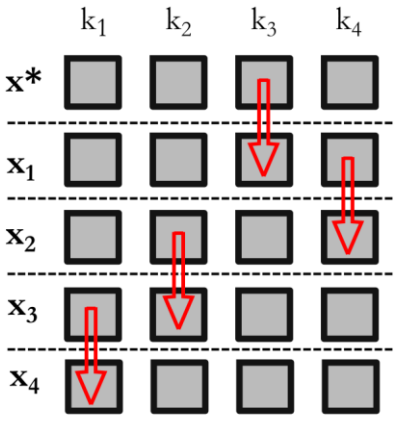

Figure 6.3. Schematic representation of a single trajectory of elementary effects composed by 5 vectors of 4 input parameters.

The distance between a pair of trajectories m and l, for a model with k parameters.

$$D_{ml} = \begin{cases} \sum_{i=1}^{k+1}\sum_{j=1}^{k+1}\sqrt{\sum_{z=1}^{k}[T_z^m(I,z) - T_z^l(j,z)]^2} & \text{for } m \neq l \\ 0 \text{ otherwise} \end{cases} \quad (6\text{-}8)$$

For a set of *r* trajectories, D_{rs}^2 is the sum of squared distances of all the possible pairs among the *r* trajectories, as defined by Eq(6-9). D_{rs} is referred as to the spread of the set of *r* number of trajectories.

$$D_{rs} = \sqrt{\sum_{m}^{r}\sum_{l}^{r} d_{ml}^2} \quad (6\text{-}9)$$

The selection of the "most" spread set of *r* trajectories can be performed by minimization of Eq(6-9). Alternatively, for this study, a random selection process was followed. It consisted in generating a sufficiently large sample of sets of *r* trajectories, selecting the one with the largest spread. Note that, in this case, the number of realizations needs to be large, as one aims at finding the least frequent values of D_{rs}, as illustrated in Figure 6.4, which depicts the distribution for all the trajectories generated for the case study of wharf BAF, by considering 10 input parameters and 5 trajectories.

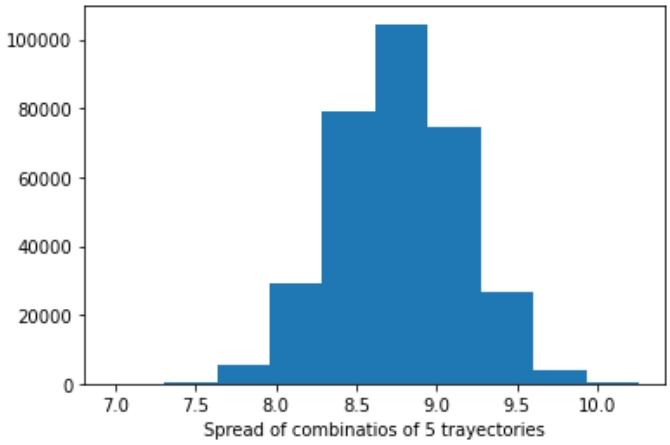

Figure 6.4. Example of the d0istribution of the spread D_{rs} for sets of 5 trajectories of vectors of input parameters with 9 elements.

6.3 APPLICATION CASE: FREE-FIELD RESPONSE OF WHARF BAF.

Deterministic (baseline) and probabilistic seismic response analyses for the wharf BAF of the Port of Gioia Tauro, were presented in Chapters 4 and 5 of this thesis, respectively. The probabilistic analyses of Chapters 5 accounted for the event-to-event variability of the earthquake excitation for different hazard levels. Results clearly indicated that liquefaction-induced lateral spreading was the most important mode of deformation characterizing the system response and controlling the seismic demands on the wharf. Nevertheless, estimates were obtained by using uniform-properties numerical models, without accounting for the uncertainty in their input parameters (e.g., soil properties, boundary conditions, etc).

Treating model parameters as random variables while at the same time considering the interevent variability of the input ground motion was impractical given the size and the complexity in modelling the system response. Notwithstanding, future analyses should, ideally, consider the uncertainty regarding key model parameters and soil properties that influence the magnitude of the lateral spreading displacement. To that end, relevant model parameters were screened using OAT and the EE sensitivity methods, for the 1D and a 2D free-field response (FF models) of wharf BAF. Soil-structure models were not considered, as Chapters 5 demonstrated that the free-field response resulted in comparable or conservative estimates of ground movements.

Figure 6.5 shows a schematic representation of the FF model, it reports the model parameters considered in the sensitivity analysis highlighted in black, and the model outputs in red. Table 6.1 contains a complete description of the model parameters and their respective statistics (i.e., mean and coefficient of variation, CoV). Response (model output) parameters are the residual crest displacement (Δ_{Crest}), lateral residual crest displacement ($\Delta_{Lateral}$) (i.e., residual displacement with respect to the lateral boundary), peak ground velocity (PGV) and peak ground acceleration (PGA) recorded at the surface of the 1D column, and the 1D lateral displacement index LDI_{ESA} computed according to Eq(4-10). Note that soil behaviour for the for the 20 meters of liquefiable materials was modelled using PM4Sand, the model parameters assigned according to the calibration presented in Chapters 4.

Mean values for the soil hydraulic conductivities in Table 6.1 were estimated according to the CPT-based relationship proposed by Robertson and Cabal. (2015), for mean Ic values of 1.5, 1.3 and 1.7, respectively. Hydraulic conductivity varies over a range of several orders of magnitude. The values for CoVs reported in Table 6.1 fall within the range recommended by Baecher and Christian (2003).

The outcropping motion applied at the base of the model was that presented in Chapter 5 for a return period of 975 years with Id of 4.

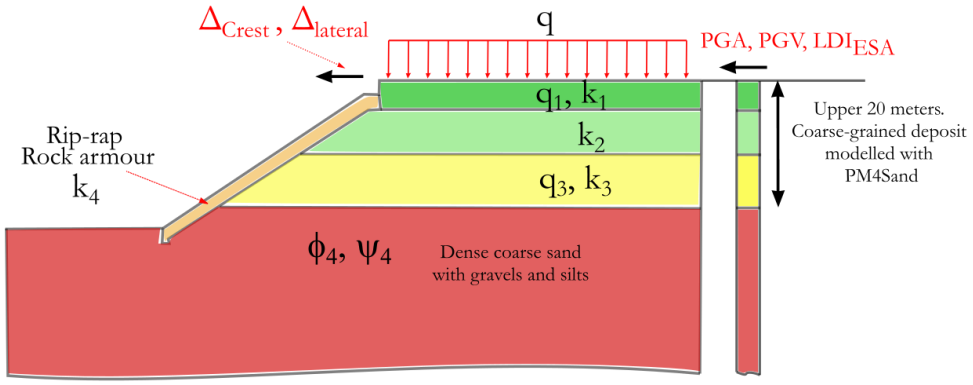

Figure 6.5. Schematic representation of the free-field (FF) model of wharf BAF

Table 6.1. Statistics of the model parameters for the free-field analysis of wharf BAGF.

Parameter	Mean	CoV	Distribution
q_{c1Ncs} for the coarse sand layer (layer 1), q_1	150	35	Lognormal
q_{c1Ncs} for the medium sand layer (layer 3), q_3	135	35	Lognormal
Surcharge on the backland container yard, q	30 KN	40	Uniform
Tangent of the friction angle for the gravelly sand, layer 4, tan(ϕ')	0.753	15	Normal
Angle of dilation for layer 4, ψ	0.2°	100	Uniform
Hydraulic conductivity of the rip-rap (scour protection) layer, k_{rr}	$5x10^{-3}$ m/s	200	Lognormal
Hydraulic conductivity of layer 1, k_1	$2.5x10^{-4}$ m/s	180	Lognormal
Hydraulic conductivity of layer 2, k_2	$1x10^{-3}$ m/s	180	Lognormal

Hydraulic conductivity of layer 3, k_3	$6.85x10^{-3}$ m/s	180	Lognormal
Hydraulic conductivity of layer 4, k_4	$2.5x10^{-4}$ m/s	180	Lognormal

qc1Ncs, normalized clean-sand-equivalent CPT tip resistance.
CoV, coefficient of variation

Regarding the results for the one-dimensional response, Figure 6.6 shows the Tornado diagrams for PGA, PGV and LDI_{ESA}. The dashed redline indicates the response obtained using median values. For each parameter, two simulations were executed using the values corresponding to the 84th and 16th percentiles. In general terms, the diagrams indicate that the normalized tip resistance for the medium danse sand (q_3) controlled the 1D response. In terms of PGA, the hydraulic conductivity of layer 3 and the friction angle of the underlaying layer 4 played an equally important role. For. LDI_{ESA}, the bars of the tornado diagram are not aligned with the response obtained using the median values, this is a manifestation of the non-linearity of the system response. In fact, as it will be later shown, results from the EE analysis indicate that LDI_{ESA} is sensitive to the interaction between different parameters.

Figure 6.7 illustrates the result obtained from the EE analysis for PGA and LDI_{ESA}, they are expressed in terms of the indices μ^* and σ^2. Input parameters are ranked according to μ^*. Results confirm the trend observed in the Tornado diagrams about the high importance of q_3, although with nuances. PGA, besides being determined by q_1, also exhibited a non-negligible dependence on the combined effect of k2 and k3, which ranked second. This means that the high frequency components of surface motion are not only dependent on the permeability of the critical layer (k_3) itself, but even more on the system configuration in terms of distribution of hydraulic conductivities.

For LDI_{ESA}, the influential parameters ranked differently, yet, q_3 ranked first. In this case, the combined effect of the hydraulic conductivities played a secondary or even tertiary role. LDI_{ESA} was mainly affected by the individual variations of q_3, the surcharge q, and the hydraulic conductivity of the top layer. However, examining the relative values μ^*, one could state that q_3 was not as dominant as in the case of PGA. Moreover, several parameters reported high values of σ^2, which indicates that the dispersion of LDI_{ESA} was high when changing the values of q, q_1, and k_3.

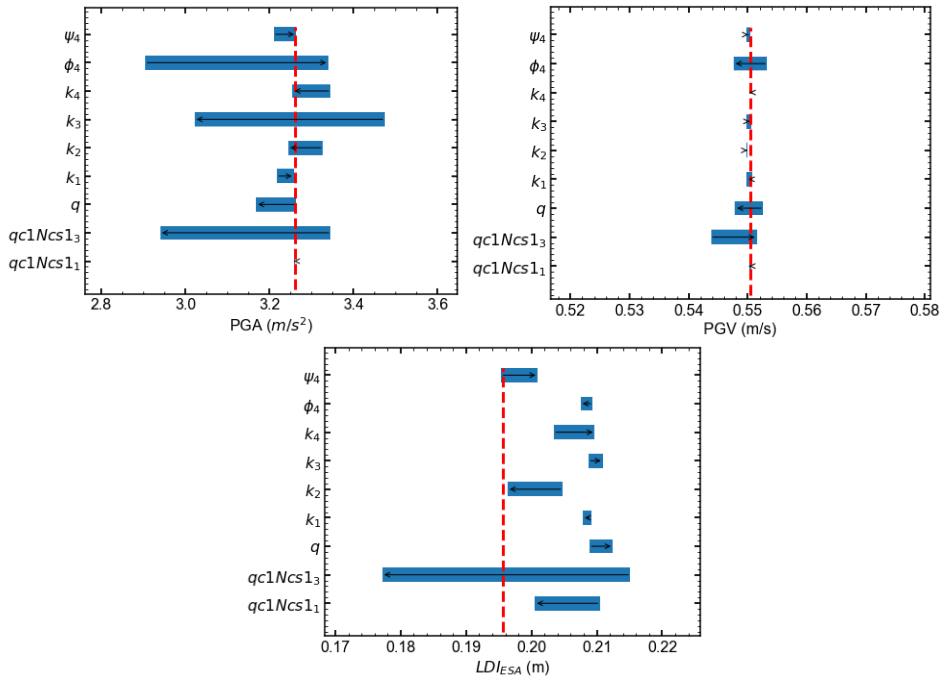

Figure 6.6. Tornado diagrams obtained from the sensitivity analysis of the 1D response of site BAF, using the input motion No 4 for T_R=975 years of Chapter 4.

Figure 6.8 reports the results for the EE analysis of Δ_{Crest} and $\Delta_{Lateral}$. Results of μ^* indicate that Δ_{Crest} was almost exclusively controlled by q_3, however all the other parameters that ranked second or third were related to the distribution of the hydraulic conductivity in the system. Recall that $\Delta_{Lateral}$, measures the lateral spreading distortion that takes place in the zone immediately behind the waterfront. Results for this parameter showed marked differences with respect to those obtained for Δ_{Crest}. The influence of q_3 was comparable to the combined effect of the hydraulic conductivities assigned to the three liquefiable layers and to the riprap (protection layer).

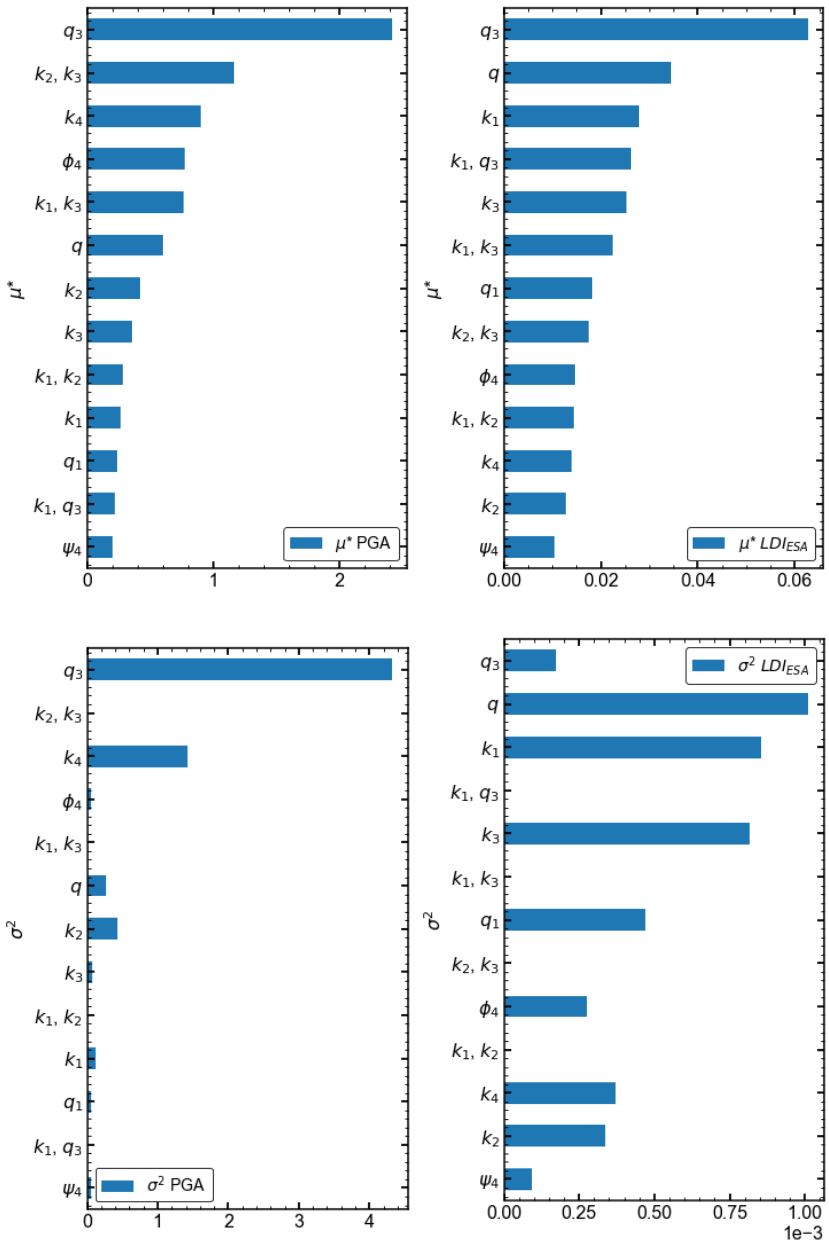

Figure 6.7 Results of the EE sensitivity analysis of the 1D response of site BAF, using the input motion No 4 for T_R=975 years of Chapter 4.

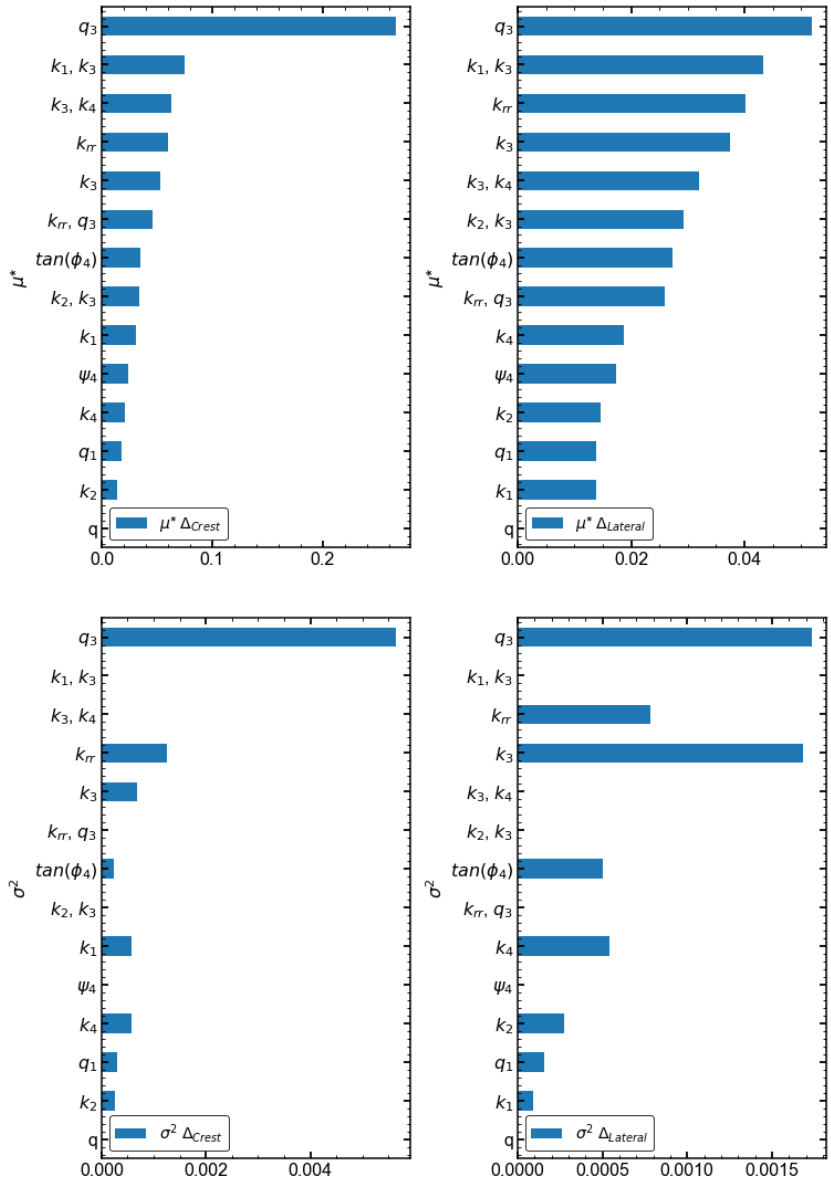

Figure 6.8. Results of the EE sensitivity analysis of the 2D response of site BAF, using the input motion No 4 for T_R=975 years of Chapter 4.

6.4 SUMMARY AND DISCUSSION.

This chapter presented a sensitivity study of the free-field response of wharf BAF, by implemented local and global sensitivity mythologies. For the former, OAT Tornado diagrams were computed for the response parameters obtained from 1D seismic effective stress analyses. The global sensitivity study consisted in the implementation of the EE method proposed by (Saltelli, 2008) on the 1D and 2D responses.

For both the 1D and 2D response parameters were controlled by the clean-sand normalized tip resistance of the medium sand layer (q_3). Tornado diagrams for the response parameter PGA of the 1D response, indicated that the second most important parameter was the hydraulic conductivity of the medium sand. This was also indicated by the EE method, albeit it provided additional insights about. It revealed that the 1D PGA exhibited a non-negligible dependence on the combined effect of k_2 and k_3, which ranked second. This means that the high frequency components of surface motion are not only dependent on the permeability of the critical layer (k_3) itself, but even more on the distribution of hydraulic conductivity of the model.

Results indicated that the response parameter LDI_{ESA} exhibited marked nonlinearity, as per the interaction between input parameters is concerned. Evidence of this was the misalignment of the tornado diagrams with respect to the assumed median response and larger relative values of the sensitivity index σ^2.

In terms of the 2D response, results again indicate a dominant role of q_3. However, all the secondary and tertiary parameters controlling the model response were related to the relative distribution of hydraulic conductivities within the finite difference model.

7. CONCLUSIONS

7.1 GENERAL SUMMARY

This research consisted of a systematic numerical study about the seismic response and seismic demand on piles-supported-wharves founded in liquefiable soils. The numerical modelling methodology involved executing non-linear time-history, 2D, plain strain, effective-stress, dynamic-soil-structure interaction (DSSI) analyses, referred in this documented as to effective stress DSSI analyses. Two different case studies were investigated, the deep waters dock at the Port of Gioia Tauro, located in Southern Italy (wharf BAF), and the Thorndon Container Wharf (TCW) at the Port of Wellington, New Zealand.

The set of analyses performed on TCW served as a verification case for the numerical methodology (Chapter 3), while wharf BAF was the subjected of two different types of studies. The first consisted of an incremental dynamic analysis using a single ground motion record, which aimed at underscoring the main features of the system response (Chapter 4). The second comprised a probabilistic seismic demand analysis aimed at testing current assumptions and recommendations about design procedures, related to the assessment of kinematic and inertial loads on pile-supported-wharves (Chapter 5).

The literature review of Chapter 2 presented an overview of the most notable case histories of earthquake-induced failures of wharves and piers, which were mostly due to liquefaction-induced lateral spreading ground deformations. It also highlighted the lack of consensus among current seismic design guidelines and standards regarding the assessment and combination of kinematic and inertial loads for simplified analysis methodologies. Nonetheless, it was shown that there is wider agreement about the idea that, for cases of lateral spreading, the critical design condition results from combining a portion of the inertial load, between 25% and 50%, with full (100%) kinematic lateral spreading loads.

Chapter 2 also provided an overview of the analytical formulation with focus on two constitutive models, PM4Sand and SDM. The key differences between these models concerns two aspects (1) dilatancy relationship, which determines the rate pore-pressure build-up, and (2) strain-rate characteristics before and after liquefaction. The latter aspect is further elaborated in Chapter 4, as it showed its effects during single element cyclic simple shear simulations, and 1D and 2D effective stress analyses.

Both case studies represent different wharf typology and subsoil conditions. Wharf BAF is supported by 4 rows of large diameter piles (Dp=1.5m) and founded on a native soil deposit comprised by heterogeneous coarse-grained soils. The CPT characterization of the site reported the presence of medium-to-dense sands, liquefiable by composition (i.e., Ic values between 0.9 and 2.0), within the upper 20 meters, idealized as a three-layered deposit

with characteristic q_{c1Ncs} of 155, >200, and 135, from top to bottom. Interbedded layers of stiff coarse sands and gravelly sands were found at greater depths by SPT soundings.

The TCW, at Wellington Centre Port, is a small diameter pile-supported wharf (Dp=0.6). The wharf is found on top of an end-dumped gravelly reclamation with characteristic q_{c1Ncs}=85 and I_c between 2.1 and 2.2. The reclamation is underlaid by a thin layer of marine sediments comprised of sands, clays, and silty clays, which rest on top the 90-135 m thick Wellington alluvion, characterized by interlayered gravels and stiff silts.

Chapter 3 introduced general aspects of the methodology behind the effective stress DSSI analyses, applied for the case study of TCW, at Wellington Centre Port. This chapter showed the main characteristics of the system response linked to the uniform and non-uniform components of the lateral spreading ground deformations. Results obtained from the numerical analyses were in reasonable agreement with the observations made after the Mw 7.8 Kaikōura earthquake. Field measurements after this event indicated that the ground moved approximately 0.8m towards the sea, while the numerical simulations estimated values around 1.2 m.

Chapter 4 presented a systematic examination of the seismic response and performance of wharf BAF at the port of Gioia Tauro, Southern Italy. The study followed the numerical methodology presented Chapter 3. Estimates of the system response were obtained for three different earthquake intensities. This was achieved through the application of a hazard-compatible ground motion record scaled to three (outcropping) PGA levels. To highlight the effects of the epistemic uncertainty about the modelling of the liquefiable soils, Chapter 4 systematically compared the results obtained by using two different constitutive models: PM4Sand (v3.1) developed by Boulanger and Ziotopoulou (2017), and SDm (v1.1) developed by Cubrinovski and Ishihara (1998a, 1998a). These models were calibrated following the CPT-based procedure presented by Ntritsos and Cubrinovski (2020). Residual horizontal displacements, recorded at the crest for the highest input intensity (Ag=0.35g), were estimated at 0.8 m and 0.5 m, by PM4Sand and SDm, respectively. In relative terms, this difference was the result of the larger post-liquefaction strain rate reproduced by PM4Sand, which caused larger concentrations of post liquefaction behind the wharf.

In terms of wharf performance, Chapter 4 presented an overview of the response obtained at the pile-deck and in-ground nodes of the trailing pile. Lateral spreading ground deformations controlled the response of the in-ground section, exhibiting nearly monotonic responses. Consequently, seismic demands at these sections were determined by the ground deformations reproduced by PM4Sand and SDm. Conversely, peak deck accelerations and pile-deck shear force attained similar values for all the intensity levels analysed and for both PM4Sand and SDm analyses. This suggests that the inertial loads exerted on the trailing pile were (1) limited by the capacity provided by the lumped plasticity model and (2) relatively insensitive to the behaviour of the liquefiable ground.

Chapter 5 dealt with the probabilistic seismic response and demand analysis of wharf BAF. The study consisted in a multiple stripe analysis performed by executing 2D effective stress DSSI simulations with a suite of 35 ground motion records, covering 5 return periods. Analyses were performed with PMSand and SDm in parallel. The analysis focused on the performance of the trailing pile of the wharf. Seismic demands were computed at the pile-deck level section (PD), and at the sections located within the liquefiable deposit, denoted as in-ground sections (IG). Clear distinctions were made between the most suitable design considerations for the cyclic and lateral spreading phases of the response.

Chapter 5 also tackled the selection of optimal intensity measures for seismic demand modelling purposes (within the performance-based earthquake engineering framework proposed by Cornell et al., 2002) of large-diameter pile-supported wharves which are typologically similar to wharf BAF. Efficiency and proficiency ranking of the tested IMs revealed that the modified acceleration intensity (MASI) was the most suitable candidate for an optimal IM.

Finally, Chapter 6 presented a sensitivity study of the free-field response of wharf BAF, by implemented local and global sensitivity mythologies. For the former, (OAT) Tornado diagrams were computed for the response parameters obtained from 1D seismic effective stress analyses performed with PM4Sand. The global sensitivity study consisted in the implementation of the EE method proposed by (Saltelli, 2008) on the 1D and 2D responses. Results revealed that, the system response sensitive to the cyclic resistance of the liquefiable soil in first place, and in second place to the distribution of the hydraulic conductivity within the model.

7.2 MAIN CONCLUSIONS

7.2.1 Lateral spreading ground displacements

For both case studies, lateral spreading displacements exhibited a pattern consistent with the observations made by Ishihara et al., (1997), who noted that ground deformations could be separated into non-uniform and uniform lateral spreading components. The former is manifested in the area immediately behind the waterfront, characterized by severe ground distress. The latter is found further inland from the waterfront, where the ground would still exhibit a constant lateral residual displacement, and liquefaction-induced damage would be mainly due to settlements or loss of bearing capacity.

The numerical simulations for wharf BAF and TCW showed that shear strains were highest, within the liquefied ground, in the zone immediately behind the wharves. For the case of TCW, residual strains in this zone reached values as high as 40% for an input intensity of Ag=0.3g. Free-Field analyses revealed that the distribution of liquefaction, in terms of CTL (cumulative thickness of liquefaction beneath a given point on the surface), was markedly uneven within first 40 to 60 inland from the wharf. CTL exhibited at least one set of successive throughs and peaks, with maximum shear strains concentrated along

the verticals with shorter CTL. Further inland from the wharf, maximum shear strains and CTL reduced to constant values. Therefore, it was concluded that the zone of non-uniform liquefaction extended for approximately 40 to 60m from the wharf.

For wharf BAF, the stiffer soil, compared to the case of TCW, exhibited lateral spreading strains as high as 18%, behind the wharf structure for Ag=0.35. Despite the rather large difference in terms of residual deformations, the 2D response featured similar liquefaction patterns for both case studies. By and large, maximum lateral spreading strains were reported along a 40 m to 60 m wide section, for both wharf BAF and TCW. Note the aforementioned results correspond to simulations performed with PM4Sand.

Furthermore, results obtained from the analyses performed on wharf BAF, in Chapter 5, highlighted the potential sensitivity of the uniform lateral spreading component to boundary effects This potential limitation of the numerical modelling methodology was assessed by conducting three verification analyses using a so-called reflected model, which consisted in a larger model made of the main finite difference grid, extended for an additional 100 m, and mirrored in the opposite direction.

The reflected and short SS (Soil-Structure) models predicted similar residual crest displacements. However, there was no agreement in terms of the residual uniform lateral spreading displacements. Given the relatively large differences between these results, it is difficult to establish a baseline for a comparison between the uniform spreading component estimated by the two models. This is because, on one hand, the free-field lateral boundaries, as proposed by Lysmer and Kuhlemeyer (1969), cannot provide sufficient restraint against permanent lateral deformations, as they are the results of the highly nonlinear response of the soil at low frequencies. And on the other hand, for the reflected model, the ground closer to the midpoint of the model could be pulled in the opposite direction by the reflected half.

7.2.2 Seismic response of wharf BAF (Gioia Tauro), comparison between PM4Sand and SDm.

In modelling the response of wharf BAF, Chapters 4 and 5 systematically compared the results produced by PM4Sand and SDm, when assigned to the uppermost 20 meters of the liquefiable ground. The former model consistently produced larger lateral spreading strains, whereas the latter resulted in more severe 1D responses. It is worth noting that the differences observed after the 1D analyses were not as critical as those obtained for the 2D analyses. From the results presented in Chapter 4 and 5 the following remarks were made:

- *Insights from element test simulations*. Under cyclic simple-shear conditions, element test simulations performed with PM4Sand and SDm reproduced equivalent LRCs. However, the models produced different 2D and 1D system responses. This is explained by the different shear strain rates, and K_α effects reproduced by the

models. Results from single-element simulations indicated that PM4Sand produces a constant rate strain rate prior and after liquefaction. Conversely, SDm generates a rapid progression of shear strains prior and during the cycles immediately after liquefaction, but reduces to a constant value, between 4% and 5%, during cyclic mobility. In terms of K_α effects, single-element cyclic simple shear simulations, under the application of sustained shear stress, indicated that SDm produced cyclic resistances 1.2 to 1.4 higher than those predicted by PM4Sand. Note that these observations are valid for q_{c1Ncs}=135.

- *K_α and system effects on the 2D response*. FF analyses reported that, compared to the soil elements located outside the submerged slope, the soil elements behind the scarp exhibited a less contractive tendency and consequently smaller strains. This resulted in a zone, or wedge, of non-liquefiable soils within the slope for low to intermediate input intensities. This was the result of three different conditions. Frist, K_α effects. In line with the results of single-element tests, the soil behind the scarp only liquefied once the ground motion intensity became severe. In such scenario, PM4Sand generated higher shear strains than SDm, as it reproduces smaller cyclic resistances under the application of sustain shear stress. Second and third, system effects. The non-liquefiable soil beneath the slope experienced relatively large stains, leading to a toe failure mechanism. This resulted in an extension of the slope towards the sea, which induced negative excess pore water pressures on one hand, and stiffness degradation that likely reduced the seismic demand transferred to the liquefiable soils on the other.
- *Different Lateral spreading deformations*. For the analyses in Chapter 4, the fast progression of post liquefaction shear strains and lower cyclic resistance within the slope explain the larger ground displacements predicted by PM4Sand. Nevertheless, the system response captured by SDm was characterised by a thicker and wider zone of liquefiable soil (i.e., $\gamma_{xy,max} > 3\%$ and $r_{u,max} > 0.95$). In contrast, large shear strains produced by PM4Sand ($\gamma_{xy,max} > 10\%$) concentrated over a thinner band. It is worth to note that, the soil response of PM4Sand and SDm also differed in terms of modulus degradation characteristics, being the latter stiffer at lower strains.
- *Similar liquefaction triggering characteristics in 1D and 2D seismic effective stress analyses*. For the analyses in Chapter 4, both models predicted the triggering of liquefaction around the same instant of time. They reproduced comparable 1D cyclic shear strains, as well as similar crest displacements during and immediately after liquefaction. After liquefaction, the horizontal displacements recorded at the crest deviated, being those produced by PM4Sand larger. This was due to differences in of post-liquefaction strain rate and K_α effects. Results from Chapter 5 indicated that, with few exceptions, both PM4Sand and SDm triggered liquefaction for T_R>475 yr
- *Different trends of the relative 2D/1D response.* The probabilistic analysis of Chapter 5 showed that PM4Sand and SDm resulted in different trends between the 2D and

1D response parameters. A situation that was aggravated by the input ground motion variability, which was interpreted differently by the two models. In general, SDm produced a larger thickness of liquefied soils which resulted in larger estimates of LDI_{ESA}, which is computed by integrating the maximum shear strains along the 1D soil column. However, SDm also predicted smaller lateral-spreading displacements. In contrast, the thickness of liquefied soils reproduced by PM4Sand, within the 1D column, was smaller, while lateral spreading displacements were larger than those of predicted by SDm.

7.2.3 Insights into design guidelines for the assessment and application of inertial and kinematic loads for pile-supported-wharves founded on liquefiable ground.

Due to their larger embedment and shorter free-length, the rows of trailing piles, of a pile-supported wharf, are expected to experience the highest level of seismic demands. Firstly, inertial shear loads (transmitted by the wharf deck) are disproportionately concentrated at the cap of these elements. Secondly, during events that trigger liquefaction, these piles are first in line for restraining the lateral moving ground. Thus, it is assumed that the trailing piles are the critical elements controlling the seismic design of pile-supported wharves.

In line with the above, Chapters 4 and 5 examined the seismic response and seismic demand obtained for the trailing pile(s) of wharf BAF by means of effective stress DSSI analyses. Chapter 4 underscored the relevant features of the pile response and highlighted key differences when using PM4Sand and SDm to model the response of the liquefiable ground. Chapter 5 presented a multiple stripe analysis aimed at examining the inertial and kinematic demands experienced by the pile for 5 different seismic hazard levels. Results obtained with PM4Sand and SDm were systematically compared as in Chapter 4.

Results from the 2D and 1D numerical simulations were examined by the grouping the model response parameters into three categories:

- *System response parameters,* with reference to the ground response: the residual horizontal displacement at the crest Δ_{Crest}, the residual lateral displacement at the crest $\Delta_{Lateral,}$ computed relative to the lateral boundary of the models, and LDI_{ESA} computed from the response of the 1D column. $\Delta_{Lateral}$ is, in essence, a measure of the non-uniform component of lateral spreading.
- *Seismic demand parameters*, computed as maximum relative rotations $\Delta\theta_{max}$ recorded at two critical sections of the trailing pile: at the pile deck node PD, and at the in-ground nodes located within the liquefiable soil, nodes IG. This displacement-based definition for the seismic demand on the piles is done to preserve consistency with the strong deck and weak pile design philosophy. Piles are expected to exploit their ductility capacity during strong events while the deck remains elastic. Thus, the recommendations laid down in this section are also

based on this principle. Note that the 2D simulations explicitly accounted for this feature of the pile response.

- *Inertial load parameters*, characterizing the inertial loads exerted by the deck on the trailing pile. These correspond to: the peak deck acceleration, PDA and the maximum (peak) shear force at node PD, $V_{max.}$.

In general terms, and under the assumption that LDI_{ESA} and Δ_{Crest} (or $\Delta_{Lateral}$) characterize the cyclic and lateral spreading phases of the ground response respectively, results showed that the kinematic loads at node PD are linked to the cyclic phase of motion, while nearly unrelated to the lateral spreading displacements. For node IG, ground deformations, both cyclic and lateral spreading, controlled the seismic demands.

This distinction proposed by Cubrinovski et al. (2009) between cyclic and lateral spreading phases (or components) of the response is preferred over the distinction between cases of no-liquefaction and cases of liquefaction. It represents a more general framework in which, for a given soil deposit, the relative importance of the cyclic and lateral spreading phases is determined by the earthquake intensity. Moreover, the verification of a single critical loading condition for design purposes by combining peak inertial and kinematic loads, as suggested by some of the current seismic design standards, such as the ASCE 61-14 and the POLA and POLB guidelines, does not represent the evolutionary nature of liquefaction-induced lateral spreading phenomena. It is then suggested to conduct two separate design verifications, one for the cyclic and one for the lateral spreading phase of the ground response. For each phase, kinematic and inertial loads can be assessed and combined following different considerations. In accordance with this reasoning, and in reference to large diameter pile supported wharves, the insights gained form the analysis presented in Chapter 4 and 5 are the following:

- *Unrelated kinematic and inertial demands in cases of liquefaction-induced lateral spreading*. Seismic demands at the IG nodes were insensitive to the inertial movement of the wharf's deck. Inertial loads and demands, V_{max} and $\Delta\theta_{max}$ PD, were uncorrelated to liquefaction-induced lateral spreading displacements. In this cases, maximum relative rotations recorded at the IG nodes were one order of magnitude greater than those at the pile-deck connection. Moreover, seismic demands recorded at node PD occurred during the strong phase of shaking, and were determined by the inertial loads, in first place ($R^2 \approx 0.85$), and by cyclic ground deformations in the second place ($R^2 \approx 0.60$). This is confirmed by the fact that PM4Sand and SDm produced comparable estimates for these demands, despite the above-mentioned differences in terms of residual displacements. It is therefore considered that kinematic and inertial demands should not be combined in design verifications for the lateral spreading phase of the response.
- *Kinematic and inertial demands for the cyclic phase of the system response*. The high correlation between the seismic demand at PD and LDI_{ESA} validate the notion that

kinematic demands could be represented by the distribution of ground displacements obtained from the estimated profile of cyclic strains, as recommended by Cubrinovski et al. (2009) and Tokimatsu and Asaka (1998). Note that in this case, reference to cyclic strains is made with respect to 1D response analyses. Regarding the inertial demands, for cases of no-liquefaction, (corresponding to $T_R \leq 475$ yr for wharf BAF) force-based estimates of V_{max} were as conservative as displacement-based estimates. However, in cases of liquefaction, force-based estimates were critically overconservative. Thus, in such cases, the design inertial load for the cyclic phase of motion should be obtained from displacement-base methods only.

- *kinematic demands for the lateral spreading phase of the response*. peak seismic demands at nodes IG were controlled by the magnitude of the residual ground displacements, characterized by Δ_{Crest} and $\Delta_{Lateral}$. This indicates the need for the adequate estimation of lateral spreading displacements along the pile length. However, it is yet difficult to produce reliable estimates for lateral spreading displacements without resorting to complex numerical or physical modelling methods. As an alternative one could opt for empirical correlation derived from case histories (Tokimatsu and Asaka, 1998; Youd et al., 2002), or for simplified approaches that are based on limit equilibrium techniques (Ashford et al., 2011; Souri et al. 2022b). In this regard, the predictive capability of 1D analyses, as examined in this study, was indeed limited. The comparison between LDI_{ESA} and the lateral spreading parameters Δ_{Crest} and $\Delta_{Lateral}$ exhibited a large scatter. PM4Sand and SDm resulted in different trends between the 2D and 1D response parameters. If the predictive potential of LDI_{ESA} were to be accepted, a factor of Δ_{Crest} / LDI_{ESA} equal to 3 would represent a conservative estimate for the lateral spreading displacements, provided that LDI_{ESA} >0.2m.

7.2.4 Optimal intensity measures for large diameter pile supported wharves.

The multiple stripe analysis presented in Chapter 5 was complemented by a preliminary evaluation of optimal intensity measures for the system response wharf BAF and engineering demand parameters for its trailing pile. The efficiency (Cornell et al., 2002) and proficiency (Mackie and Stojadinović, 2005) ranking reported in Table 5.4 indicated that the modified acceleration spectrum intensity (MASI), is the most suitable candidate for an optimal intensity measure as in resulted in large correlation with all the response parameters considered, while ranking high in proficiency.

7.2.5 Effects of model uncertainty

The numerical methodology employed in this thesis consisted in assuming uniform-properties layers, either liquefiable or non-liquefiable. The probabilistic treatment of the system response presented in Chapter 5 dealt exclusively with the effects of ground motion (record-to-record) variability. Up to that point the effect of the epistemic uncertainty was

partially accounted for by employing two different constitutive models for the liquefiable ground in parallel.

Chapter 6 aimed at completing the study by providing a preliminary estimation of the most relevant model parameters that could drive the variability of the estimated response. This was done by means of the elementary effects method, a global sensitivity analysis methodology. The advantage of this method is that it is directly link to variance-based assessments, and it can estimate the combined effect of multiple model parameters.

1D and 2D free-field response parameters, obtained with simulations employing PM4Sand, were highly sensitive to the liquefaction resistance of the critical layer, which was assigned to a median q_{c1Ncs} value of 135. More interestingly, the analysis revealed that the second most important effects in the system response were produced by the variation of the hydraulic conductivity of all the soil materials included in the model.

7.3 FUTURE WORK

This thesis has laid the groundwork for a future study about the calibration of simplified design methods of pile-supported wharves founded on liquefiable ground conditions, within the framework of pseudo static BNWF methodologies. The design verification for the cyclic phase of the response could make use of the results provided by 2D effective stress DSSI analysis to calibrate the combination factors applied to the design inertial and kinematic loads. The former estimated using well-known displacement-based methos, while the latter is represented by the profile of ground displacements derive from the distribution of maximum (1D) cyclic shear strains. For the lateral spreading phase, the formulation of a robust simplified methodology for estimation of liquefaction-induced lateral spreading design displacement remains open.

The probabilistic study in Chapter 5 would require further improvements in terms of the record selection methodology for the multiple stripe analysis. Ideally, conditional seismic hazard methods should be considered, as those proposed by Baker and Allin Cornell (2006) and; Bradley (2012). This could allow the generation of fragility models for the wharf structure.

To extend the range applicability of the insights provided in the previous section the following avenues can be explored:

- *Effects of 3D response of the wharf.* In cases of no-liquefaction or during the cyclic phase of response where limited lateral spreading deformations occur, the inertial response of the wharf can significantly affect the soil-structure response. For such cases the torsional mode should be considered, as highlighted by Blandon (2007) and Shafieezadeh (2011).

- *Consideration of a different type of controlling events*. Being situated in Southern Italy, near source crustal events dominate the seismic hazard at the site of wharf BAF. Therefore, the suite of earthquake ground motions employed in Chapter 5 is constituted by time histories of relatively short duration. The effect of long-duration strong motion produced by subduction events may produce different outcomes in terms of the kinematic and inertial loads and demands, and their interaction.

Moreover, the effective stress DSSI analysis could be refined by incorporating the following additional features:

- *Interface elements between soil and piles*. In term of numerical modelling, one additional dimension of complexity could be added to the systematic study presented in this thesis, that is the consideration of interface elements between piles and the surrounding ground.
- *Calibration of advanced constitutive models for a target post liquefactions train rate*. Chapter 4 and 5 showed that, for modelling of liquefaction-induced lateral spreading, the rate of post-liquefaction strain accumulations is one critical aspect to be considered during the calibration of advanced constitutive models. To the knowledge of the author, the only reference in literature linking soil density and cyclic resistance with post-liquefaction strain accumulation is the work presented by Tasiopoulou et al. (2020)

8.REFERENCES

Alarcon-Guzman A and Leonards GA (1988) Undrained Monotonic and Cyclic Strength of Sands. *Journal of Geotechnical Engineering* 114(10): 21.

Ancheta TD, Darragh RD, Stewart JP, et al. (2013) PEER NGA-West Database, PEER Report No. 2013-03. Pacific Earthquake Engineering Research Center.

Andreotti G and Lai CG (2017a) A nonlinear constitutive model for beam elements with cyclic degradation and damage assessment for advanced dynamic analyses of geotechnical problems. Part I: theoretical formulation. *Bulletin of Earthquake Engineering* 15(7): 2785–2801.

Andreotti G and Lai CG (2017b) A nonlinear constitutive model for beam elements with cyclic degradation and damage assessment for advanced dynamic analyses of geotechnical problems. Part II: validation and application to a dynamic soil–structure interaction problem. *Bulletin of Earthquake Engineering* 15: 2803–2825.

Armstrong RJ, Boulanger RW and Beaty MH (2014) Equivalent Static Analysis of Piled Bridge Abutments Affected by Earthquake-Induced Liquefaction. *Journal of Geotechnical and Geoenvironmental Engineering* 140(8): 04014046.

ASCE (2014) Seismic design of piers and wharves. ASCE/COPRI 61-14.

Ashford SA, Boulanger RW and Brandenberg SJ (2011) Recommended Design Practice for Pile Foundations in Laterally Spreading Ground. *Pacific Earthquake Engineering Research Center*: 57.

Baecher GB and Christian JT (2003) *Reliability and Statistics in Geotechnical Engineering*. Wiley.

Baker JW and Allin Cornell C (2006) Spectral shape, epsilon and record selection. *Earthquake Engineering & Structural Dynamics* 35(9): 1077–1095.

Barani S, Spallarossa D and Bazzurro P (2009) Disaggregation of Probabilistic Ground-Motion Hazard in Italy. *Bulletin of the Seismological Society of America* 99(5): 2638–2661.

Blandon CA (2007) Seismic analysis and desing of pile supported wharves. PhD Dissertation Istituto Universitario di Studi Superiori di Pavia Università degli Studi di Pavia.

Bolton MD (1986) The strength and dilatancy of sands. *Géotechnique* 36(1): 65–78.

Boulanger RW and Idriss IM (2014) CPT and SPT Based Liquefaction Triggering Procedures. Report No. UCD/CGM-14/01. Center for Geotechnical Modeling, Department of Civil and Environmental Engineering, University of California, Davis.

Boulanger RW and Idriss IM (2016) CPT-Based Liquefaction Triggering Procedure. *Journal of Geotechnical and Geoenvironmental Engineering* 142(2): 04015065.

Boulanger RW and Tokimatsu K (eds) (2005) Evaluating Pile Pinning Effects On Abutments Over Liquefied Ground. In: *Seismic Performance and Simulation of Pile Foundations in Liquefied and Laterally Spreading Ground*, University of California, Davis, California, United States, 31 October 2005. American Society of Civil Engineers.

Boulanger RW and Ziotopoulou K (2013) Formulation of a sand plasticity plane-strain model for earthquake engineering applications. *Soil Dynamics and Earthquake Engineering* 53: 254–267.

Boulanger RW and Ziotopoulou K (2017) "PM4Sand (version 3.1): A sand plasticity model for earthquake engineering applications." Report No. UCD/CGM-17/01. Center for Geotechnical Modeling, Department of Civil and Environmental Engineering, University of California, Davis, CA.

Boulanger RW and Ziotopoulou K (2019) A constitutive model for clays and plastic silts in plane-strain earthquake engineering applications. *Soil Dynamics and Earthquake Engineering* 127: 105832.

Boulanger RW and Ziotopoulou K (2022) "PM4Sand (version 3.2): A sand plasticity model for earthquake engineering applications." Report No. UCD/CGM-22/02. Center for Geotechnical Modeling, Department of Civil and Environmental Engineering, University of California, Davis, CA.

Boulanger RW, Chang D, Brandenberg SJ, et al. (2007) Seismic Design of Pile Foundations for Liquefaction Effects. In: Pitilakis KD (ed.) *Earthquake Geotechnical Engineering*. Geotechnical, Geological and Earthquake Engineering. Dordrecht: Springer Netherlands, pp. 277–302. Available at: http://link.springer.com/10.1007/978-1-4020-5893-6_12 (accessed 29 October 2021).

Bowen HJ and Cubrinovski M (2008) EFFECTIVE STRESS ANALYSIS OF PILES IN LIQUEFIABLE SOIL: A CASE STUDY OF A BRIDGE FOUNDATION. *Bulletin of the New Zealand Society for Earthquake Engineering* 41(4): 17.

Bozzoni F, Famà A, Lai CG, et al. (2014) Seismic Risk Assessment Of Seaports Using Gis: The Port Of Gioia Tauro In Southern Italy. *PIANC World Congress San Francisco, USA 2014*. Epub ahead of print 2014.

Bradley BA (2012) The seismic demand hazard and importance of the conditioning intensity measure. *Earthquake Engineering & Structural Dynamics* 41(11): 1417–1437.

Bradley BA, Cubrinovski M, Dhakal RP, et al. (2010) Probabilistic seismic performance and loss assessment of a bridge–foundation–soil system. *Soil Dynamics and Earthquake Engineering* 30(5): 395–411.

Bradley BA, Wotherspoon LM, Kaiser AE, et al. (2018) Influence of Site Effects on Observed Ground Motions in the Wellington Region from the Mw 7.8 Kaikōura, New Zealand, Earthquake. *Bulletin of the Seismological Society of America* 108(3B): 1722–1735.

Brandenberg SJ, Boulanger RW, Kutter BL, et al. (2005) Behavior of Pile Foundations in Laterally Spreading Ground during Centrifuge Tests. *Journal of Geotechnical and Geoenvironmental Engineering* 131(11): 1378–1391.

Bray JD, Cubrinovski M, Dhakal R, et al. (2019) Seismic Performance of CentrePort Wellington. In: *Geo-Congress 2019*, Philadelphia, Pennsylvania, 21 March 2019, pp. 76–89. American Society of Civil Engineers. Available at: https://ascelibrary.org/doi/10.1061/9780784482100.009 (accessed 25 January 2024).

Brunet S, De La Llera JC, Jacobsen A, et al. (2012) Performance of Port Facilities in Southern Chile during the 27 February 2010 Maule Earthquake. *Earthquake Spectra* 28(1_suppl1): 553–579.

California State Lands Commission (2010) California code of regulations, Part 2, California Building Code, Chapter 31F, Title 24, commonly reffered to as the Marine Oil Terminal Engineering and Maintenance Standards (MOTEMS).

Caltrans (California DOT) (2012) Guidelines for foundation loading and deformation due to liquefaction induced lateral spreading. Caltrans.

Cetin KO, Bilge HT, Wu J, et al. (2009) Probabilistic Model for the Assessment of Cyclically Induced Reconsolidation (Volumetric) Settlements. *Journal of Geotechnical and Geoenvironmental Engineering* 135(3): 387–398.

Conca D, Bozzoni F and Lai CG (2020) Interdependencies in Seismic Risk Assessment of Seaport Systems: Case Study at Largest Commercial Port in Italy. *ASCE-ASME Journal of Risk and Uncertainty in Engineering Systems, Part A: Civil Engineering* 6(2): 04020006.

Corigliano M, Lai CG, Rota M, et al. (2012) ASCONA: Automated Selection of COmpatible Natural Accelerograms. *Earthquake Spectra* 28(3): 965–987.

Cornell CA, Jalayer F, Hamburger RO, et al. (2002) Probabilistic Basis for 2000 SAC Federal Emergency Management Agency Steel Moment Frame Guidelines. *Journal of Structural Engineering* 128(4): 526–533.

Cremen G and Baker JW (2021) Variance-based sensitivity analyses and uncertainty quantification for FEMA P-58 consequence predictions. *Earthquake Engineering & Structural Dynamics* 50(3): 811–830.

Cubrinovski M and Ishihara K (1998a) Modelling of sand behaviour based on state concept. *SOILS AND FOUNDATIONS* 38(3): 115–127.

Cubrinovski M and Ishihara K (1998b) State Concept and Modified Elastoplasticity for Sand Modelling. *SOILS AND FOUNDATIONS* 38(4): 213–225.

Cubrinovski M and Ntritsos N (2023) 8th Ishihara lecture: Holistic evaluation of liquefaction response. *Soil Dynamics and Earthquake Engineering* 168: 107777.

Cubrinovski M, Ishihara K and Poulos H (2009) Pseudo-static analysis of piles subjected to lateral spreading. *Bulletin of the New Zealand Society for Earthquake Engineering* 42(1): 28–38.

Cubrinovski M, Bray JD, De La Torre C, et al. (2017) Liquefaction effects and associated damages observed at the Wellington CentrePort from the 2016 Kaikoura earthquake. *Bulletin of the New Zealand Society for Earthquake Engineering* 50(2): 152–173.

Dafalias YF and Manzari MT (2004) Simple Plasticity Sand Model Accounting for Fabric Change Effects. *Journal of Engineering Mechanics* 130(6): 622–634.

Dhakal R (2022) Liquefaction assesment metodologies for reclaimed land. A case study of the Port of Wellington, New Zealand (Centre Port). PhD Dissertation University of Canterbury.

Dhakal R (2023) Personal communication.

Dhakal R, Cubrinovski M and Bray JD (2020) Geotechnical characterization and liquefaction evaluation of gravelly reclamations and hydraulic fills (Port of Wellington, New Zealand). *Soils and Foundations* 60(6): 1507–1531.

Dhakal R, Cubrinovski M and Bray J (2022) Input Ground Motion Selection for Site Response Analysis at the Port of Wellington (New Zealand). In: Wang L, Zhang J-M, and Wang R (eds) *Proceedings of the 4th International Conference on Performance Based Design in Earthquake Geotechnical Engineering (Beijing 2022)*. Geotechnical, Geological and Earthquake Engineering. Cham: Springer International Publishing, pp. 888–895. Available at: https://link.springer.com/10.1007/978-3-031-11898-2_64 (accessed 8 February 2024).

Facciorusso J and Vannucchi G (2003) LIQUEFACTION HAZARD MAPS OF THE HARBOUR AREA OF GIOIA TAURO (ITALY) BY GEO-STATISTICAL METHODS. *Proceedings of the 4th International Conference of Earthquake Engineering and Seismology, Tehran, Islamic Republic of Iran*: 9.

Famà A, Bozzoni F and Lai CG (2014) Valutazione in ambiente GIS del danno sismico distrutture portuali marittime: il caso del porto di Gioia Tauro. *Progettazione Sismica* (2): 49–72.

Feng K, Lu Z and Yang C (2019) Enhanced Morris method for global sensitivity analysis: good proxy of Sobol' index. *Structural and Multidisciplinary Optimization* 59(2): 373–387.

Ghayoomi M and Dashti S (2015) Effect of Ground Motion Characteristics on Seismic Soil-Foundation-Structure Interaction. *Earthquake Spectra* 31(3): 1789–1812.

Giovenale P, Cornell CA and Esteva L (2004) Comparing the adequacy of alternative ground motion intensity measures for the estimation of structural responses. *Earthquake Engineering & Structural Dynamics* 33(8): 951–979.

Green RA, Olson SM, Cox BR, et al. (2011) Geotechnical Aspects of Failures at Port-au-Prince Seaport during the 12 January 2010 Haiti Earthquake. *Earthquake Spectra* 27(1_suppl1): 43–65.

Grifoll M, Karlis T and Ortego M (2018) Characterizing the Evolution of the Container Traffic Share in the Mediterranean Sea Using Hierarchical Clustering. *Journal of Marine Science and Engineering* 6(4): 121.

Gruppo di Lavoro MPS (2004) Redazione della mappa di pericolosità sismica prevista dall'Ordinanza PCM 3274 del 20 marzo 2003, Rapporto conclusivo per il dipartimento di Protezione Civile. INGV, Milano - Roma. Available at: http://zonesismiche.mi.ingv.it/documenti/rapporto_conclusivo.pdf.

Idriss IM and Boulanger RW (2008) *Soil Liquefaction during Earthqukes*. Earthquake Engineering Research Institute (EERI).

Iervolino I, Baltzopoulos G, Chioccarelli E, et al. (2017) Seismic actions on structures in the near-source region of the 2016 central Italy sequence. *Bulletin of Earthquake Engineering*. Epub ahead of print 9 December 2017. DOI: 10.1007/s10518-017-0295-3.

Ishihara K (1993) Liquefaction and flow failure during earthquakes. *Géotechnique* 43(3): 351–415.

Ishihara K, Yoshida K and Kato M (1997) Characteristics of Lateral Spreading in Liquefied Deposits During the 1995 Hanshin-Awaji Earthquake. *Journal of Earthquake Engineering* 1(1): 23–55.

Itasca Consulting Group, Inc (2019) FLAC- Fast Lagrangian Analysis of Continua, Ver. 8.1.

Iwasaki T, Arakawa T and Tokida K-I (1984) Simplified procedures for assessing soil liquefaction during earthquakes. *Soil Dynamics and Earthquake Engineering* 3(1): 49–58.

Johnson K, Villiani M, Bayliss K, et al. (2023) Global Earthquake Model (GEM) Seismic Hazard Map (version 2023.1 - June 2023). Available at: doi.org/10.5281/zenodo.8409647.

Juno W, Delaney A, Keepa C, et al. (2021) CentrePort Wellington: Resilient Recovery – Risk-guided regeneration. Epub ahead of print 2021.

Kabilamany K and Ishihara K (1990) Stress dilatancy and hardening laws for rigid granular model of sand. *Soil Dynamics and Earthquake Engineering* 9(2): 66–77.

Kayen RE, Mitchell JK, Seed RB, et al. (1998) Soil liquefaction in the east bay during the earhtquake. In: *The Loma Prieta, California, Earthquake of October 17,1989 - Liquefaction*.

Kramer SL and Mitchell RA (2006) Ground Motion Intensity Measures for Liquefaction Hazard Evaluation. *Earthquake Spectra* 22(2): 413–438.

Lanzo G, Luzi L, Russo E, et al. (2018) Engineering Strong Motion Database (ESM) flatfile. Istituto Nazionale di Geofisica e Vulcanologia (INGV). Available at: https://doi.org/10.13127/esm/flatfile.1.0.

Ledezma C and Tiznado JC (2017) LIQUEFACTION EFFECTS ON THE NORTHERN CORONEL PIER DURING THE 2010 MAULE CHILE EARTHQUAKE. Epub ahead of print 2017.

Luco N and Cornell CA (2007) Structure-Specific Scalar Intensity Measures for Near-Source and Ordinary Earthquake Ground Motions. *Earthquake Spectra* 23(2): 357–392.

Lysmer J and Kuhlemeyer RL (1969) Finite Dynamic Model for Infinite Media. *Journal of Engineering Mechanics Division* 95(4).

Mackie KR and Stojadinović B (2005) Comparison of Incremental Dynamic, Cloud, and Stripe Methods for Computing Probabilistic Seismic Demand Models. In: *Structures Congress 2005*, New York, New York, United States, 18 April 2005, pp. 1–11. American Society of Civil Engineers. Available at: http://ascelibrary.org/doi/10.1061/40753%28171%29184 (accessed 25 February 2024).

Mondal G and Rai DC (2008) Performance of harbour structures in Andaman Islands during 2004 Sumatra earthquake. *Engineering Structures* 30(1): 174–182.

Na UJ, Chaudhuri SR and Shinozuka M (2008) Probabilistic assessment for seismic performance of port structures. *Soil Dynamics and Earthquake Engineering* 28(2): 147–158.

Na UJ, Chaudhuri SR and Shinozuka M (2009) Performance Evaluation of Pile-Supported Wharf under Seismic Loading. In: *TCLEE 2009*, Oakland, California, United States, 24 June 2009, pp. 1–10. American Society of Civil Engineers. Available at: http://ascelibrary.org/doi/10.1061/41050%28357%2998 (accessed 18 January 2022).

National Research Institute for Earth Science and Disaster Resilience (2019) NIED K-NET, KiK-net. National Research Institute for Earth Science and Disaster Resilience.

Ntritsos N and Cubrinovski M (2020) A CPT-based effective stress analysis procedure for liquefaction assessment. *Soil Dynamics and Earthquake Engineering* 131: 106063.

OCDI OCADI of J (2020) Technical standards and commentaries for port and harbour facilities in japan 2020. Epub ahead of print 2020.

Padgett JE, Nielson BG and DesRoches R (2008) Selection of optimal intensity measures in probabilistic seismic demand models of highway bridge portfolios. *Earthquake Engineering & Structural Dynamics* 37(5): 711–725.

PIANC (ed.) (2001) *Seismic Desing Guidelines for Port Structures*. Rotterdam.

POLA P of LA (2010) The Port of Los Angeles code for seismic design, upgrade and tepair of container wharves. Epub ahead of print May 2010.

POLB P of LB (2012) Port of Long Beach wharf design criteria. Epub ahead of print February 2012.

Porter K, Kennedy R and Bachman R (2007) Creating Fragility Functions for Performance-Based Earthquake Engineering. *Earthquake Spectra* 23(2): 471–489.

Priestley MJN, Seible J and Chai YH (1992) Design guidelines for assessment retrofit and repair of bridges for seismic performance. *University of California. Sand Diego, SSRP-93/01*: 266.

Rathje EM, Abrahamson NA and Bray JD (1998) Simplified Frequency Content Estimates of Earthquake Ground Motions. *Journal of Geotechnical and Geoenvironmental Engineering* 124(2): 150–159.

Razavi SA, Fakher A and Mirghaderi SR (2007) An insight into the bad reputation of batter piles in seismic performance of wharves. *4th Internation Conference on Earthquake Geotechical Engineering*. Epub ahead of print June 2007.

Robertson PK and Cabal, K. L. (2015) Guide to Cone Penetration Testing for Geotechnical Engineering. *Corporate Headquarters, Signal Hill, California*. Epub ahead of print 2015.

Saltelli A (ed.) (2008) *Global Sensitivity Analysis: The Primer*. Chichester, England ; Hoboken, NJ: John Wiley.

Schofield A and Wroth CP (1968) *Critical State Soil Mechancis*. McGraw-Hill.

Seed RB, Dickenson SE and Idriss IM (1991) Principal Geotechnical Aspects of the 1989 Loma Prieta Earthquake. *Soils and Foundations* 31(1): 1–26.

Sengupta D and Lazarus ED (2023) Rapid seaward expansion of seaport footprints worldwide. *Communications Earth & Environment* 4(1): 440.

Shafieezadeh A (2011) Seismic Vulnerability Assessment of Wharf Structures. PhD Dissertation Giorgia Institute of Technology.

Shafieezadeh A, DesRoches R, Rix GJ, et al. (2012) Seismic Performance of Pile-Supported Wharf Structures Considering Soil-Structure Interaction in Liquefied Soil. *Earthquake Spectra* 28(2): 729–757.

Sobol' IM (2001) Global sensitivity indices for nonlinear mathematical models and their Monte Carlo estimates. *Mathematics and Computers in Simulation* 55(1–3): 271–280.

Souri M, Khosravifar A, Dickenson S, et al. (2022a) Pile-Supported Wharves Subjected to Inertial Loads and Lateral Ground Deformations. I: Experimental Results from Centrifuge Tests. *Journal of Geotechnical and Geoenvironmental Engineering* 148(11): 04022090.

Souri M, Khosravifar A, Dickenson S, et al. (2022b) Pile-Supported Wharves Subjected to Inertial Loads and Lateral Ground Deformations. II: Guidelines for Equivalent Static Analysis. *Journal of Geotechnical and Geoenvironmental Engineering* 148(11): 04022091.

Stucchi M, Meletti C, Montaldo V, et al. (2011) Seismic Hazard Assessment (2003-2009) for the Italian Building Code. *Bulletin of the Seismological Society of America* 101(4): 1885–1911.

Tasiopoulou P, Ziotopoulou K, Humire F, et al. (2020) Development and Implementation of Semiempirical Framework for Modeling Postliquefaction Shear Deformation Accumulation in Sands. *Journal of Geotechnical and Geoenvironmental Engineering* 146(1): 04019120.

Tokimatsu K and Asaka Y (1998) EFFECTS OF LIQUEFACTION-INDUCED GROUND DISPLACEMENTS ON PILE PERFORMANCE IN THE 1995 HYOGOKEN-NAMBU EARTHQUAKE. *SOILS AND FOUNDATIONS* 38(Special): 163–177.

Tokimatsu K, Suzuki H and Sato M (2005) Effects of inertial and kinematic interaction on seismic behavior of pile with embedded foundation. *Soil Dynamics and Earthquake Engineering* 25(7–10): 753–762.

Tonkin & Taylor Ltd (2013) Damage Report: Earthquake events dated 21 July and 16 August 2013. Prepared for CentrePort Limited. Ref No. 85726.

Vamvatsikos D and Fragiadakis M (2009) Incremental dynamic analysis for estimating seismic performance sensitivity and uncertainty. *Earthquake Engineering & Structural Dynamics*: n/a-n/a.

Verdugo R and Ishihara K (1996) The Steady State of Sandy Soils. *Soils and Foundations* 36(2): 81–91.

Wang X, Shafieezadeh A and Ye A (2018) Optimal intensity measures for probabilistic seismic demand modeling of extended pile-shaft-supported bridges in liquefied and laterally spreading ground. *Bulletin of Earthquake Engineering* 16(1): 229–257.

Yee E, Stewart JP and Tokimatsu K (2013) Elastic and Large-Strain Nonlinear Seismic Site Response from Analysis of Vertical Array Recordings. *Journal of Geotechnical and Geoenvironmental Engineering* 139(10): 1789–1801.

Yi S, Satish AB, Nair AS, et al. (2023) Sensitivity Analysis and Bayesian Calibration of OpenSees Models Using quoFEM. In: Di Trapani F, Demartino C, Marano GC, et al. (eds) *Proceedings of the 2022 Eurasian OpenSees Days*. Lecture Notes in Civil

Engineering. Cham: Springer Nature Switzerland, pp. 63–72. Available at: https://link.springer.com/10.1007/978-3-031-30125-4_6 (accessed 29 August 2023).

Youd TL, Hansen CM and Bartlett SF (2002) Revised Multilinear Regression Equations for Prediction of Lateral Spread Displacement. *Journal of Geotechnical and Geoenvironmental Engineering* 128(12): 1007–1017.

Zhang G, Robertson PK and Brachman RWI (2004) Estimating Liquefaction-Induced Lateral Displacements Using the Standard Penetration Test or Cone Penetration Test. *Journal of Geotechnical and Geoenvironmental Engineering* 130(8): 861–871.

Zhang J, Andrus RD and Juang CH (2005) Normalized Shear Modulus and Material Damping Ratio Relationships. *Journal of Geotechnical and Geoenvironmental Engineering* 131(4): 453–464.

APPENDIX A. MODELLING DETAILS FOR 2D SEISMIC EFFECTIVE STRESS DSSSI ANALYSES WITH FLAC

A.1. IMPLEMENTATION OF THE LUMPED PLASTICITY MODEL FOR STRUCTURAL ELEMENTS.

For a single plastic hinge, the lumped plasticity model proposed by Andreotti and Lai (2017a, 2017b) enforces a non-linear moment-curvature relationship by modifying the flexural stiffness of the two elements connected by the hinged node. Figure A.1 shows the geometrical description of the model for a cantilever column, composed by three (Euler-Bernoulli) beam elements. The bottom two elements (b_1 and b_2) make for the plastic zone, while the upper element is modelled elastic. As the monotonic, or cyclic load F (applied at the top the of the column) increases, the plasticity model enforces the moment curvature relationship at node 2 by modifying the stiffnesses (EI) of elements b_1 and b_2. This means that the combine length of elements b_1 and b_2 has degraded properties to simulate the formation of a hinge at the base of the column. Andreotti and Lai (2017a, 2017b) refer to the length of plastic hinge L_{ph} as the length of the plastic zone made of elements b_1 and b_2. The curvature can be computed as the relative rotation between nodes 3 and 1 divided by the length of the plastic hinge L_{ph}.

One important limitation of implementing the model in FLAC, is that it does not allow for the manipulation of single element properties, instead one must modify the properties of the material assigned to a given element. This implies that the user must be careful in assigning b_1 and b_2 with unique material definition. The model should have as many structural element materials as plastic zones, each property assigned just to the two elements composing a single zone. In FLAC, the command "`hinge`" is used to allow for relative rotation at node 2 that connects elements b_1 and b_2.

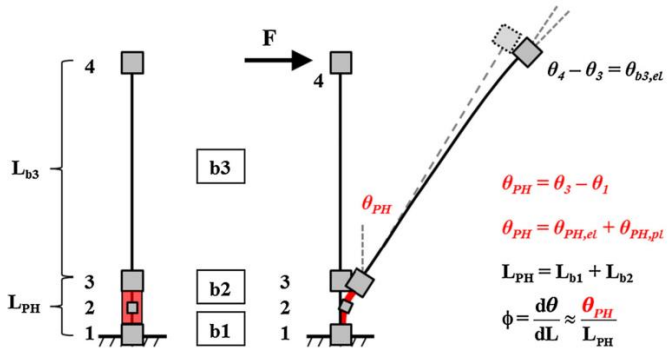

Figure A.1. Schematic representation of the formulation made by Andreotti and Lai (2017a, 2017b). Taken from (Andreotti and Lai, 2017b)

A.1.1. Numbering order for the elements comprising a single plastic zone.

The identifier of the central node (node 2 in Figure A.1) is stored by the model and later used to access the information of the elements it connects. The model assumes that the nodes and elements are numbered in accordance with the global reference frame. For instance, refer to the arrangement shown in Figure A.2, nodes and elements are numbered in an ascending order following the positive vertical direction. If done otherwise, even though FLAC may not prompt an error message, it could produce unreasonable responses of the structural elements.

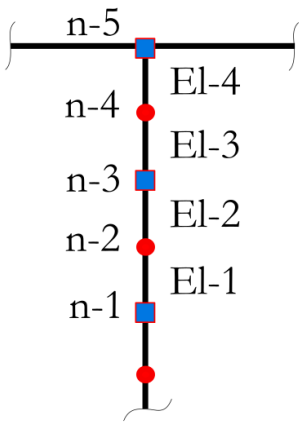

Figure A.2. Numbering convention for nodes and elements of the distributed plasticity model used for beam elements in FLAC.

A.1.2. *Fish* function for assigning hinge nodes.

With reference to Figure A.2, all the nodes in red must allow for relative rotations once the plastic moment capacity is overcome, they are in essence hinge nodes. However, using FLAC commands, a plastic hinge is not assigned directly to the hinged node, instead the hinge node is established by indicating the software which elements share a plastic connection. For the top hinge in Figure A.2, one would have to write the command "`struct hinge 3 4`". This tells FLAC that elements 3 and 4 share a hinged connection at their connecting node, which is node 4. If a subsequent command is used stating "`struct hinge 1 2`", it would create a hinged connection at node 2. However, it also creates a hinge at node 3 because FLAC assumes that all the elements tagged with the command "`hinge`" are connected through plastic connections at their common nodes. This is a problem for the implementation of the lumped plasticity model, because it assumes that the elements comprising a plastic zone have a unique hinge node.

For the current version of the mode, this limitation is sorted by manually assigning the hinge nodes through a *fish* function. An excerpt of the code is shown in Figure A.3, it

accesses FALC's linked lists arrays. Information about of arrays structure can be found in Section 4 in chapter "*FISH in FLAC*" of FLAC's manual.

```
def $manualhinge
    ;assigns the first node of the element as ph
    loop $nn_elem(1,$nn_hinges)

    $mem_num=$initial_element +2*($nn_elem-1)
    $get_mem_addr
    $node1_addr = imem($get_mem_addr+$keln1)
    imem($node1_addr+$kndhin)=1
    end_loop
end
```

Figure A.3. Excerpt of the *fish* function used to assign a hinge at the central node of a given plastic zone.

A.1.3. Sensitivity to the plastic zone length

When considering dynamic soil-structure interaction problems, the significantly larger relative stiffness of structural elements can render the solution time-step unpractically small. FLAC uses a unique time-step for all the nodes comprising the finite difference grid, for structural and soil elements alike. It computes the minimum time-step based on the stiffnesses (*dynamic masses* in FLAC's manual) assigned to all the grid points. Thus, there is a practical limit on the level of refinement of structural element mesh.

In the case of the lumped plasticity model, the combine length of elements b_1 and b_2 should be, ideally, equal to L_{ph}. Note that, the model, as implemented in FLAC, uses L_{ph} as an input (material) parameter, but it does not compute L_{ph} as the sum of the lengths of b_1 and b_2. Instead, the sizes of b_1 and b_2 have a direct effect on the definition of the relative rotation (see Figure A.1). This grants the suer with a margin for selecting the lengths of elements b_1 and b_2. Therefore, this study explored the sensitivity of the response of a cantilever column to the size of the plastic zone at its base.

The cantilever column is shown in the right panel of Figure A.4Figure A.4, it resembles that shown in Figure A.1. In this case, the lengths of elements b_1 and b_2 are referred to as L_{ph1} and L_{ph2}. The column was subjected to displacement-controlled tests considering the combinations of L_{ph1} and L_{ph2} reported by Table A.1. It is important to recall that the combine length of L_{ph1} and L_{ph2} does not represent the target length of plastic hinge (L_{ph}), which is fixed for all the tests with a value 1.5m, as a (model) parameter used by the lumped plasticity model.

In Figure A.4, panels *a* and *b* show the moment – relative rotation response recorded at the hinge node. At the local level, the pre-failure moment-curvature characteristics are almost identical for all the arrangements. Key features are well reproduced, such as: cracking moment and rotation (Mcr, θcr); yield moment and rotation (My,θy); and unloading and

reloading stiffnesses. However, Test 4, which considered elements of 2m, failed at capturing the cracking point, and slightly underpredicted the virgin loading stiffness. Clear deviations appear at the post-failure response. The coarser arrangements, represented by tests 1 and 4 critically underpredicted the port-failure capacity of the hinge.

At the system level, results show important discrepancies between the predicted load-displacement responses of the column before failure. In the case of Test 4, the initial stiffness and yield capacity were visibly larger than in the other cases. This is in part a geometrical effect given that this test used extremely large element lengths for the plastic zone. Moreover, at the onset of yielding, all the models reported the same bending moment at the hinge node, yet its location along column was different for each test. For Test 4, the hinge node is 2m above the ground, making the elastic element relatively shorter. Nonetheless, the values for the yield displacement were similar for all the cases. Finally, regarding the post failure response, Test 4 predicted an early failure with a significant capacity reduction.

Table A.1. Analysis properties used for the tests performed on the cantilever column of Figure A.4

Test No	L_{ph1} (m)	L_{ph2} (m)	Time-step (s) (before concrete cracks)
1	1.15 (0.75D)	1.15 (0.75D)	6.670×10^{-5}
2	0.75 (0.5D)	0.75 (0.5D)	7.210×10^{-6}
3	0.2	2.1	4.303×10^{-7}
4	2 (4/3D)	2 (4/3D)	1.104×10^{-4}
5	0.2	1.3	2.800×10^{-7}

D: pile diameter

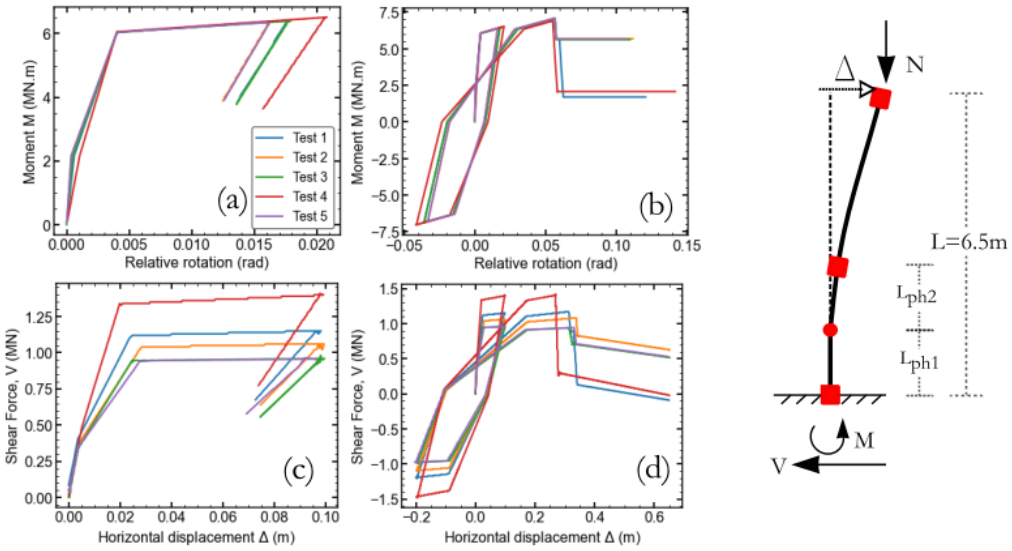

Figure A.4. Sensitivity of the monotonic (a,c) and cyclic (b,d) response of a cantilever column modelled different combinations of L_{ph1} and L_{ph2}. Results are shown in terms of moment-relative rotation (a,b) and shear force-displacement (c,d)

These results led to the following conclusions:

- Using an element length of 0.75m or 0.5D appears to be a reasonable trade-off between computational time and model accuracy. Concrete cracking and yielding are well captured. As well as the onset failure. The post-failure behaviour is however poorly reproduced.
- Larger lengths would overpredict the element capacity and the onset of failure, while capturing the yield displacements and rotations relatively well. Thus, the scope of future analysis is limited to the pre-failure behaviour. It is worth to mention that failure verification and the post-failure behaviour can be turned off while initializing the lumped plasticity model.

A.2. FREE-FIELD LATERAL BOUNDARY CONDITIONS

Ideally, in simulating 2D wave propagation phenomena, the model boundaries should adequately for energy radiation. To allow this feature, FLAC considers the classical free-field boundary condition proposed by Lysmer and Kuhlemeyer (1969), hereafter referred

as to L&K BC. However, FLAC does not allow for the implementation of this type of boundary condition for user-defined constitutive models. Thus, they are not available for their use with PM4Sand and SDm. To overcome this limitation, the numerical modelling methodology presented in this document made use of "*user-defined*" L&K BC specifically coded for PM4Sand and SDm.

For elastic wave propagation problems, the L&K BCs are proven to be efficient in allowing energy radiation through the lateral boundaries of the model. However, for problems involving soil-liquefaction and lateral spreading, the efficiency of the L&K BC is hindered by the highly non-linear response of the soil. Thus, the need to assess the accuracy of these of boundary conditions for the case study of wharf BAF, at Gioia Tauro. Three different "*Free-field*" models were constructed by using three different approaches to model the radiation of energy through the lateral boundaries: models with L&K BC with (1) and without elastic buffer (2), and a reflected model (3). Moreover, a 100 m shorter version of the L&K was also tested. Note that the elastic buffer is reality model as a linear viscoelastic material with equivalent modulus degradation and damping properties reproduced by PM4Sand.

The relative effectiveness of the models listed above was evaluated with respect to the sensitivity exhibited by distribution of residual horizontal displacements. The analyses were made with reference to the native soil model shown in Figure 4.10, while Table A.2 reports the calibration parameters used for PM4Sand. The input motion was applied to the base of the model and, it corresponds record use in Chapter 4with an outcropping PGA (Ag) of 0.35g.

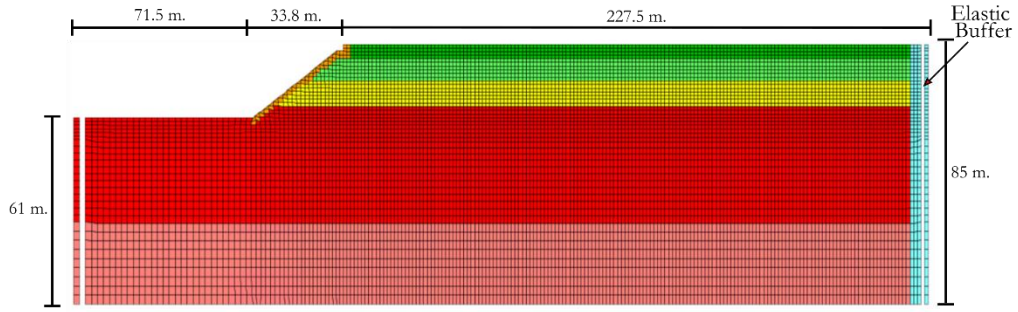

Figure A.5. Free-Field model for wharf BAF using L&K BCs with an elastic buffer.

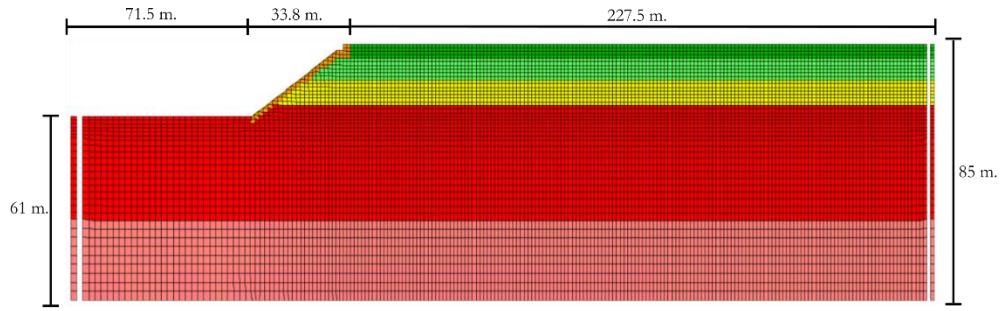

Figure A.6. Free-Field model for wharf BAF using L&K BCs without elastic buffer.

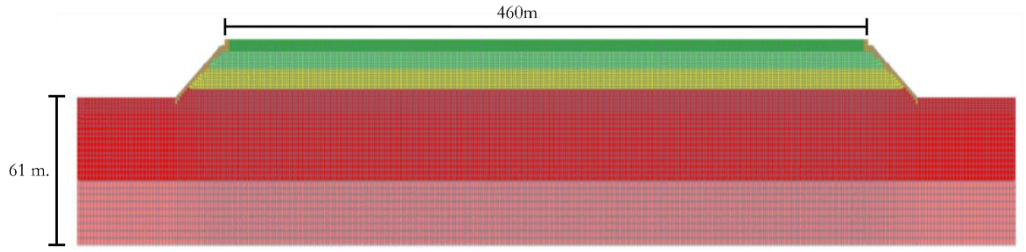

Figure A.7. Reflected free-field mode for wharf BAF.

Table A.2. PM4Sand parameters used for the lateral boundary-sensitivity analyses.

qc1ncs	Layer 1 (0-5m)	Layer 2 (5-12m)	Layer 3 (12-20m)
Dr	0.75	0.85	0.55
Go	1100	950	950
hpo	0.15	0.2	0.4
ho	0.6	0.6	0.6

Figure A.8 shows the distribution of residual horizontal displacement along the surface of each model. All the models resulted in comparable residual displacements near the waterfront, except for the L&K model with elastic buffer. Differences become more significant when moving away from the crest. When making the distinction between non-

uniform and uniform components of lateral spreading, it is apparent that the L&K models and the reflected model reproduce similar non-uniform lateral spreading displacements.

The model that employed an elastic buffer led to a more severe concentration of laterals spreading strains inside and behind the slope (see Figure A.9). It appears that the use of an elastic buffer created a lateral stiffness contrast that on one hand, restrained the lateral movement of the model, and on other, led to higher seismic demands transferred into liquefiable soil near the slope. Note that this could have been partially due to smaller strains being reproduced within the elastic buffer, which were lower than the 1D (cyclic) strains This meant that a lower reduction of the shear modulus occurred during shaking.

Far from the crest, the interpretation of the uniform lateral spreading component is less straight forward. In relative terms, L&K models provided the least amount of restraint against the lateral spreading, although it is unclear whether this represents a realistic condition. Nonetheless, the distance at which uniform spreading occurs, in terms of residual displacements, is almost the same for the short and longer versions of the L&K model.

In the case of the reflected model, as one moves away from the waterfront, residual displacements increased in the opposite direction, inside the mirrored portion of the model. This feature of the model response, as far as residual displacements are concerned, impeded the identification of the zone of uniform lateral spreading. Figure A.9 and Figure A.10 provide additional insights into the model response in terms maximum shear strains. As it can be noticed, non-uniform lateral spreading strains reached maximum values around 12%, for the reflected model, within the first 80 m measured from the crest of the slope. Inside the zone between 80 and 160 m from the crest, maximum strains gently reduced to 1D levels. Thus, this latter area is interpreted as the zone of uniform spreading.

As a summary Table A.3 reports results in terms of residual displacements computed at the crest (Δ_{Crest}), and the lateral boundary ($\Delta_{Boundary}$), and the difference of the two ($\Delta_{Lateral}$). The latter one isolates the non-uniform component of the lateral spreading displacement. However, as previously discussed, $\Delta_{Boundary}$ is quite sensitive to lateral boundary effects. In contrast, Δ_{Crest} exhibited less variability, as the results obtained for the L&K models and the reflected model were quite similar. Thus these models are considered effective in modelling the ground response in the vicinity of the slope.

Table A.3. Summary of the lateral spreading displacements obtained using different methodologies to model the lateral boundaries.

Model	**Δ_{Crest} (m)**	**$\Delta_{Boundary}$ (m)**	**$\Delta_{Lateral}$ (m)**
L&K short model	0.698	0.332	0.366
L&K short model	0.663	0.266	0.397
L&K short model with elastic buffer	0.806	-0.124*	0.94
Reflected model	0.638	0.093**	0.545

*Positive sign indicates movement towards the sea

$\Delta_{Boundary}$ **computed at 160 m from the crest

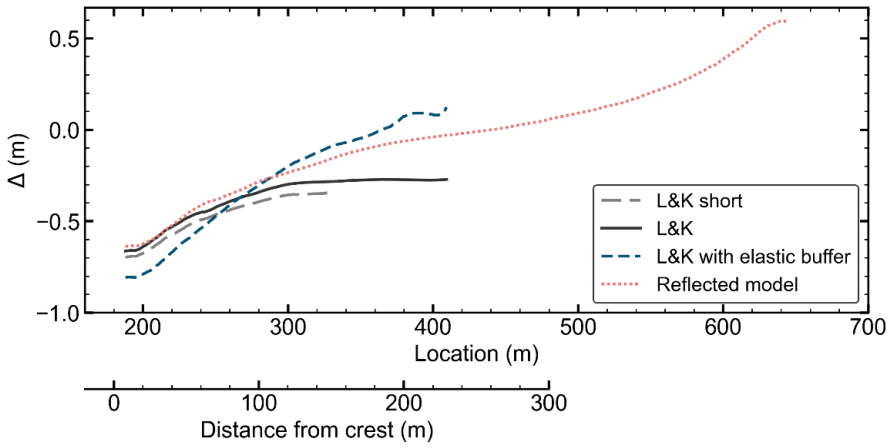

Figure A.8. Distribution of residual horizontal displacements obtained at the surface of the models shown in Figure A.5 (L&K short and long models), Figure A.6 (L&K with elastic buffer), and Figure A.7.

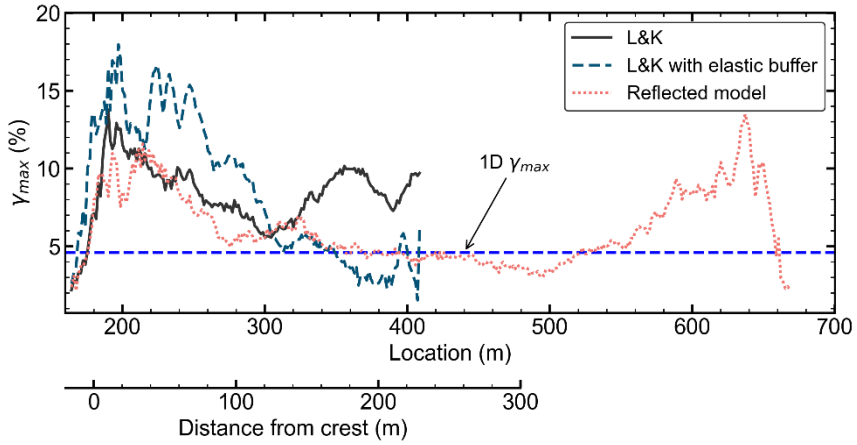

Figure A.9. Distribution of maximum shear strain recorded along the verticals comprising the models L&K (long version), L&K with elastic buffer and reflected.

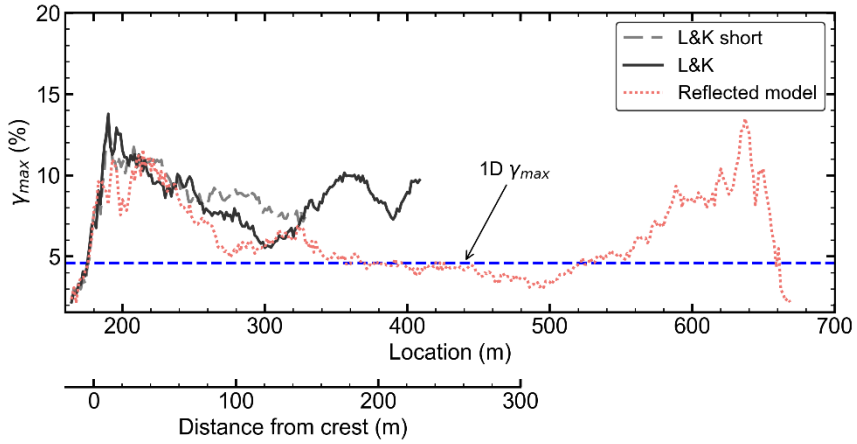

Figure A.10. Distribution of maximum shear strain recorded along the verticals comprising the models L&K (short version) and reflected.